Quark and Gluon Jets From Z^0 Decays Produced By e^+e^- Interactions at the LEP Collider

William John Maitland
Department of Physics and Astronomy
University of Glasgow

Thesis submitted for the degree of
Doctor of Philosophy[1]

April 5, 1994

ProQuest LLC.
789 East Eisenhower Parkway
P.O. Box 1346
Ann Arbor, MI 48106 – 1346

Abstract

This thesis describes a study of quark and gluon jets produced from decays of the Z^0 boson to $q\bar{q}g$ and $q\bar{q}\gamma$ final-states. These were obtained from 1.2 million hadronic events produced by the LEP e^+e^- collider and recorded in the ALEPH detector at CERN during 1990-92. A sample of gluon jets was obtained by identifying b-quark jets in $b\bar{b}g$ events where the b-quark had decayed semileptonically. Quark jets were identified in $q\bar{q}\gamma$ events where one of the jets contained an isolated photon. The mean particle multiplicity, transverse momentum, rapidity of tracks and fragmentation function of the quark and gluon jets were compared as a function of the energy of the jets. The angular size of the jet cores also were analysed to determine the relative particle multiplicity in the jet cores. The quark and gluon jet differences were found to be greatest in the jet cores compared to the whole jet. The gluon/quark jet ratio of particle multiplicities in the jet cores was found to be closer to the perturbative QCD prediction for gluon radiation from the partons.

The particle flow between the quark jets was measured in $q\bar{q}g$, $b\bar{b}g$ and $q\bar{q}\gamma$ events and compared to JETSET Monte Carlo predictions and a QCD calculation of the soft gluon flow in these event types. The JETSET predictions matched the particle flow data reasonably well, whereas the soft gluon calculation did not represent the data.

Acknowledgements

This thesis describes an analysis of data from the ALEPH detector collected during the period 1990-1992. The construction and operation of the detector and the preliminary analysis of data involved the efforts of a large number of people. The lepton-tagging method used to identify b-jets involved development by a number of people from the Heavy Flavour working group. Likewise, the isolated photon analysis used to select $q\bar{q}\gamma$ events was developed by a number of people from the $Q\overline{Q}\gamma$ working group. I would like to thank all members of the ALEPH Collaboration for their effort. I am also grateful for the help I have received from the support staff at CERN and at the Department of Physics & Astronomy in Glasgow.

Special thanks go to Mark Parsons and Ingrid Tenhave who wrote the lepton-tagging program that I used. Similarly I am grateful to Mike Smith, John Thompson and Stan Thompson for much help with the $q\bar{q}\gamma$ analysis. I also appreciate the advice and support given by Ron Settles and the other members of the QCD working group. I am indebted to Ian Knowles for advancing my theoretical knowledge of QCD and much assistance with my theory chapter. I would also like to thank my supervisor Robert Turnbull for his guidance during my studies and his painstaking proofreading of my thesis.

My Ph.D. studies have not just been about work. My time with Glasgow University has been memorable thanks to those people whose banter and adventures have made me laugh (rather often), whose company and activities have been so stimulating and who have encouraged me on the bad days. The following people places and organisations are acknowledged for helping to make it all worthwhile (All names are fictional and all comments have no intended bearing to any living person.):

Andy (for the north face of Ben Nevis); Bobby (for salted tea); Bomber (for possession of a very large stomach indeed); Boozy (for buying the pints and getting stuck in the ALEPH lift); the B.P. Mob (Graham & Lyn, Lesley, Stephen & Gill, for a roof over my head from time to time); The Cabin Boy (for the Weissbier); Café des Delices (deux litres de Gamay); Caffeine Man (for the chillie wars, Alternative Supervisor and much mad chicken disease); The Capricorn Mountaineering Club (for so many wild weekends in the Highlands); The Caledonian Brewery (for Deuchars IPA); Capi' (for much fun and laughter); Carol-Anne (for liquid refreshments); CERN van (Hey....I think I'll have one too); Clog (for much encouragement); coffee (of the thick, dark, sludgy 11am variety, the morning starts here); Eric ("Bring me sunshine"); Et Al (for Foxtrot Alpha Tango on Central Station at 6:30am); The Friday meeting; G'daymateursitgoin' ("fancy a coffee?"); The GFT (for so many good flicks); GLPHV3 (for not wiping my thesis off the disk....I see you have the machine that goes....Well hello Special

Lover!!); George Formby (and other rhyming slang); George the Janny (for his mail deliveries and witty humour); The Good Parson (for getting professional about his programming, his mutual support and entertaining nicotine withdrawal symptoms); The Gouda Cheese Kid (for much coffee brewed); Grassy ("Quebec Charlie Delta to the floor of Charlie's"); H.J. (for his bum slide in leather shorts and for insisting on wearing gargoyles); The Highlands and Islands of Scotland (the place to be); Hitman (for his study of population dynamics); The IBM (stoke her up); The I.C. Mob (Dave, Jane, Jeremy, Gavin and Ann for rescuing a dazed Wullie from Les Contamines); Jazz Metro; Jim (for SC Gully, Glencoe and other rambles); Jimmy Mac the Enforcer (for the BarBQ's); Jethro (for farming tips); The Laser Team (for many fun and frustrating hours down t'pit); Mad Doug (for being mad); Monte Blanc (for appearing on sunny days); Mr Bean; Mr Big (for guidance in ale matters, for loan of his turn-ups and bonnet, also "Allumez vos phares"...."pigsmeat", "frrr", "Doucement!!", "students...boot" etc); Parc des Bastions (for hours of contemplation); Pat (for giving me directions to his house from the phone box at the bottom of his driveway); The Polmont Joggers (for making me run occasionally); Prickler (for falling out of things); Le Reculet (for being the view from the office window); The Rev. Hippy (for clapped out Morris); Rigor (for encouragement); Ron and the Research Club girls (for serving liquid refreshments and good humour); Sav (for his skills with a sharp knife on Ben Narnain, but what is this "castara simpatica"?); The SERC hitsquad (for ensuring that all is in order); The Skipper (for letting his hat roll down the Cornettes des Bises and for driving me through Florence during rush hour); The Spanish Inquisition (for less nagging); Stu' (a fellow scribbler at the end); Student Grant (for gate-crashing Spanish parties with me); The Super Caravelle (few things in life are more decadent); Swiss customs officials; Tennant's Bar (home from home); Thomas (for the Bishorn, Mont Blanc de Tacul, Pollux and other high points); The Tory Councillor (for sticking to his misguided ideals); Tucker (but me name's Dave! The CERN Famine, for ensuring that we ate every night at 6pm on the dot.); The Velos (for drawing blood only once, ride-'em cowboy!); Viz (for 20 things you never knew about the French); Von Vrrrh; The Weans (Master Farfalla, Mutley and the SiFi twins, for the "'Tache-away Point" and plenty of "ho ho" and "Salut"); Wee Val (for the fun times); Where's Rent Boy (for his orange joke and for so many hilarious predicaments); Whispering Pete ("Where's yer jacket gone, it was here 5 minutes ago!"); The Wibbler ("the veins cannae take it Cap'n, he's going to explode, set Wibbler to stun, it's a complaint Jim, but not as we know it"); Yankee Jeeem (for his green box and so many rides in his magnificent automobile); Yob (for producing Christmas crackers in the bothy).

Contents

List of Figures

List of Tables

Chapter 1

Introduction.

1.1 The fundamental structure of matter.

According to current understanding, two types of elementary particles exist, those with $\frac{1}{2}$ integer spin called fermions, and those with integer spin called bosons. Matter is built up from these particles, which are held together by four fundamental interactions, the strong and weak nuclear forces, electromagnetism and gravity. Below the scale of the atom the effects of gravity are generally insignificant, so it will not be discussed in any detail here. The forces can be described by gauge field theories, in which the responses between fermions are mediated by bosons. These are summarised in Table 1.1. Incorporated into the framework of the theories are symmetries, which give rise to the properties of the interactions. The introduction of the symmetries into the theories gives the raison d'etre for the gauge bosons.

1.2 Electroweak interactions and the Standard Model.

Quantum electrodynamics (QED), the field theory describing electromagnetism, involves the symmetry group $U(1)$ [1]. Transformations under this symmetry can be considered as rotations in complex phase space, which can be performed in any order. Symmetry groups whose transformations commute are known as abelian groups. A consequence of this abelian nature is that charge must be locally conserved, so that the boson propagator of the $U(1)$ group, the photon, cannot carry charge and thus cannot form self-interactions. The perturbative calculation of QED cross-sections involve higher-order internal loop processes which are divergent. However the theory is renormalisable, such that the

Interaction	*Symmetry group*	*Gauge bosons*	*Fermion interactions*
Electromagnetism	$U(1)_Y$	photon	quarks, charged leptons
Weak	$SU(2)_L$	W^+, W^-, Z^0	quarks, leptons
Strong	SU(3)	gluon (8 flavours)	quarks
Gravity	SL(2,C)	graviton	particles with mass

Table 1.1: Summary of the four forces in nature.

predicted interactions between the fermions are finite. The renormalisation introduces an effective charge, mass and wave function for the electron, governed by a coupling constant α which determines the strength of the coupling of the electron to the photon.

The theory of electromagnetism has been combined with weak theory to form the theory known as the Standard Model of electroweak interactions [2], where the couplings of the bosons are unified at energies of $\sim 10^{15}$ GeV. The Standard Model is an $SU(2)_L \otimes U(1)_Y$ gauge theory, that is, it is symmetric under both the $SU(2)_L$ and $U(1)_Y$ groups. Compared to the $U(1)$ group, transformations under $SU(2)$ are more complex, involving a set of 2×2 unitary matrices with determinant 1. These do not commute, so the $SU(2)$ group is non-abelian. To maintain invariance of the theory under local $SU(2)$ transformations, the additional gauge bosons, known as the W^+, W^- and Z^0, carry weak charge and can undergo self-interactions. The symmetries in the theory are broken by the Higgs mechanism to give masses to the W^+, W^- and Z^0. Local non-abelian gauge theories have been proved to be renormalisable, such that the weak interactions are finite.

In the Standard Model there exists three generations of fermions organised in a hierarchy according to mass. Each family consists of a neutrino, a charged lepton, an up-type quark and a down-type quark, plus the antiparticle of each fermion. These particles are summarised in Table 1.2. The existence of all these fermions and the four electroweak gauge bosons have been shown experimentally in high energy interactions, apart from the top quark and tau neutrino. However these are required to exist within the framework of the Standard Model and high precision electroweak measurements are strong evidence for the existence of both the top quark and tau neutrino. The measurements indicate that the top quark

will probably be seen by the CDF and D0 experiments at Fermilab.

1.3 Quantum chromodynamics.

Leptons are influenced by electromagnetism, the weak nuclear force and gravity. Quarks also feel the strong nuclear force, which is described by quantum chromodynamics (QCD), a gauge theory with $SU(3)$ symmetry [3]. The bosons carrying this force are the gluons. There is strong experimental evidence both for the existence of gluons, and that $SU(3)$ is the correct symmetry group in the theory [4]. QCD introduces an additional quantum number called colour. The strong nuclear force is considered to act between particles with colour charge in the same way that electromagnetism acts between particles with electric charge. The theory involves three types of colour charge. Each quark is given a red, green or blue colour charge for example, whilst each antiquark has anti-red, anti-green or anti-blue colour charge. Transformations under $SU(3)$ involve a set of 3×3 unitary matrices with determinant 1. These do not commute, so QCD is a non-abelian gauge theory. To maintain local invariance of QCD under its transformations, the gluon propagators must carry colour charge and can form self-interactions via tree level three-gluon and four-gluon vertices. This has a large influence on the properties of QCD, in particular at low energies where the coupling of the gluons, α_s, increases rapidly and "confinement" occurs, such that the quarks and gluons are bound together to form hadrons. The strength of α_S at low energies has consequences for the calculation of the interactions of quarks and gluons, since perturbation theory cannot be used in this regime. Another property of QCD is that of asymptotic freedom, where the coupling goes to zero as the separation becomes small, equivalent to high momentum transfer Q^2.

	Generation		
	1	2	3
Quarks	Up Down	Charm Strange	Top Bottom
Leptons	e-neutrino Electron	μ-neutrino Muon	τ-neutrino Tau

Table 1.2: The three generations of fermions in the Standard Model.

1.4 Z^0 boson production at the LEP Collider.

The Large Electron Positron Collider, LEP, at CERN, Geneva has a primary purpose of investigating electroweak interactions [5]. Electrons and positrons are accelerated in opposite directions inside a 27 kilometre beam pipe to energies of 45.6 GeV (see Figure 1.1). The e^+ and e^- are collided with a total centre of mass energy of 91.2 GeV. This energy is very close to the mass of the Z^0 boson and at a resonance in the cross-section for the interaction of the e^+ and e^- via the production and decay of a Z^0. The basic process is depicted in the Feynman diagram in Figure 1.2. The Z^0 boson produced in the interaction decays to a fermion and anti-fermion pair ($f\overline{f}$), each carrying away half the centre of mass energy. Excluding the top quark, any of the fermions within the Standard Model can be produced. The ALEPH experiment has been designed to observe the decays of the Z^0. The detector is located around the beam pipe at one of the collision points of the e^+ and e^- beams, and is described in Chapter 3.

1.5 Radiation of gluons and photons in Z^0 decays.

The cross-section for $f\overline{f}$ production is modified by higher order processes such as initial-state radiation from the e^+ and e^- (Figure 1.3a), final-state radiation from the fermion or anti-fermion (Figure 1.3b), or internal loops. When a $q\overline{q}$ pair is produced, either the q or $\overline{q}$ may radiate a hard photon or gluon. To first order these processes are similar, but differ in the strength of the coupling of the quark to each boson. The quark, antiquark and hard gluons may then lose energy by further radiation of gluons. At some energy scale, the quarks and gluons present form hadrons, which appear in the detector as jets of particles, pointing in approximately the same direction as the original hard partons.

1.6 Gluon radiation and hadronic jet formation.

The radiation of photons or gluons from quarks can be calculated in perturbation theory. However the production of hadrons in $q\overline{q}\gamma$ and $q\overline{q}g$ events is also partly a non-perturbative process, which cannot at present be calculated. The hadronic jet formation process is described in more detail in the following chapter. By studying the jets and the particle flow in these events, an attempt can be made to assess the influence of perturbative and non-perturbative mechanisms in hadronic events.

The analyses presented in Chapters 4 - 6 has made use of over 900,000 hadronic Z^0 decays recorded in the ALEPH detector in 1990, 1991 and 1992. These statistics were sufficient to select particular types of event where the jets

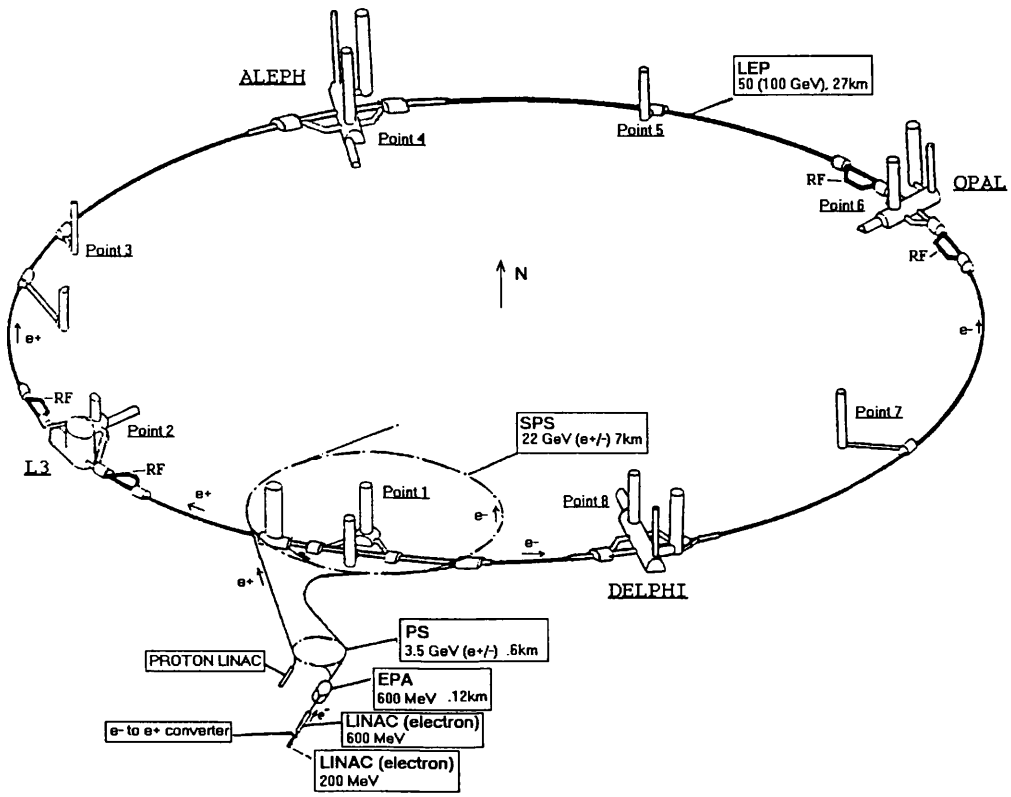

Figure 1.1: *Diagram showing the main features of the LEP collider.*

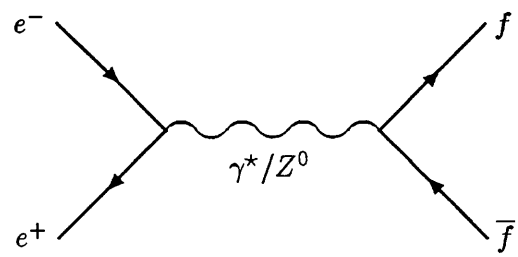

Figure 1.2: *The process* $e^+e^- \longrightarrow f\overline{f}$ *at LEP.*

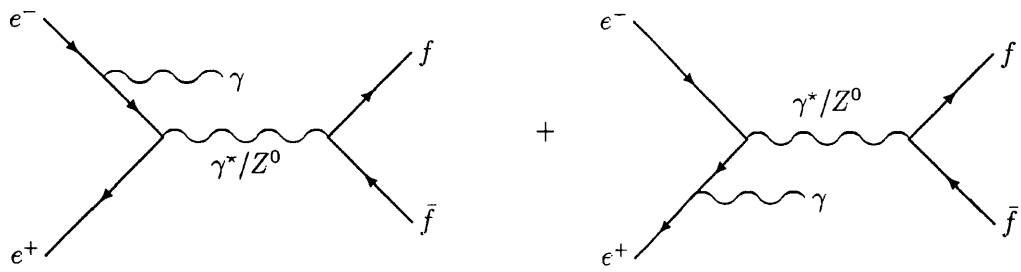

(a) Initial-state radiation from the e^+ or e^-

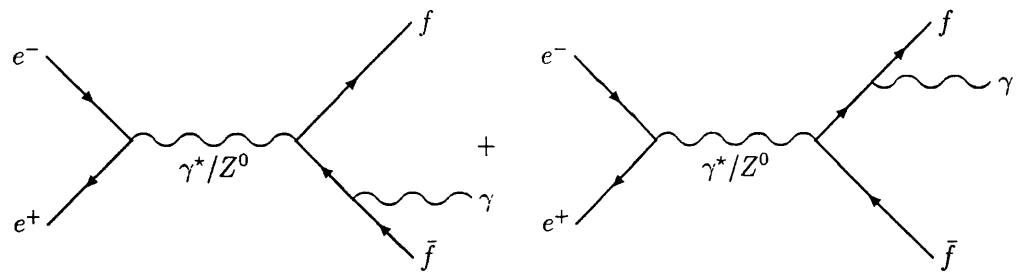

(b) Final-state radiation from the f or $\bar{f}$

Figure 1.3: *The lowest-order processes giving rise to initial-state or final-state radiation at LEP.*

emanating from quarks and from hard gluons could be readily identified. The capability to pick out photons and leptons in the hadronic data was used to distinguish $q\bar{q}\gamma$ events and pinpoint jets from b and c quarks in $q\bar{q}g$ events. This enabled a clear comparison to be performed of quark and gluon jets with a range of energies (Chapter 5). The particle flow in between the jets was also compared to a perturbative calculation of the soft gluon flow in the event (Chapter 6). From these analyses conclusions are drawn in Chapter 7 about the role of perturbative physics in describing the jet formation process.

Chapter 2

Hadronic jets from e^+e^- collisions.

2.1 The process $e^+ + e^- \longrightarrow$ hadrons.

The formation and decay of the Z^0 boson in e^+ e^- interactions was outlined in the previous chapter. The most common decay mode of the Z^0 is to a $q\overline{q}$ pair, as depicted by the Feynman diagram in Figure 2.1, with the q and $\overline{q}$ each carrying half the Z^0 energy. As the q and $\overline{q}$ move apart, they "fragment" into jets of hadrons due to the strength of the strong nuclear force. This Z^0 decay is thus seen as a pair of back-to-back jets in the detector. In Figure 2.2 a two-jet event is depicted on the ALEPH event display. At LEP energies, events commonly occur with three, four or more hadronic jets. These multi-jet events provide strong evidence [4] for the existence of gluons as the bosons mediating strong interactions. In the case of a three-jet event (Figure 2.4), the basic process is the radiation of a hard gluon by the primary q or $\overline{q}$, as shown in Figure 2.3. A four-jet event (Figure 2.6) can be initiated in several different ways. Both q and $\overline{q}$ can radiate a hard gluon (Figure 2.5a), or one primary parton can radiate two hard gluons (Figure 2.5b). Alternatively, one hard gluon may be radiated, which can itself radiate a gluon or split into a $q\overline{q}$ pair as depicted in Figures 2.5c and 2.5d.

2.2 Multi-jet events.

The number of jets in a hadronic event can be defined using a jet-clustering algorithm. These involve some measure of the separation between particles and a method of combining the momentum and energy of the tracks if their separation is small. The "JADE" algorithm [6] has been used in many analyses to cluster hadrons into jets. Here an invariant mass M_{ij} is computed for each pair of tracks

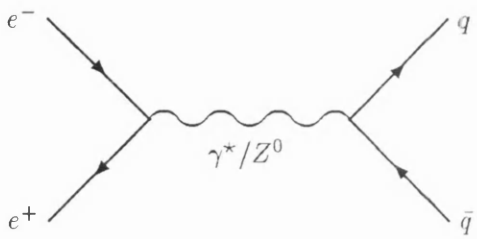

Figure 2.1: *The process* $e^+ + e^- \longrightarrow q + \bar{q}$ *at LEP.*

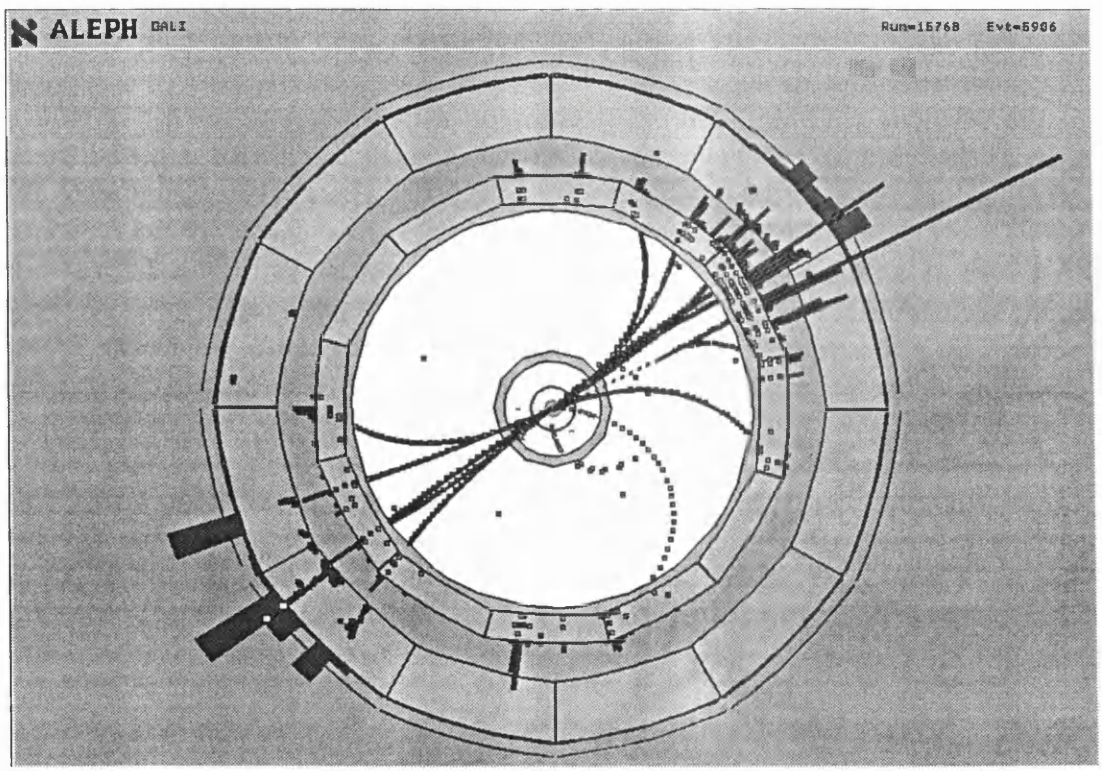

Figure 2.2: *ALEPH event display depicting a two-jet event recorded in the detector. This shows an end-view through the barrel section with hits in the tracking chambers and energy deposits in the calorimeters.*

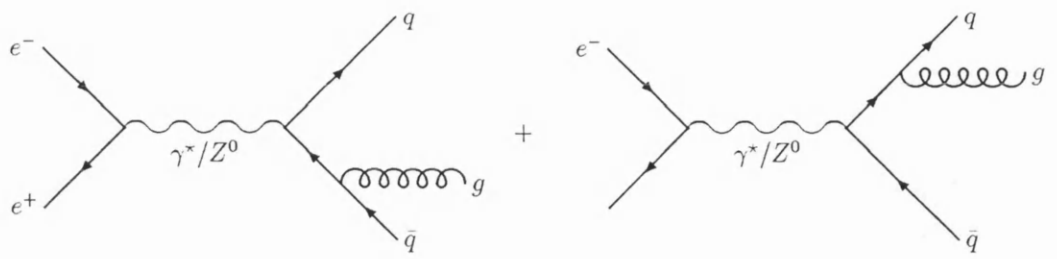

Figure 2.3: *The lowest-order processes which give rise to a 3-parton final-state at LEP.*

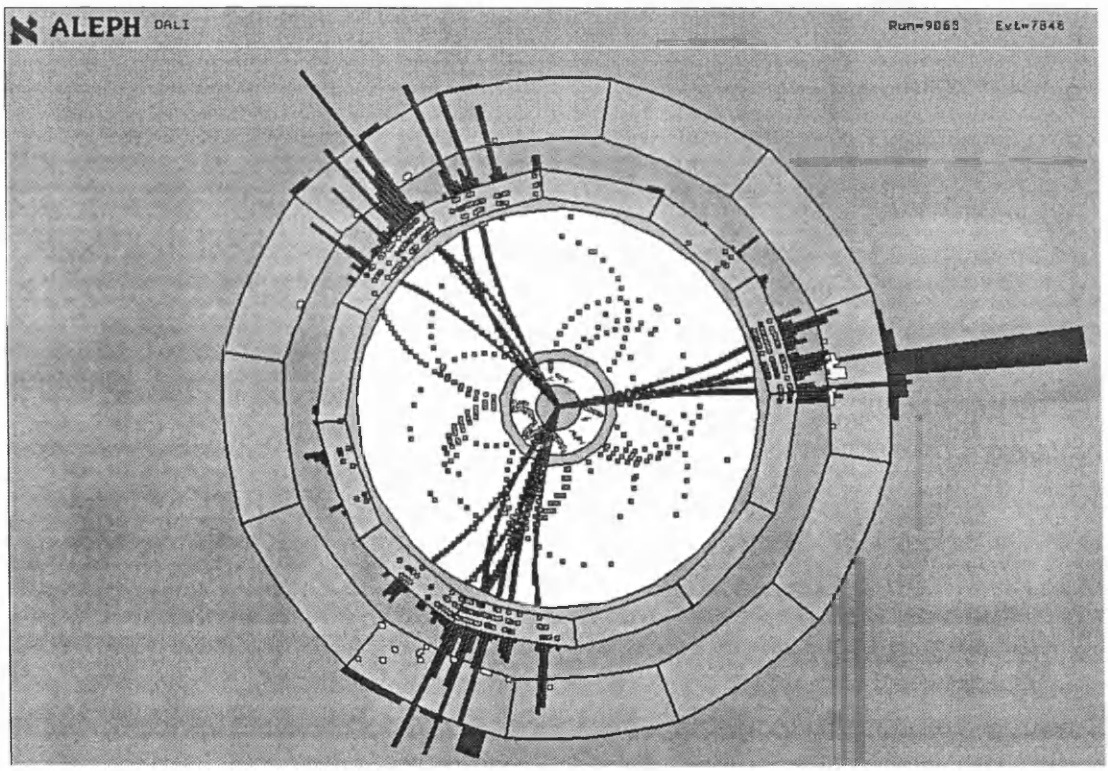

Figure 2.4: *ALEPH event display depicting a three-jet event recorded in the detector. This shows an end-view through the barrel section with hits in the tracking chambers and energy deposits in the calorimeters.*

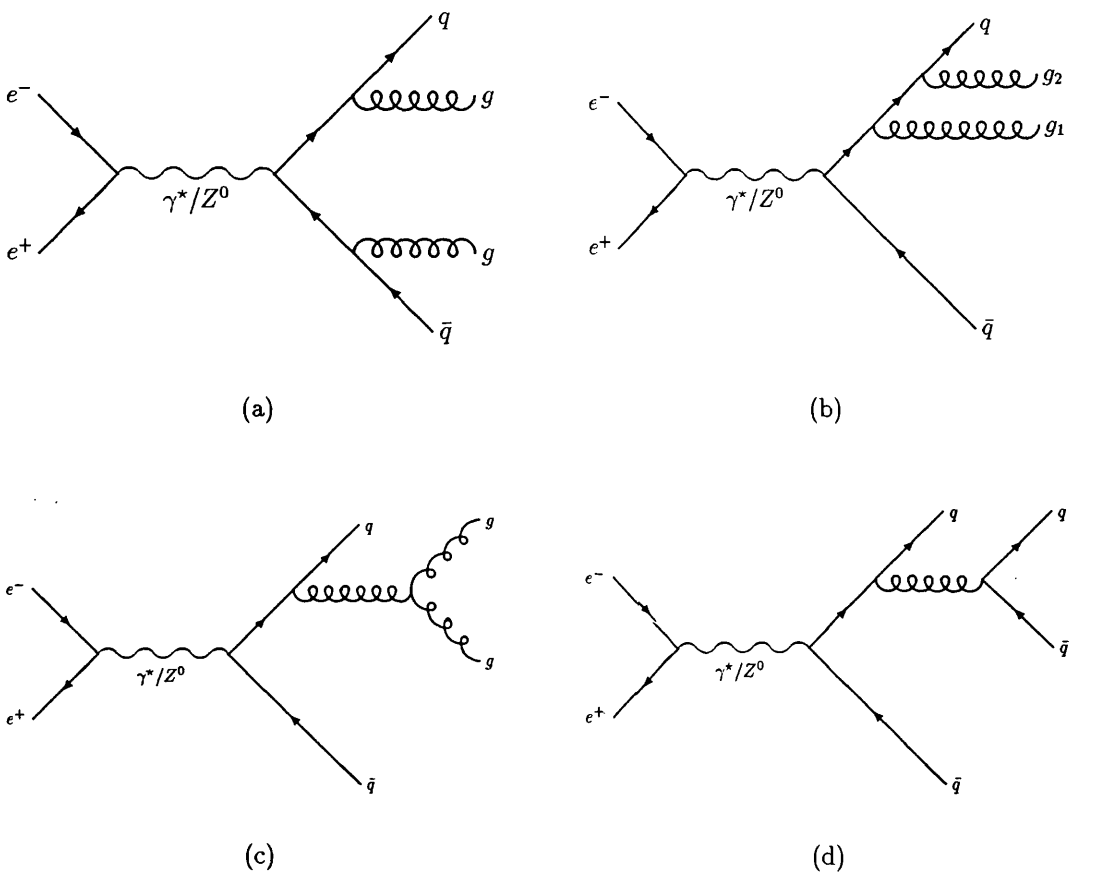

Figure 2.5: *Examples of the lowest-order processes which give rise to a 4-parton final-state at LEP. This list of diagrams is not exhaustive since some terms involving gluon radiation from the antiquark and terms with the gluons crossed have not been included.*

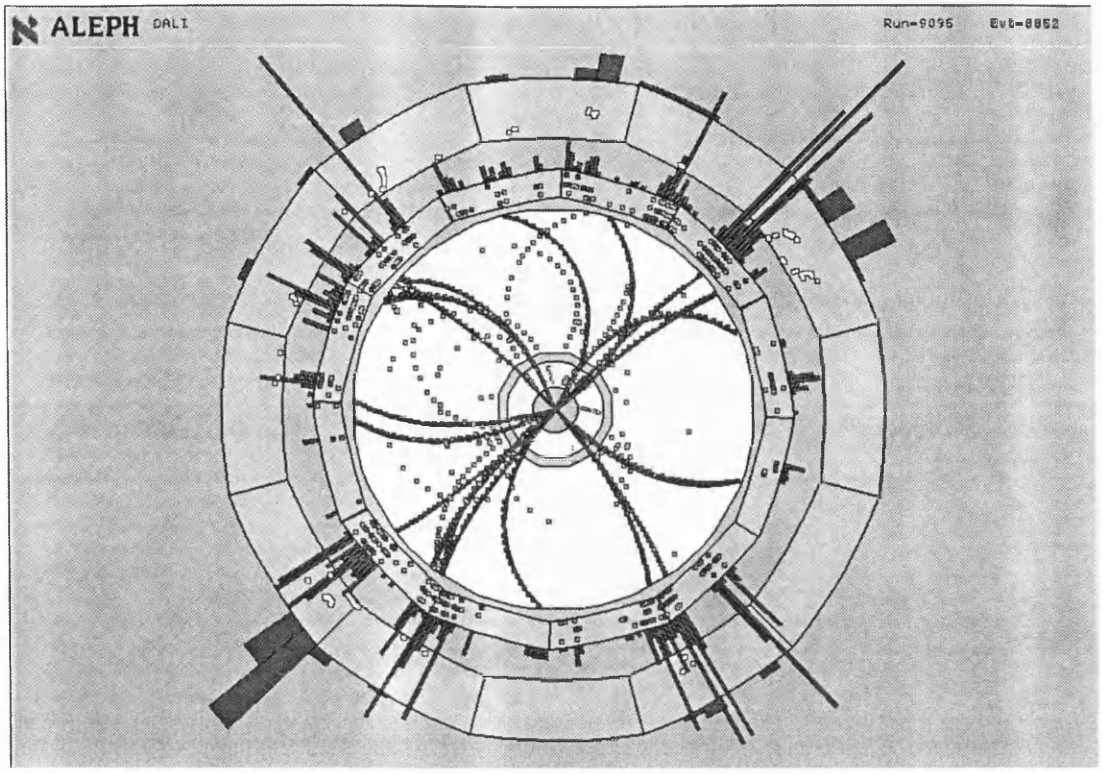

Figure 2.6: *ALEPH event display depicting a four-jet event recorded in the detector. This shows an end-view through the barrel section with hits in the tracking chambers and energy deposits in the calorimeters.*

i and j, given by the formula:

$$M_{ij}^2 = 2E_iE_j(1 - \cos\theta_{ij})$$

The pair of particles with the lowest invariant mass are then merged to form a "pseudo-particle" with a combination of the momentum and energy of the two particles. M_{ij}^2 is recomputed for the pseudo-particle and the remaining tracks. This process is repeated until the invariant mass between all the remaining particles and pseudo-particles is greater than some user defined cut-off y_{cut}, given by:

$$y_{cut} = \frac{M_{ij}^2}{E_{TOT}^2}$$

Scheme	E	E_0	P
Energy	$E_{ij} = E_i + E_j$	$E_{ij} = E_i + E_j$	$E_{ij} = \|p_{ij}\|$
Momentum	$p_{ij} = p_i + p_j$	$p_{ij} = \frac{E_{ij}}{\|p_i+p_j\|}(p_i + p_j)$	$p_{ij} = p_i + p_j$

Table 2.1: *Combination schemes for the JADE clustering algorithm.*

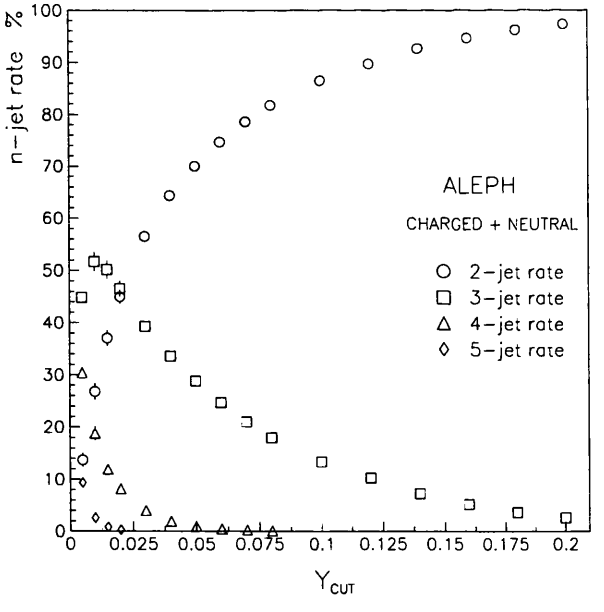

Figure 2.7: *Jet rates measured by ALEPH using the JADE jet clustering algorithm with E combination scheme.*

The clusters that remain are taken to be the jets. The tracks can be combined together according to different schemes, which are summarized in Table 2.1. The E scheme combines the tracks in a Lorentz invariant way that leads to pseudoparticles with mass. However in QCD calculations jets are generally treated as massless objects. The other combination schemes combine 4-vectors to form massless objects.

The jet rates measured by the ALEPH Collaboration [7] are shown in Figure 2.7 for the E scheme. The jet rates for the JADE algorithm have been calculated using second-order QCD perturbation theory [8]. This calculation has been fitted to the data to obtain values for α_s. Due to the effect of higher-orders, the 3- and 4-jet rates are incorrect in the calculation. To obtain a better fit to the data, an optimised QCD scale was used. The coupling constant $\alpha_s(\mu^2)$ at a particular renormalisation scale μ^2 is related to the QCD scale parameter $\Lambda_{\overline{MS}}$ by

$$\alpha_s(\mu^2) = \frac{12\pi}{(33-2N_f)\ln\left(\frac{\mu}{\Lambda_{\overline{MS}}}\right)^2}\left[1 - 6\frac{(153-19N_f)}{(33-2N_f)^2}\frac{\ln\left[\ln\left(\frac{\mu}{\Lambda_{\overline{MS}}}\right)^2\right]}{\ln\left(\frac{\mu}{\Lambda_{\overline{MS}}}\right)^2}\right]$$

where N_f, the number of active flavours is 5. $\Lambda_{\overline{MS}}$ and the scale μ^2 are not determined by perturbation theory and have been obtained by fitting the second-order jet rates to data [9]. More recently, the jet rates have been determined using the DURHAM clustering algorithm [10]. This operates in a similar manner to the JADE algorithm, but the invariant mass squared is replaced by:

$$M_{ij}^2 = 2\min\left(E_i^2, E_j^2\right)(1-\cos\theta_{ij})$$

This is a measure of the transverse momentum k_T of each particle with respect to the other particle. This algorithm clusters softer particles in a more intuitive manner than JADE, where they can be clustered to form separate jets. Another advantage of the k_T-based DURHAM algorithm is that it allows a good approximation of the QCD jet rates calculation to all-orders. The leading logarithms and next-to-leading logarithms for each order in the calculation can be summed leaving only the subleading terms. This calculation gives a good fit to the data [11] for a large variation in the scale parameter μ^2, including $\mu^2 = M_Z^2$. Various measurements of α_s by ALEPH [11, 12] are summarized in Table 2.2. The result using the all-orders summation predictions gives a lower error than the exact second-order calculations and is compatible with the other measurements

Method	*Measured* $\alpha_s(M_Z)$ *value*
QCD *corrections to* Z^0 *line shape.*	0.118 ± 0.018
Second-order differential 2-jet rate using JADE E_0 *clustering algorithm.*	0.121 ± 0.008
Second-order energy-energy correlations	0.117 ± 0.005
Hadronic τ*-decays*	0.118 ± 0.005
All-orders resummed predictions for differential 2-jet rate, heavy jet mass and thrust variables.	0.125 ± 0.005

Table 2.2: *Summary of* $\alpha_s(M_Z)$ *measurements by ALEPH.*

2.3 Fragmentation.

The jet formation process is known as "fragmentation". This is depicted in Figure 2.8. With the assumption of "local parton-hadron duality", perturbative QCD can successfully predict the jet rates, particularly if higher orders are approximated. This is represented by the perturbative region (i) in the schematic diagram. After a certain amount of gluon radiation, the virtuality for the interactions of the partons drops and α_s increases. At some point α_s becomes sufficiently large that perturbative QCD is no longer valid. In the absence of any simple QCD description at this scale, a number of phenomenological Monte Carlo models [13]- [21] have been devised to describe the non-perturbative region (ii). This stage in the jet formation process is known as "hadronisation", since it is here that "colourless" hadrons are formed from the colour-charged partons. The final stage of fragmentation (iii), involves the decay of unstable hadrons. The lifetimes and branching ratios for many decays have been measured and the results incorporated in the Monte Carlo models. A simulation of the effects of detectors on the hadrons is often added to the Monte Carlo so that the prediction can be compared directly with experimental measurements.

Perturbative QCD can be used to predict certain inclusive distributions where

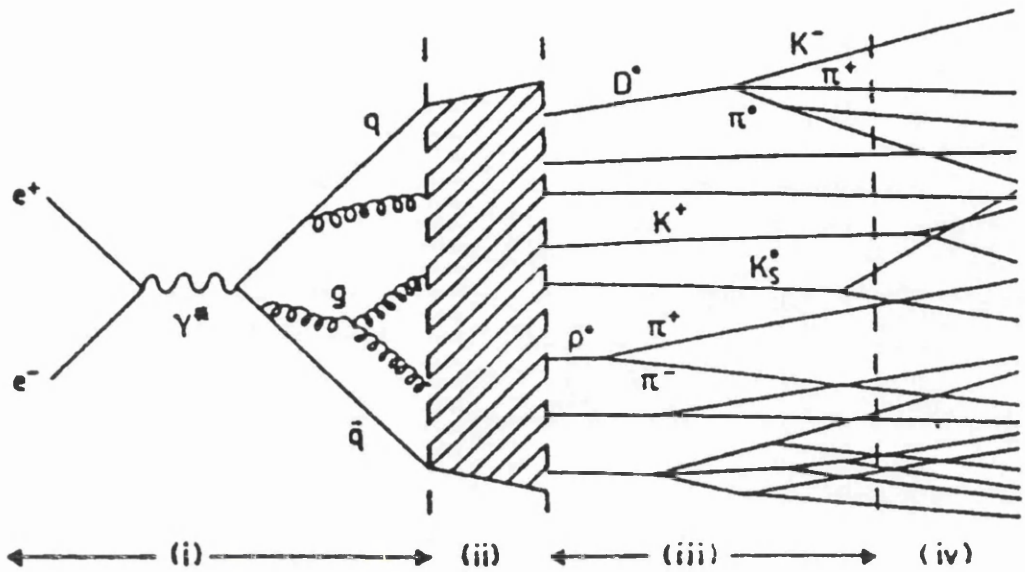

Figure 2.8: *Diagram depicting the various stages on the fragmentation of partons into hadrons.*

the local parton-hadron duality hypothesis can be applied. This states that the hadron distributions follow the parton distributions. The hypothesis originated from analytical studies of the inclusive momentum spectra of partons compared to hadrons [22]. Perturbative QCD also predicts successfully the energy-energy correlations and the thrust distributions of hadrons. The calculations cannot be applied to event features which are not infrared safe. Furthermore, perturbative QCD is not able to predict the final hadron species produced in fragmentation, although the theory does involve flavour generating mechanisms.

The prediction of the inter-jet particle flow in three-jet events can be made using analytical QCD with certain approximations. This is outlined in Sections 2.6.1 - 2.6.4. Perturbative QCD cannot be used to describe all the features of hadronic events. Instead Monte Carlo models are used which have the perturbative physics incorporated together with some mechanism for generating the non-perturbative physics.

2.3.1 Monte Carlo fragmentation models.

The purpose of Monte Carlo fragmentation models is to attempt to describe fully the features of hadronic events, and to give further understanding to the underlying fragmentation mechanisms. The models tend to be subdivided into the processes depicted in Figure 2.8. The perturbative QCD process (Stage i) can be treated using an exact second-order matrix element calculation, or more commonly using leading-logarithm approximations, known as the parton shower approach, which gives a better description of the shape of events. The nature of hadronic events is influenced by coherence effects, where the radiation of soft gluons at wide angles for successive gluon radiation is suppressed. If a parent parton radiates a gluon and either of these partons then radiates a softer gluon, where the softer gluon is radiated at an angle greater than the first branching, it acts as if it were radiated from the initial parton. This is equivalent to ordering in the emission angles of gluons.

Hadronisation (Stage ii) is treated in several different ways in the models. Independent fragmentation was first used to describe the fragmentation of a jet [13]. In this method hadrons are split off from each parton, leaving it with scaled down energy. An energy-independent fragmentation function is used to describe the fraction of the remaining energy removed by each hadron. Independent fragmentation models have fallen into disrepute and are rarely used in LEP studies, since they do not model the data well, particularly in three-jet events [23, 24]. This may be due in part to the lack of theoretical study of these models, however other models now exist with more intuitive features. Collinear divergences can cause problems with independent fragmentation models and they can also suffer from non-conservation of flavour, energy and momentum. Instead of independent fragmentation, two hadronisation schemes are widely used, known as cluster fragmentation and string fragmentation. These are embodied in the HERWIG and JETSET models, which are described briefly in the following sections.

Cluster Fragmentation in the Herwig model.

In the HERWIG model [20], a parton shower is used to describe the perturbative stage of the jet fragmentation. This follows the modified leading-logarithm approach with coherence effects implicit in the process. At some shower cut-off scale, specified by a parameter in the model, the gluons present are split into quark-antiquark pairs. The non-perturbative region is treated using "preconfinement", with the quarks and antiquarks combined to form colourless clusters with cluster mass of a few GeV. The clusters are considered as superpositions of a series of broad resonances. The cluster decays are treated as two body decays which are dominated by phase space, with the decays isotropic in the rest frame of the cluster. Each allowed cluster decay channel is given a weight according to the

density of states of the decay products. This gives a very simple treatment of hadronisation, with few free parameters in the model.

String Fragmentation in the Jetset model.

The JETSET model [21] uses either a parton shower or the second-order matrix element calculation to generate the perturbative stage of fragmentation. In the non-perturbative region a linear confinement principle is evoked, with the colour field lines from each colour charge confined between the partons. This colour flux tube is approximated by a string at its centre, stretched between the partons, and with constant energy per unit length of $\sim$1 GeV/fm. As the partons move apart, the string between is stretched such that the potential energy of the string increases. At some point the string may break by the production of a quark-antiquark pair, with each joined by a string-piece to one of the original partons. Further breaks in the string-pieces may occur if their invariant mass is large enough. During this process, the remaining string pieces form the hadrons. Where a string break occurs, an energy-independent fragmentation function is used to describe the fraction of energy taken by each string-piece. This fragmentation function is symmetric and can be applied to either end of the string, as the string breaks are causally disconnected.

Where there is only a quark and antiquark present after the perturbative step, the string is stretched directly between the two partons. If in addition there are gluons present, these are treated as kinks in the string, with each gluon attached to two string pieces. This formulation, unlike Independent Fragmentation models, is safe from collinear divergences. In the limit of vanishing gluon energy, the two parton string picture is regained, so string fragmentation is infra-red safe. As a consequence of the gluon having two strings attached, the ratio of the gluon to quark string force is two. Compared to cluster fragmentation, this allows more scope for quark and gluon jet differences to arise in the non-perturbative hadronisation stage. The effect of the string model on gluon jet fragmentation is discussed further in Section 2.6, where the string is seen to have an influence on the particle flow in three-jet events generated using JETSET.

2.4 Final-state radiation from quarks.

Photon radiation from leptons is a QED process which can be successfully calculated using perturbation theory. Quarks carry charge, enabling them to radiate photons in the same way as leptons, but with a lower coupling to the photon due to the fractional charge of quarks. Photon radiation from quarks is complicated by competion with gluon radiation. The lowest-order Feynman diagram for photon radiation from a final-state quark is shown in Figure 2.9.

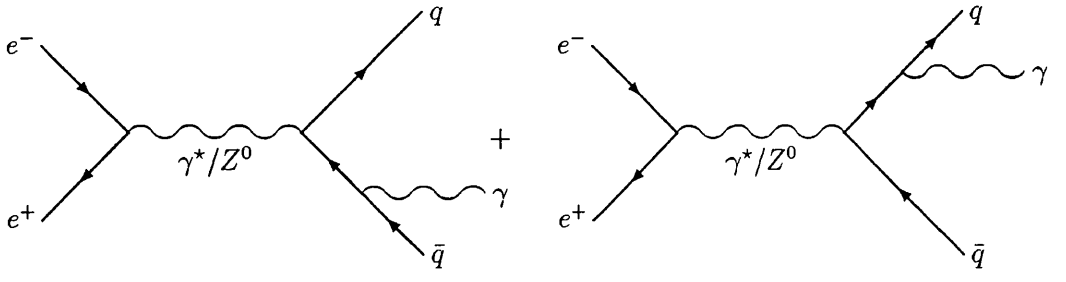

Figure 2.9: *Final-state radiation from the primary q or $\bar{q}$ at LEP.*

Comparing this to Figure 2.3, where a gluon is radiated from the final-state quark, it can be seen that to first-order the two processes are similar. The relative rates for these two processes to first-order is given by the ratio of the coupling of the quark to the photon or gluon, that is $e_q^2\alpha_{QED}/C_F\alpha_S$. The higher-order processes are more complicated in QCD, due to the effects of colour and the triple and quartic-gluon vertex.

When combining photon and gluon radiation together, the calculation of the rates of events with multi-jets and photons becomes more involved [25]. After the first radiation of a photon or gluon, the energy of the quark available for further radiation is reduced. Furthermore, the quark recoils during emission to conserve transverse momentum. There is also the problem of time-ordering, where the photon can be emitted before or after gluon radiation. It was explained in Section 2.3.1 that when gluons are successively radiated from a quark, angular-ordering occurs, and the later gluons are emitted with lower transverse momentum. Using the same idea, if a soft photon is emitted from a quark with a transverse wavelength which is long compared to the interaction region, then it cannot resolve the details of the interaction, and must be emitted at a later time than the gluon. The order of photon and gluon emission thus depends on the relative energies that each carries. In events with two jets and an isolated photon, the photon has high transverse momentum with respect to the jet axis, so it is likely to have been emitted before gluon radiation had occurred. In events of this type, the initial radiation of the photon is thus kinematically similar to the radiation of a hard gluon, which initiates a three-jet event. By comparing these two event types, the effect of the radiation of a hard gluon on the perturbative and non-perturbative stages of fragmentation can be studied.

The rates of events with an isolated photon and a number of hadronic jets has been studied by the LEP collaborations and compared with Monte Carlo results. The analyses involve clustering of hadronic events using a jet algorithm,

identification of photons from a background of neutral hadrons and some form of isolation criterion to define a photon from final-state radiation. Contradictory results have been obtained because the event cuts used in each analysis can limit the available phase space to measure photon emission in different ways. The isolation condition for the photon has been defined using an isolation cone method [26, 27] and using a jet clustering algorithm [28]. However, if either of these methods is introduced in the theoretical calculations, then problems such as infrared singularities can occur.

2.5 Gluon jets.

Three-jet events from e^+ e^- collisions were first seen by the TASSO Collaboration at the PETRA collider, running at a centre of mass energy $\sqrt{s}$ of 27 GeV [29]. These provided evidence for the existence of gluons. Less was known about the fragmentation of gluons than about quark fragmentation, since at $\sqrt{s} \sim 30 - 35$ GeV the jets are often poorly separated for the purpose of jet comparisons. Furthermore, the difficulty in identifying gluon jets from quark jets gives rise to some differences in the results between experimental studies.

2.5.1 Theoretical prediction for quark and gluon jet multiplicities.

The gluon jet fragmentation is initially influenced by the ggg-coupling, instead of the qqg-coupling in the case of quark jets. To first order and in the limit of infinite jet energy, this gives a predicted ratio between gluon and quark jet multiplicities of $\frac{C_A}{C_F} = \frac{9}{4}$. Higher order corrections have been calculated [30] which modify this ratio to:

$$\frac{< n >_{gluon}}{< n >_{quark}} = \frac{9}{4}\left[1 - \sqrt{\frac{\alpha_s(Q^2)}{2\pi}}\left(\frac{1}{3} + \frac{N_f}{3C_A} - \frac{2N_f C_F}{3C_A^2}\right)\right]$$

giving a ratio of $\sim$2 at the e^+e^- collider energies. The fragmentation of heavy quarks gives softer jets with higher multiplicity, compared to jets from lighter quarks, so the presence of b-quark jets will further reduce the ratio of multiplicities of gluon and quark jets.

2.5.2 Experimental quark and gluon jet measurements.

Most of the experimental measurements of quark and gluon jet properties have been made at e^+e^- colliders. Some analyses used energy-ordering to separate

quark and gluon samples. Quark jets have also been taken from two-jet events for comparison. Some attempts have been made to unfold the quark and gluon jet properties from the samples, but identification of the quark and gluon jets remains the greatest challenge in the experimental studies.

The JADE collaboration [31] selected three-jet events from e^+e^- data at $\sqrt{s} = 33$ GeV. The lowest energy jet (jet 3) in each event had energies in the range 6-10 GeV and was assumed to be the gluon jet. These were compared to the medium energy jet (jet 2) in three-jet events at $\sqrt{s} = 22$ GeV, which had jet energies in the same range, and was assumed to be a quark jet. Another comparison was made with quark jets from two-jet events (jet 1) at $\sqrt{s} = 14$ GeV. The ratio of the mean transverse momentum of tracks in the jet:

$$r_{ij} = \frac{< p_\perp >_i}{< p_\perp >_j}$$

was determined, comparing the gluon jet sample (jet 3) and the quark jet samples (jet 2 or jet 1). For the first comparison, $< r_{32} >$ was measured to be 1.13 ± 0.04 for all particles and 1.10 ± 0.05 for charged particles only. In the second comparison $< r_{31} >$ was 1.16 ± 0.02 between jet 3 and jet 1 from the two-jet events. From the first comparison, the ratio of multiplicities was measured as 1.06 ± 0.02 for all particles and 1.07 ± 0.02 for charged particles only.

The HRS Collaboration [32] studied three-fold-symmetric three-jet events with $\sqrt{s} = 29$ GeV at PEP. The jets in each event were ranked by multiplicity and the jet with highest multiplicity was "tagged" as the gluon jet. After corrections the ratio $< n_g > / < n_q >$ was measured as $1.29^{+0.17}_{-0.32} \pm 0.20$.

The MARK II Collaboration [33] examined the fractional momentum distribution $x_p = \frac{p_i}{E_j}$ for charged track i in jet j for the three-fold-symmetric three-jet events at $\sqrt{s} = 29$ GeV. Compared to two jet events at $\sqrt{s} = 19.3$ GeV, the gluon-tagged jets had fewer particles with $x_p > 0.4$. The TASSO Collaboration [34] carried out a similar measurement for three-jet events at $\sqrt{s} \sim 35$ GeV compared to two-jet events at $\sqrt{s} \sim 22$ GeV and reported no significant difference between quark and gluon jets.

The AMY Collaboration [35] have analysed asymmetric three-jet events from TRISTAN with $\sqrt{s} = 50 - 60.8$ GeV. A mean core energy fraction was defined as the fraction of the jet energy within a cone of half angle 60° around the jet axis. The lower energy jets with higher gluon content were found to contain a smaller mean core energy fraction than the higher energy jets in each event. The former also had a lower mean rapidity for the leading particle in the jet.

The VENUS Collaboration [36] selected three-fold symmetric $q\bar{q}g$ and $q\bar{q}\gamma$ events at a centre of mass energy of 58 GeV. The x_p spectrum was found to be softer in the jets from the $q\bar{q}g$ compared to the $q\bar{q}\gamma$ jets.

Comparing the results from all the pre-LEP e^+e^- colliders, it is seen that gluon jets have slightly higher multiplicities than quark jets, and a softer particle spectrum. Furthermore, gluon jets tend to be broader than quark jets, although there is conflicting evidence from $p_\perp$ measurements due to the difficulty in identifying quark and gluon jets. The data has been compared to three-jet events generated using independent fragmentation, cluster fragmentation and string fragmentation models. Parton shower Monte Carlo models incorporating cluster or string fragmentation describe the data significantly better than independent fragmentation models. This has contributed to the decline in popularity of independent fragmentation.

At the higher centre of mass energy of the LEP collider, the jets in hadronic events are better collimated and there is wider separation between the jets in three-jet events. In addition, running at the Z^0 resonance gives a vast increase in statistics, permitting adequate jet samples to be selected with the quark jets "tagged" from the decays of primary b-quarks. This gives samples of quark and gluon jets that are well defined and high in purity.

The OPAL Collaboration have made two studies of symmetric "Y" events [37, 38], where the angles between the highest energy jet and the two lower energy jets in the three-jet events was in the range $150 \pm 10°$. In these events, the two lower energy jets have a similar range of energies of 16.9-31.7 GeV and the mean energies of the jet samples are 24.5 ± 0.5 GeV. In the first study, the gluon jet was "anti-tagged" by requiring a high momentum lepton in one of the lower energy jets. A second sample was prepared with no tagging of the two lower energy jets to give a 50% quark jet and 50% gluon jet mixture. The ratio of gluon to quark multiplicities was found to be $1.03 \pm 0.03^{+0.15}_{-0.00}$and the charged multiplicity ratio $1.02 \pm 0.04^{+0.06}_{-0.00}$. Fitting a gaussian to the momentum distribution versus angle to each jet axis, a ratio of $1.42 \pm 0.08^{+0.04}_{-0.00}$ was measured for the widths of the gluon and quark jets. The second study by OPAL used vertex tagging to "anti-tag" the gluon jets. A ratio of $1.267 \pm 0.043 \pm 0.055$ was measured for the multiplicities and $1.326 \pm 0.054 \pm 0.073$ for the charged multiplicities of the gluon and quark jets. The quark jets were seen to be narrower, with 31% of the jet energy within a cone of 5° half angle around the jet axis, compared to 14% for the gluon jets. In these studies, JETSET and HERWIG describe the data reasonably well, where as the independent fragmentation model COJETS [19] does not.

2.6 The "String Effect".

At e^+e^- colliders the particles flow in the event plane of three-jet events has been extensively studied [23, 24, 32, 39-44]. In the region between the q and $\bar{q}$ jets, a lower particle flow has been measured compared to the particle flow

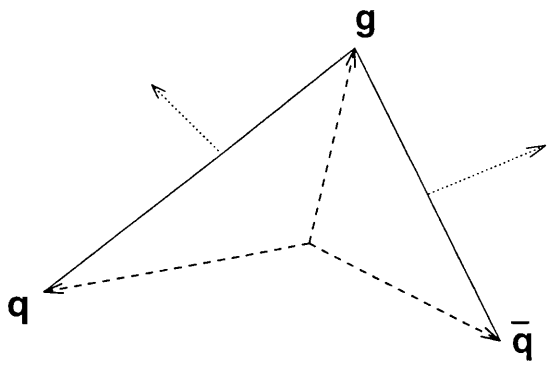

Figure 2.10: *Diagram depicting the string topology in a three-parton final-state. The parton directions are represented by the thick dotted lines, the string by the solid lines and the string direction by the thin dotted lines.*

in the regions between the q and g jets and between the $\overline{q}$ and g jets. This phenomenon has been called the "string effect", since it was first explained using string fragmentation. However coherent gluon emission in perturbative QCD can also be shown to describe this behaviour in three-jet events [22], so it has also been called the "drag effect", since the radiation of a hard gluon appears to drag the particle flow in the same direction.

The string explanation arises from the string topology in three-jet events according to these models. It was mentioned in Section 2.3.1 that if gluons are present after the parton shower, then these form kinks in the string stretched from q to $\overline{q}$. If a hard gluon is emitted from the q or $\overline{q}$ (Figure 2.10), then the string pieces between q and g and between g and $\overline{q}$ move in a direction given by the vector sum of the momenta of the partons at either end of the string piece. Hadronisation occurs by quark-antiquark pairs being produced at string breaks. This is determined in the rest frame of the string, so the quarks and antiquarks are boosted along the direction of motion of the string. In a three-jet event this causes the hadrons to be boosted away from the region between q and $\overline{q}$ to the inter-jet regions on either side of the hard gluon.

2.6.1 Analytical QCD derivation of the "string effect".

A perturbative QCD explanation for the string effect can be achieved by considering the radiation of soft gluons in $q\overline{q}g$ and $q\overline{q}\gamma$ events. If the energy of the gluons is much less than that of the partons from which they are radiated, then their wavelength is too long to resolve the structure of individual partons. This gives two distinct advantages in the calculation of the particle flow. The

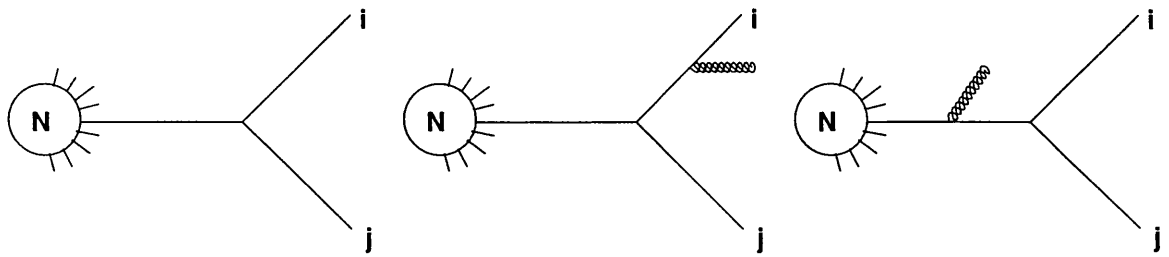

(a) *No soft gluon radiation associated with external lines i or j.*

(b) *Soft gluon radiation from external line i.*

(c) *Soft gluon radiation from an internal line.*

Figure 2.11: *Diagrams representing all processes (N) that produce external partons i and j.*

first benefit is that only the radiation of soft gluons from external partons need be determined. Consider the Feynman diagram in Figure 2.11a, where the left hand side represents a summation of the diagrams that produce the two external partons i and j. The propagator for the internal parton line is:

$$\frac{1}{(p_i + p_j)^2 + i\epsilon} \simeq \frac{1}{2p_i.p_j}$$

for massless partons. The denominator here is significantly non-zero, so the propagator is a small factor. If a soft gluon with 4-momentum k radiates from external parton i, as depicted by Figure 2.11b, then this gives rise to an additional propagator term given by:

$$\begin{aligned} \frac{1}{(p_i + k)^2} &\simeq \frac{1}{2p_i.k} \\ &\simeq \frac{1}{2E_i\omega(1 - \cos\theta)} \end{aligned}$$

where E_i and ω are the energies of the parton i and soft gluon, and θ is the angle of emission of the soft gluon. Since ω is small, this propagator is significant. If instead the soft gluon is radiated from an internal parton line, represented by Figure 2.11c, then the additional propagator is:

$$\frac{1}{(p_i + p_j + k)^2} \simeq \frac{1}{2p_i.p_j + 2\omega(E_i + E_j)(1 - \cos\theta')}$$

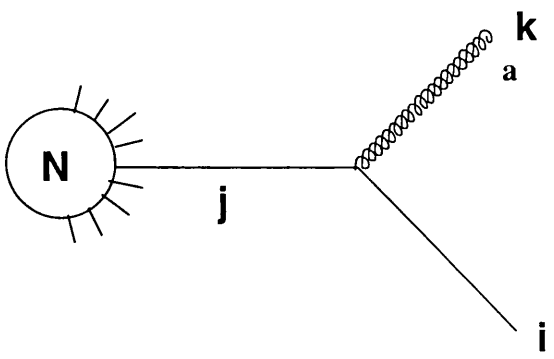

Figure 2.12: *Soft gluon radiation from an external quark line.*

Here again the denominator is non-zero, giving a propagator term that is negligible compared to the previous propagator for the on-shell parton, so diagrams for radiation from internal partons can be dropped.

If the radiated gluons are too soft to resolve the structure of the partons, this suggests that the same description can be used for all the soft gluons in an event, whether they were emitted from spin $\frac{1}{2}$ quarks or spin 1 gluons. The radiation of soft gluons from quarks and hard gluons is combined in the calculation by treating the partons collectively as antennae for the radiation of gluons, and summing the contributions from each radiating dipole. This formulation is outlined in Sections 2.6.2 - 2.6.3.

For $q\overline{q}\gamma$ events, the radiative pattern is similar to that for two jet events, but boosted into the rest frame of the q and $\overline{q}$. If there is a gluon present rather than a γ, this gives rise to additional gluon radiation in the direction of the gluon. However the interference between the radiation from the gluon and from the q and $\overline{q}$ causes less gluon radiation in the opposite direction. The relative difference in the gluon radiation in the interjet regions is determined in Section 2.6.4 for symmetric $q\overline{q}\gamma$ and $q\overline{q}g$ events.

2.6.2 The matrix element for soft gluon radiation.

Consider a soft gluon with 4-momentum k and polarisation $\epsilon(k)$, radiated from a quark q that is nearly on-mass shell. This can be represented by the Feynman diagram in Figure 2.12, where the left hand side of the diagram, N, represents a summation of all possible diagrams giving rise to the external quark. The matrix element for this process $M_i^{(N+g)}$ can be written:

$$M_i^{(N+g)}(q) = \overline{u}(q) i g_s T_{ij}^a \gamma_\mu \frac{(\not{q} + \not{k} + m)}{(\not{q} + \not{k})^2 - m^2} M_j^{(N)'}(q+k)\epsilon^{*\mu}(k)$$
$$= i g_s T_{ij}^a \overline{u}(q) \frac{(2q_\mu - \not{q}\gamma_\mu + m\gamma_\mu + \gamma_\mu \not{k})}{2q.k} M_j^{(N)'}(q+k)\epsilon^{*\mu}(k) \quad (2.1)$$

where a light quark mass has been assumed. Here T_{ij}^a is the quark colour factor for the process and $M_j^{(N)}(q) = \overline{u}(q).M_j^{(N)'}(q)$ is the matrix element for the processes giving rise to N. Since $\overline{u}(q)(\not{q} - m) = 0$, Equation 2.1 becomes:

$$M_i^{(N+g)} = i g_s T_{ij}^a \overline{u}(q) \frac{(2q_\mu + \gamma_\mu \not{k})}{2q.k} M_j^{(N)'}(q+k)\epsilon^{*\mu}(k)$$

The gluon energy $\omega \ll E_i$, the energy of the quark. This enables the Eikonal approximation to be applied, such that the recoil of the quark during the process can be neglected. Dropping the soft gluon term in the numerator gives the simplified expression:

$$M_i^{(N+g)} = i g_s T_{ij}^a \frac{q.\epsilon^*(k)}{q.k} M_j^{(N)}(q) \quad (2.2)$$

Consider now the more complicated case of the soft gluon radiated from a hard gluon g, represented by Figure 2.13.
The matrix element $M_b^{(N+g)}$ can be written:

$$M_b^{(N+g)} = M_{c\sigma}^{(N)'}(g+k) \frac{d^{\sigma\tau}(g+k)}{(g+k)^2 + i\epsilon} . g_s f^{abc}$$
$$. [(g-k)_\tau \eta_{\mu\nu} - (2g+k)_\mu \eta_{\nu\tau} + (2k+g)_\nu \eta_{\tau\mu}]$$
$$. \epsilon^{*\mu}(k)\epsilon^{*\nu}(g)$$

where $d^{\sigma\tau}(g+k)$ in the numerator represents the sum over possible gluon polarisations. For a nearly on-mass shell gluon, this is dominated by the transversely polarised states, so $d^{\sigma\tau}(g+k) = \sum_{\lambda=T} \epsilon_\lambda^{*\sigma}(g+k)\epsilon_\lambda^\tau(g+k)$. The f^{abc} factor represents the colour factors for this process. With $\epsilon(g).g = 0$ and $\epsilon(k).k = 0$, the matrix element becomes:

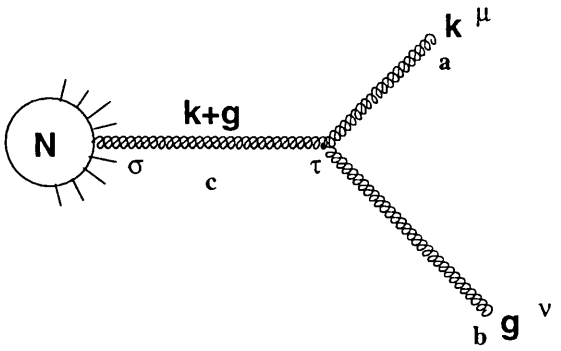

Figure 2.13: *Soft gluon radiation from an external gluon line.*

$$\begin{aligned} M_b^{(N+g)} &= g_s f^{abc} M_{c\sigma}^{(N)'}(g+k)\frac{d^{\sigma\tau}(g+k)}{2g.k} \\ &\quad .[(g-k)_\tau \eta_{\mu\nu} - 2g_\mu \eta_{\nu\tau} + 2k_\nu \eta_{\tau\mu}] \\ &\quad .\epsilon^{*\mu}(k)\epsilon^{*\nu}(g) \end{aligned}$$

But $g^\tau . d^{\sigma\tau}(g) \sim 0$, so:

$$\begin{aligned} M_b^{(N+g)} &= g_s f^{abc} M_{c\sigma}^{(N)'}(g+k)\frac{d^{\sigma\tau}(g+k)}{2g.k} \\ &\quad .[-2k_\tau \eta_{\mu\nu} - 2g_\mu \eta_{\nu\tau} + 2k_\nu \eta_{\tau\mu}] \\ &\quad .\epsilon^{*\mu}(k)\epsilon^{*\nu}(g) \end{aligned}$$

Neglecting the recoil of the hard gluon gives:

$$\begin{aligned} M_b^{(N+g)} &= g_s f^{abc} M_{c\sigma}^{(N)'}(g)\frac{d^{\sigma\tau}(g)}{2g.k}. - 2g_\mu \eta_{\nu\tau}.\epsilon^{*\mu}(k)\epsilon^{*\nu}(g) \\ &= -g_s f^{abc}\frac{g.\epsilon^*(k)}{g.k} M_c^{(N)} \end{aligned}$$

This expression for the matrix element for soft gluon emission from a hard gluon is now in a similar form to Equation 2.2 for soft gluon emission from a hard quark.

Since the soft gluons cannot resolve the structure of the partons, the matrix element for soft gluon emission in the event is just the sum of the contributions from the partons.

$$M^{(N+g)} = g_s \sum_i \hat{T}_i^a \frac{p_i^\mu . \epsilon_\mu^*(k)}{p_i.k} . M^{(N)}$$

where $\hat{T}_i^a$ represents the colour factors for gluon radiation from each parton i.

$$\begin{aligned} \left|M^{(N+g)}\right|^2 &= J'^\mu(k) J'^\nu(k) \sum_T \epsilon_\mu^*(k) \epsilon_\nu(k) . \left|M^{(N)}\right|^2 \\ &= J'^\mu(k) J'^\nu(k) d_{\mu\nu}(k) . \left|M^{(N)}\right|^2 \end{aligned}$$

where $J'^\mu(k) = g_s \sum_i \hat{T}_i^a \frac{p_i^\mu}{p_i.k}$. If the Axial gauge is chosen, then the gluon propagator is

$$\begin{aligned} d_{\mu\nu}(k) &= -\eta_{\mu\nu} + \frac{k_\mu n_\nu + k_\nu n_\mu}{n.k} - \frac{n^2 k_\mu k_\nu}{(n.k)^2} \\ &= -\left(\eta_{\mu\sigma} - \frac{n_\sigma k_\mu}{n.k}\right)\left(\eta_\nu^\sigma - \frac{n^\sigma k_\nu}{n.k}\right) \end{aligned}$$

The matrix element squared is then:

$$J'^\mu J'^\nu d_{\mu\nu}(k) \left|M^{(N)}\right|^2 = -\left(J'_\sigma - \frac{k.J'}{n.k} n_\sigma\right)\left(J'^\sigma - \frac{k.J'}{n.k} n^\sigma\right) \left|M^{(N)}\right|^2$$

Here $k.J' = k.g_s \sum_i \hat{T}_i^a \frac{p_i}{p_i.k} = g_s \sum_i \hat{T}_i^a$, so

$$\begin{aligned} \left|M^{(N+g)}\right|^2 &= -g_s^2 \left[\sum_i \hat{T}_i^a \left(\frac{p_i}{p_i.k} - \frac{n}{n.k}\right)\right]^2 \left|M^N\right|^2 \\ &= -J^\mu(k) J^\nu(k) \left|M^N\right|^2 \end{aligned} \tag{2.3}$$

with insertion current defined as:

$$J_\mu = g_s \sum_i \hat{T}_i^a \left(\frac{p_i}{p_i.k} - \frac{n}{n.k}\right)$$

Equation 2.3 can be further simplified since:

$$\sum_i T_i^a \frac{n}{n.k} = \frac{n}{n.k} \sum_i T_i^a$$

which is zero for a net colour zero source such as a Z^0 decay. This gives:

$$\begin{aligned} \left|M^{(N+g)}\right|^2 &= -g_s^2 \sum_{i,j} \hat{T}_i^a . \hat{T}_j^a \frac{p_i.p_j}{(p_i.k)(p_j.k)} \left|M^N\right|^2 \\ &= -g_s^2 \left[2 \sum_{i>j} \hat{T}_i^a . \hat{T}_j^a \frac{p_i.p_j}{(p_i.k)(p_j.k)} + \sum_i (\hat{T}_i^a)^2 \frac{p_i^2}{(p_i.k)^2} \right] \left|M^N\right|^2 \end{aligned} \quad (2.4)$$

The first sum in Equation 2.4 represents the interference between the gluon emission sources. The sum of all possible colour charges is zero, so $\hat{T}_i + \sum_{j \neq i} \hat{T}_j = 0$ and $(\hat{T}_i)^2 = \hat{T}_i.(-\sum_{j \neq i} \hat{T}_j)$. Substituting this into Equation 2.4 leads to:

$$\left|M^{(N+g)}\right|^2 = -g_s^2 2 \sum_{i>j} \hat{T}_i^a \hat{T}_j^a \left[\frac{p_i.p_j}{(p_i.k)(p_j.k)} - \frac{1}{2} \frac{p_i^2}{(p_i.k)^2} - \frac{1}{2} \frac{p_j^2}{(p_j.k)^2} \right] \left|M^N\right|^2$$

This can be further simplified by setting $p_i^2 = p_j^2 = 0$ in the massless quark limit, such that only the first term need be considered. From this equation it can be seen that the soft gluon distribution is independent of the energies of the partons. The effects of interference of gluons emitted from partons i and j can be shown by considering the term

$$W_{ij} = \frac{p_i.p_j}{(p_i.k)(p_j.k)}$$

Here

$$\begin{aligned} p_i.k &= \omega E_i (1 - \cos\theta_{ik}) \\ &= \omega E_i \zeta_{ik} \end{aligned}$$

so W_{ij} becomes singular at $\theta_{ik} = \theta_{jk} = 0$. Splitting W_{ij} into a term corresponding to each parton gives:

$$\begin{aligned}
\omega^2 W_{ij} &= \frac{\zeta_{ij}}{\zeta_{ik}\zeta_{jk}} \\
&= \frac{1}{2}\left[\frac{\zeta_{ij}}{\zeta_{ik}\zeta_{jk}} - \frac{1}{\zeta_{ik}} + \frac{1}{\zeta_{jk}}\right] + \frac{1}{2}\left[\frac{\zeta_{ij}}{\zeta_{ik}\zeta_{jk}} + \frac{1}{\zeta_{ik}} - \frac{1}{\zeta_{jk}}\right] \\
&= \frac{1}{2}\left[\frac{1}{\zeta_{ik}}\left(\frac{\zeta_{ij}-\zeta_{ik}}{\zeta_{jk}} + 1\right)\right] + \frac{1}{2}\left[\frac{1}{\zeta_{jk}}\left(\frac{\zeta_{ij}-\zeta_{jk}}{\zeta_{ik}} + 1\right)\right] \\
&\equiv W_{ij}^{i}(k) + W_{ij}^{j}(k)
\end{aligned}$$

Consider the term:

$$\begin{aligned}
W_{ij}^{i}(k) &= \frac{1}{2}\frac{1}{\zeta_{ik}}\left(\frac{\zeta_{ij}-\zeta_{ik}}{\zeta_{jk}} + 1\right) \\
&= \frac{1}{2}\frac{1}{(1-\cos\theta_{ik})}\left(\frac{(1-\cos\theta_{ij}) - (1-\cos\theta_{ik})}{(1-\cos\theta_{jk})} + 1\right)
\end{aligned}$$

For the angles θ_{ij}, θ_{ik}, θ_{jk} and ϕ defined in Figure 2.14, the function inside the bracket can be written:

$$= \frac{cos\theta_{ik} - \cos\theta_{ij}}{1 - (\cos\theta_{ij}\cos\theta_{ik} + \sin\theta_{ij}\sin\theta_{ik}\cos\phi)} + 1$$

This shape of this term is plotted as a function of ϕ in Figure 2.15 for $\theta_{ik} < \theta_{ij}$ and $\theta_{ik} > \theta_{ij}$. Where $\theta_{ik} < \theta_{ij}$ this term is positive for all values of ϕ, with a mean value of 2.
However if $\theta_{ik} > \theta_{ij}$ then the function can be negative, having a mean value of zero. This demonstrates that destructive interference can occur between partons during soft gluon radiation. For some angles θ_{ij} and θ_{ik} the function $W_{ij}^{i}(k)$ is more sharply peaked at $\phi = 0°$, i.e. between partons i and j.

2.6.3 Calculation of the particle flow in 3-jet events.

From Equation 2.3 it is possible to see that the cross-section for soft gluon radiation is given by $\sigma \sim -J.J|M^{(N)}|^2$. Thus the relative particle flow can be

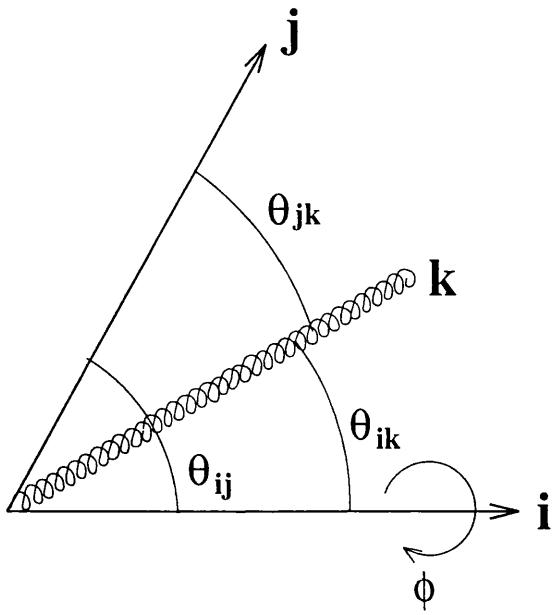

Figure 2.14: *Definition of the angles θ_{ij}, θ_{ik}, θ_{jk} and ϕ between two partons i and j and a soft gluon k*

obtained from the square of the insertion current J^2. This can be approximated by:

$$\begin{aligned} J^2 &\sim 2\sum_{i>j} \hat{T}_i.\hat{T}_j \frac{p_i.p_j}{(p_i.k)(p_j.k)} \\ &\sim 2\sum_{i>j} \hat{T}_i.\hat{T}_j W_{ij} \end{aligned}$$

Thus for a $q\bar{q}\gamma$ event (Figure 2.16a) the square of the insertion current is given by:

$$J^2 \sim 2\hat{T}_q\hat{T}_{\bar{q}}W_{q\bar{q}} \tag{2.5}$$

and for a $q\bar{q}g$ event (Figure 2.16b):

$$J^2 \sim 2\left[\hat{T}_q\hat{T}_{\bar{q}}W_{q\bar{q}} + \hat{T}_q\hat{T}_g W_{qg} + \hat{T}_g\hat{T}_{\bar{q}}W_{\bar{q}g}\right] \tag{2.6}$$

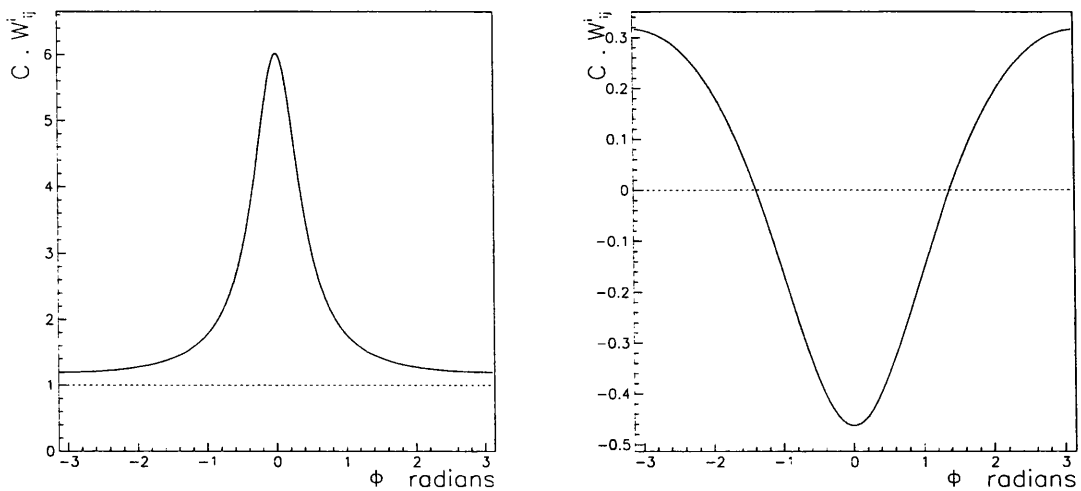

(a) $\theta_{ij} = 70°$, $\theta_{ik} = 50°$.

(b) $\theta_{ij} = 70°$, $\theta_{ik} = 150°$.

Figure 2.15: *Function* $C \times W^i_{ij}(k)$ *plotted for different values of* ϕ. $C = 2.\omega^2.(1 - \cos\theta_{ik})$ *is a constant. The function has been plotted for* $\theta_{ik} < \theta_{ij}$ *and* $\theta_{ik} > \theta_{ij}$.

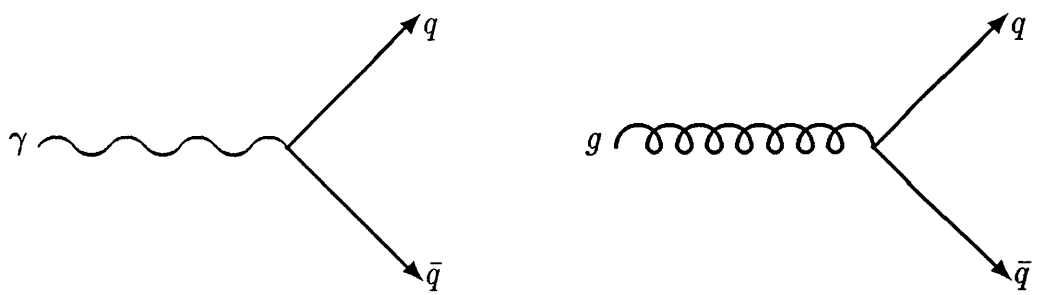

(a) (b)

Figure 2.16:

The following equalities can be used to evaluate Equations 2.5 and 2.6:

$$\hat{T}_q + \hat{T}_{\bar{q}} + \hat{T}_g = 0$$

$$\begin{aligned} \hat{T}_q.\hat{T}_q &= C_F \\ &= \frac{N_c^2 - 1}{2N_c} \end{aligned}$$

$$\begin{aligned} \hat{T}_g.\hat{T}_g &= C_A \\ &= N_c \end{aligned}$$

$$\hat{T}_{\bar{q}} = -\hat{T}_q$$

Thus for the $q\bar{q}\gamma$ event:

$$J^2 \sim 2C_F W_{q\bar{q}} \tag{2.7}$$

For the $q\bar{q}g$ event:

$$\begin{aligned} \frac{J^2}{2} &= \hat{T}_q.\hat{T}_{\bar{q}} W_{q\bar{q}} + \hat{T}_q.\hat{T}_g W_{qg} + \hat{T}_g.\hat{T}_{\bar{q}} W_{\bar{q}g} \\ &= \hat{T}_q.\hat{T}_{\bar{q}} W_{q\bar{q}} + \hat{T}_{q\cdot} - (\hat{T}_q + \hat{T}_{\bar{q}}) W_{qg} + \hat{T}_{\bar{q}\cdot} - (\hat{T}_q + \hat{T}_{\bar{q}}) W_{\bar{q}g} \\ &= \hat{T}_q.\hat{T}_{\bar{q}}(W_{q\bar{q}} - W_{qg} - W_{\bar{q}g}) - C_F(W_{qg} + W_{\bar{q}g}) \end{aligned} \tag{2.8}$$

$\hat{T}_q.\hat{T}_{\bar{q}}$ can be determined from:

$$\begin{aligned} \hat{T}_g{}^2 &= (\hat{T}_q + \hat{T}_{\bar{q}})^2 \\ C_A &= 2C_F + 2\hat{T}_q.\hat{T}_{\bar{q}} \end{aligned}$$

which gives

$$\hat{T}_q.\hat{T}_{\bar{q}} = \frac{1}{2N_c}$$

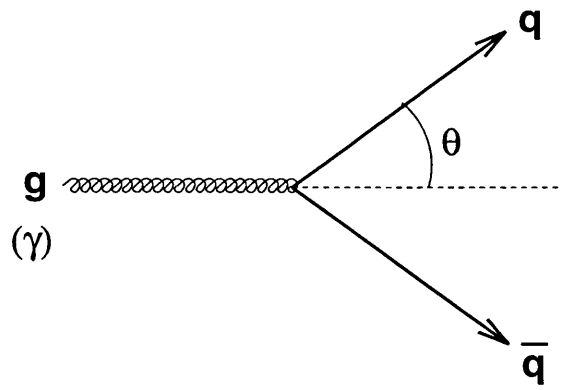

Figure 2.17:

Substituting this in Equation 2.8:

$$\begin{aligned}\frac{J^2}{2} &= \frac{1}{2N_c}(W_{q\bar{q}} - W_{qg} - W_{\bar{q}g}) - \frac{N_c^2-1}{2N_c}(W_{qg} + W_{\bar{q}g}) \\ &= \frac{N_c}{2}W_{qg} + \frac{N_c}{2}W_{\bar{q}g} - \frac{1}{2N_c}W_{q\bar{q}} \end{aligned} \tag{2.9}$$

The relative particle flow in $q\bar{q}\gamma$ and $q\bar{q}g$ events is thus given by the simple expressions 2.7 and 2.9 respectively. For the $q\bar{q}\gamma$ event, there is just one term which relates to the colour antenna between the q and $\bar{q}$. The particle flow in the $q\bar{q}g$ event has three terms, two of these relating to antennae between the q and g and between the $\bar{q}$ and g. The third term corresponds to a weaker antenna between the q and $\bar{q}$. To evaluate the particle flow in a specific three-jet event configuration, the three factors $W_{q\bar{q}}$, W_{qg} and $W_{\bar{q}g}$ need to be calculated. This is shown in the following section for a symmetric "Y" event topology.

2.6.4 Ratio of particle flows in symmetric $q\bar{q}\gamma$ and $q\bar{q}g$ events.

Consider symmetric $q\bar{q}\gamma$ and $q\bar{q}g$ events aligned as in Figure 2.17, where the q, $\bar{q}$ and γ or g have the following 4-vectors:

$$\begin{aligned}\hat{q} &= (1, \sin\theta, 0, \cos\theta) \\ \hat{\bar{q}} &= (1, -\sin\theta, 0, \cos\theta) \\ \hat{g} &= (1, 0, 0, -1)\end{aligned}$$

where the energy is normalised to unity. For soft gluon radiation g_{soft} directly between q and $\bar{q}$, the 4-vector is $\hat{g}_{soft} = (1,0,0,1)$. $W_{q\bar{q}}$, W_{qg} and $W_{\bar{q}g}$ are given by:

$$\begin{aligned}
W_{q\bar{q}} &= \frac{\hat{q}.\hat{\bar{q}}}{(\hat{q}.\hat{g}_{soft})(\hat{\bar{q}}.\hat{g}_{soft})} \\
&= \frac{1-\cos^2\theta+\sin^2\theta}{(1-\cos\theta)(1-\cos\theta)} \\
&= \frac{2\sin^2\theta}{(1-\cos\theta)^2} \\
W_{qg} &= \frac{\hat{q}.\hat{g}}{(\hat{q}.\hat{g}_{soft})(\hat{g}.\hat{g}_{soft})} \\
&= \frac{1+\cos\theta}{(1-\cos\theta).2} \\
&= W_{\bar{q}g}
\end{aligned}$$

The ratio of the particle flows $q\bar{q}\gamma$ to $q\bar{q}g$ is then:

$$\begin{aligned}
\frac{J^2(q\bar{q}\gamma)}{J^2(q\bar{q}g)} &= \frac{C_F W_{q\bar{q}}}{\frac{N_c}{2}W_{qg}+\frac{N_c}{2}W_{\bar{q}g}-\frac{1}{2N_c}W_{q\bar{q}}} \\
&= \frac{\left(\frac{N_c^2-1}{2N_c}\right)\left(\frac{2\sin^2\theta}{(1-\cos\theta)^2}\right)}{\frac{N_c}{2}\left(\frac{1+\cos\theta}{1-\cos\theta}\right)-\frac{1}{2N_c}\left(\frac{2\sin^2\theta}{(1-\cos\theta)^2}\right)} \\
&= \left(\frac{N_c^2-1}{N_c^2}\right)\left(\frac{2\sin^2\theta}{\sin^2\theta-\frac{2}{N_c^2}\sin^2\theta}\right) \\
&= \frac{8}{9}\left(\frac{2}{1-\frac{2}{9}}\right) \\
&= \frac{16}{7} \\
&= 2.29
\end{aligned}$$

Given the initial parton 4-momenta, the mean relative particle flows can be predicted in a similar manner for any three-jet event.

Ratio $0.3 < \frac{\theta_{13}}{\theta_{12}} < 0.7$	*Data*	*JETSET*	*Hoyer*
All particles	1.39 ± 0.04	1.33 ± 0.03	1.09 ± 0.03
Charged only	1.42 ± 0.06	1.27 ± 0.03	1.04 ± 0.04
All $p_{\perp}^{out} > 0.3$ GeV/c	1.73 ± 0.13	1.55 ± 0.07	1.12 ± 0.07
Charged $p_{\perp}^{out} > 0.3$ GeV/c	1.82 ± 0.16	1.52 ± 0.08	1.14 ± 0.09
Kaons	1.9 ± 0.2	1.7 ± 0.15	1.14 ± 0.1
Energy flow	1.56 ± 0.04	1.50 ± 0.03	1.20 ± 0.03

Table 2.3: *Measurements of the ratio of inter-jet particle flows by JADE compared to predictions from the JETSET string fragmentation model and Hoyer independent fragmentation model.*

2.6.5 Experimental measurements of the "string effect".

The particle flow in three-jet events has been studied by a number of experiments. The JADE collaboration [23, 39] took hadronic events at a centre of mass energy of 30-36 GeV and ranked the jets in three-jet events by energy. The matrix element for $q\bar{q}g$ is at a maximum for low gluon energy, so the lowest energy jet is most often the gluon jet. The ratio of the particle flows between jets 1 and 3 and between jets 1 and 2 was measured and is shown in Table 2.3 along with the predictions from the JETSET string model and the Hoyer independent fragmentation model [14]. The depletion in the particle flows in between jets 1 and 2 can clearly be seen. The independent fragmentation model clearly fails to describe this effect. It is shown in a later paper [39] that the HERWIG model also describes the string effect, whilst independent fragmentation models by Ali [15] and by Gottschalk [18] do not describe the depletion in particle flow between jets 1 and 2. Similar results have been obtained by the HRS [32], TPC [40] and TASSO [41] collaborations.

An alternative method of analysis involved comparing three-jet events with $q\bar{q}\gamma$ events. The radiative pattern of a $q\bar{q}\gamma$ event is similar to a two-jet event, but

Ratio $0.3 < \frac{\theta_{qg}}{\theta_{q\overline{q}}} < 0.7$	*Data*	*JETSET*	*JETSET (generator level)*	*COJETS (generator level)*
All particles	1.62 ± 0.07	1.67 ± 0.07	1.54 ± 0.02	1.02 ± 0.01
Charged only	1.66 ± 0.09	1.65 ± 0.08		
Energy flow	1.68 ± 0.09	1.78 ± 0.09		

Table 2.4: *Measurements of the ratio of inter-jet particle flows by OPAL compared to predictions from the JETSET string fragmentation model and the COJETS independent fragmentation model.*

with the radiative pattern boosted into the rest frame of the $q\overline{q}$ system. A similar effect is seen with string fragmentation, where the fragmentation occurs in the rest frame of the string stretched between the two q and $\overline{q}$. Thus the particle flow between the q and $\overline{q}$ is enhanced. Comparing the particle flows between the quark jets in the $q\overline{q}g$ and $q\overline{q}\gamma$ events, the TPC Collaboration [42], MARK II Collaboration [43] and the JADE Collaboration [44] measured a ratio of 0.6-0.7 halfway between the quark jets.

In the aforementioned analyses, the gluon jet is identified as the lowest energy jet. This is not particularly satisfactory, since this is only true in up to 65% of cases, depending on the event selection. This makes it difficult to interpret the data and remove any additional effects caused by the energy-ordering of the jets. The higher statistics available at LEP and the ability to tag b-quark jets, gives some scope for improved analyses. The OPAL Collaboration [24] has made a study of three-jet events where one or both of the quark jets had been tagged as a b-quark jet using a lepton-tag. Using this method, the gluon jets were identified with about 84% purity. Comparing the region between the q and g jets with that between q and $\overline{q}$ jets, a ratio of 1.6-1.7 was found for the particles flows (Table 2.4), but this depended on the exact configuration of the three jets in the events analysed. The predicted ratio for "Mercedes" (three-fold symmetric) events from the soft gluon calculation outlined in Section 2.6.4 is $\frac{22}{7}$. The JETSET string model was again found to reproduce the results of the data, where as the COJETS independent fragmentation model [19] showed no difference in the particle flow when comparing the inter-jet regions.

2.7 Summary.

From the late 1970's to the present, a large number of multi-jet hadronic events have been recorded at e^+e^- colliders. This has lead to high-precision measurements of α_s, the strong coupling constant, from the observed three-jet rate. Analytical QCD and parton shower Monte Carlo models can describe well the overall properties of hadronic events. The theoretical models make predictions for the particle flow in three-jet events and the properties of quark and gluon jets. However the impact of experimental results has been limited by low statistics and the inability in most analyses to successfully identify quark and gluon jets in three-jet events. This has lead to some uncertainty in the nature of quark and gluon jets, so there is a gap between what experimentalists can measure and what theory predicts. Studies of three-jet events at LEP by the OPAL collaboration, where quark jets have been successfully identified, have provided a comparison of non-leading quark and gluon jets at ~24 GeV in a symmetric three-jet event topology. Further studies of three-jet events using different analysis procedures and a wider range of event topologies and jet energies are required to fully understand the nature of quark and gluon jets, and their formation in hadronic events. It is hoped that the analysis described in Chapters 4- 6 will help to fulfill this requirement.

Chapter 3

The ALEPH detector.

3.1 Introduction.

This chapter provides a brief introduction to the ALEPH detector, followed by a description of the main sub-detectors that were used in the analyses described in Chapters 4- 6. The identification of electrons, muons and photons is then discussed. A more detailed description of the ALEPH detector can be found in [45, 46]. The identification of leptons in hadronic events is discussed in more detail in [47].

3.2 Detector overview.

The purpose of the ALEPH detector is to study the electroweak and strong nuclear forces by measuring the decays of the Z^0 boson, and to search for new phenomena. The events produced from Z^0 decays can be complex, with particles distributed over 4π solid angle. In the case of hadronic decays, such as Figures 2.2, 2.4 and 2.6, the events can have high multiplicity. To fully measure the products of Z^0 decays, the detector's tracking system and highly granular calorimeters cover close to 4π in solid angle. A superconducting magnet provides a uniform magnetic field to measure the momenta and polarity of charged particles. Ionisation measurements from the tracking system and profiles of energy deposits in the calorimeters allow identification of leptons, photons and hadrons in the detector.

The detector (Figure 3.1) has a cylindrical main barrel section built around the superconducting magnet, and two end-caps (Figure 3.2) to cover the remaining solid angle. The electron-positron interactions take place inside an aluminium alloy beam pipe running through the axis of the barrel section. The magnet provides an axial magnetic field of 1.5 T to facilitate the measurement of charged particle momenta. Around the interaction point is a silicon strip vertex

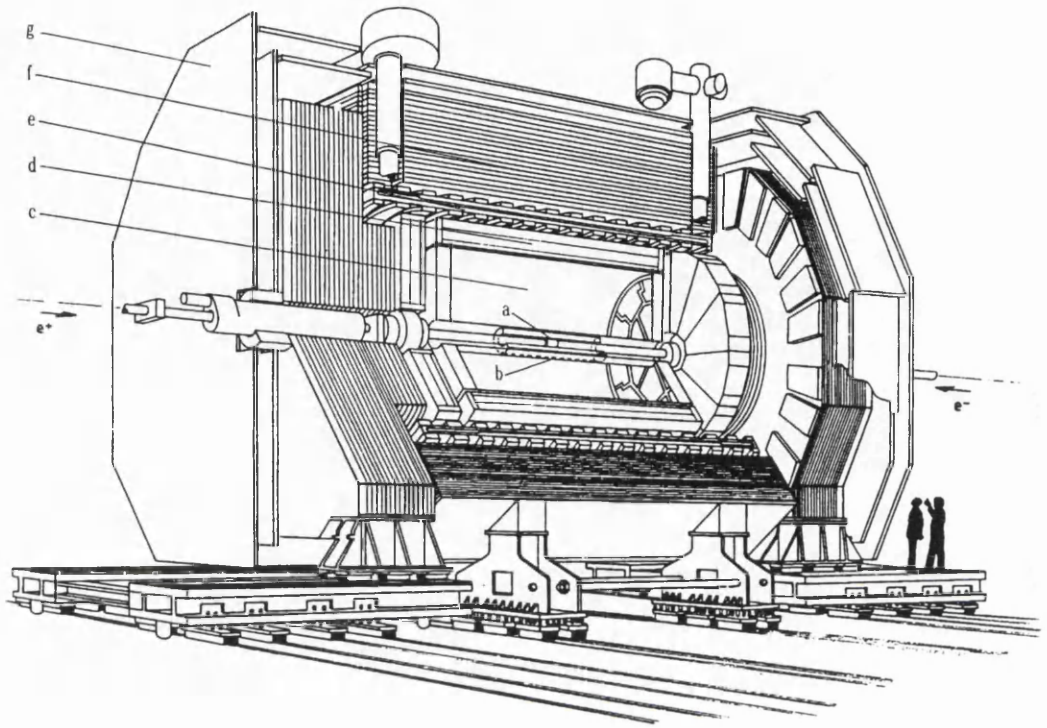

Figure 3.1: *Cut-away diagram of the ALEPH detector showing the main components. These are labelled a-g as follows: a - vertex detector (VDET); b - inner tracking chamber (ITC); c - time projection chamber (TPC); d - electromagnetic calorimeter (ECAL); e - superconducting magnet; f - hadron calorimeter (HCAL); g - muon chambers.*

detector (VDET), which measures the point resolution of tracks with down to 12μm precision in $r\phi$. Surrounding the beam pipe is the inner tracking chamber (ITC), a wire chamber of 2m length, and inner and outer radii of 13cm and 29cm (Figure 3.3). This gives up to eight track coordinates in the plane perpendicular to the beam line with a precision of 100μm in $r\phi$. Outside the ITC is a cylindrical time projection chamber (TPC) of length 4.4m and outer radius 1.8m (Figure 3.4), which provides three-dimensional track coordinates. Combining track coordinates from the TPC, ITC and vertex detector, the momentum resolution for charged tracks $\delta p/p^2 \sim 6.6\times10^{-4}$ GeV/c. The TPC also gives a measurement of the energy loss $\frac{dE}{dx}$ of charged particles passing through the chamber, which contributes to the particle identification capability of the ALEPH detector.

Outside the TPC are two sampling calorimeters (Figure 3.5). Between the TPC and the magnetic coil is the electromagnetic calorimeter, ECAL, consisting

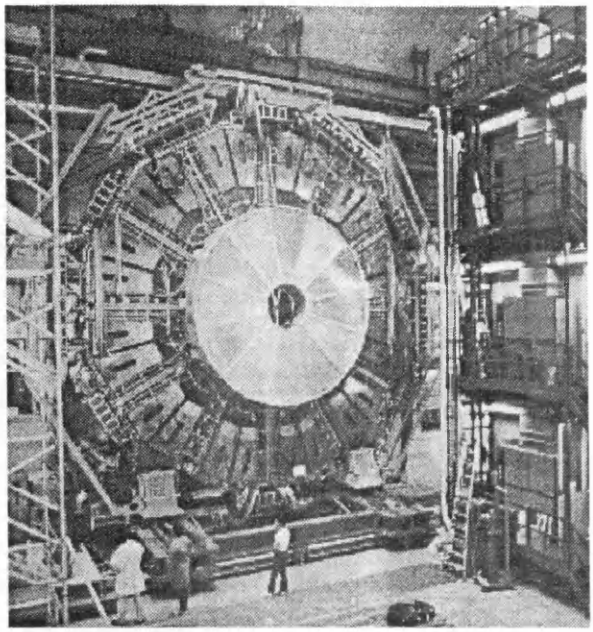

(a) Face view of end-cap.

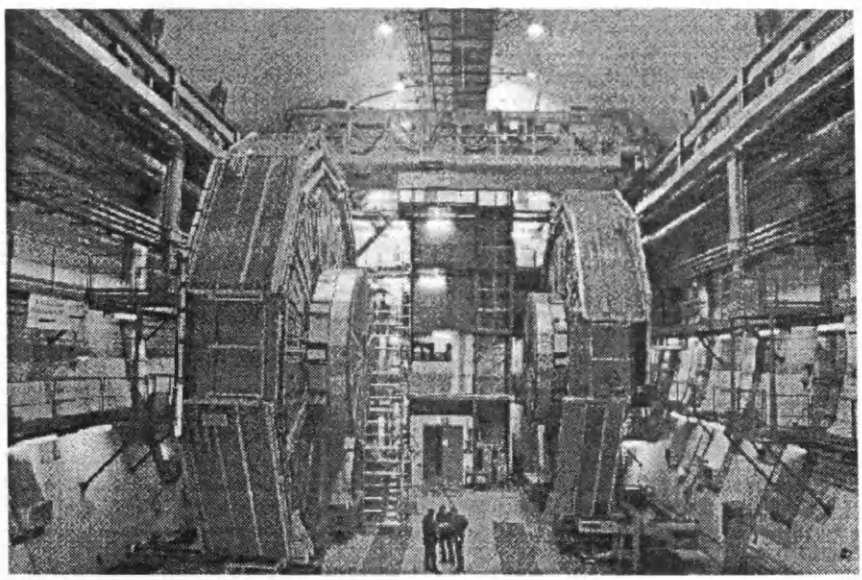

(b) Side view of end-caps.

Figure 3.2: *Views of the detector end-caps retracted from barrel section, showing electromagnetic calorimeter in the centre of the pictures surrounded by the hadron calorimeter.*

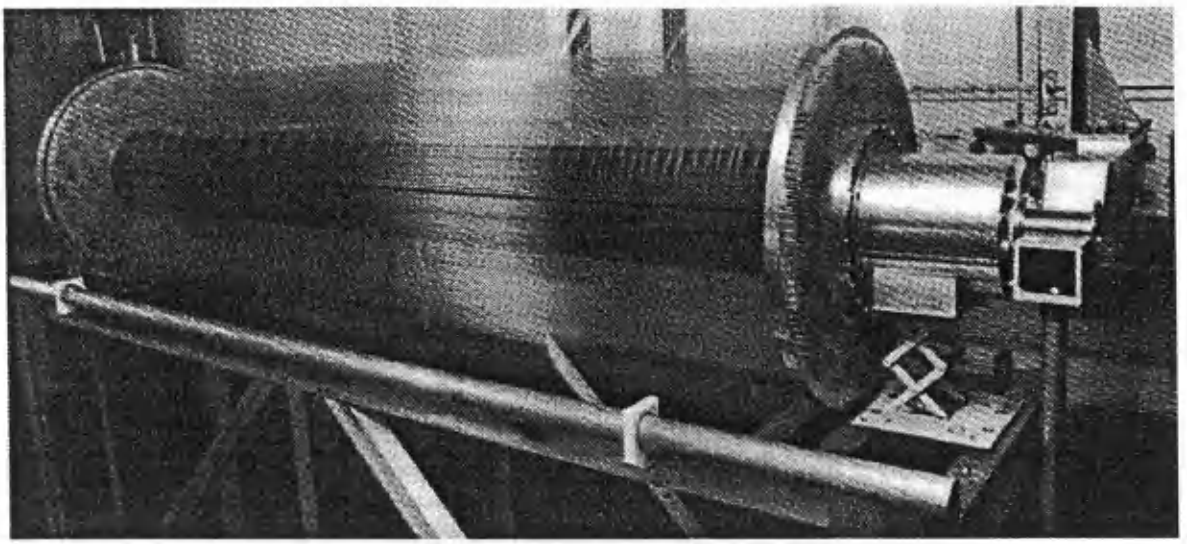

Figure 3.3: *View of the inner tracking chamber (ITC) before insertion into the ALEPH detector.*

of interleaved lead sheets and proportional tubes. Outside the magnetic coil is the hadron calorimeter, HCAL, consisting of alternating layers of iron plates and limited-streamer tubes (Figure 3.6). The position and angle of muons leaving the hadron calorimeter is measured using muon chambers, consisting of two layers of limited streamer tubes outside the hadron calorimeter. The luminosity is determined from the rate of Bhabha events at small scattering angles. This is measured using luminosity monitors in the endcaps, close to the beam line.

3.3 Time projection chamber.

The time projection chamber (Figure 3.7) is a cylindrical volume of gas with uniform magnetic and electric fields along its axis. The electric field runs from each end-plate to a central diaphragm which divides the chamber into two halves. The inner and outer cylindrical walls of the TPC form a field cage to maintain a constant and uniform electric field. Charged particles passing through the volume of the TPC cause ionisation of the argon/methane mixture contained within. The electrons from the ionised tracks drift to the end-plates of the chamber, where they cause ionisation avalanches in a plane of wire chambers. These induce signals on cathode pads located behind the wires. The r and ϕ coordinates of tracks are given by interpolating between signals on cathode pads. The z coordinates are given by the drift time of the electrons travelling with constant drift velocity from

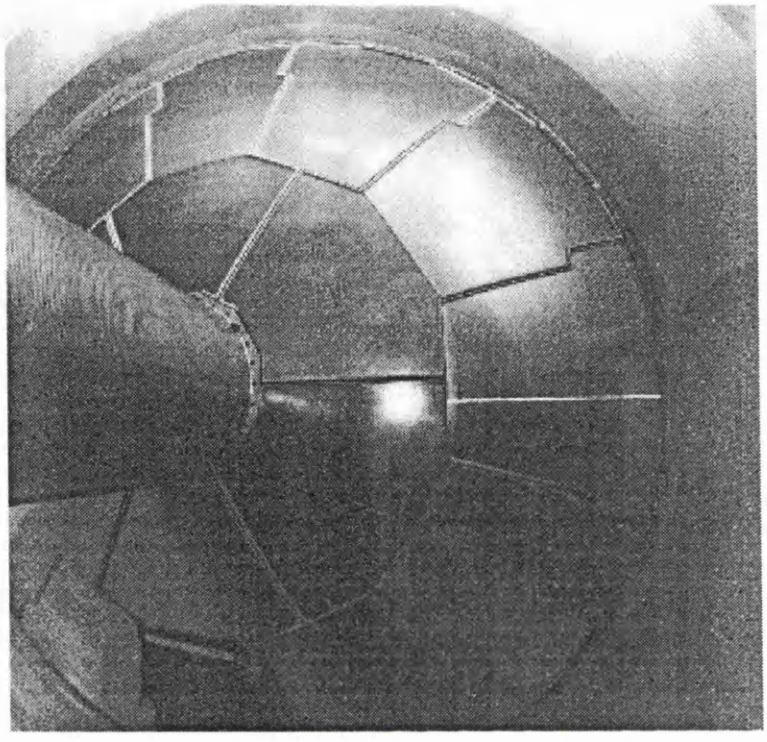

Figure 3.4: *View from inside the TPC volume, showing the inner and outer walls of the TPC and the sectors on the end-plates.*

the ionised track to the end-plate.

3.3.1 The laser calibration system.

The gas inside the TPC is maintained with a stable argon/methane mixing ratio at atmospheric pressure with O_2 and H_2O contamination kept to a minimum, to ensure long-term stability of the drift velocity and gas gain. The drift velocity is calibrated from the tracks of laser beams fired into the chamber. Thirty pulsed laser beams are directed from the interaction point into the chamber, causing straight ionised tracks at specific angles, from which the drift time is determined. The laser calibration system is depicted in Figure 3.8. The Nd-YAG lasers produce a pulsed beam at a frequency of 266nm, with an energy of several mJ per pulse. Each beam is reflected from a beam switch to an actuator box where the beams can be steered. The beam is directed from the actuator box to a splitter ring on the TPC end-plate and split into three beams, which are reflected along the inside surface of the TPC to mirrors, which send the beams

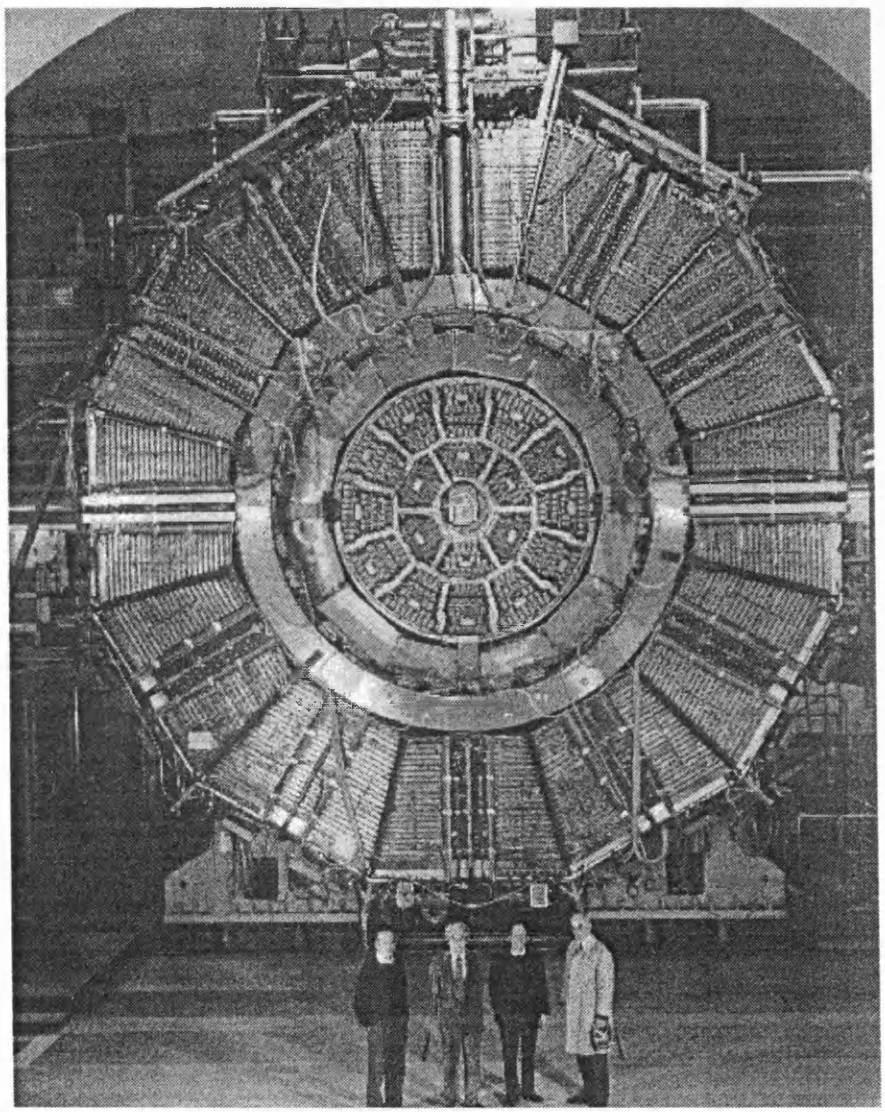

Figure 3.5: *End-view of barrel section before cabling, showing the TPC sectors. The TPC is surrounded by the ECAL modules, superconducting magnet and HCAL modules.*

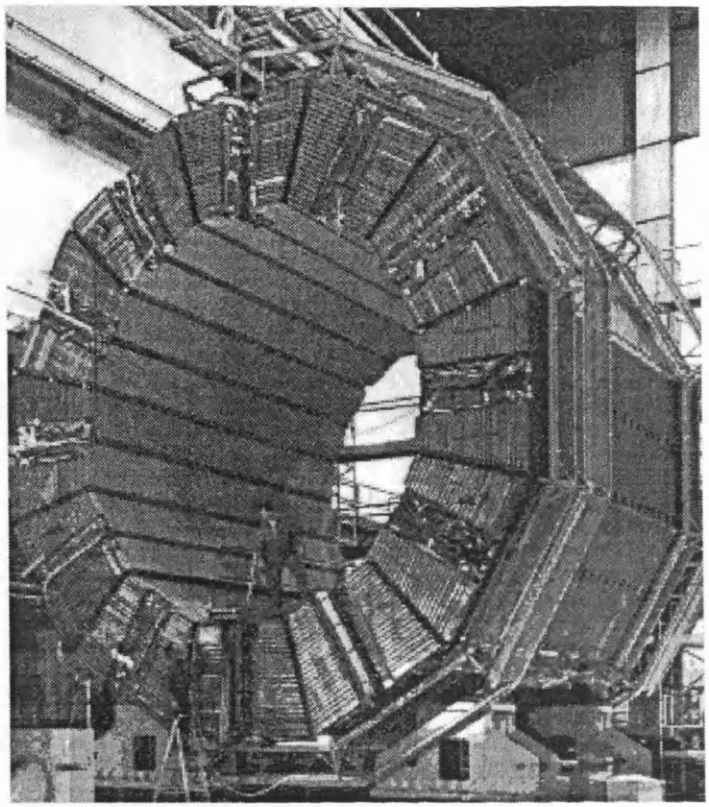

Figure 3.6: *View of the HCAL barrel section during construction of ALEPH. The twelve modules consisting of layers of iron can be seen.*

into the TPC volume in 30 directions away from the interaction region. At the actuator box and splitter ring there are light sensitive diodes, which can be used to measure the beam positions, and steer the beams using motorised mirrors.

3.3.2 Energy loss $\frac{dE}{dx}$ in the TPC.

The amount of ionisation produced by tracks can be measured on up to 340 wires, depending on the angle and curvature of tracks in the TPC. This gives a resolution on the $\frac{dE}{dx}$ of $\sim 4.4\%$ for a track that is perpendicular to the beam pipe. The $\frac{dE}{dx}$ is measured in TPC tracks where there are at least 50 wire measurements associated to the track. To avoid fluctuations in the Landau tail of the $\frac{dE}{dx}$ measurements, a truncated mean is determined for the lowest 60% of measurements only. This mean value is then corrected for the length of each track that is projected on to each wire and for attenuation in the ionisation caused by the drift distance

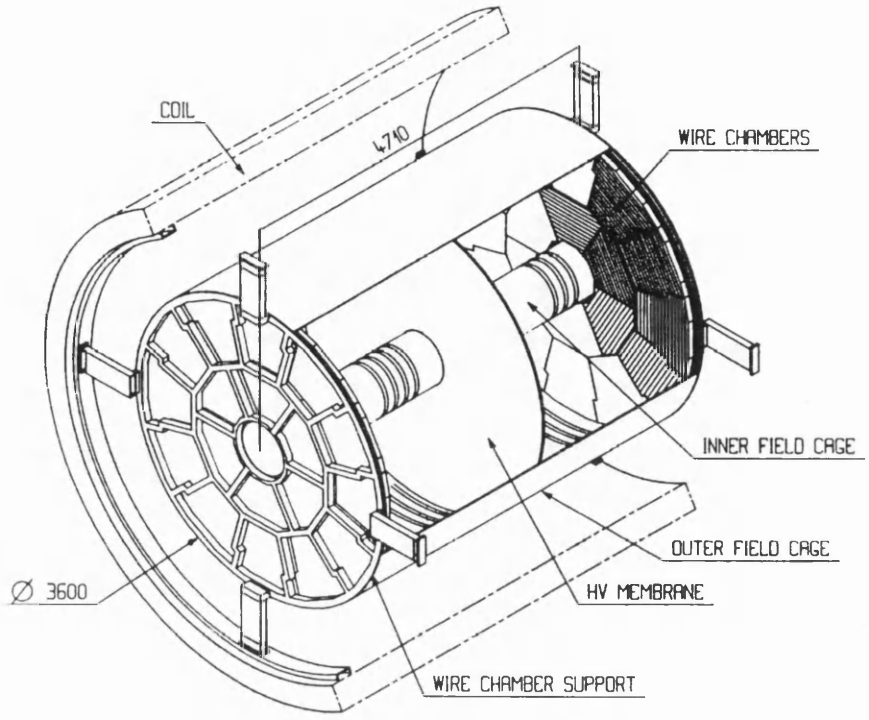

Figure 3.7: *Cut-away view of the TPC.*

variation. The variations in the TPC temperature and pressure affect the gain of the avalanche at the TPC wires. This is corrected for on a run by run basis to keep the ionisation of minimum ionising pions constant.

The $\frac{dE}{dx}$ for particles is given by the modified Bethe-Bloch formula below:

$$\langle \frac{dE}{dx} \rangle = \frac{P_1}{\beta^{P_3}} [P_2 + 2\log_{10}(\beta\gamma) - \beta^{(P_3)} - \delta]$$

where the density function δ is a polynomial of order 5 and P_1, P_2 and P_3 are free parameters. To calibrate the $\frac{dE}{dx}$ curves, 50 GeV electrons from Bhabha events are used to measure the plateau region, the relativistic rise is measured using muons from di-muon events and τ events and minimum ionising pions fix the minimum ionisation level. Tracks from kaons, pions and protons in hadronic events also are used to tune the parameters in the low velocity region. A plot of the $\frac{dE}{dx}$ of tracks in a number of events is shown in Figure 3.9 with the expected mean values for electrons, pions, kaons and protons superimposed. The $\frac{dE}{dx}$ can be used to give significant separation between pions and electrons, particularly at low momenta.

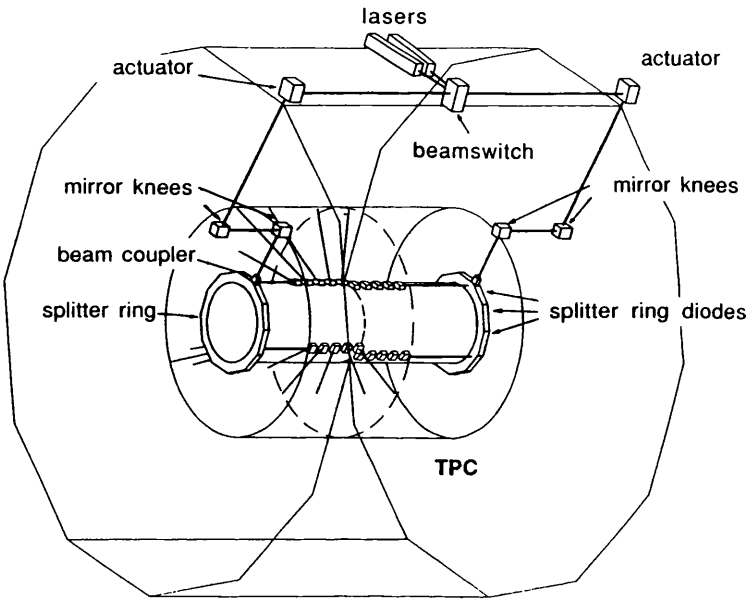

Figure 3.8: *Schematic diagram of the TPC laser calibration system.*

3.4 Electromagnetic calorimeter.

The electromagnetic calorimeter (ECAL) is a sampling calorimeter, each module consisting of 45 sandwiched lead/proportional wire chamber layers, providing 22 radiation lengths. The wire chambers are made from corrugated aluminium extrusions with a number of $25\mu m$ wires running along the length (Figure 3.10). The open side of the chamber is covered by a thin mylar "window", behind which the readout pads are located. The electromagnetic showers developed in the lead sheets cause ionisation in the wire chambers. The subsequent avalanches around the wires can be measured from the signal on the cathode pads. The gas inside the chambers is a mixture of 80% Xe and 20% CO_2 maintained at 60mbar above atmospheric pressure. The gas temperature, pressure and Xe content are monitored to limit fluctuations in gas gain. The position and total energy of electromagnetic showers can be determined from the $30 \times 30\ mm^2$ cathode pads, which are connected internally to form "towers" pointing from the interaction point. Each tower is split into 3 storeys corresponding to the first stack of 10 layers of lead providing 4 radiation lengths, the second stack of 23 layers giving 9 radiation lengths, and the final stack of 12 layers providing 9 radiation lengths.

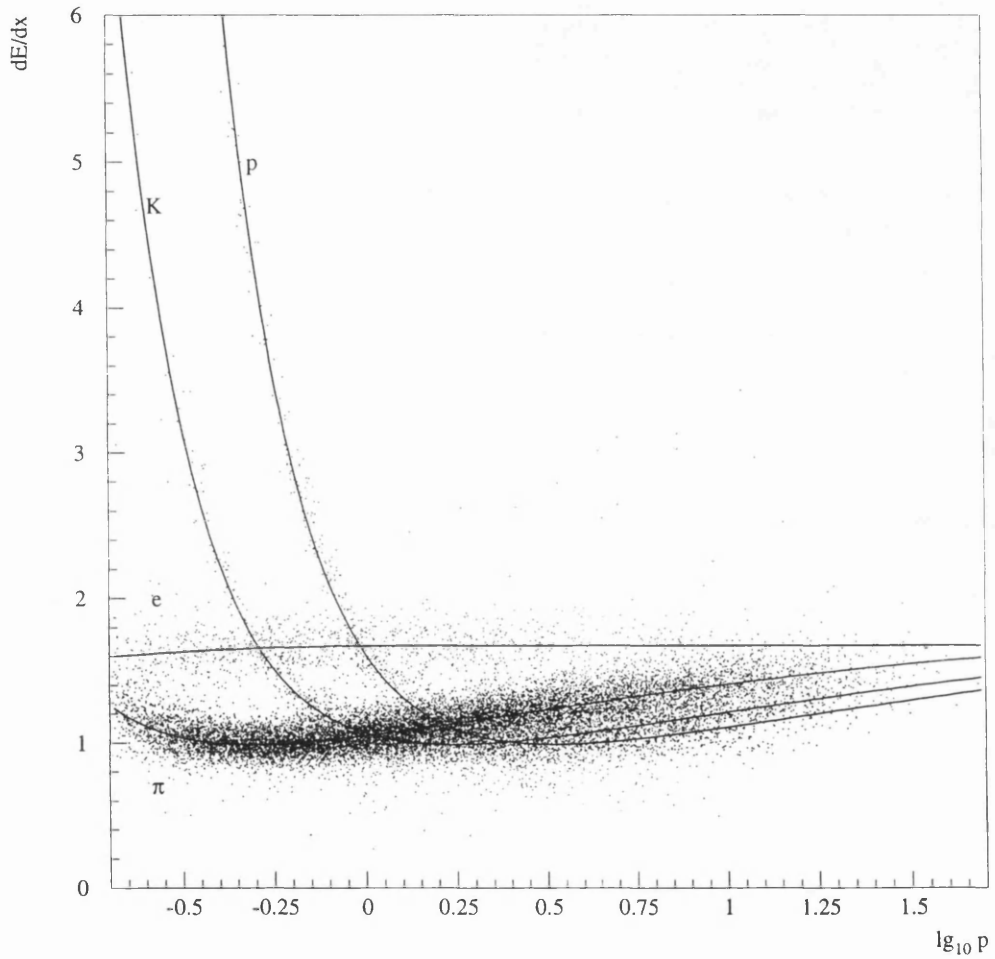

Figure 3.9: *Measurements of the $\frac{dE}{dx}$ of pions, kaons, protons and electrons in the TPC with the parameterised curves overlayed.*

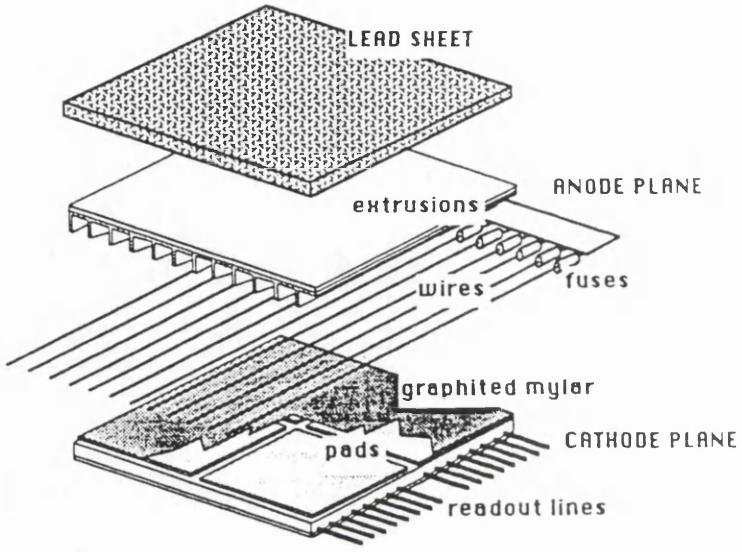

Figure 3.10: *Diagram showing the construction of one ECAL stack layer. Each calorimeter module consists of 45 layers.*

The total of 73,728 towers cover a solid angle of 3.9π, with cracks covering 2% of the barrel region and 6% of the endcaps. The electromagnetic energy resolution of the calorimeter is $18\%/\sqrt{E} + C$, where C is a constant term.

3.5 Hadron calorimeter and muon chambers.

The hadron calorimeter consists of 22 layers of iron with limited streamer tubes as readout between each layer. The iron structure of the barrel section and endcaps forms the return yoke for the magnet. The 5cm thick iron layers provide a total thickness of 1.2 m. The PVC streamer tubes consist of strips of 8 long cells containing an Ar + CO_2 + isobutane mixture, with a $100\mu m$ anode wire running up the middle of each cell. The streamer tubes work in a similar manner to proportional counters, but at a slightly higher voltage. Incident charged particles cause an ionisation avalanche around the cathode wires. The size of the ionisation is independent of the amount of primary ionisation caused by the primary particle.

This ionisation causes signals to be induced on cathode pads on the side of the eight-cell unit. The signals from pads in different layers are summed to form projective towers pointing from the interaction point, which subtend an azimuthal angle of 3.7°. Opposite the pads aluminium strips are positioned parallel to the wires. These give a digital signal each time the cell fires, to give a two-dimensional picture of the hadronic shower and to assist in muon identification.

Outside the iron of the calorimeter are two layers of streamer tubes, forming the muon chambers. These do not contribute to the energy measurement, but provide the coordinates of muons passing out of the calorimeter. These are read out by means of strip electrodes parallel and perpendicular to the cell wires, which allow the muon direction to be measured to 10-15mrad.

3.6 Trigger system.

The luminosity of LEP is such as to allow all e^+e^- interactions to be recorded. The trigger system is designed to perform this task, whilst keeping background events to a reasonable level. The main background comes from beam-gas interactions and beam particles hitting the collimators on either side of the experiment. The trigger is divided into three levels, to provide increasing refinement in trigger decisions. The level 1 is triggered by signals from the ITC, TPC, ECAL and HCAL. The detector is divided into segments, with signals from certain detectors in each segment causing a trigger. The triggers from individual segments are then combined to be tested by a number of defined physics triggers. These triggers then deliver a decision on whether to proceed to the next level. The total decision time for the level 1 trigger is $5\mu s$.

The level 2 trigger looks for tracks in the TPC coming from the interaction region. This is based on signals from special pads situated between the standard pads in the TPC. The ECAL clearing time and TPC drift time total $61\mu s$. To ready the experiment to accept the third bunch crossing after a level 1 trigger, the level 2 decision must be made and transmitted around the detector in a maximum of $6\mu s$ after the end of the TPC drift time. This is achieved using hard-wired processors to search for tracks in a number of zones within the TPC. Most events are processed before the end of the drift time, and tracks close to the middle membrane of the TPC are processed within $2.25\mu s$ after the end of the TPC drift time. An affirmative decision from the level 2 trigger causes the entire detector to be read out.

The level 3 trigger takes place after the data from the detector has been read out and sent to the on-line computer system. The trigger decision is based on the complete set of digitisations from events passed by levels 1 and 2. Rather than achieve high reconstruction precision over the whole detector, the trigger

concentrates on pattern recognition in those parts of the detector fired by the level 1 and 2 triggers.

3.7 Electron identification.

Electrons are identified using $\frac{dE}{dx}$ measurements from the TPC and from the shape of showers in the ECAL. These are quantified using normally-distributed estimators, whose mean value and resolution are measured in events with a clean electron signal. A cut is applied on each estimator to select electron candidates.

3.7.1 $\frac{dE}{dx}$ estimator.

The expected ionisation $\langle\frac{dE}{dx}\rangle$ for an electron is given by the parameterised form described in Section 3.3.2. For each track, the measured $\frac{dE}{dx}$ is compared to the expected $\frac{dE}{dx}$ for an electron using the following estimator:

$$R_I = \frac{dE/dx - \langle\frac{dE}{dx}\rangle}{\sigma_{dE/dx}}$$

where $\sigma_{dE/dx}$ is the parameterised $\frac{dE}{dx}$ resolution for the track, given by the number of $\frac{dE}{dx}$ wire measurements for the track. This estimator is nearly gaussian for a pure sample of electrons, such as gamma conversions in the detector. A cut is applied to electron candidates such that $R_I > -2.5$

3.7.2 Estimators for electromagnetic shower profiles.

Electrons are identified in ECAL from the transverse size and longitudinal profile of clusters. TPC tracks with associated ECAL clusters are projected into the ECAL. To define the transverse size the energy, E_4, in the four central calorimeter towers surrounding the track projection is summed. This is measured for pure samples of electrons to determine an expected value $\langle E_4/p\rangle$ for the electron, where p is the momentum of the track measured in the TPC. This is compared to the measured E_4/p using the estimator

$$R_T = \frac{E_4/p - \langle E_4/p\rangle}{\sigma_{E_4/p}}$$

where $\sigma_{E_4/p}$ is the parameterised resolution of the E_4 measurement.

At a depth t in radiation lengths, the longitudinal energy distribution for an electromagnetic shower can be described by the following function $f(t)$:

$$f(t) = \frac{1}{E_0}\frac{dE}{dt} = (1 - \frac{b}{\beta})\frac{\beta^\alpha}{\Gamma(\alpha)}t^{\alpha-1}e^{-\beta t} + be^{-\beta t}$$

where E_0 is the incident energy of the electron, $\Gamma(\alpha)$ is a function which normalizes f(t), α and β are free parameters and b describes the ionisation component of the shower, which is negligible for incident electrons with energy E_0 greater than 0.5 GeV. The parameters α and β can be obtained from pure samples of electrons to determine the mean ratio $\langle\beta/\alpha\rangle$ and $\sigma(\beta/\alpha)$. A normally distributed estimator, R_L, was defined using the ratio β/α as:

$$R_L = \frac{\beta/\alpha - \langle\beta/\alpha\rangle}{\sigma(\beta/\alpha)}$$

The following cuts were made on R_T and R_L to optimize rejection of hadrons whilst minimising loss in efficiency for electron identification:

- $-1.8 < R_L < 3.0$
- $R_T > -1.6$

3.8 Muon identification.

Muons are identified using the muon chambers and the pattern of digital hits from the digital readout pads in the HCAL. TPC tracks with momentum greater than 1.5 GeV/c are extrapolated through the HCAL. If an extrapolated track intersects an HCAL plane within an active region then the plane would be expected to fire. Allowance is made for multiple scattering of muons by up to 3 standard deviations in the extrapolation uncertainty. Hits are only included if there are no more than 3 adjacent firing tubes. To ensure all muons exit the HCAL, only tracks with momentum greater than 3 GeV/c are selected. Penetrating tracks are defined using the following cuts:

- $N_{fir}/N_{exp} \geq 0.4$
- $N_{exp} \geq 10$
- $N_{10} > 4$

where N_{fir} and N_{exp} are the number of HCAL planes that fired and the number expected to fire within the region of the extrapolated track. N_{10} is the number of planes firing out of the last 10 planes of HCAL. To give further discrimination

of muons from hadrons which have "punched" through the HCAL, the number of hits per plane within 30cm of the extrapolated track are determined. A cut is then applied using X_{mult}, the mean hit multiplicity per fired plane such that:

- $X_{mult} \leq 1.5$

Finally, each muon candidate is required to have fired at least one of the two planes of the muon chambers within four standard deviations of the estimated multiple scattering from the extrapolated TPC track.

3.9 Photon identification.

Photons are identified in the ECAL from the shape of neutral electromagnetic clusters, with additional rejection using photon and π^0 estimators. Cluster shapes are measured for photons and π^0 in clean events. Neutral clusters are those ECAL clusters with no associated TPC track. To differentiate between electromagnetic and hadronic clusters, the photon conversion depth is estimated and the deviation from the parameterized mean electromagnetic shower shape is determined. The decay of neutral pions to two gammas can mimic single photons. These π^0 are identified from the transverse shape of clusters. In addition the compactness of clusters from single photons can be characterised by the fraction F_4 of the total cluster energy contained in the leading 2×2 adjacent towers. A cut is made on single photon candidates such that $F_4 > 0.75$.

3.10 Summary.

The ALEPH detector provides excellent measurement of the momentum and energy of particles originating from Z^0 decays over nearly 4π solid angle. In addition the detector has the capability to identify electrons, muons and single photons from a background of hadrons. The overall detector design, and the construction of those subdetectors relevant to the analysis in Chapters 4 and 5, has been discussed. Further details of the design of individual components of the detector can be found in [45, 46].

Electrons can be identified in hadronic events from $\frac{dE}{dx}$ measurements in the TPC and from the shape of the ECAL energy deposits. Muons can be identified from the digital patterns in the HCAL and the position of hits in the muon chambers. These lepton identification procedures are fully discussed in [45, 46, 47]. The identification of hadronic jets emanating from heavy quarks using electrons and muons is described in the following chapter. Single photons in hadronic events are identified from the shape of neutral clusters in the ECAL.

The selection of events with two hadronic jets and an isolated photon is also discussed in Chapter 4.

Chapter 4

Selection of $q\bar{q}g$ and $q\bar{q}\gamma$ events.

4.1 Introduction.

The decay of the Z^0 to form $q\bar{q}g$ and $q\bar{q}\gamma$ events, and the fragmentation of the partons into three jets was discussed in Chapter 2. The experimental definition of three-jet events used in this analysis and the characteristics of these events are now outlined. The three "tagging" methods that have been used to identify quark and gluon jets are discussed and the estimation of the purity of the quark and gluon jet samples from Monte Carlo events is explained.

4.2 Selection of three-jet hadronic events.

The data used in this study come from a sample of ~1.2 million Z^0 decays recorded in the ALEPH detector in 1990, 1991 and 1992, originating from $e^+ e^-$ collisions at a centre of mass energy of 91.2 GeV. Hadronic events were selected by requiring at least 5 good charged tracks, where a good charged track has the following attributes:

- minimum distance in the $x - y$ plane from track projection to beam spot, $d_0 < 2.0$cm;
- minimum distance in z from track projection to beam spot, $z_0 < 10.0$cm;
- number of TPC hits ≥ 4;
- polar angle of track such that $|\cos\theta| < 0.95$;
- transverse momentum of track with respect to beam axis > 0.2 GeV/c.

A total of 932,336 events passed these cuts. The charged tracks and neutral objects in each event were clustered into jets using the DURHAM jet clustering

algorithm, with the E_0 reconstruction scheme (Section 2.2). Here the energy of the event was taken to be the total visible energy. Three-jet events were selected at $Y_{cut} = 0.01$. A sufficiently high three-jet rate of ~31% was obtained using this value of Y_{cut}, whilst selecting well-defined three-jet events with high sphericity and a good separation between the jets. In Section 4.7.3 it is shown that there is an acceptable match between jets at parton and hadron level above $Y_{cut} \sim 0.008$. Theoretical calculations of the jet rates diverge from the measured rates [11] below $Y_{cut} = 0.01$. The tagged jet samples were then taken from the remaining sample of 3-jet events. This is outlined in the following section. Further event cuts used to produce an improved three-jet event selection are described in Section 4.6.

4.3 Identification of quark and gluon jets.

4.3.1 Energy-ordering.

The exact $O(\alpha_s)$ three-jet cross-section [48] is given by:

$$\frac{1}{\sigma}\frac{d\sigma}{dx_q dx_{\bar{q}}} = \frac{2\alpha_s}{3\pi}\frac{x_q^2 + x_{\bar{q}}^2}{(1-x_q)(1-x_{\bar{q}})}$$

where x is the fraction of the beam energy carried by the partons. From this cross-section it can be seen that the quark and anti-quark are more likely to carry off high x, and thus the gluon is more likely to carry lower x than the two other partons. Thus energy-ordering can be used to separate samples of quark and gluon jets.

In this analysis, the jets were ranked using the energy calculated from the jet directions (Section 4.5). The highest energy jets formed a high-purity (mean P_q ~95%) sample of quark jets, whilst the second-highest energy jets in each event formed a sample of quark jets with mean purity of ~70%. The lowest energy jets formed a sample of gluon jets with mean purity ~65%. For ease of description the three jet samples are labelled here $JET^{(1)}_{q\bar{q}g}$, $JET^{(2)}_{q\bar{q}g}$ and $JET^{(3)}_{q\bar{q}g}$ respectively. To avoid confusion, the energy-ordered events from the normal mixture of hadronic events are labelled Sample A.

4.3.2 Energy-ordering with lepton-tagging.

Heavy-flavour quark states can decay semileptonically, giving rise to electrons or muons with high momentum. Due to the hard fragmentation of the b-quark, the leptons can have high transverse momentum with respect to the direction of the

parent b-hadron. The presence of these leptons can thus identify jets originating from b- or c-quarks. This has been used in a number of ALEPH electroweak and heavy flavour studies [49].

The identification of electrons was described in Section 3.7. Electrons were selected from electromagnetic energy clusters with an associated charged track, which satisfied the following cuts:

- $\frac{dE}{dx}$ estimator, $R_I > -2.5$;
- For the longitudinal shower profile estimator R_L, $-1.8 < R_L < 3.0$;
- Transverse shower profile estimator $R_T > -1.6$.

Muon identification was outlined in Section 3.8. The following cuts were made on TPC tracks with associated muon chamber hits:

- $N_{fir}/N_{exp} \geq 0.4$;
- $N_{exp} \geq 10$;
- $N_{10} \geq 4$;
- $X_{mult} \leq 1.5$.

For each hadronic event containing leptons, the tracks were clustered into jets using the JADE algorithm at a Y_{cut} of 0.0044. The transverse momentum of each lepton was determined with respect to its associated jet. This was defined for the momentum of the jet with the lepton momentum subtracted as follows:

$$p_t = \frac{|\vec{p}_l \times (\vec{p}_{jet} - \vec{p}_l)|}{|\vec{p}_{jet} - \vec{p}_l|}$$

From Monte Carlo studies, these JADE clustered jets were found to represent best the direction of the parent b-hadron. The leptons were assumed to have originated from the semileptonic decay of a heavy quark if it satisfied the following cuts:

- $p > 3.0$ GeV/c;
- $p_t > 1.0$ GeV/c.

Identification of both quark jets in a three-jet event using high p, high p_t leptons results in an extremely low efficiency for quark jet identification. Instead the lepton-tagging method was combined with energy-ordering of jets. For each event containing one or more high p, high p_t leptons, the jets clustered using the

DURHAM algorithm at $Y_{cut} = 0.01$ were ranked by the calculated energy of the jet in the same manner as Sample A. The highest energy jet was again assumed to be a quark jet. Events were selected where one of the two lower energy jets contained a lepton which passed the p and p_t cuts. For these events, the highest energy jets formed a sample of predominantly heavy quark jets, with a mean quark jet purity of ~96%. The lepton-tagged jets formed a sample of jets with ~85% mean quark jet purity. The remaining lower-energy jet in each event formed a sample of gluon jets with ~81% mean gluon jet purity. These three jet samples are labelled here $JET^{(1)}_{b\bar{b}g}$, $JET^{(lepton)}_{b\bar{b}g}$ and $JET^{(gluon)}_{b\bar{b}g}$. Events with a high-$p_t$ lepton in one of the lower energy jets are labelled Sample B.

4.3.3 Isolated photons in hadronic events.

A sample of $q\bar{q}\gamma$ events were identified as those events where one of the jets contained a photon whose energy made up a high proportion of the visible energy of one jet. The two remaining jets in each event, ranked by energy, formed two highly pure quark jet samples. Photon identification was discussed in Section 3.9. Photons were selected from neutral electromagnetic energy clusters using photon and π^0 estimators. Events were chosen from the three-jet sample where one of the two lower energy jets contained a photon that carried a fraction of the jet energy $Z_\gamma > 0.9$. For clarity this jet is labelled $JET^{(\gamma)}_{q\bar{q}\gamma}$. The remaining two jets in each event were ranked by energy to form a higher-energy quark jet sample and a lower energy quark jet sample. These are labelled $JET^{(1)}_{q\bar{q}\gamma}$ and $JET^{(quark)}_{q\bar{q}\gamma}$ respectively. Events with a photon comprising one of the lower energy jets are labelled here Sample C. A study was made of the photon purity and origin using JETSET Monte Carlo events. These purity values are given in Table 4.1 for each quark jet sub-sample in the event. With the event cuts used, the background from initial-state radiation is minimal. However, in the Monte Carlo events there is ~2% background from π^0 mis-identification, which rises to ~15% in the quark jet samples below 20 GeV. A Monte Carlo study [50] has indicated that these high energy isolated π^0 originate from high energy quarks that have not lost energy by gluon radiation and have merely converted into a π^0. This would suggest that the quark jet sample ($JET^{(quark)}_{q\bar{q}\gamma}$) may contain up to 15% background from gluon jets below 20 GeV energy.

4.4 Definition of the plane of three-jet events.

At parton level in $q\bar{q}g$ and $q\bar{q}\gamma$ events the particles all lie in the same plane, because of momentum conservation. Assuming local parton-hadron duality [22], the same should be true of the three jets at hadron level. A plane was defined

Energy range GeV	*Purity F.S.R.*	*Purity I.S.R.*	*Purity Hadronic*
$JET^{(1)}_{q\bar{q}\gamma}$			
30-35	100.0	0.0	0.0
35-40	97.9 ± 1.4	2.1 ± 1.4	0.0
40-45	95.9 ± 1.1	0.0	4.2 ± 1.1
$JET^{(quark)}_{q\bar{q}\gamma}$			
10-15	85.0 ± 8.0	0.0	15.0 ± 8.0
15-20	85.3 ± 6.1	0.0	14.7 ± 6.1
20-25	96.3 ± 2.6	1.9 ± 1.8	1.9 ± 1.8
25-30	98.2 ± 1.8	0.0	1.9 ± 1.8
30-35	98.2 ± 1.7	0.9 ± 0.9	0.9 ± 0.9
35-40	100.0	0.0	0.0
40-45	100.0	0.0	0.0

Table 4.1: *Photon purity in $q\bar{q}\gamma$ events for different quark jet energies. The proportions of final-state radiation (F.S.R.), initial-state radiation (I.S.R.) and hadronic background come from JETSET Monte Carlo events.*

for each event using the sphericity tensors [51]. The first tensor defines the axis of greatest activity in the event, and will generally lie close to the direction of the most energetic jet. The second tensor defines an axis of greatest activity in the plane perpendicular to the first tensor. The angle of each jet to this event plane is shown in Figure 4.1 for each of the jet samples described in Section 4.3. The jets with higher energy tend to have more influence over the definition of the event plane. Thus the highest energy jet in each tagged sample generally lies closest to the event plane. The lower energy jets tend to lie within $10 - 15°$ of the plane. For the $q\bar{q}\gamma$ events, the jet containing the photon ($JET^{(\gamma)}_{q\bar{q}\gamma}$) has a well defined direction, and lies closer to the event plane. The projections of each jet onto the event plane were determined, and the angles between these projections (Figure 4.2) were used to calculate the energy of the jets. The jet projections were also used to define further event selection criteria described in Section 4.6. For the analysis of the string effect, the projections in the event plane were determined

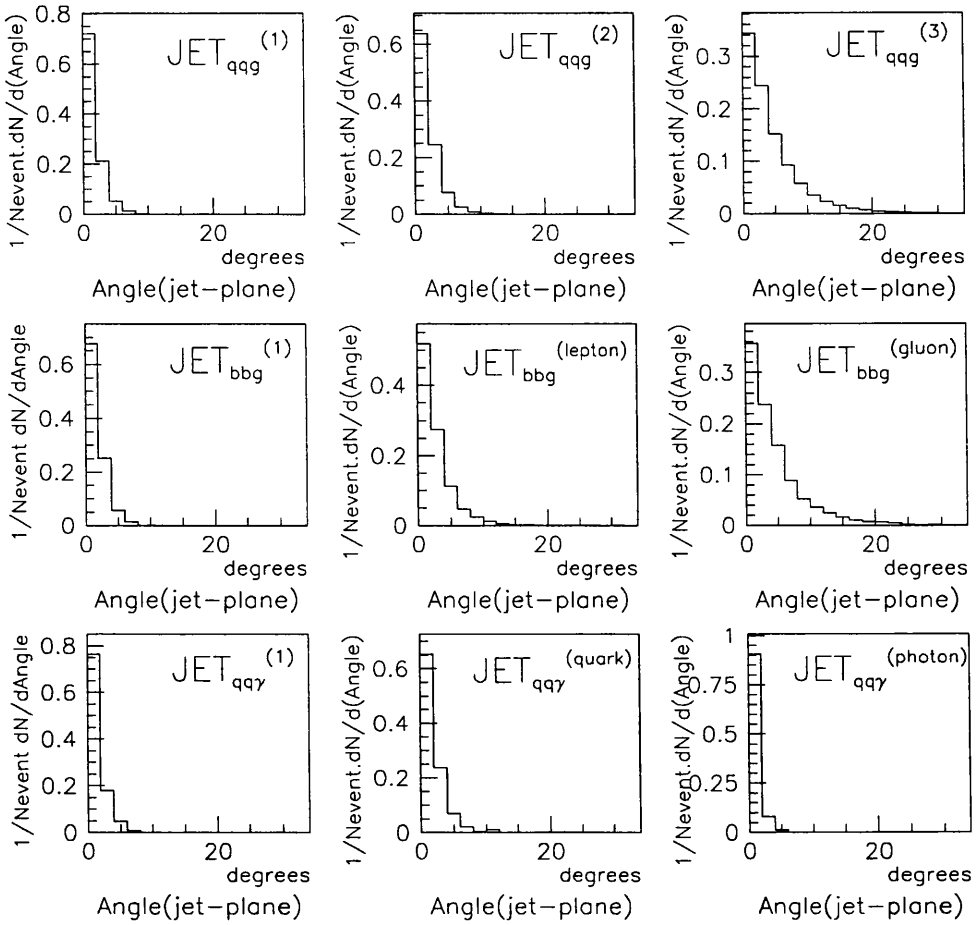

Figure 4.1: *Angle between each jet sub-sample and the event plane.*

for the charged tracks and neutral objects.

4.5 Determination of the energy of jets.

The visible energies of the jets in each tagged sample are shown in Figure 4.3. In each event sample the jets have a broad range of visible energies. For some b-jets, and particularly the lepton-tagged jets ($JET_{b\bar{b}g}^{(lepton)}$) in Sample B, there is

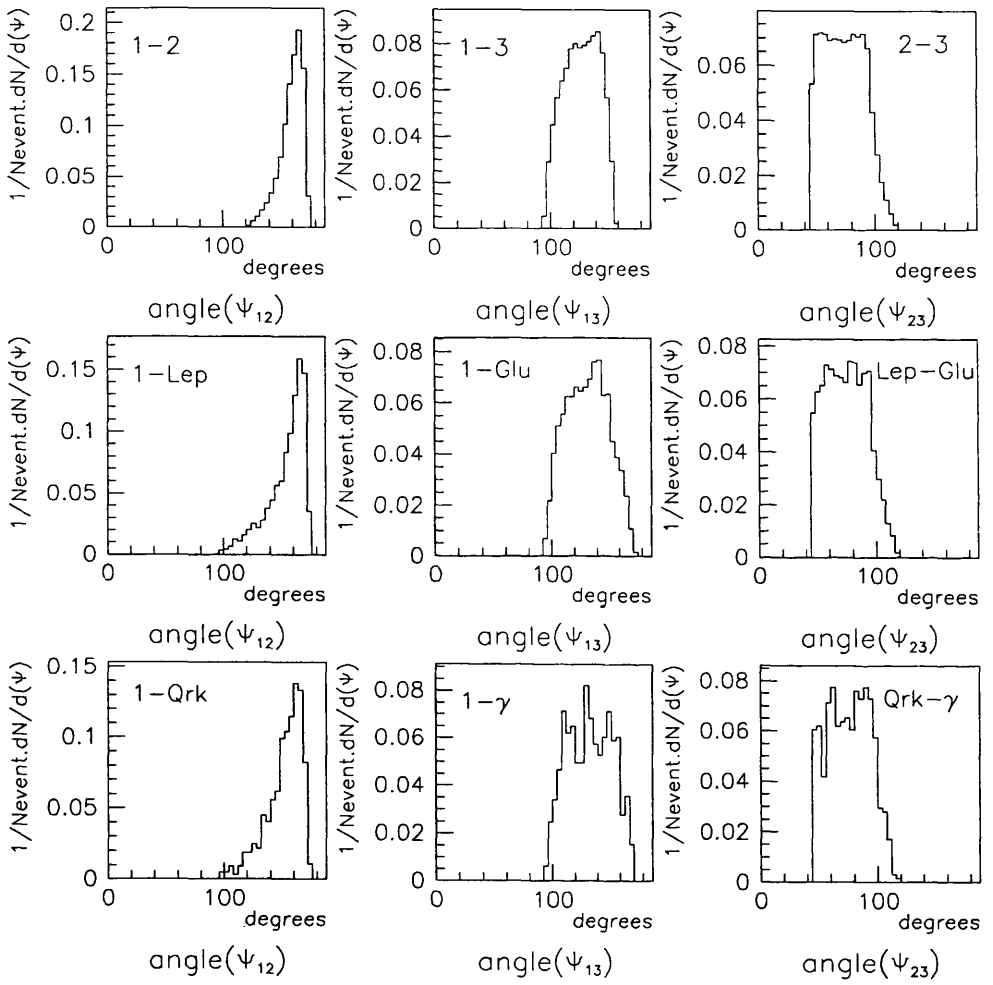

Figure 4.2: *Angle between the jet projections in each three-jet event sample.*

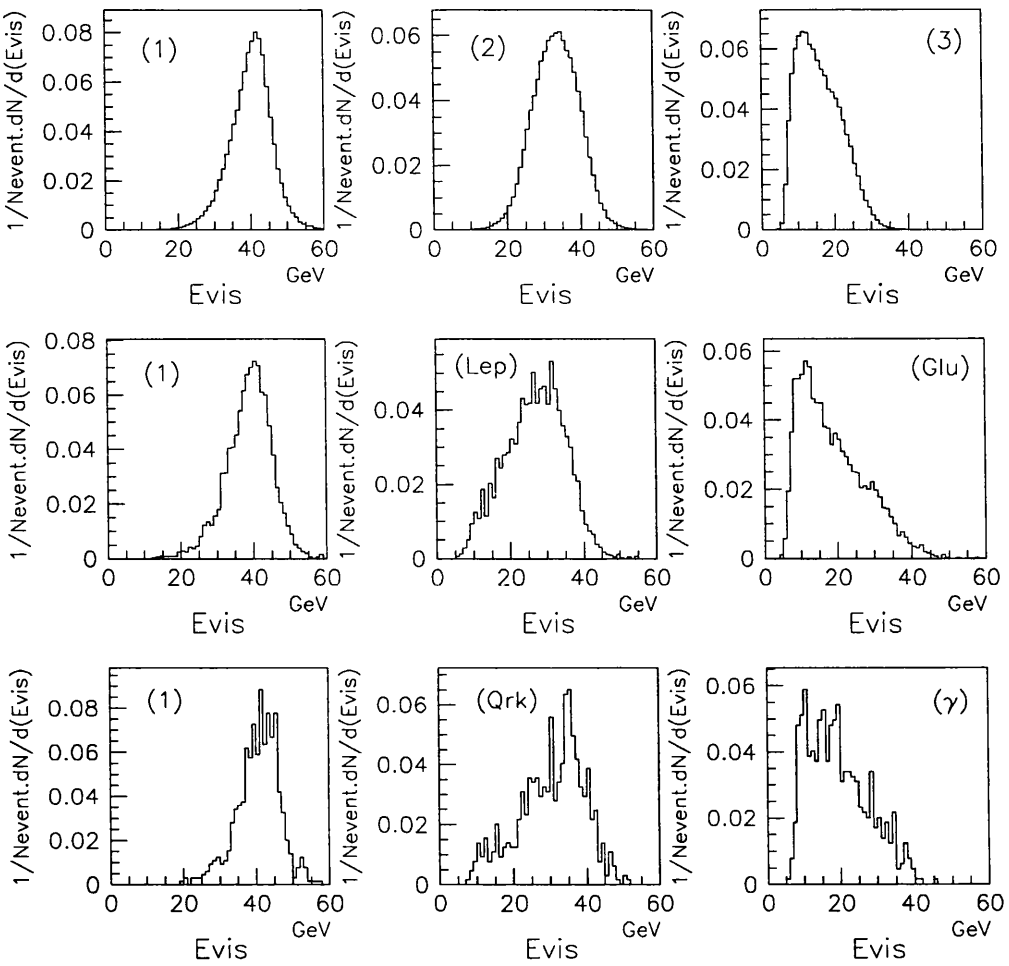

Figure 4.3: *Visible energy of the jet sub-samples.*

a significant amount of missing energy that has been carried away by neutrinos after semi-leptonic decays of heavy hadrons. To avoid this problem and define the jet energies with greater precision, they were determined from the angles between the jet projections.

For a three body decay, the energy of each particle can be determined from the angles between the particles. Consider partons i, j and k, with inter-jet angles ψ_{ij}, ψ_{ik} and ψ_{jk}. For massless partons, the energy of parton i is approximately

given by:

$$E^{(i)}_{CALC} = \frac{E_{CM}}{2} \frac{\sin\psi_{jk}}{\sin\psi_{ij} + \sin\psi_{ik} + \sin\psi_{jk}}$$

With the assumption of local parton-hadron duality, the energies of the jets were calculated from the angles between the jet projections using this formula. These calculated energies are shown in Figure 4.4 for each tagged sample.

To demonstrate that the calculated energy represents the jet energy well, the quantity E_{RES} was determined, defined by:

$$E_{RES}(JET^{(i)}) = \frac{E_{CALC}(JET^{(i)}) - E_{VIS}(JET^{(i)})}{E_{CALC}(JET^{(i)})}$$

This is shown plotted in Figure 4.5 for each jet sample. E_{RES} has a symmetric distribution around zero for Sample A, Sample C and for $JET^{(g)}_{b\bar{b}g}$ in Sample B. The missing energy is clearly evident in the lepton-tagged jets ($JET^{(lepton)}_{b\bar{b}g}$), but also noticeable in the highest energy jets in Sample B ($JET^{(1)}_{b\bar{b}g}$). The jets containing the photon in Sample C ($JET^{(\gamma)}_{q\bar{q}\gamma}$) have a very good match between E_{VIS} and E_{CALC}.

4.6 Additional cuts to refine the event samples.

The event samples were further refined with the following criteria:

- $\omega_{ij} + \omega_{ik} + \omega_{jk} > 358.5°$, where the ω are the angles between jets i, j and k; (This removes events where the jet axes are not coplanar.)
- for each pair of jet projections, $\psi_{ij} < 180°$; (This removes a small number of events with poor jet clustering.)
- $\psi_{ij} > 45°$; (This improves the separation between the two lower energy jets in each sample.)
- for polar angle θ between each jet and the beam line, $\theta(JET^i) > 30°$; (This removes events where part of the jet may have been lost down the beam pipe.)

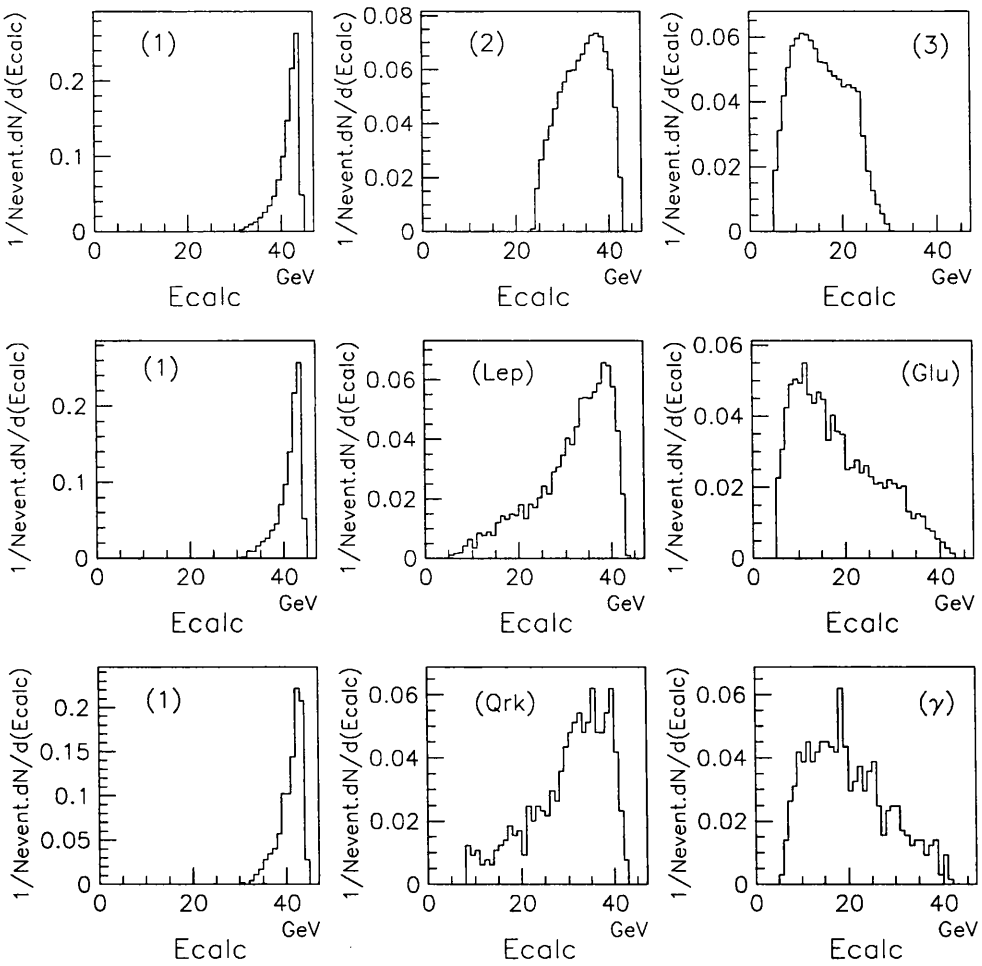

Figure 4.4: *Calculated energy of the jet sub-samples. The jet energies were determined from the angles between the jet projections.*

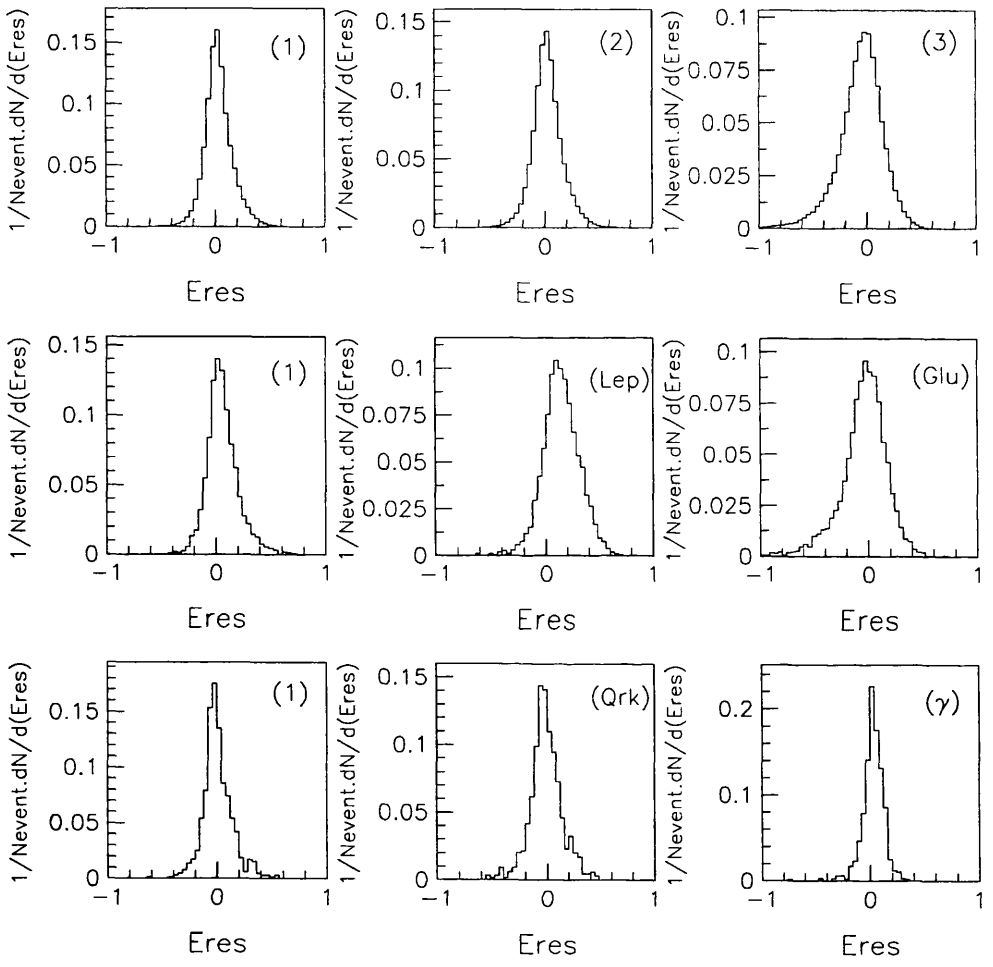

Figure 4.5: *Comparison of the calculated and visible energies of the jet subsamples.*

Event cut	*Energy ordered*		*Lepton-tagged*		$q\bar{q}\gamma$	
	Events	%	*Events*	%	*Events*	%
Sum of jet angles $> 358.5°$	6961	2.4	347	3.8	11	0.9
$\psi_{ij} < 180°$	258	0.1	21	0.2	0	-
$\psi_{ij} > 45°$	68081	23.0	1942	21.5	182	15.5
$30° < \theta_{JET} < 150°$	75357	25.5	1991	22.0	330	28.1
Minimum jet energy > 5 *GeV*	2517	0.9	152	1.7	2	0.2
Jet multiplicity ≥ 3	1301	0.4	35	0.4	4	0.3
Events passing cuts	140907	47.7	4561	50.4	645	54.9

Table 4.2: *The number and proportion of events failing each successive cut in each sample of three-jet events.*

- for each jet, $E_{CALC} > 5$ GeV; (This removes jets with poorly defined, or badly clustered jets.)
- for jet multiplicity n of each jet, except the photon jet ($JET^{(\gamma)}_{q\bar{q}\gamma}$) in Sample C, $n(JET^{i}) \geq 3$.

The number of events rejected by each successive cut is given in Table 4.2 for samples A, B and C. The cuts remove a similar proportion of events in Sample A and Sample B, compared to the initial number of tagged events in each sample. Proportionally fewer events are removed by the cuts for the $q\bar{q}\gamma$ events (Sample C), since these events have more well-defined jets. For the Monte Carlo events studied, the above cuts were seen to remove a significant proportion of events where the number of partons or the direction of the parton jets did not match the jets at hadron level.

For the quark and gluon jet comparison, the jets in samples A, B and C were split into sub-samples according to E_{CALC} in 5 GeV intervals. This enabled a comparison to be made of jets with similar energy. To analyse the string effect, a further event cut was made using the polar angle of the normal to the event plane with respect to the beam line, such that:

- $120° < \theta_{\perp} < 60°$

This removes events where part of the event plane is close to the beam line.

Within each energy range, the mean calculated energies of the jets from each jet sub-sample (Table 4.3) lie approximately in the centre of the range. Some jet properties, such as multiplicity, are heavily dependent on the energy of the jet. To allow for any mis-match in the energies of the quark and gluon jet samples, each jet in the samples was assigned a weight, such that the weighted mean energy

	Energy-ordered events			*Lepton-tagged events*			$q\bar{q}\gamma$ *events*		
Energy GeV	*No. of jets*	E_{CALC} *GeV*	E_{VIS} *GeV*	*No. of jets*	E_{CALC} *GeV*	E_{VIS} *GeV*	*No. of jets*	E_{CALC} *GeV*	E_{VIS} *GeV*
$JET^{(1)}$									
30-35	4381	33.5	32.9	169	33.5	32.2	22	33.7	35.7
35-40	27289	38.1	37.1	914	38.1	35.9	169	38.2	38.1
40-45	109235	42.5	41.0	3478	42.5	39.8	454	42.4	41.8
Quark									
5-10				68	8.4	9.4	14	8.9	10.5
10-15				165	12.7	12.6	27	12.5	13.1
15-20				314	17.6	15.9	50	17.6	17.5
20-25				397	22.6	20.0	66	22.8	23.7
25-30	27813	27.8	27.6	641	27.7	23.5	101	27.8	28.5
30-35	42873	32.6	32.0	1053	32.7	27.8	163	32.5	32.8
35-40	49973	37.5	36.2	1363	37.6	31.6	177	37.5	37.5
40-45	17846	41.2	38.9	561	41.2	33.5	47	41.0	38.7
Gluon									
5-10	28150	8.0	9.6	889	7.9	9.4			
10-15	41802	12.5	13.1	1098	12.4	12.8			
15-20	35047	17.4	17.7	862	17.4	17.7			
20-25	29177	22.3	22.4	586	22.5	22.3			
25-30				488	27.5	27.1			
30-35				390	32.2	31.4			
35-40				209	37.1	35.8			
40-45				40	41.1	38.1			

Table 4.3: *The number of jets and the mean calculated and visible jet energies are shown for each jet sub-sample divided by 5 GeV energy intervals.*

of the sub-sample lay in the middle of each energy range. The same weight was then applied for each jet distribution used in the quark/gluon comparison. This did not change the final jet distributions significantly.

4.7 Study of the purity of the jet sub-samples.

The quark or gluon jet purities of the tagged sub-samples described in the previous section were estimated using Monte Carlo simulated events. It was necessary first of all to give a definition of quark and gluon jets in Monte Carlo events. For convenience in this analysis, jets formed by anti-quarks are labelled also as quark jets. The various stages in the modelling of a Monte Carlo event were described in Section 2.3.1. Jets were defined at three levels of the events as follows:

- at parton level, after the development of the perturbative parton shower from the primary q and $\overline{q}$;
- at hadron level, following the non-perturbative hadronisation of the partons into hadrons, and the decay of unstable hadrons;
- at detector level, with the particles from the hadron level passed through a simulation of the ALEPH detector. The jets here have been defined by the event selection cuts, and the DURHAM clustering algorithm, with E_0 reconstruction scheme at a Y_{cut} of 0.01, as described in Sections 4.2 and 4.6.

4.7.1 The definition of quark and gluon jets at parton level.

The concept of jets at hadron level is in a sense artificial, although it is necessary to categorize hadronic events using some scheme in order to analyse processes occurring at parton level. It was explained in Section 2.6.1 that at parton level, the processes giving rise to particle flow can be calculated by considering the hard partons as antennae for the radiation of soft gluons. Since the hard partons contribute to the radiation of soft gluons over the whole event, the concept of jets at parton level is rather meaningless. Nevertheless, for the purpose of this study it was necessary to define the source of each jet at hadron level. At parton level there may be one or more partons responsible for each jet at hadron level, and gluons may split into q and $\overline{q}$ pairs. Some gluons may also be emitted between the jets, giving rise to inter-jet particle flow. To cope with this situation the partons were clustered into jets using the same jet clustering algorithm that was used at detector level. However, of the JETSET or HERWIG Monte Carlo events that clustered to three jets at detector level, ~20% of these events did not cluster to three parton jets at $Y_{cut} = 0.01$ [52]. Instead the Y_{cut} was left free, and the events were clustered until three parton-level jets were obtained. In ~1% of three-jet events, no gluon radiation occurred during the parton shower, so only the primary q and $\overline{q}$ were present after the parton shower. These events could not be clustered into three jets at parton level and were termed "ambiguous". Of the remaining

events which had three parton jets, the two jets containing the primary quark and anti-quark were labelled as quark jets, and the third jet was labelled the gluon jet. The primary q and $\overline{q}$ were clustered into the same jet in a tiny fraction of events, so these also were labelled "ambiguous".

4.7.2 The definition of quark and gluon jets at hadron and detector levels.

With the two quark jets and the gluon jet defined at parton level, it was then necessary to match the parton jets with jets at hadron level and detector level, in order also to define quark and gluon jets at those levels. The events all had been selected with three jets at detector level. The particles at hadron level were clustered into jets using the same DURHAM algorithm, but Y_{cut} was again left free, since a significant number of events did not have three jets at $Y_{cut} = 0.01$.

To match jets between parton level and hadron level, and then between hadron level and detector level, a number of schemes were tried [52], involving matching of the jet energies, angles or a combination of the two. The closest angle between the jets at each level was found to give the best results. Each jet at hadron level was matched to the parton jet closest in angle. These matching angles are shown in Figure 4.6 for the jets at parton level compared to hadron level ranked by energy, in HERWIG Monte Carlo events clustered to $y_{cut} = 0.01$. The lowest-energy jet has the worst angular matching between parton and hadron level, but in most events the worst matching is less than 40°. In some events, two of the hadron level jets were closest to the same parton level jet. These events were termed "ambiguous". Other events were labelled "ambiguous" where the closest matching angle of one of the hadron jets was greater than 40°. The successfully matched hadron jets were labelled as quark or gluon jets from the corresponding parton jets. The angular matching process was then repeated between hadron level and detector level. Here there also were a few events labelled as "ambiguous" where the jets could not be matched. The detector level jets were identified as quark or gluon jets from the corresponding hadron level jets.

4.7.3 A study of the "ambiguous" events.

In order to define quark and gluon jets at detector level, a number of events were labelled "ambiguous" for the following reasons:

- no gluon radiation occurred during the parton shower, so only the primary quark and anti-quark were present at parton level and these could not be clustered into three jets;

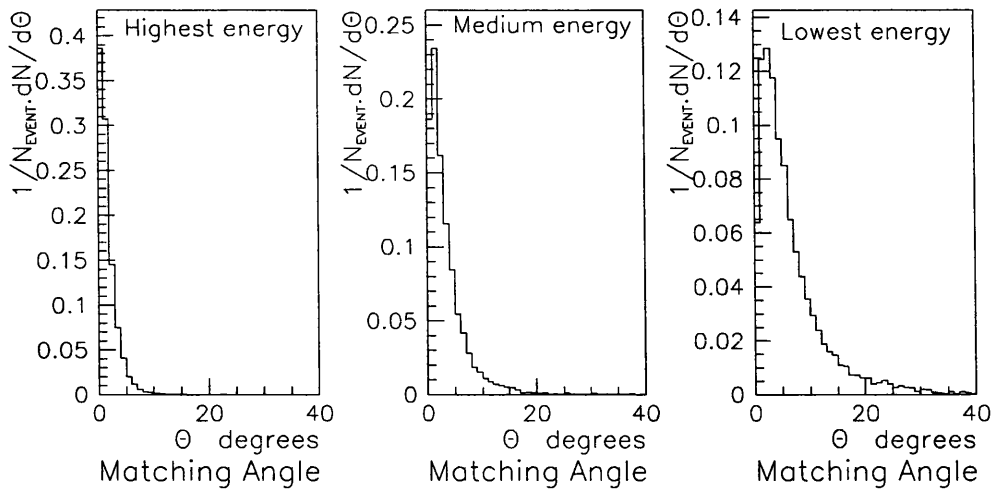

Figure 4.6: *Matching angle between jets at parton level and hadron level in HERWIG Monte Carlo events with the jets energy-ordered.*

- an insignificant fraction of events where both primary q and $\overline{q}$ were clustered into the same parton-level jet;

- two jets at one level were closest in angle to the same jet at a different level in the Monte Carlo. This did not allow reliable matching between the levels. A large number of these ambiguous events appeared to be almost two-jet-like in topology, with one jet clustered into two jets at one level in the Monte Carlo, and at the next level the jet from the opposite hemisphere clustered into two jets;

- when matching between levels, the matching angle of the jets was greater than a specified 40°. The exact magnitude of this angle was arbitrary. However the uncertainty in the definition of the quark and gluon jets becomes greater as this matching angle increases, so a cut-off point was desirable.

Many of these ambiguities came from Monte Carlo events where the topology at parton level was "four-jet-like", or from "two-jet-like" events where the angular spacing of the jets was not significant. Particularly in the latter cases, two of the jets in the event are not really initiated by a quark and gluon separately, but merely appear to arise from a quark jet that is split into two jets. Events of this type cannot really be corrected for in the data, and complicate the study of particle flow and the nature of jets in three-jet events. Some of the experimental cuts outlined in Section 4.6 were made in an effort to remove these events as far as possible. The proportion of ambiguous events are shown in Figure 4.7 as a function of Y_{cut} for JETSET and HERWIG events. The percentage of ambiguous events increased rapidly below $Y_{cut} = 0.01$, but decreased only marginally above this value. The proportion of ambiguous events could be reduced by a factor of $\sim$2, for three-jet events clustered at $Y_{cut} = 0.01$, by specifying a minimum angle of 45° between the lowest energy jets. Using all the cuts specified in Section 4.6, the level of these "ambiguous" events was reduced to $\sim$4.5% of the total tagged-events. In symmetric "Y" events, where the jets were well spaced apart, this number dropped to 1-2%.

4.7.4 Estimation of the purity of jet samples.

Using the jet identification method outlined in the previous section, the jets in each sample of tagged Monte Carlo detector-simulated events were identified as correctly tagged, wrongly tagged or from events defined as "ambiguous". The wrongly tagged jets can be corrected for in the data using two jet samples with different quark and gluon jet purities. The "ambiguous" jets cannot be corrected

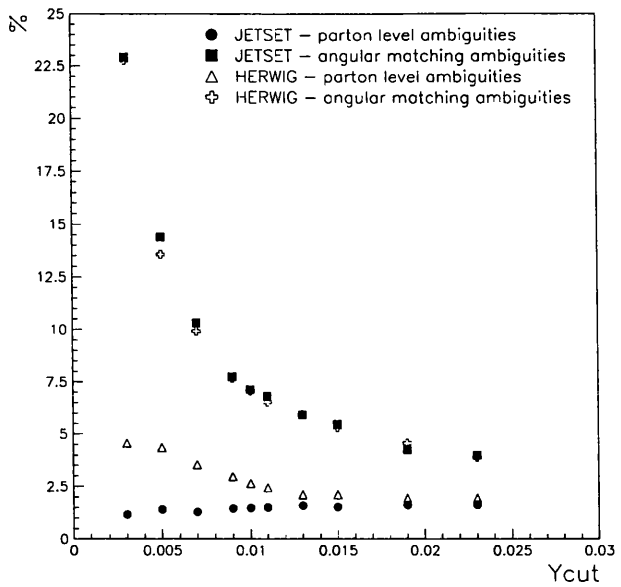

Figure 4.7: *Percentage of ambiguous events at parton and hadron level in JETSET and HERWIG three-jet events at various Y_{cut}. All event cuts from Section 6 have been applied at detector level, apart from the minimum jet angle cut ($\psi_{ij} > 45°$).*

for in the data without using Monte Carlo events, so the purity was determined ignoring the ambiguous events,

$$P = \frac{C}{C+W}$$

The "ambiguities" were considered as an uncertainty in the purity value. Assuming that a minimum of A/2, and a maximum of A events were correctly tagged, a systematic error in P was determined from the maximum and minimum possible values of P from

$$P_{min} = \frac{C+A/2}{C+W+A}$$

$$P_{max} = \frac{C+A}{C+W+A}$$

The minimum possible fraction of events correctly tagged is strictly given by $\frac{C}{C+W+A}$. However many of the ambiguous events seem to be two-jet event background, rather than wrongly tagged. For $C > W$, a minimum of half the "ambiguous" events were assumed to be correctly tagged. The purities were determined in JETSET events for each sub-sample of jets used, and are given in Table 4.4. The purities of the quark jet samples improve as the energy of the jets increases. The reverse is true for the gluon jet samples. This is to be expected, since the mean energy of quark jets in three-jet events is higher than the mean energy of gluon jets.

4.8 Summary of three-jet event samples.

Three samples of three-jet events were obtained containing $q\overline{q}g$, $b\overline{b}g$ and $q\overline{q}\gamma$ events, with the jets in each sample tagged using energy-ordering, energy-ordering with lepton-tagging and photon identification respectively. An event plane was defined for these events, and the jet energies determined from the angles between the jets. As far as possible the samples were selected using the same criteria and event cuts, so that the events had a similar range of topologies and jet configurations. Each sample of events was then split into jet sub-samples with 5 GeV energy ranges. Using JETSET Monte Carlo events, the quark and gluon jet purity of the sub-samples was estimated with a few percent error.

A comparison of quark and gluon jets is made in Chapter 5 using the jet sub-samples. In Chapter 6 an analysis is made of the string effect using the complete event samples.

Jet	*Energy range GeV*	*Purity Lepton-tagged sample*	*Purity Energy-ordered sample*
$JET^{(1)}$	30-35	68.1 ± 3.6	77.7 ± 0.8
q purity	35-40	88.5 ± 1.2	90.7 ± 0.8
	40-45	96.6 ± 2.7	97.3 ± 3.0
$JET^{(lepton)}_{b\bar{b}g}$, $JET^{(2)}_{q\bar{q}g}$	5-10	45.7 ± 8.3	
	10-15	68.3 ± 4.3	
q purity	15-20	77.1 ± 2.6	
	20-25	85.5 ± 1.8	
	25-30	92.2 ± 1.3	60.8 ± 1.1
	30-35	94.9 ± 1.7	75.9 ± 0.9
	35-40	98.0 ± 3.5	88.0 ± 2.3
	40-45	98.6 ± 5.9	94.6 ± 5.5
$JET^{(gluon)}_{b\bar{b}g}$, $JET^{(3)}_{q\bar{q}g}$	5-10	97.2 ± 4.8	90.6 ± 4.9
	10-15	94.4 ± 2.0	83.1 ± 1.8
g purity	15-20	91.0 ± 1.9	71.6 ± 0.9
	20-25	84.9 ± 1.6	57.2 ± 1.1
	25-30	75.7 ± 2.0	
	30-35	63.4 ± 2.7	
	35-40	54.3 ± 5.0	
	40-45	24.0 ± 6.8	

Table 4.4: *Estimated quark and gluon jet purities for each jet subsample in the lepton-tagged and energy-ordered three-jet samples.*

Chapter 5

Quark and gluon jet comparison.

5.1 Introduction.

The selection of three samples of three-jet events was described in the previous chapter. The jets in each sample were tagged as originating from a quark, b-quark, gluon or photon. These jets were then split into sub-samples according to jet energy in 5 GeV intervals. The different sub-samples are summarised in the next section. The particle flow, energy flow and other jet characteristics were measured in each sub-sample. A comparison of the properties of these jet sub-samples is given in Section 5.3. The variation in the jet properties with energy is difficult to observe in these uncorrected measurements, since the quark and gluon purities of the sub-samples vary with their energy. Each jet distribution was corrected for the quark and gluon purities. This procedure is described in Section 5.4, followed by a comparison of the corrected quark and gluon jet properties with energy (Section 5.5). Finally, systematic effects in the quark/gluon jet comparison are discussed in Section 5.6.

5.2 Summary of the jet sub-samples.

Four categories of jets were obtained from the samples of three-jet events: a highest energy quark jet sub-sample, a quark jet sub-sample with lower energy, a gluon jet sub-sample and finally some other jets not used in the comparison. Each category of jet sub-sample is summarised below.

5.2.1 Highest-energy quark jets.

The highest-energy jets in the events can be categorised into three sub-samples of quark jets with very high purity and energies in the range 30-45 GeV. These

were as follows:

- $JET^{(1)}_{q\bar{q}g}$ **from the energy-ordered three-jet sample (Sample A)**
  The quark purity in this sub-sample was estimated to be ~97% in the 40-45 GeV energy range and ~78% in the 30-35 GeV energy range. Its quark flavour composition was the "normal mixture" of quark flavours.

- $JET^{(1)}_{b\bar{b}g}$ **from the energy-ordered sample with lepton-tagging of one of the two lower energy jets (Sample B)**
  This sub-sample was estimated ~97% quark purity in the 40-45 GeV energy range, but only ~68% in the 30-35 GeV energy range. Monte Carlo studies showed the flavour composition to be ~80% b-quarks, ~10% c-quarks and ~10% uds-quarks.

- $JET^{(1)}_{q\bar{q}\gamma}$ **from the events with two jets and an isolated photon jet (Sample C)**
  The ~4% π^0 background in the photon jets is unlikely to affect the highest energy jet, so this jet should be virtually free of gluon jet background. The photon coupling to the quarks results in this sub-sample being composed mainly of u and c quarks, with few b-quarks (~11%).

These highest-energy quark jets could not be used in quark and gluon jet comparisons, because their mean energy was higher than the gluon jet sub-samples. However $JET^{(1)}_{q\bar{q}g}$, $JET^{(1)}_{b\bar{b}g}$ and $JET^{(1)}_{q\bar{q}\gamma}$ were compared to see differences arising from the flavour composition of each three-jet sample.

5.2.2 Lower-energy quark jets.

Quark jet sub-samples were obtained from one of the two lower-energy jets in Sample A, and from the lower-energy hadronic jet in Sample C, as follows:

- $JET^{(2)}_{q\bar{q}g}$ **from the energy-ordered three-jet sample (Sample A)**
  The second-highest energy jet in each three-jet event contributed to quark jet sub-samples with energy between 25 and 45 GeV. The estimated purity varied between ~61% and 95% in this energy range. In a study of Monte Carlo events the flavour composition was seen to remain close to the "normal mixture" over the whole energy range.

- $JET^{(quark)}_{q\bar{q}\gamma}$ **from the events with two jets and an isolated photon jet**
  (Sample C)
  The lower-energy hadronic jet contributed to quark jet sub-samples with

energy in the range 10-45 GeV. Above 20 GeV quark jet energy, the π^0 background in the photon jet was estimated to be less than 2% (Section 4.3.3). The quark jet sub-samples can be assumed to be highly pure above this energy. However, where the quark jets have energy below 20 GeV, the background in the photon jet rises to ~15%. This suggests that there may be up to 15% gluon jet background in the quark jet sample below 20 GeV. Even at these lower energies this quark jet sub-sample was assumed to have high purity. The effect of a possible 15% gluon jet background on the corrected quark and gluon jet distributions is discussed in Section 5.6. The flavour composition of these quark jet sub-samples can be assumed to be dominated by u and c quarks, with a small proportion of b-quarks (11%).

5.2.3 Gluon jets.

The lowest-energy jet in Sample A, and one of the two lower-energy jets in Sample B, were used to form gluon jet sub-samples as follows:

- $JET^{(3)}_{q\bar{q}g}$ **from the energy-ordered three-jet sample (Sample A)**
  The lowest-energy jets formed gluon jet sub-samples with energy between 5 and 25 GeV. The estimated gluon jet purity varied between ~91% and 57% over this energy range. The flavour composition of the quark jet background in Monte Carlo events is approximately the same "normal mixture" in each sub-sample.

- $JET^{(gluon)}_{b\bar{b}g}$ **from the energy-ordered sample with lepton-tagging of one of the two lower-energy jets (Sample B)**
  The jets remaining untagged in Sample B formed gluon jet sub-samples with 5-40 GeV energy. Over this range the gluon purity varied between ~97% and ~54%. The flavour composition of the quark jet background in Monte Carlo events appears to be very different to that in the previous gluon jet sub-samples, with ~50% b-quark jets. The effects of b-quark jets on the jet properties were ignored in the quark and gluon jet comparison. This bias, which is present in all the jet sub-samples, is discussed in Section 5.6.

5.2.4 Other jets.

The lepton-tagged jet in Sample B, and the photon jet in Sample C were not analysed in great detail. For completeness these jets are described below:

- $JET^{(lepton)}_{b\bar{b}g}$ from the energy-ordered sample with lepton-tagging of one of the two lower energy jets (Sample B). The lepton-tagged jets formed sub-samples of b-jets with a semi-leptonic decays, with energies between 10 and

45 GeV. The quark purity of these jets is between ~68% and 99%. The flavour composition was estimated to be ~84% b-quarks, ~10% c-quarks and ~16% u-, d- and s-quarks. The properties of the lepton-tagged jets were seen to be significantly altered by the presence of a high p, high p_t lepton (see Section 5.3).

- $JET^{(\gamma)}_{q\bar{q}\gamma}$ from the events with two jets and an isolated photon jet (Sample C). Since the photon was required to carry at least 90% of the jet energy, there was little else associated with the photon jets, apart from a few soft particles in some events.

The jet properties of the sub-samples are compared in the next section.

5.3 Particle and energy flow in the jet samples.

The particle and energy flow properties of each quark and gluon jet sub-sample were analysed. A description of each distribution is outlined below. The mean value of the distributions is plotted against the weighted mean energy of each sub-sample (Section 4.6). Examples of each distribution are given in Appendix A for some of the jet sub-samples.

5.3.1 Overall mean jet multiplicity.

The particles in each event were associated with the three jets by the DURHAM E_0 clustering algorithm. The multiplicity of charged tracks and neutral energy flow objects was measured in each sub-sample (Figures A.1 - A.3). The mean multiplicities are shown in Figure 5.1. The highest-energy jets ($JET^{(1)}$) in each event sample are compared in Figure 5.1a. $JET^{(1)}_{q\bar{q}g}$ and $JET^{(1)}_{q\bar{q}\gamma}$ have similar multiplicity in the 40-45 GeV energy range, where both have high quark jet purity. At lower energy $JET^{(1)}_{q\bar{q}g}$ has higher multiplicity than $JET^{(1)}_{q\bar{q}\gamma}$. Here $JET^{(1)}_{q\bar{q}g}$ has a significant gluon contamination, whilst $JET^{(1)}_{q\bar{q}\gamma}$ remains highly pure, so differences between the samples may be expected. The b-jet sub-sample, $JET^{(1)}_{b\bar{b}g}$, has significantly higher multiplicity than the other two samples of ~1.5 particles. This is no surprise, since similar differences have been seen in the past for b-jets compared to light quark jets [53].

The effect of a semi-leptonic decay on the mean multiplicity of a b-jet is demonstrated in Figure 5.1b, where $JET^{(lepton)}_{b\bar{b}g}$ is compared to $JET^{(2)}_{q\bar{q}g}$. The lepton-tagged jets have a lower multiplicity than the "normal mixture" sample of ~2 particles, even at 40-45 GeV where both sub-samples have high quark jet purity. The high momentum lepton ($p > 3$ GeV/c) appears to be carrying a

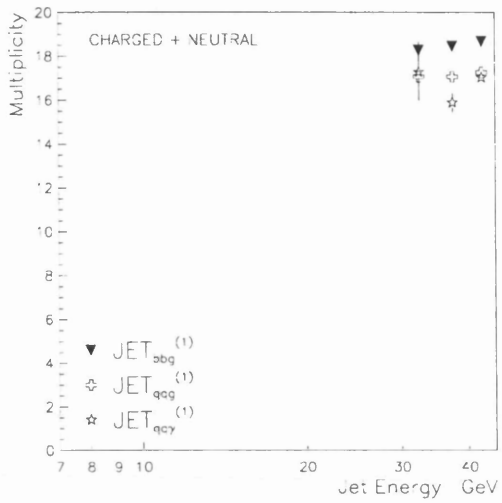

(a) Highest-energy quark jet sub-samples

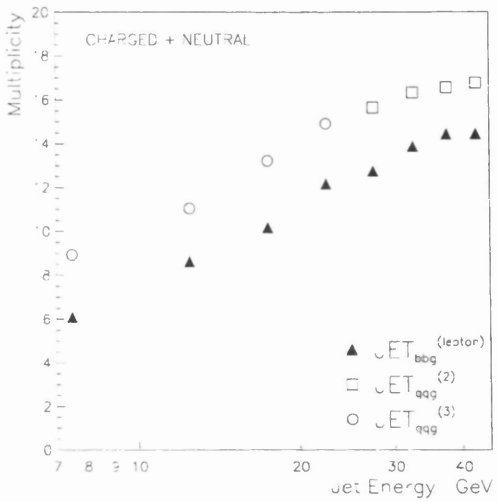

(b) Lepton-tagged quark jet sub-samples compared with energy-ordered jet sub-samples

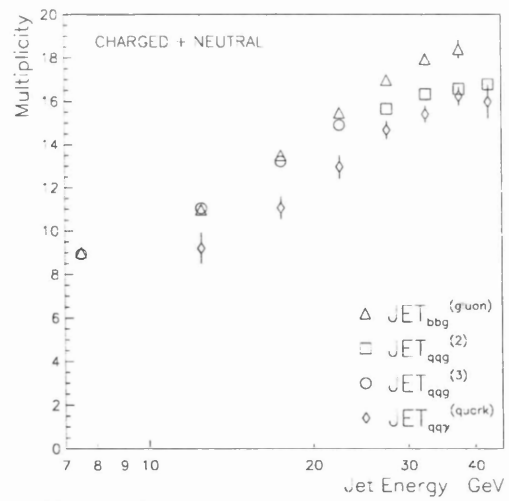

(c) Quark and gluon jet sub-samples

Figure 5.1: *Mean multiplicity of all charged and neutral particles in the quark and gluon jet sub-samples.*

significant fraction of the energy of the jet that would otherwise be available for particle production.

A comparison of the quark and gluon jet sub-samples is shown in Figure 5.1c. The mean multiplicity of the jets rises with energy, but the gluon jet sub-sample $JET^{(gluon)}_{b\bar{b}g}$ has ~2 particles higher multiplicity than the quark jet sub-sample $JET^{(quark)}_{q\bar{q}\gamma}$ over the whole energy range. The gluon jet sub-sample, $JET^{(3)}_{q\bar{q}g}$, has similar multiplicity to the other gluon jet sub-sample ($JET^{(gluon)}_{b\bar{b}g}$) between 5-15 GeV, but at higher energies the multiplicity drops towards the quark jet multiplicity ($JET^{(quark)}_{q\bar{q}\gamma}$) as the level of quark contamination in the $JET^{(3)}_{q\bar{q}g}$ sub-sample increases. Likewise, the two quark jet sub-samples ($JET^{(quark)}_{q\bar{q}\gamma}$ and $JET^{(2)}_{q\bar{q}g}$) have a reasonable match at 35-45 GeV, but the energy-ordered sample ($JET^{(2)}_{q\bar{q}g}$) has higher mean multiplicity at lower energy, where it contains a high gluon jet contamination.

Similar trends in the jet multiplicities are seen for the separated charged and neutral multiplicities of the jet sub-samples (Figures 5.2 and 5.3). There does seem to be greater differences in the mean charged multiplicities of quark and gluon jets (Figure 5.2c) compared to the mean neutral multiplicities (Figure 5.3c). The ratio of charged multiplicity to neutral multiplicity in each jet sub-sample is plotted in Figure 5.4. The highest-energy jet sub-samples ($JET^{(1)}$ in Figure 5.4a) all have similar ratios close to 1. The effect of the lepton on the multiplicity of the $JET^{(lepton)}_{b\bar{b}g}$ jets can clearly be seen in Figure 5.4b, where the charged to neutral ratio is high, particularly at low energies. For jet energies greater than 25 GeV/c, the quark and gluon jet sub-samples (Figure 5.4c) also have similar ratios close to 1. At lower energies the charged to neutral ratio in the gluon sub-samples increases to ~1.2, whilst the ratio drops to ~0.85 in the quark sub-sample ($JET^{(\gamma)}_{q\bar{q}\gamma}$) at low energy.

The ratio of the multiplicity in the gluon jet sub-samples ($JET^{(gluon)}_{b\bar{b}g}$ and $JET^{(3)}_{q\bar{q}g}$) to the multiplicity in the quark jet sub-samples ($JET^{(quark)}_{q\bar{q}\gamma}$ and $JET^{(2)}_{q\bar{q}g}$) is shown in Figure 5.5 for various combinations of gluon and quark jet sub-sample. The overall gluon/quark multiplicity ratio (Figure 5.5a) remains approximately constant with jet energy with a value around 1.2. At low jet energies the variation in the ratio is significantly different for charged particles only (Figure 5.5b) from that for neutral particles only (Figure 5.5c). The gluon/quark charged multiplicity ratio rises from 1.2 with decreasing jet energy. The ratio for neutral particles decreases as the energy of the jets decreases.

5.3.2 Mean transverse momentum of particles in jets.

The transverse momentum of each particle with respect to its jet axis was

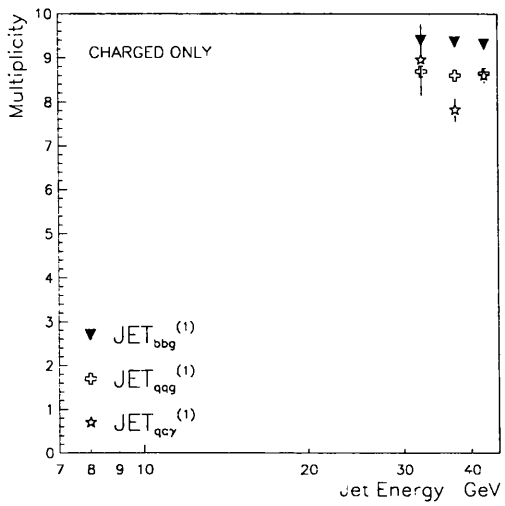

(a) Highest-energy quark jet sub-samples

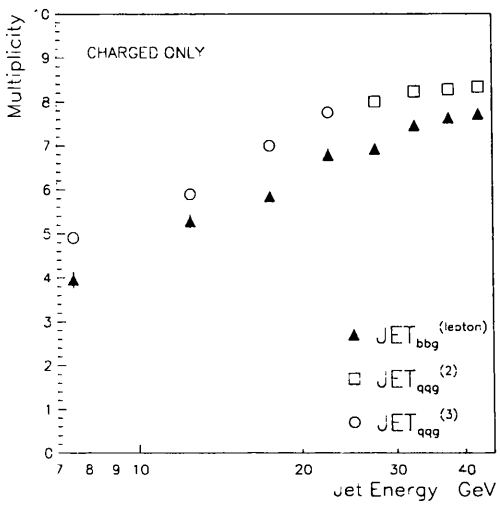

(b) Lepton-tagged quark jet sub-samples compared with energy-ordered jet sub-samples

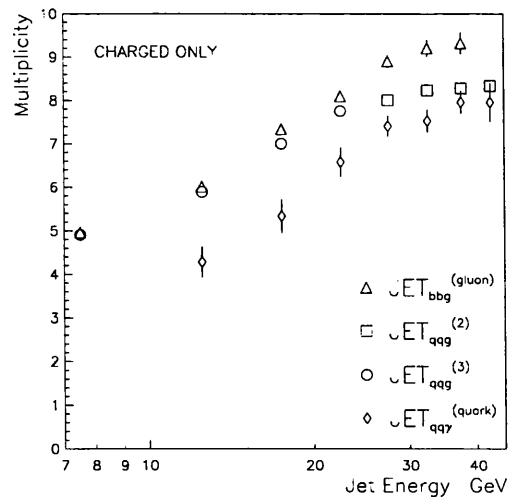

(c) Quark and gluon jet sub-samples

Figure 5.2: *Mean charged multiplicity of the quark and gluon jet sub-samples.*

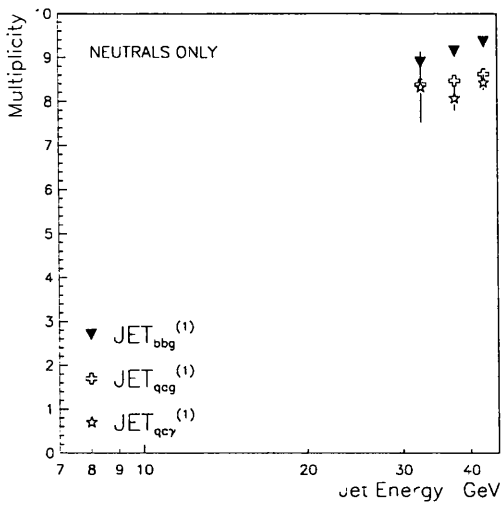

(a) Highest-energy quark jet sub-samples

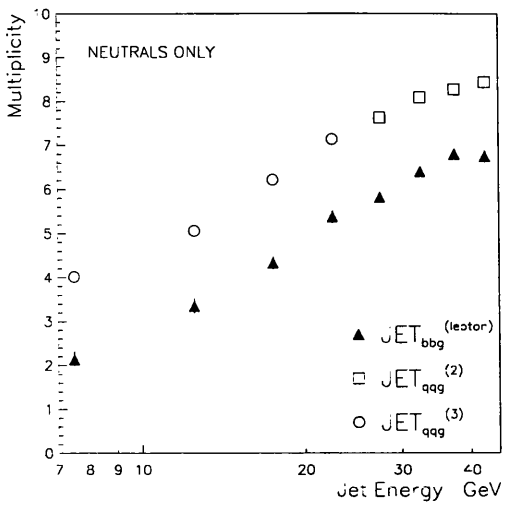

(b) Lepton-tagged quark jet sub-samples compared with energy-ordered jet sub-samples

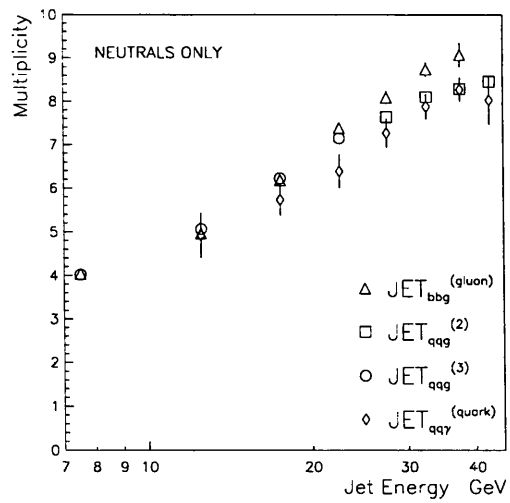

(c) Quark and gluon jet sub-samples

Figure 5.3: *Mean neutral multiplicity of the quark and gluon jet sub-samples.*

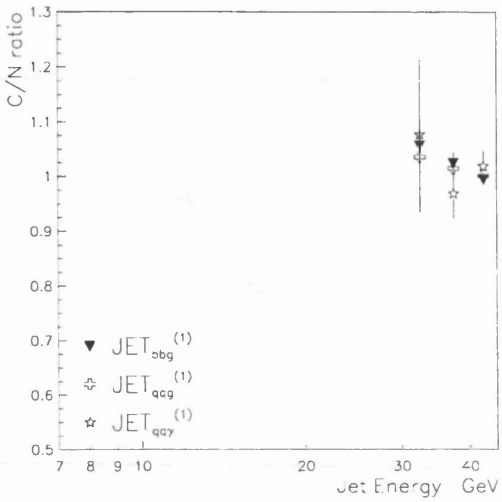

(a) Highest-energy quark jet sub-samples

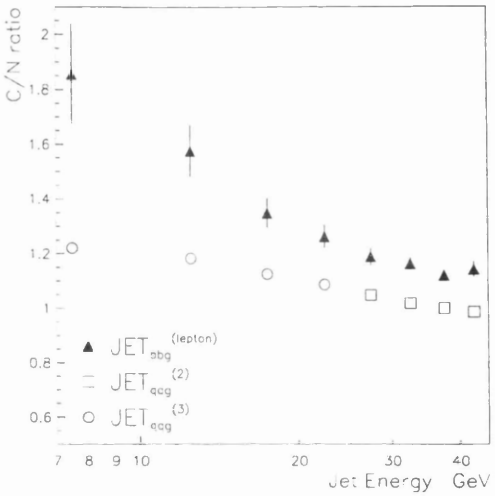

(b) Lepton-tagged quark jet sub-samples compared with energy-ordered jet sub-samples

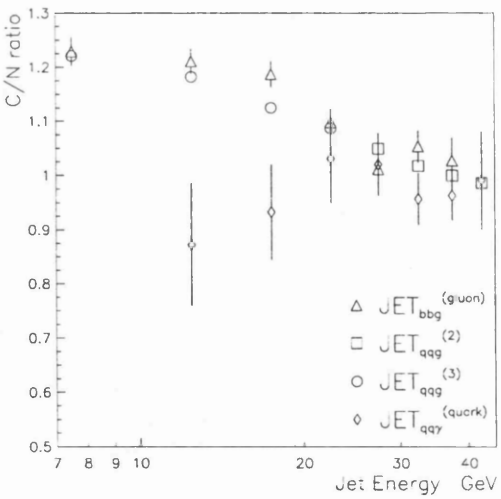

(c) Quark and gluon jet sub-samples

Figure 5.4: *Mean charged/neutral multiplicity ratio of the quark and gluon jet sub-samples.*

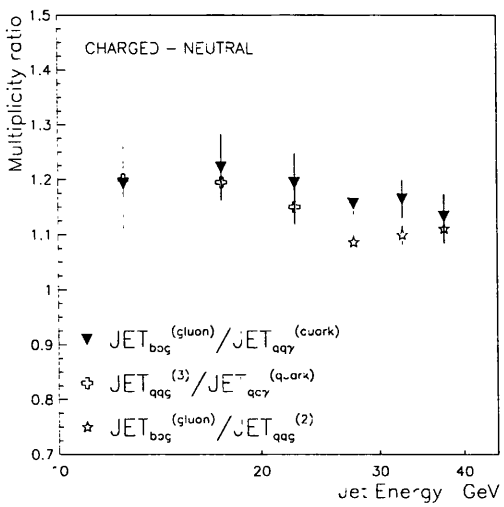

(a) Ratio of charged and neutral particles

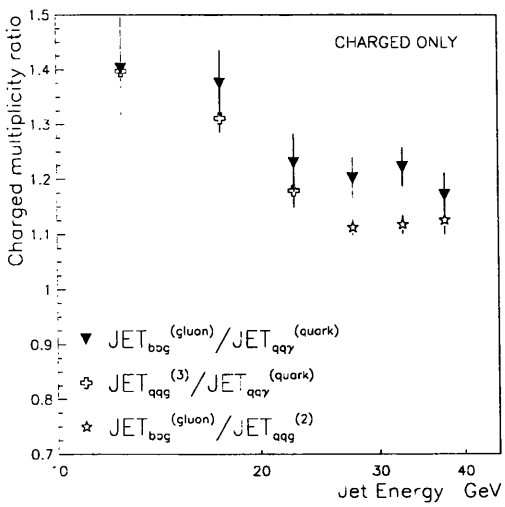

(b) Ratio of charged particles only

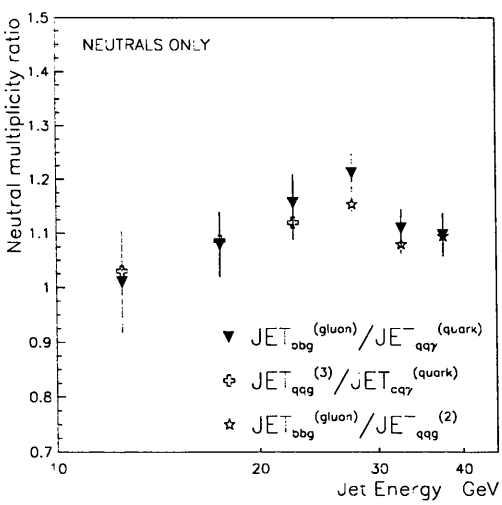

(c) Ratio of neutral particles only

Figure 5.5: *Gluon/quark jet mean multiplicity ratios of the jet sub-samples.*

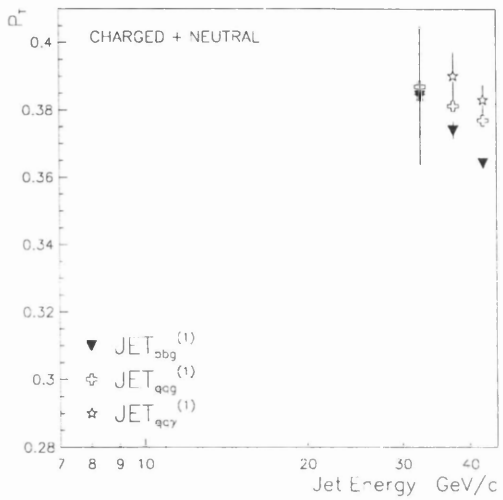

(a) p_t in highest-energy quark jet sub-samples

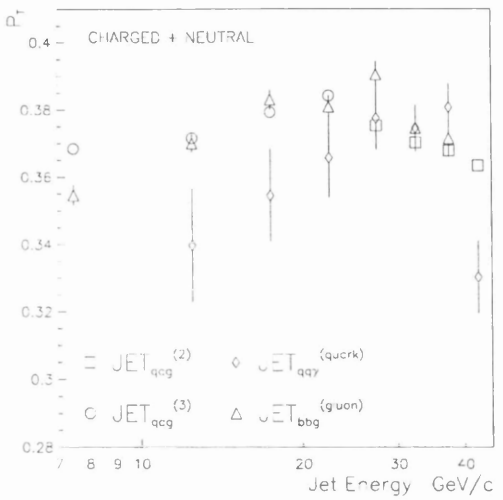

(b) p_t in quark and gluon jet sub-samples

Figure 5.6: *Mean p_t of all charged and neutral particles in the jet sub-samples.*

determined in each jet sub-sample (Figures A.4 and A.5). The mean p_t of the highest-energy quark jet sub-samples ($JET^{(1)}$) is shown in Figure 5.6a. There seems to be a difference between the sub-samples, particularly at 40-45 GeV jet energy, where the $JET^{(1)}_{q\bar{q}\gamma}$ sub-sample has the highest mean p_t, the $JET^{(1)}_{q\bar{q}g}$ has a slightly lower mean p_t and the $JET^{(1)}_{b\bar{b}g}$ p_t is significantly lower. This appears to correspond to the fraction of b-jets in the sample. In Section 5.3.1, the b-jets were shown to have higher multiplicity. This would result in a softer energy spectrum in b-jets, leading to a lower mean p_t.

The mean transverse momentum in the quark and gluon sub-samples is compared in Figure 5.6b. At low jet energy, the gluon sub-samples ($JET^{(gluon)}_{b\bar{b}g}$ and $JET^{(3)}_{q\bar{q}g}$) have higher mean p_t, but the p_t increases faster in the quark sub-samples ($JET^{(quark)}_{q\bar{q}\gamma}$ and $JET^{(2)}_{q\bar{q}g}$) as the energy of the jets rises. In jets with at least 25 GeV energy, the quark and gluon jets have similar mean p_t. Similar trends are seen for the mean charged p_t in the jet sub-samples (Figure 5.7), but the differences between the quark and gluon sub-samples are less pronounced.

5.3.3 Mean rapidity of particles and energy flow in jets.

The rapidity of tracks in a jet was determined with respect to the axis of

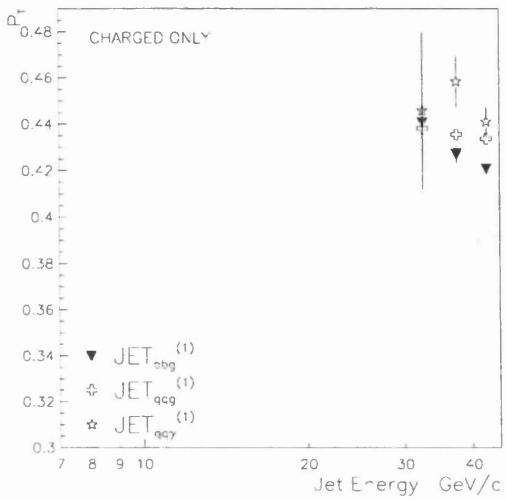

(a) p_t in highest-energy quark jet sub-samples

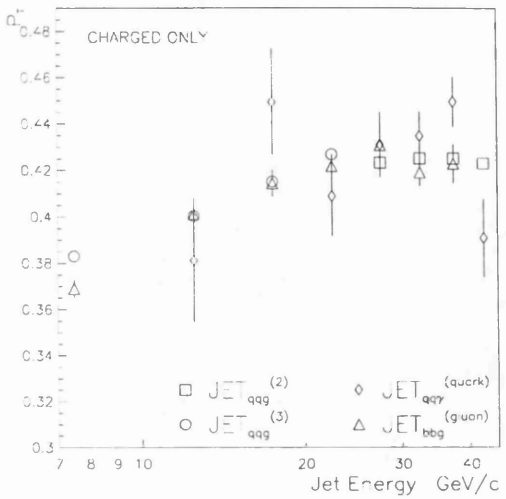

(b) p_t in quark and gluon jet sub-samples

Figure 5.7: *Mean p_t of charged particles in the jet sub-samples.*

the jet (Figures A.6 and A.7). The mean rapidity of tracks in the highest-energy quark jet sub-samples ($JET^{(1)}$ in Figure 5.8a) appears to be similar at 40-45 GeV energy. The differences in mean rapidity at 30-40 GeV could be explained by the different gluon impurity in these sub-samples. The quark jet sub-samples ($JET^{(quark)}_{q\bar{q}\gamma}$ and $JET^{(2)}_{q\bar{q}g}$ in Figure 5.8b) have tracks with higher mean rapidity than the gluon jet sub-samples ($JET^{(gluon)}_{b\bar{b}g}$ and $JET^{(3)}_{q\bar{q}g}$), this difference being more apparent at lower jet energy. This suggests that the tracks in quark jets lie closer on average to the jet axis. The mean rapidity of tracks in all the sub-samples increases with jet energy, showing that the jets become more collimated at higher energy. A similar variation in mean rapidity is seen in Figure 5.9 for the charged tracks. However the mean rapidity of charged tracks appears shifted to lower values compared to the results for all tracks. This would indicate that neutral particles lie closer on average to the jet axis than charged particles in a jet.

The rapidity of the energy flow was determined for each jet sub-sample (Figures A.8 and A.9). In Figure 5.10a the mean rapidity of the energy flow seems to be lower for the b-jet sub-sample ($JET^{(1)}_{b\bar{b}g}$) than the sub-samples containing more lighter quarks ($JET^{(1)}_{q\bar{q}\gamma}$ and $JET^{(1)}_{q\bar{q}g}$). This would indicate that for lighter

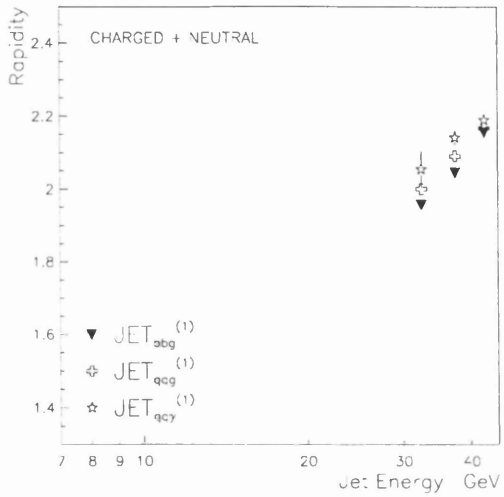

(a) Rapidity of particles in highest-energy quark jet sub-samples

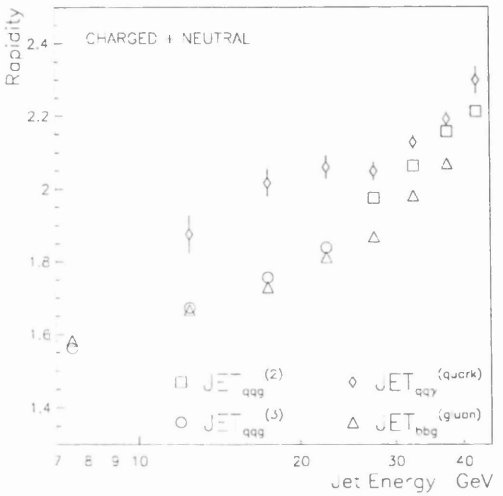

(b) Rapidity of particles in quark and gluon jet sub-samples

Figure 5.8: *Mean rapidity of all charged and neutral particles in the jet sub-samples.*

quark jets, a larger fraction of the jet energy is carried by those particles closer to the jet axis. The mean rapidity of energy flow in the gluon jet sub-samples ($JET_{b\bar{b}g}^{(gluon)}$ and $JET_{q\bar{q}g}^{(3)}$ in Figure 5.10b) also appears to be lower than that in the quark jet sub-samples ($JET_{q\bar{q}\gamma}^{(quark)}$ and $JET_{q\bar{q}g}^{(2)}$), indicating that the particles close to the axis in a light quark jet also carry a greater fraction of the jet energy than those particles in a gluon jet. Using the charged energy flow alone (Figure 5.11) gives similar values to the charged and neutral energy flow combined.

5.3.4 Mean fragmentation function of tracks.

The energy of each track was divided by the calculated energy of the jet, to give a measure of the fraction of the jet energy carried by the particles (Figures A.10 and A.11. The mean values of this "fragmentation function" are shown in Figure 5.12 for each jet sub-sample. The highest-energy b-jet sub-sample ($JET_{b\bar{b}g}^{(1)}$ in Figure 5.12a) has more soft particles than the two sub-samples containing lighter quarks ($JET_{q\bar{q}\gamma}^{(1)}$ and $JET_{q\bar{q}g}^{(1)}$). This is to be expected since this b-jet sub-sample was shown to have higher multiplicity than the other sub-samples, so the b-jet energy is shared over more particles.

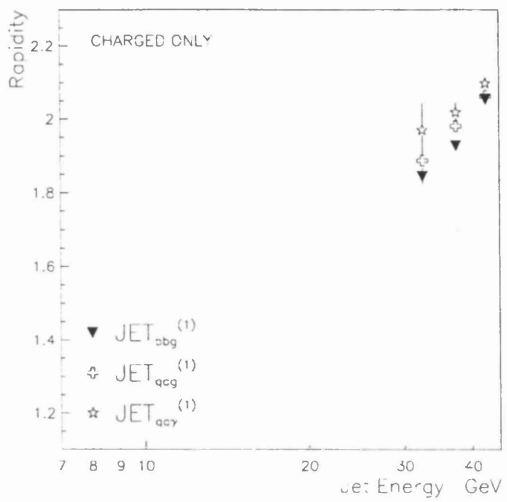

(a) Rapidity of charged particles in highest-energy quark jet sub-samples

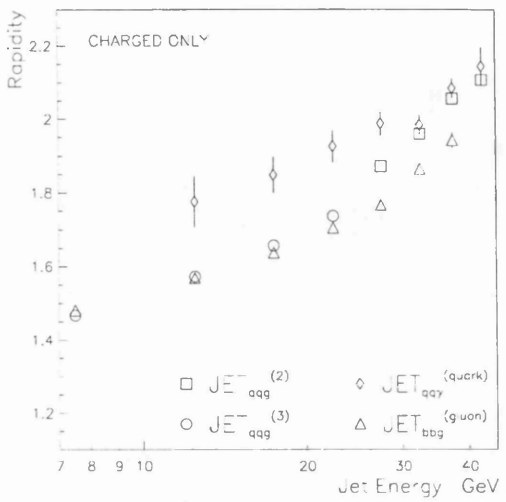

(b) Rapidity of charged particles in quark and gluon jet sub-samples

Figure 5.9: *Mean rapidity of charged particles in the jet sub-samples.*

The gluon jet sub-samples ($JET_{b\bar{b}g}^{(gluon)}$ and $JET_{q\bar{q}g}^{(3)}$ in Figure 5.12b) also appear to have a greater proportion of soft particles than the quark jet sub-samples ($JET_{q\bar{q}\gamma}^{(quark)}$ and $JET_{q\bar{q}g}^{(2)}$). A higher multiplicity was seen in the gluon jets compared to the quark jet sub-samples, so this result also is not unexpected. There seem to be larger differences in the fragmentation function between the jet sub-samples if charged particles are considered separately (Figure 5.13).

5.3.5 Jet core widths.

Using the calculated energies of the jets, the jet cores were defined by a cone containing 90%, 75%, 50% and 25% of the jet energy. The width of these cores was defined by the half angle of the cones. The energy flow normalised by the calculated energy was plotted against the angle to the jet axis in each sub-sample (Figure A.12). A fit was made to these distributions to obtain the half-angles of the jet cores defined above. These angles are shown in Figure 5.14, for the four different core definitions. The cores are seen to narrow with increasing jet energy. The gluon jet sub-samples have wider cores than the quark jet sub-samples.

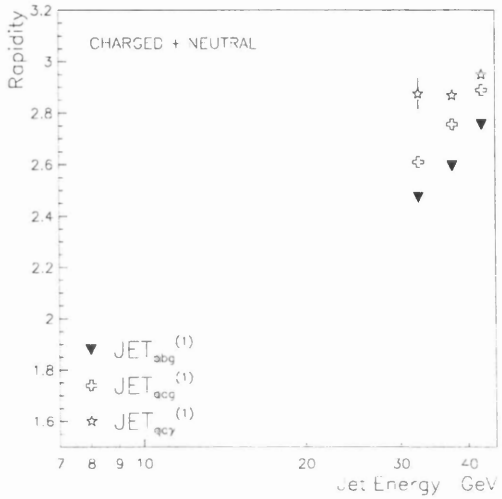

(a) Rapidity of energy flow in highest-energy quark jet sub-samples

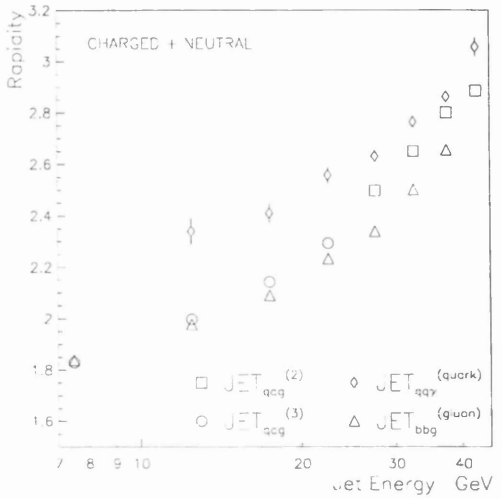

(b) Rapidity of energy flow in quark and gluon jet sub-samples

Figure 5.10: *Mean rapidity of charged and neutral energy flow in the jet sub-samples.*

5.3.6 Multiplicity ratio in jet cores.

The multiplicity in each jet sub-sample was plotted against the angle to the jet axis (Figures A.13 and A.14). A fit was made to this distribution to obtain the mean multiplicity in the jet cores defined above. The core multiplicity ratio for the gluon jet sub-samples ($JET_{b\bar{b}g}^{(gluon)}$ and $JET_{q\bar{q}g}^{(3)}$) compared to the quark jet sub-samples ($JET_{q\bar{q}\gamma}^{(quark)}$ and $JET_{q\bar{q}g}^{(2)}$) is shown in Figure 5.15, for the four different core sizes. The ratio appears to be approximately constant with the energy of the jets, and marginally higher than the overall gluon sub-sample/quark sub-sample multiplicity ratios (Figure 5.15a). The core charged multiplicity ratios (Figure 5.16) are significantly higher than the overall charged multiplicity ratios (Figure 5.16b), particularly at low jet energy. The core charged multiplicity ratios fall with jet energy in a similar manner to the overall charged multiplicity ratios.

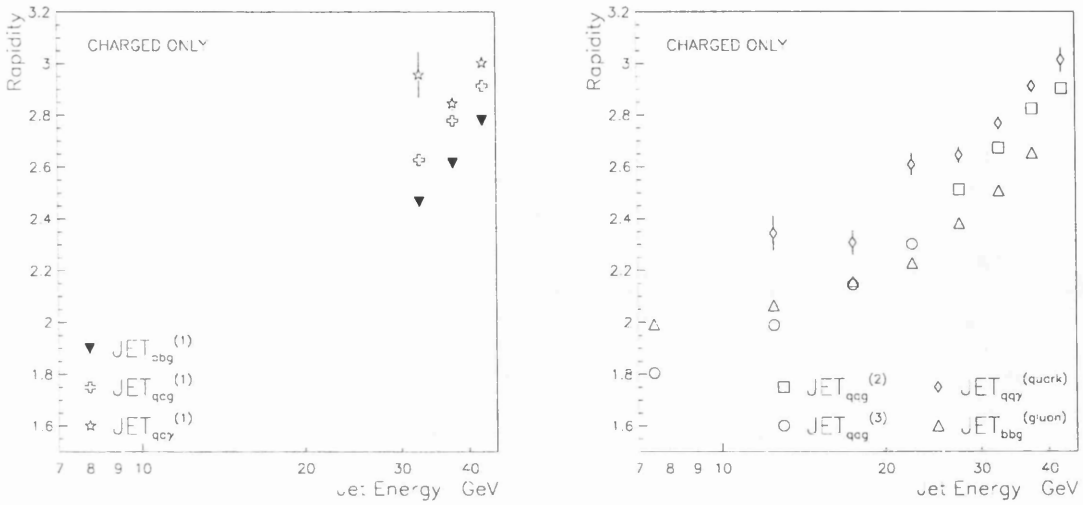

(a) Rapidity of charged energy flow in highest-energy quark jet sub-samples

(b) Rapidity of charged energy flow in quark and gluon jet sub-samples

Figure 5.11: *Mean rapidity of charged energy flow in the jet sub-samples.*

5.4 Unfolding the jet distributions.

Each jet sub-sample contains a certain fraction of gluon jets (P^{gluon}_{sample}), *udsc*-quark jets (P^{udsc}_{sample}), *b*-jets (P^{b}_{sample}) and "ambiguous" jets ($P^{ambiguous}_{sample}$). These fractions have been estimated from JETSET Monte Carlo events. Each fraction of jets contributes to measured quantity such as multiplicity (n) in the following way:

$$n_{sample} = P^{gluon}_{sample}.n^{gluon}_{true} + P^{udsc}_{sample}.n^{udsc}_{true} + P^{b}_{sample}.n^{b}_{true} + P^{ambiguous}_{sample}.n^{ambiguous} \quad (5.1)$$

The "ambiguous" jets cannot be measured in the data, but a large proportion of the events containing these jets have been removed from the data samples using some of the event cuts described in Section 4.6. It has been estimated that there are less than ~4% of these jets remaining in the jet sub-samples over the whole energy range, except at 40-45 GeV where the fraction rises to ~6-8%. The "ambiguous" jets were therefore ignored in the jet correction process. The *b*-jet fraction is estimated to be ~4-10% of the $JET^{(3)}_{q\bar{q}g}$ sub-sample, ~13-19% of the $JET^{(2)}_{q\bar{q}g}$ sub-sample, ~2-18% of the $JET^{(gluon)}_{b\bar{b}g}$ sub-sample and ~11% of the $JET^{(quark)}_{q\bar{q}\gamma}$ sub-sample. Particularly at high jet energy, the *b*-jet fraction appears

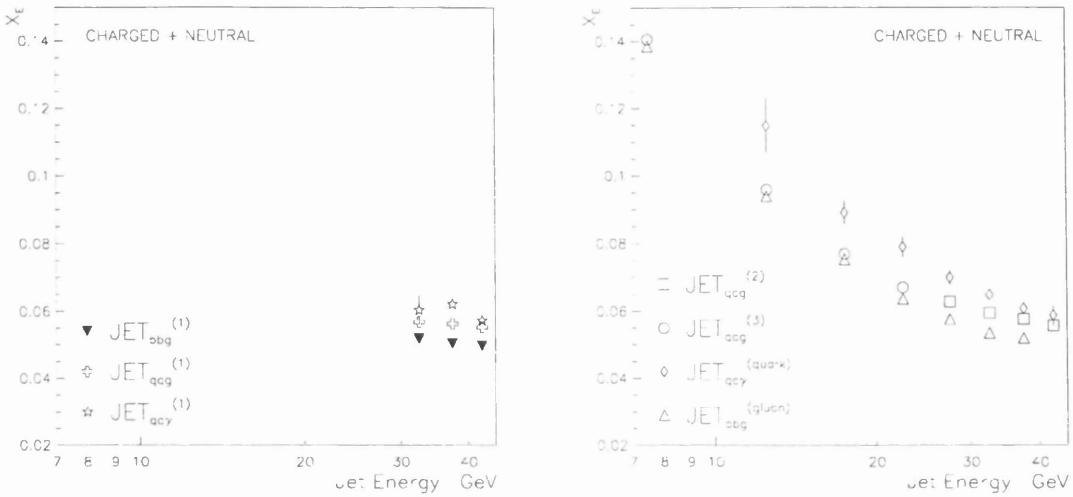

(a) Fragmentation function in highest-energy quark jet sub-samples

(b) Fragmentation function in quark and gluon jet sub-samples

Figure 5.12: *Mean fragmentation function of all charged and neutral particles in jet sub-samples* ($X_e = E_{particle}/E_{jet}$).

to be significant. However to simplify the unfolding process and reduce reliance on Monte Carlo measurements, the b-jet fraction in the quark and gluon jet samples was incorporated into the fraction of $udsc$-jets, such that Equation 5.1 reduced to:

$$n_{sample} = P^{gluon}_{sample}.n^{gluon}_{true} + P^{udscb}_{sample}.n^{udscb}_{true} \tag{5.2}$$

A very low level of background was measured in Monte Carlo $q\bar{q}\gamma$ events, except in events where $JET^{(quark)}_{q\bar{q}\gamma}$ has less than 20 GeV energy. Here there is $\sim$15% π^0 background in the photon jet. However all forms of background were ignored in the $JET^{(quark)}_{q\bar{q}\gamma}$ sub-sample, such that:

$$n_{q\bar{q}\gamma} = n^{udscb}_{true} \tag{5.3}$$

The unfolded quark and gluon jet distributions were obtained by solving Equation 5.2 and Equation 5.3 for different combinations of quark and gluon jet sub-samples. The bias from the purity simplifications on the unfolded quark and gluon jet distributions are considered in Section 5.6. Using the four quark and gluon jet sub-samples ($JET^{(quark)}_{q\bar{q}\gamma}$, $JET^{(2)}_{q\bar{q}g}$, $JET^{(gluon)}_{b\bar{b}g}$ and $JET^{(3)}_{q\bar{q}g}$), five unfolded quark and gluon jet measurements could be made as follows:

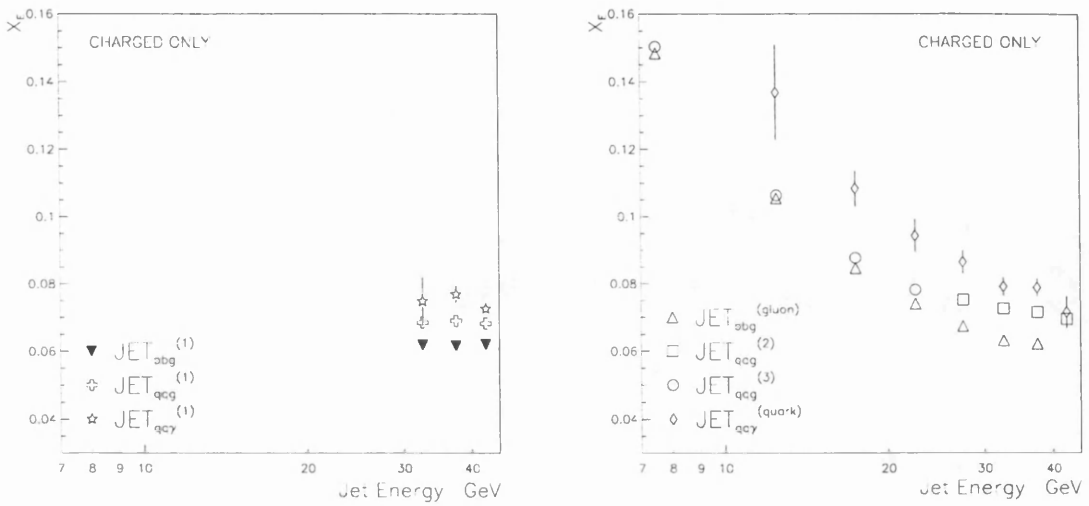

(a) Fragmentation function of charged particles in highest-energy quark jet sub-samples

(b) Fragmentation function of charged particles in quark and gluon jet sub-samples

Figure 5.13: *Mean fragmentation function of charged particles in the jet sub-samples* ($X_e = E_{particle}/E_{jet}$).

- QUARK(C) was the set of jet distributions obtained from the $JET^{(quark)}_{q\bar{q}\gamma}$ sub-sample from event Sample C. Six distributions for each variable were obtained for jets in the range 10-40 GeV.

- QUARK(A-B) was obtained using $JET^{(2)}_{q\bar{q}g}$ from event Sample A and $JET^{(gluon)}_{b\bar{b}g}$ from event Sample B. Three distributions for each variable were obtained for jets in the range 25-40 GeV.

- GLUON(B-C) was obtained using $JET^{(gluon)}_{b\bar{b}g}$ from event Sample B and $JET^{(quark)}_{q\bar{q}\gamma}$ from event Sample C. Six distributions for each variable were obtained for jets in the range 10-40 GeV.

- GLUON(B-A) was obtained using $JET^{(gluon)}_{b\bar{b}g}$ from event Sample B and $JET^{(2)}_{q\bar{q}g}$ from event Sample A. Three distributions for each variable were obtained for jets in the range 25-40 GeV.

- GLUON(A-C) was obtained using $JET^{(3)}_{q\bar{q}g}$ from event Sample A and $JET^{(quark)}_{q\bar{q}\gamma}$

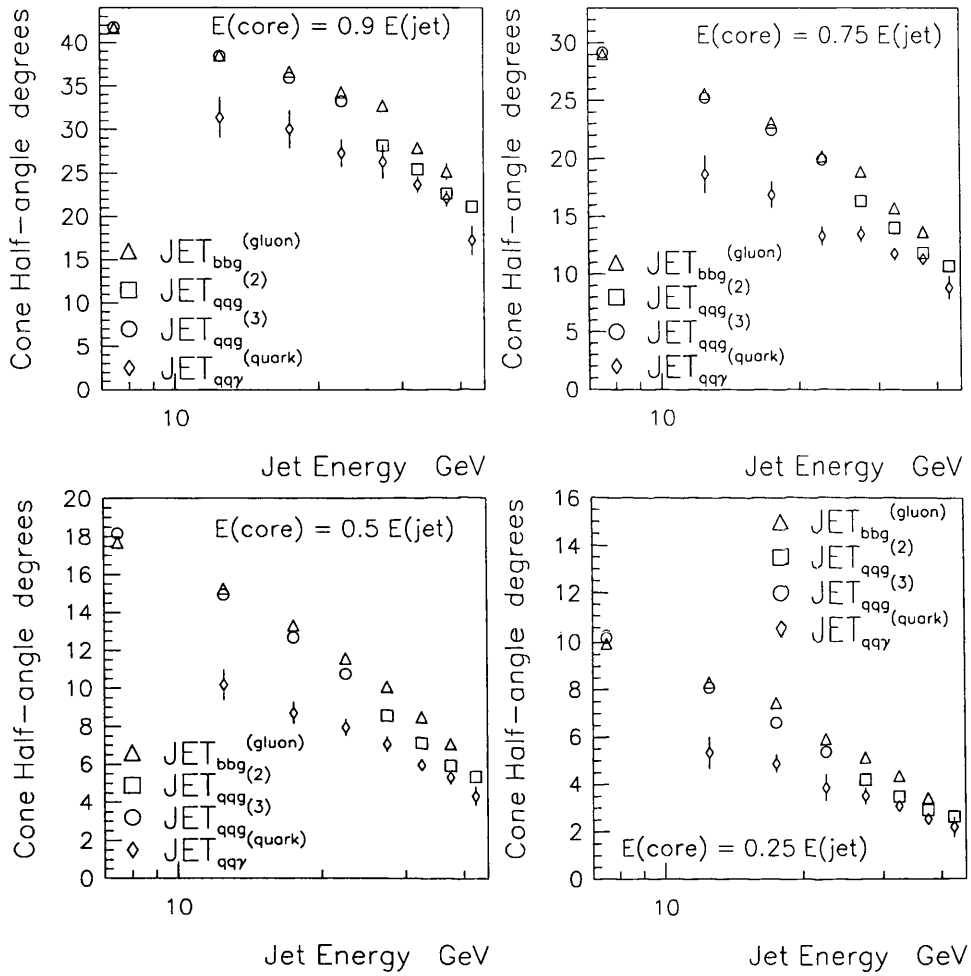

Figure 5.14: *Half-angle of mean cones containing different core energy fractions (90%, 75%, 50% and 25%) in the quark and gluon jet sub-samples.*

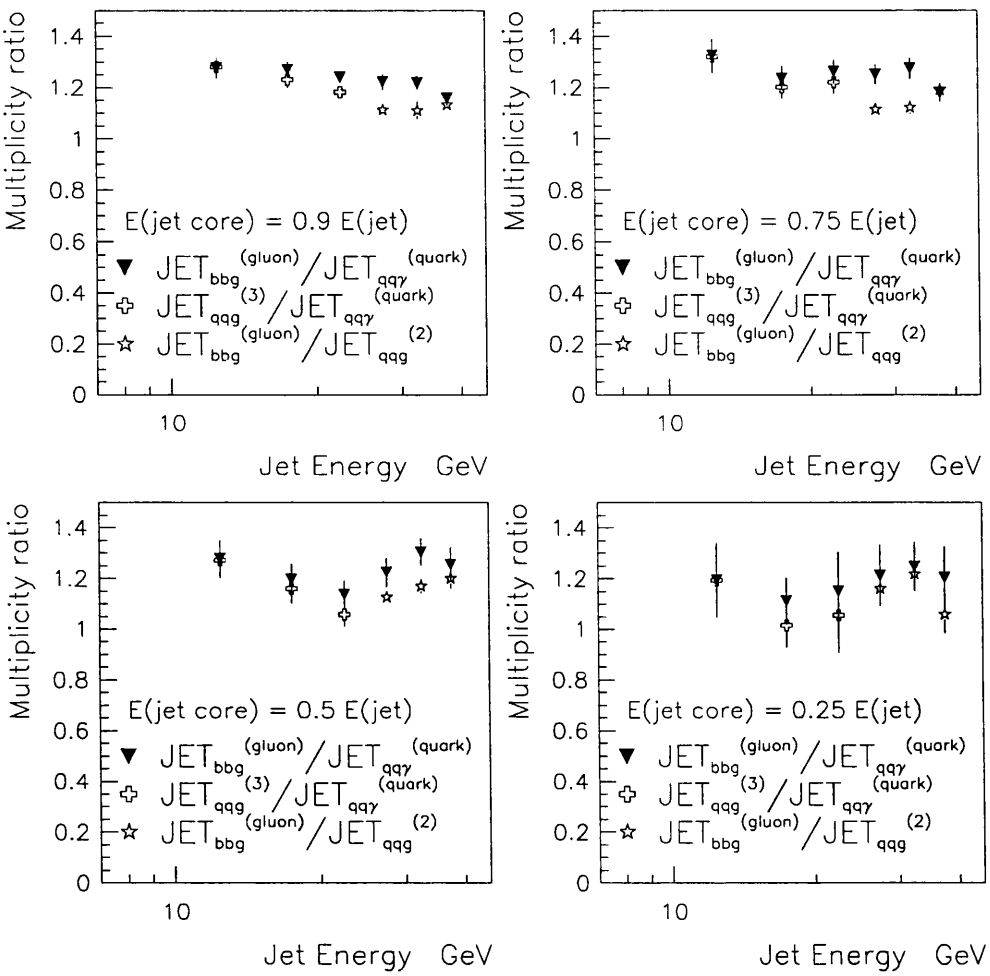

Figure 5.15: *Gluon/quark mean multiplicity ratio for different core energy fractions (90%, 75%, 50% and 25%) in the quark and gluon jet sub-samples.*

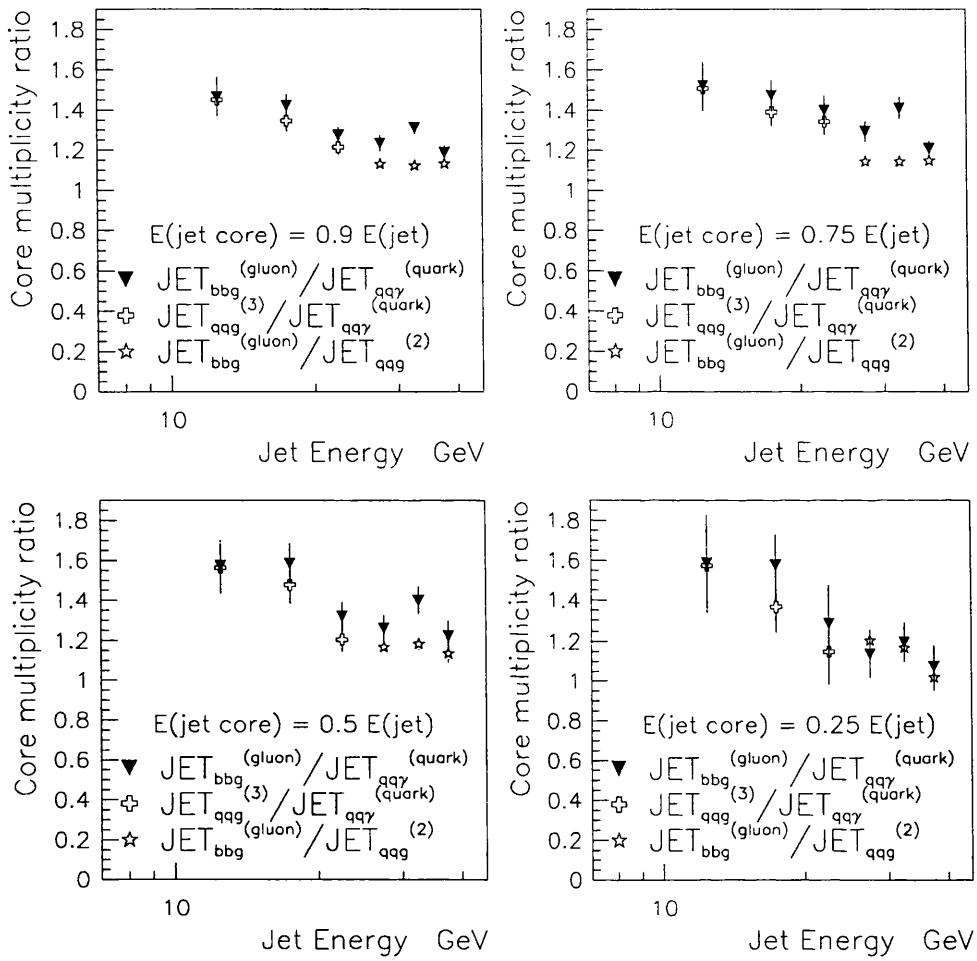

Figure 5.16: *Gluon/quark mean charged multiplicity ratio for different core energy fractions (90%, 75%, 50% and 25%) in the quark and gluon jet sub-samples.*

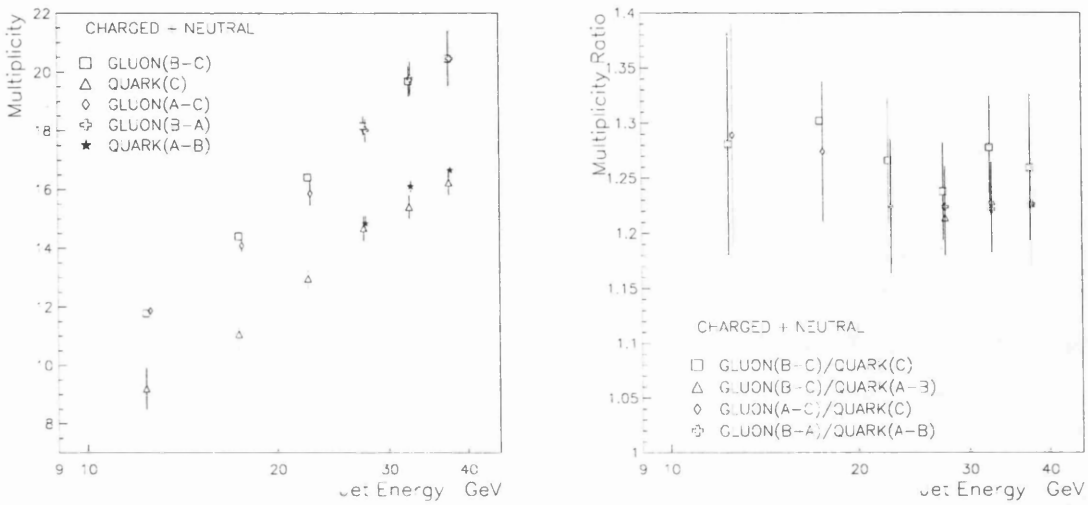

(a) Jet multiplicities

(b) Gluon/quark jet multiplicity ratio

Figure 5.17: *Mean multiplicity of quark and gluon jet samples after purity correction.*

from event Sample C. Three distributions for each variable were obtained for jets in the range 10-25 GeV.

Since there was some overlap of the corrected jet distribution for most quark and gluon jet energies, this allowed a check of the bias in each distribution from the purity correction. This is discussed in Section 5.6.

5.5 Unfolded quark and gluon jet properties.

The raw data distributions were corrected to give the five sets of corrected distributions detailed above. The unfolded distributions are shown in Appendix B. A mean value of each variable was determined for each energy range. The energy dependence of these mean values is described below.

5.5.1 Mean multiplicity of jets.

The unfolded multiplicity distributions are shown in Figures B.1 - B.3. The mean overall multiplicity is shown in Figure 5.17a. The results for the quark measurements match up reasonably well, as do the gluon measurements. The

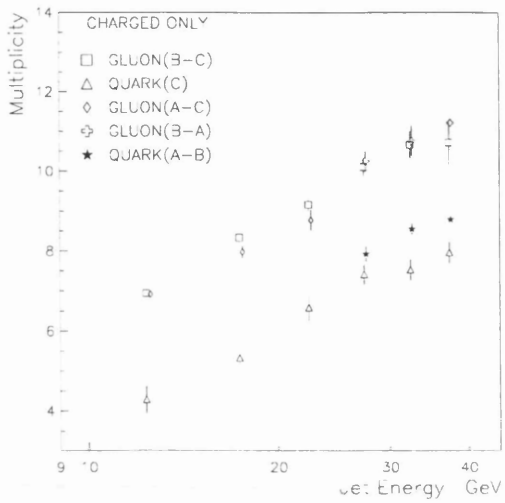

(a) Jet charged multiplicities

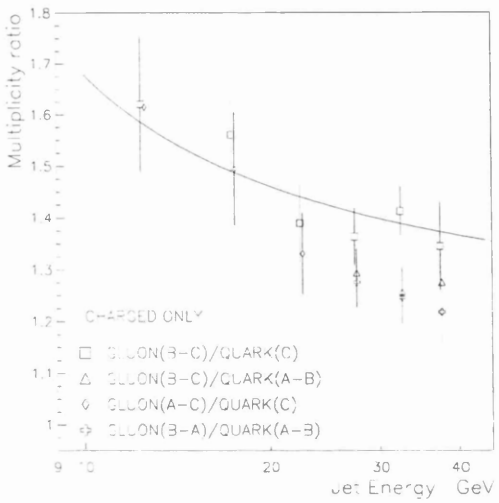

(b) Gluon/quark jet charged multiplicity ratio

Figure 5.18: *Mean charged multiplicity of quark and gluon jet samples after purity correction. The ratio GLUON(B-C)/QUARK(C) of the fits to the charged multiplicity is plotted on (b).*

multiplicity of the jets has an approximately logarithmic variation with jet energy. The gluon jets have a multiplicity ~2-3 particles higher than the quark jets in the same energy range. The ratio of the gluon jet multiplicity to the quark jet multiplicity (Figure 5.17b) is approximately constant at ~1.25 over the whole energy range. There may be a slight reduction in the ratio with energy.

The is again a reasonable match in the mean charged multiplicity measurements for the gluon jets (Figure 5.18)a. The quark jet measurements (QUARK(C) and QUARK(A-B)) are slightly different, possibly due to the different fractions of b-jets in the jet sub-samples. The variation in charged multiplicity with energy is again approximately logarithmic, with the gluon jets containing ~2 more charged particles than the quark jets. The QUARK(C) and unfolded GLUON(B-C) measurements were fitted with functions of the form $n_{ch}(JET) = A.\log(E)+constant$ and $n_{ch}(JET) = A.\log(E) + B.\log^2(E) + constant$. The results of these fits are shown in Table 5.1. The χ^2 values for each fit are not included due to the relatively large systematic errors from the unfolding procedure. The ratio of the charged multiplicities (Figure 5.18b) shows a decrease, from ~ 1.6 at low jet energy down

Jet sample	*Constant term*	*log(E) term*	*log²(E) term*
GLUON(B-C)	-2.75 ± 0.57	8.85 ± 0.47	-
QUARK(C)	-4.21 ± 1.10	7.85 ± 0.78	-
GLUON(B-C)	-6.34 ± 0.54	14.6 ± 0.8	-2.27 ± 0.35
QUARK(C)	-15.8 ± 1.0	25.4 ± 1.2	-6.54 ± 0.54

Table 5.1: *Fits to the charged multiplicity variation with energy for the QUARK(C) and unfolded GLUON(B-C) measurements. The charged multiplicity n(JET) was fitted with a functions of the form* $n(JET) = A.\log(E) + constant$ *and* $n(JET) = A.\log(E) + B.\log^2(E) + constant$.

to ~ 1.3 at higher jet energies. The ratio of the $n_{ch}(JET) = A.\log(E) + constant$ fits to the multiplicity is superimposed on Figure 5.18b. However an $R = constant$ fit was also made to the charged multiplicity ratio GLUON(B-C)/QUARK(C) (100% core fit in Table 5.3. This demonstrates that a constant variation in the charged multiplicity ratio cannot be ruled out statistically.

The mean unfolded neutral multiplicity of the jets is shown in Figure 5.19a. There again appears to be a small mismatch in the quark jet measurements (QUARK(C) and QUARK(A-B)). The neutral multiplicities also show a logarithmic increase with energy, but the differences between the quark and gluon jets are much smaller. The gluon jets have ~ 1 particle more than quark jets at the same energy. The ratio of the neutral multiplicities remains approximately constant at ~ 1.2 over the whole energy range (Figure 5.19b).

The charged to neutral multiplicity ratio is plotted in Figure 5.20 for quark and gluon jets. The ratio for the gluon jets decreases slightly with energy from ~ 1.2 to just below 1.1. The quark jets show an increase in the charged to neutral multiplicity ratio, from below 0.9 at 10-15 GeV to $\sim$1 above 25 GeV.

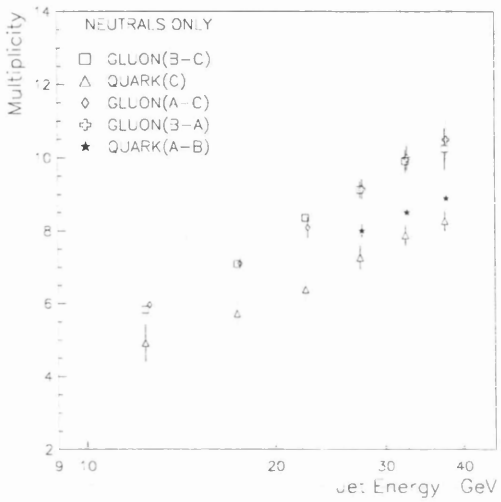

(a) Jet neutral multiplicities

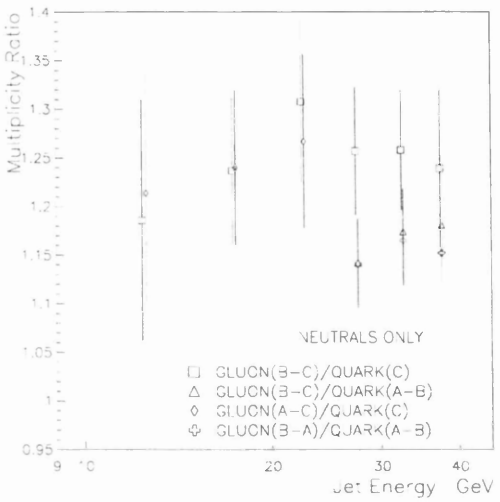

(b) Gluon/quark jet neutral multiplicity ratio

Figure 5.19: *Mean neutral multiplicity of quark and gluon jet samples after purity correction.*

5.5.2 Mean transverse momentum of particles in jet.

The unfolded P_t distributions are shown in Figures B.4 and B.5. The mean P_t of particles in the jets is shown in Figure 5.21a for all particles, and in Figure 5.21b for charged particles only. The quark and gluon jets appear to have similar values, except at low energies, where the mean P_t in quark jets seems to be lower. The ratio of the gluon jet P_t to the quark jet P_t is plotted in Figure 5.22. There is a slight decrease in this ratio with energy, from ~1.1 at low energy, to ~1.0 at high energy. The charged particle mean P_t ratio is closer to 1 than for all the particles.

5.5.3 Mean rapidity of particles in jet.

The unfolded particle rapidity distributions are significantly different for the quark and gluon jets (Figures B.6 and B.7). The mean rapidity of particles in quark and gluon jets is shown in Figure 5.23a for all particles, and in Figure 5.23b for charged particles only. The quark and gluon measurements from different jet sub-samples match up reasonably well. The increase in the mean rapidity

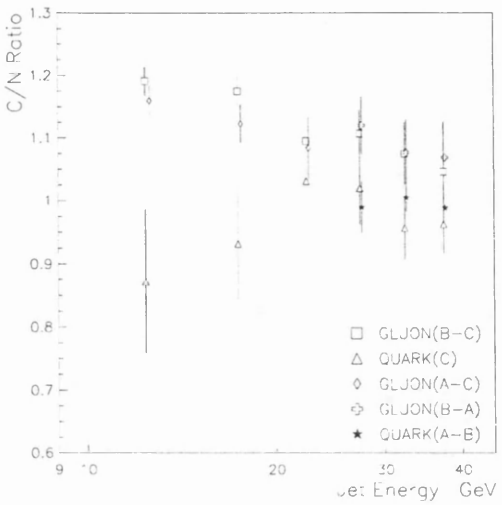

Figure 5.20: *Mean charged/neutral multiplicity ratio of quark and gluon jet samples after purity correction.*

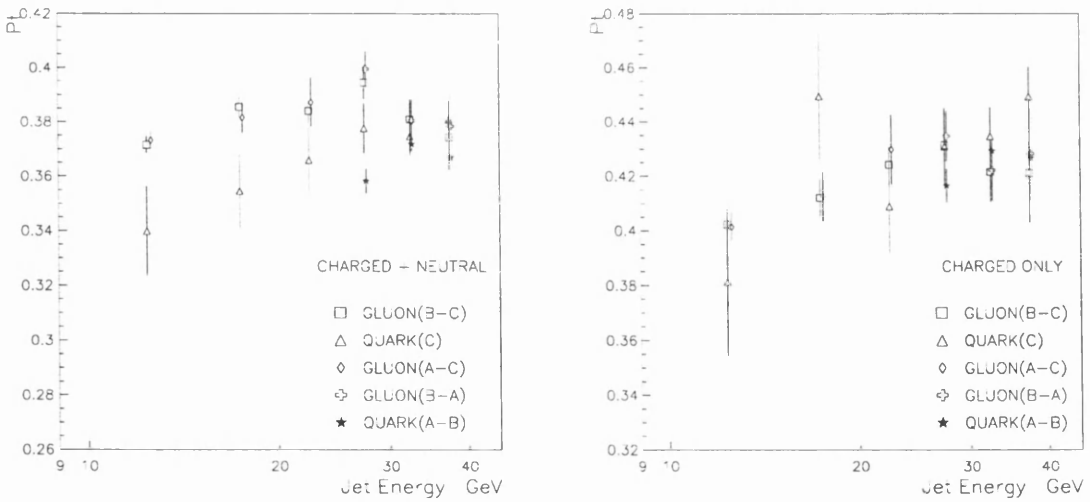

(a) p_t of charged and neutral particles

(b) p_t of charged particles

Figure 5.21: *Mean p_t of particles in quark and gluon jet samples after purity correction.*

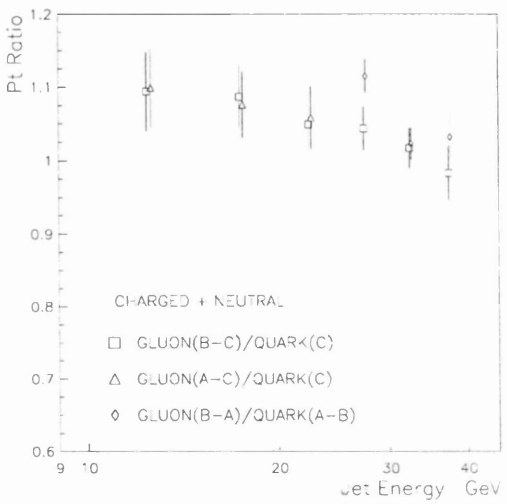

(a) Gluon/quark jet p_t ratio of charged and neutral particles

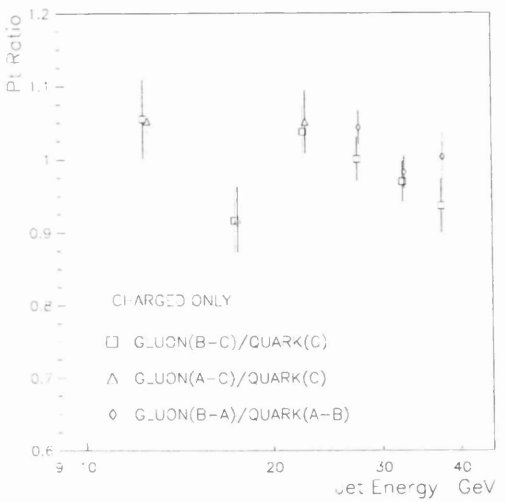

(b) Gluon/quark jet p_t ratio of charged particles

Figure 5.22: *Gluon/quark jet mean p_t ratio of particles in quark and gluon jet samples after purity correction.*

with energy indicates that the particles in the jets are more collimated at higher energies. The particles in the quark jets clearly have higher mean rapidity, showing that quark jets are narrower than the gluon jets. The mean charged rapidity values are lower than for all particles. The ratio of the mean particle rapidities in gluon jets compared to quark jets (Figure 5.24) is approximately constant at about 0.85-0.90 with jet energy.

The unfolded energy rapidity distributions are shown in Figures B.8 and B.9. The mean rapidity of the energy flow (Figure 5.25a) also increases with the energy of the jet, demonstrating that the energy flow is also more collimated in jets at high energy. The energy flow in quark jets has higher mean rapidity than gluon jets at the same energy. Similar results are seen for the energy flow of charged particles only (Figure 5.25b). The ratio of the mean rapidity of energy flow of gluon jets compared to quark jets (Figure 5.26) is approximately constant at 0.85-0.9 with jet energy.

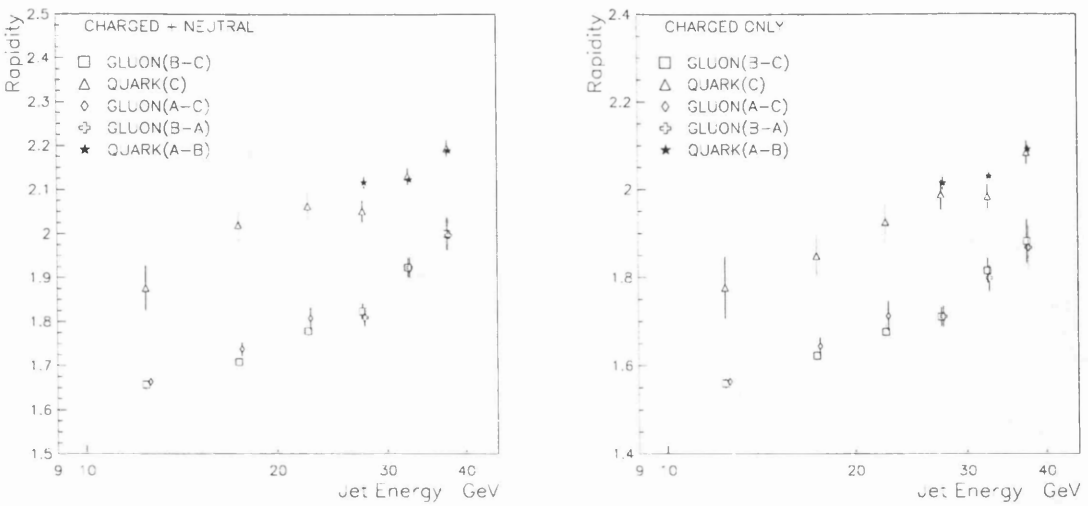

(a) Mean rapidity of particles in jet

(b) Mean rapidity of charged particles in jet

Figure 5.23: *Mean rapidity of particles in quark and gluon jet samples after purity correction.*

5.5.4 Mean fragmentation function of tracks.

The unfolded fragmentation function of particles ($X_e = \frac{E_{particle}}{E_{jet}}$) is shown in Figures B.10 and B.11 for the quark and gluon jets. The mean values are plotted in Figure 5.27a for the quark and gluon jets. There is a good match between the results obtained from different jet sub-samples. The gluon jets are seen to have a significantly lower fragmentation function than the quark jets. The fragmentation function for charged particles only (Figure 5.27b) is higher than the fragmentation function for all particles. The ratio of the fragmentation function for gluon jets compared to quark jets (Figure 5.28) is approximately constant with energy at ~0.80 for all particles and ~0.75 for charged particles only.

5.5.5 Mean jet core width.

The core energy fraction is shown as a function of the cone angle in Figure B.12 for the unfolded quark and gluon jets. The half-angles of the mean cones containing 90%, 75%, 50% and 25% of the jet energy are shown in Figure 5.29. There is a reasonable match between the results from different jet sub-samples. The jet core widths are seen to narrow by approximately a factor of 2 between

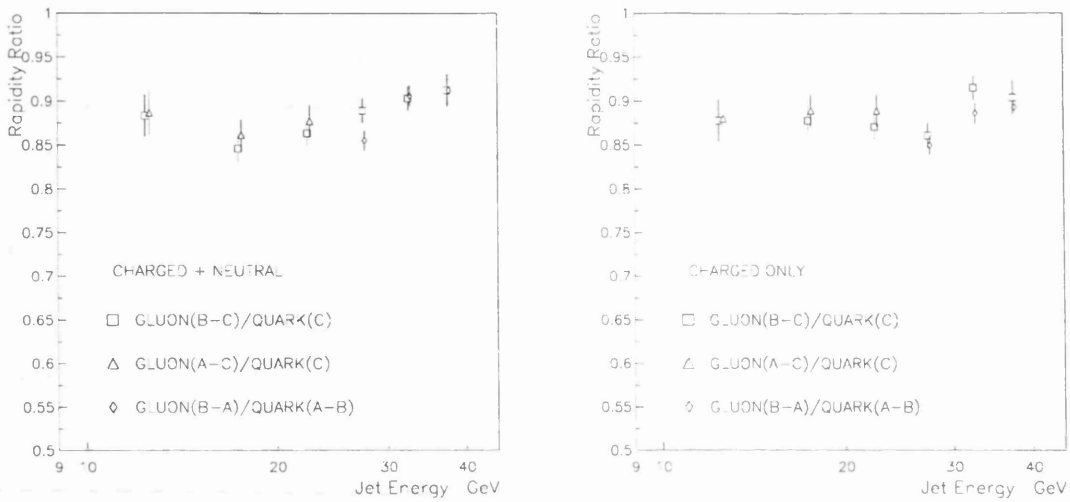

(a) Rapidity ratio for all particles

(b) Rapidity ratio for charged particles

Figure 5.24: *Gluon/quark jet mean particle rapidity ratio after purity correction.*

10-40 GeV. The core widths of the gluon jets are significantly wider than the widths of the quark jets. The ratio of the gluon jet width to the quark jet width (Figure 5.30) is approximately constant with jet energy, but increases to ~1.7 for small core energy fraction. The core width ratios for the QUARK(C) and unfolded GLUON(B-C) measurements were fitted with $W = constant$ functions. The results are shown in Table 5.2 for the various jet core sizes, but no χ^2 values are given since the systematic errors from the unfolding procedure are large. The fits show an increase in the core width ratio for decreasing jet core size.

5.5.6 Mean multiplicity ratio in jet cores.

The multiplicity as a function of the angle to the jet axis is shown in Figures B.13 and B.13. For each jet core energy fraction, the mean gluon/quark multiplicity ratios in the jet cores (Figure 5.31) are approximately constant with jet energy. The ratio increases from ~1.25 for the whole jet to ~1.4 in narrow jet cores containing a small core energy fraction. The mean gluon/quark charged multiplicity ratios in the jet cores (Figure 5.32) show a different behaviour. The ratios decrease slightly with increasing jet energy. The charged multiplicity ratios increase with decreasing core energy fraction. For small core energy fraction, the

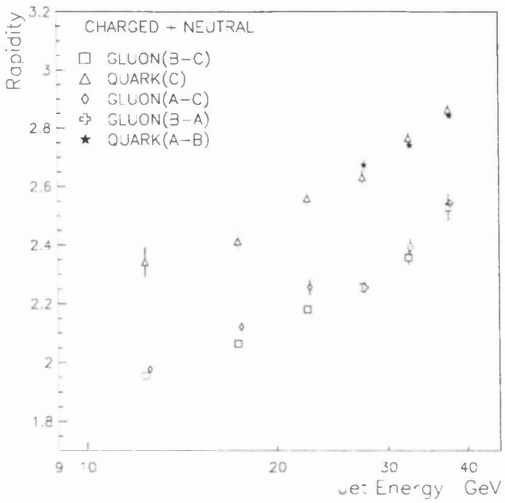

(a) Mean rapidity of energy flow in jet

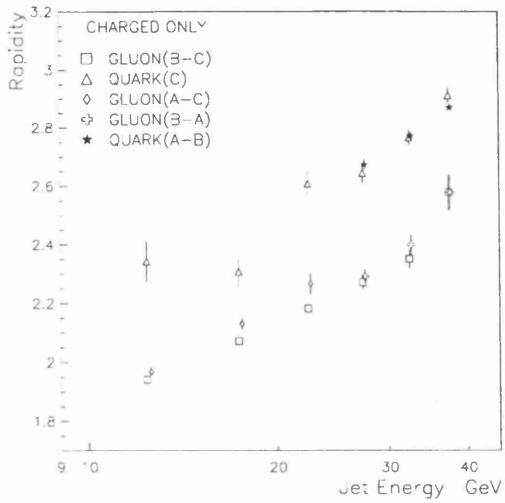

(b) Mean rapidity of charged energy flow in jet

Figure 5.25: *Mean rapidity of energy flow in quark and gluon jet samples after purity correction.*

Jet Core	*Constant term*
90% E_{JET}	1.26 ± 0.04
75% E_{JET}	1.47 ± 0.04
50% E_{JET}	1.59 ± 0.04
25% E_{JET}	1.68 ± 0.08

Table 5.2: *Fits to the gluon/quark jet core width ratio variation with energy. The jet core width is defined by the half-angle of the cone containing 90 %, 75 %, 50 % and 25 % of the jet energy. For each core width size a function W = constant was fitted to the core width ratio W.*

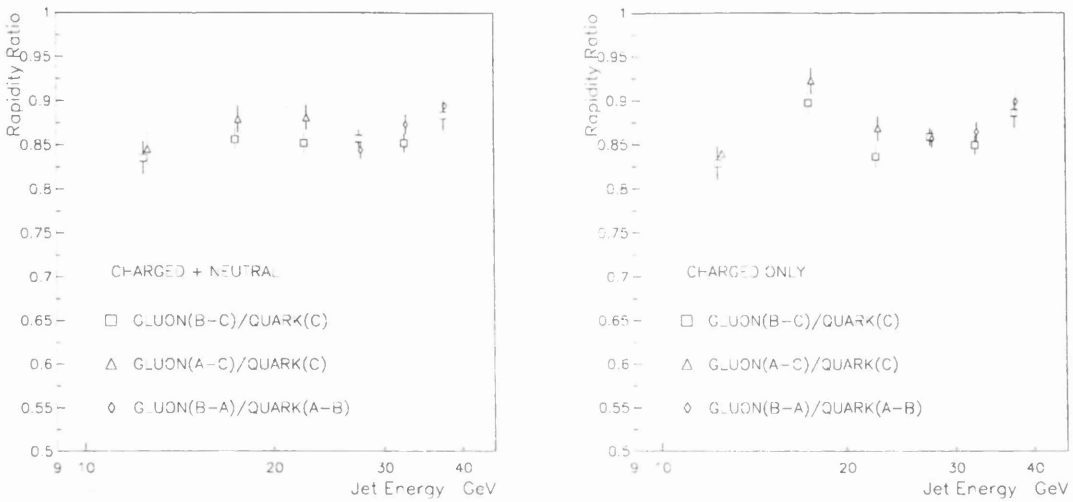

(a) Rapidity ratio for charged and neutral energy flow

(b) Rapidity ratio for charged energy flow

Figure 5.26: *Gluon/quark jet mean energy flow rapidity ratio after purity correction.*

ratio varies between ~1.8 for 10-15 GeV jets and ~1.45 for 35-40 GeV jets. An $R = constant$ fit was made to the charged multiplicity ratio GLUON(B-C)/QUARK(C) for each jet core size (Table 5.3). The fits show that there is a significant increase in the ratio comparing the 90% core to the 50% and 25% jet cores (4.6 and 2.5 standard deviations respectively).

5.6 Discussion of possible biases in jet samples.

The dominant systematic bias in the uncorrected jet sub-samples is the quark and gluon jet purity of the sub-samples, which varies with jet energy. A correction was made for this, which was outlined in Section 5.4. The subsequent comparison of quark and gluon jet properties with energy (Section 5.5) has produced some new and perhaps unexpected results. OPAL has found a similar value [38] for the gluon/quark multiplicity ratio of ~1.27 for 25 GeV jets. However the ratio appears to be constant or decrease slightly with jet energy (Figure 5.17b), and the charged multiplicity ratio (Figure 5.18b) appears to decrease significantly

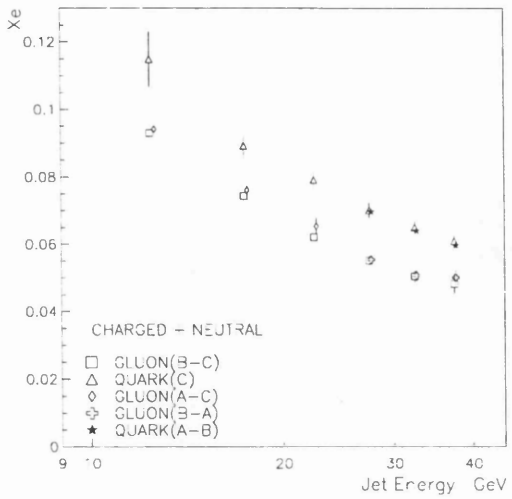

(a) Mean fragmentation function of particles in jets

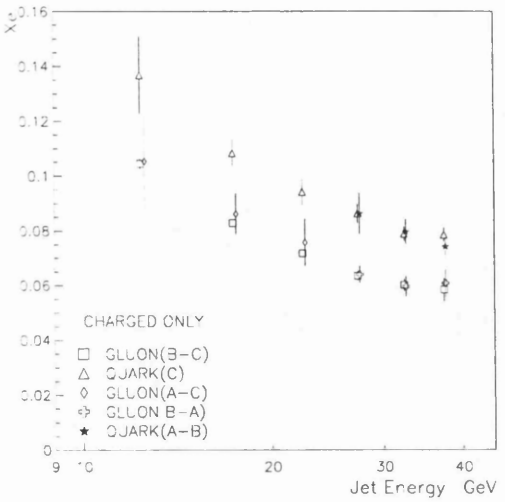

(b) Mean fragmentation function of charged particles in jets

Figure 5.27: *Mean fragmentation function of particles in quark and gluon jet samples after purity correction* ($X_e = E_{particle}/E_{jet}$).

Jet Core	*Constant term*	χ^2/d.f.	*Probability*
100% E_{JET}	1.41 ± 0.03	1.12	~ 35 %
90% E_{JET}	1.32 ± 0.02	1.91	~ 9 %
75% E_{JET}	1.43 ± 0.03	1.23	~ 25 %
50% E_{JET}	1.49 ± 0.04	1.46	~ 20 %
25% E_{JET}	1.48 ± 0.07	0.91	~ 45 %

Table 5.3: *Fits to the gluon/quark jet charged multiplicity ratio variation with energy. For each jet core size, a function R = constant was fitted to the multiplicity ratio R.*

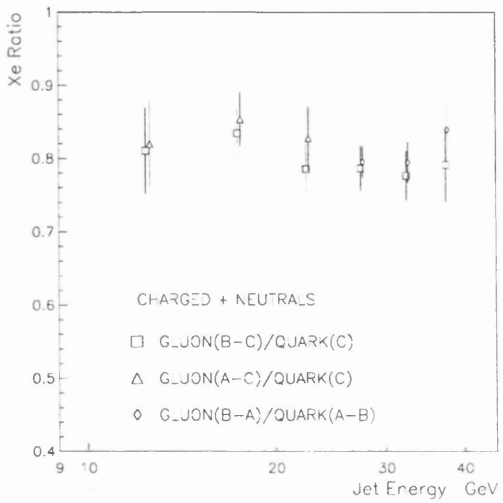

(a) Gluon/quark jet X_e ratio

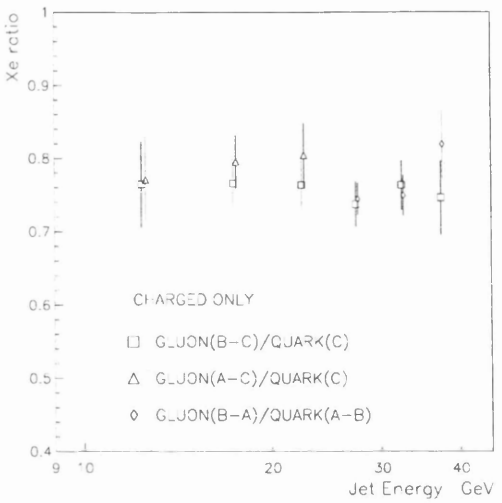

(b) Gluon/quark jet charged particle X_e ratio

Figure 5.28: *Gluon/quark jet ratio of mean particle fragmentation function after purity correction.*

with jet energy. For all jet energies, the multiplicity ratios in the jet cores have been measured to be higher than the overall ratio for the whole jet (Figures 5.31 and 5.32). The mean p_t of particles in gluon jets was seen to be slightly higher than for quark jets at low jet energy, but was similar at higher jet energies. In this section the **possible biases** in the jet sub-samples, and systematic effects due to the purity correction are discussed, to see if they could possibly cause the above results. No attempt was made to correct these possible systematic effects, since the final results would then become more reliant on Monte Carlo events, which may not model the data correctly.

5.6.1 Possible biases due to the selection of 3-jet event samples.

The $JET^{(quark)}_{q\bar{q}\gamma}$ sub-sample comes from $q\bar{q}\gamma$ events, which have different predicted particle flow properties to $q\bar{q}g$ events. The "ideal quark/gluon jet study" might involve a comparison of events containing two quark jets with those containing two gluon jets. The $q\bar{q}\gamma$ events have only two quark jets in the event, but the $q\bar{q}g$

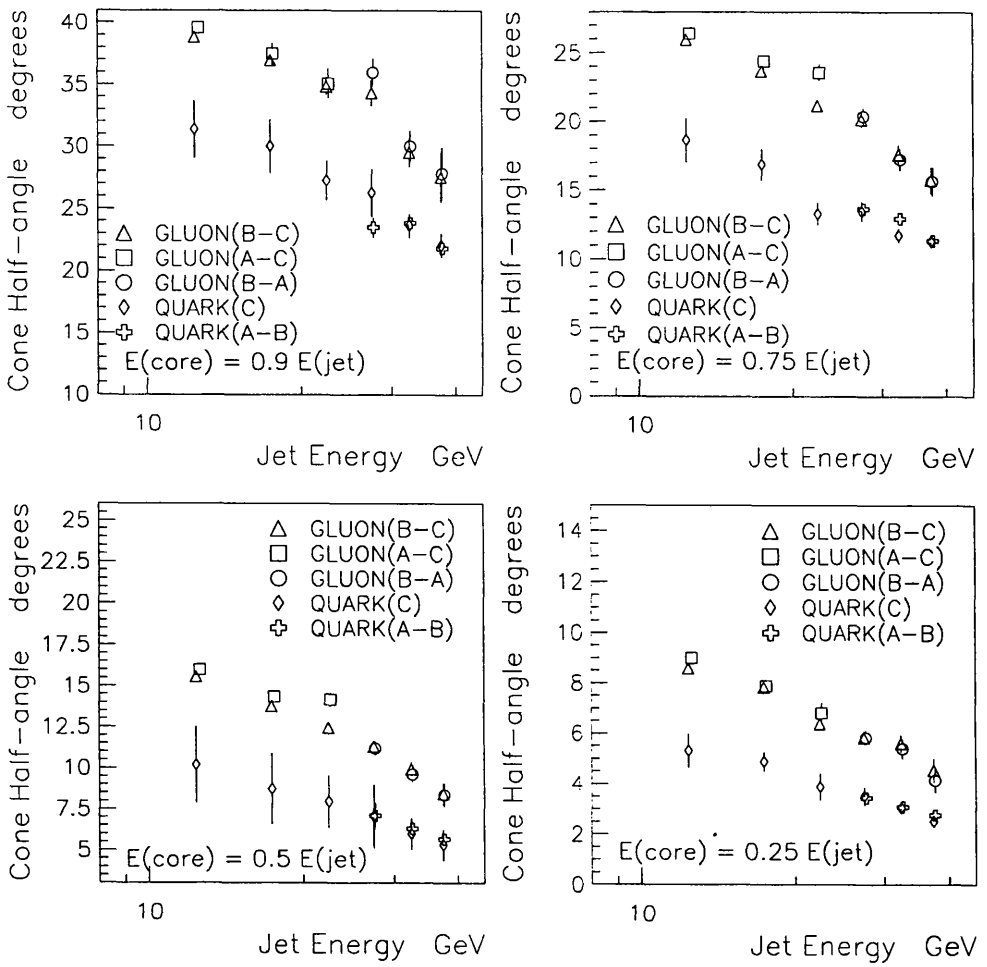

Figure 5.29: *Half-angle of the mean cones containing 90%, 75%, 50% and 25% of the jet energy, after purity correction.*

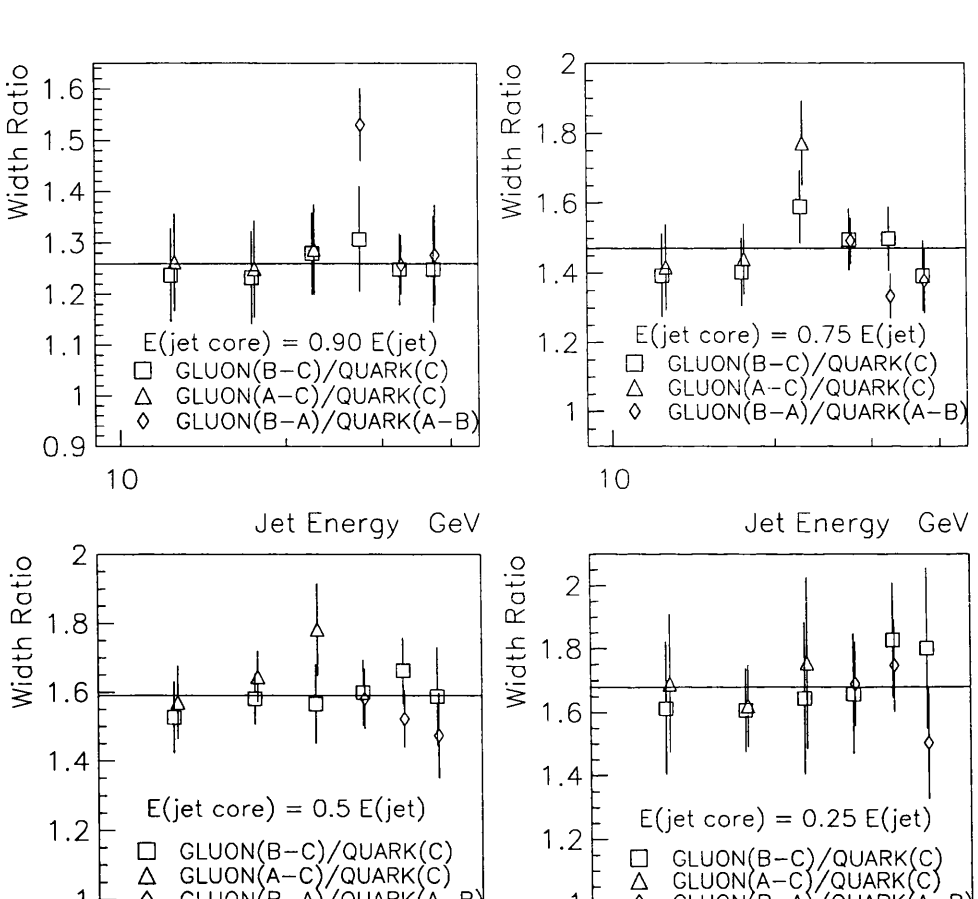

Figure 5.30: *Gluon/quark jet ratio of the half-angles of the mean jet cores, after purity correction. The horizontal lines show the fits to the data points.*

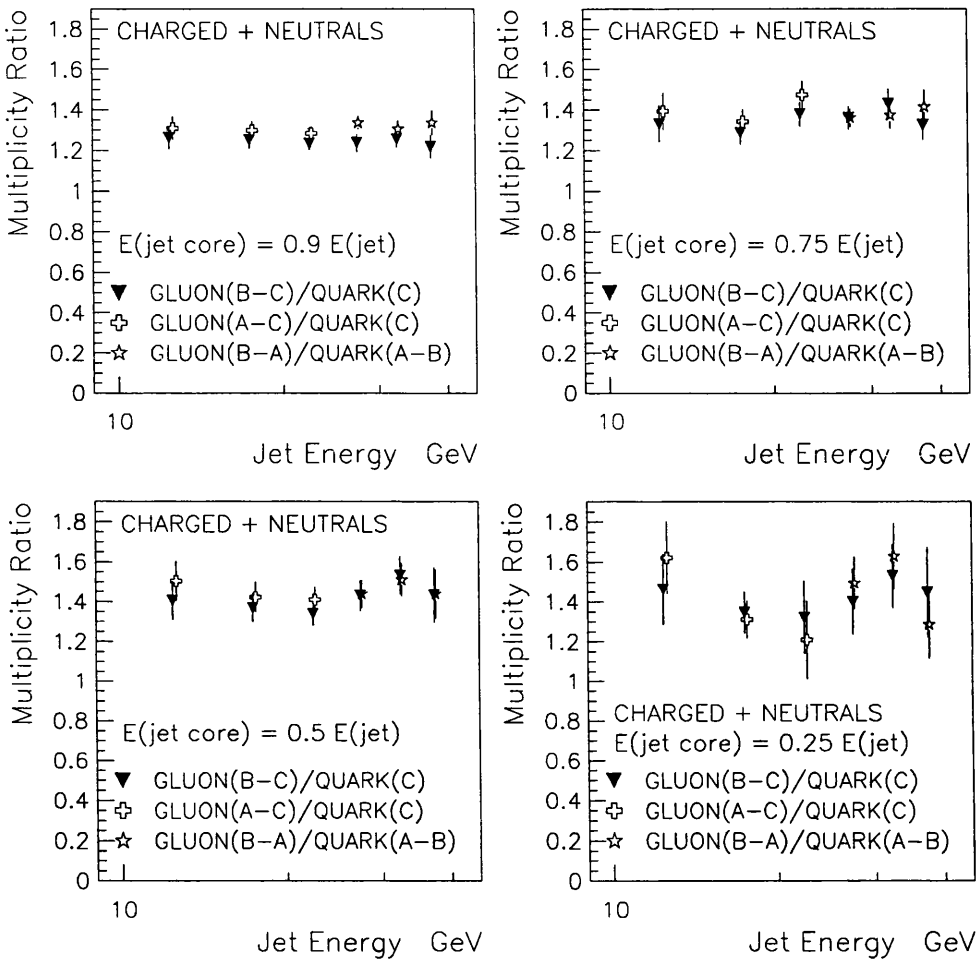

Figure 5.31: *Gluon/quark jet mean jet core multiplicity ratio, after purity correction.*

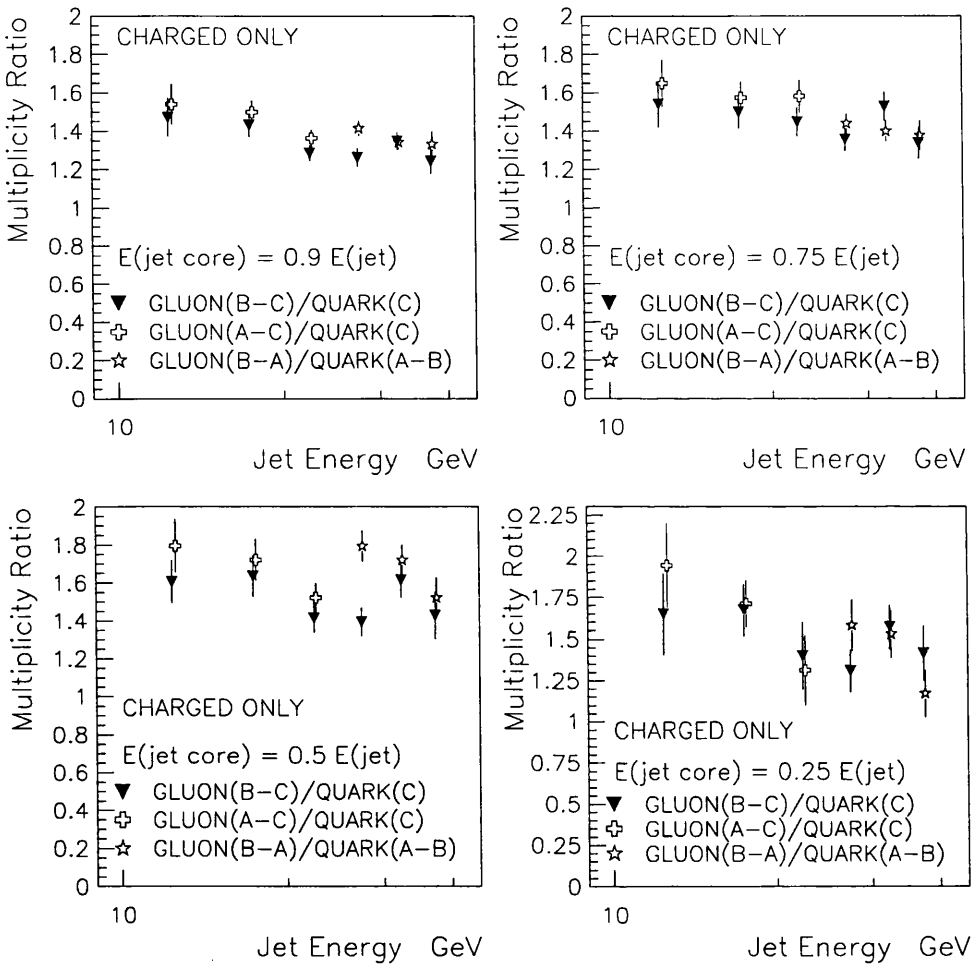

Figure 5.32: *Gluon/quark jet mean jet core charged multiplicity ratio, after purity correction.*

Event configuration	$q\bar{q}g$ *multiplicity*	$q\bar{q}\gamma$ *multiplicity*
$120° < \phi_{12} < 130°$ $120° < \phi_{13} < 130°$	49.9 ± 0.2	34.0 ± 2.1
$130° < \phi_{12} < 140°$ $130° < \phi_{13} < 140°$	48.6 ± 0.2	33.4 ± 1.6
$140° < \phi_{12} < 150°$ $140° < \phi_{13} < 150°$	47.1 ± 0.1	33.0 ± 1.1

Table 5.4: *Total multiplicity in symmetric $q\bar{q}g$ and $q\bar{q}\gamma$ events for different opening angles between the leading quark jet and the two lower energy jets.*

events contain both quark and gluon jets. The perturbative soft gluon calculation (Section 2.6.2) predicts that each parton contributes to soft gluon radiation over the whole event. Consider then a $q\bar{q}g$ event. The gluon may contribute soft gluon radiation to the quark jets and vice versa. The effect of this would be to cause the quark and gluon jet multiplicities to become more alike.

The topology of the hadronic event may also affect the jet properties. The total multiplicity in symmetric $q\bar{q}g$ and $q\bar{q}\gamma$ events is shown in Table 5.4 for different opening angles (ϕ_{12} and ϕ_{13}) between the leading quark jet and the two lower energy jets. The events with jet opening angles close to the "Mercedes" configuration (three-fold-symmetric) have higher total multiplicity than those events where the opening angles ϕ_{12} and ϕ_{13} are larger. This demonstrates that the jet properties to be influenced by the type of event from whence they came.

The methods of selecting the three samples of 3-jet events were relatively simple. The energy-ordering tag involved the whole 3-jet sample, and did not influence the event selection. The other two tagging methods selected small subsets of the data, but appeared to give event samples with similar topologies and kinematic properties. In Sample B the lepton-tagged jet was thrown away, leaving an "anti-tagged" gluon jet sub-sample. In Sample C the photon jet was thrown away leaving an "anti-tagged" quark jet sample. The subsequent event

cuts removed similar proportions of events from each event sample. Any biases due to the selection of the three-jet events are likely to be as small as possible, without resorting to small sub-sets of the data containing both restricted jet opening angles and restricted jet energies.

5.6.2 Possible biases due to background in the jet sub-samples.

In the gluon jet samples ($JET^{(gluon)}_{b\bar{b}g}$ and $JET^{(3)}_{q\bar{q}g}$) there was a significant quark jet background, which increased with the energy of the jet sub-samples. In the $JET^{(2)}_{q\bar{q}g}$ quark jet sub-sample, there was also a large gluon jet background, which increased with decreasing energy. A study was made of these backgrounds in Monte Carlo events and a correction was made to remove their effects. The $JET^{(\gamma)}_{q\bar{q}\gamma}$ quark jet sub-sample was assumed to be 100% pure. The photon purity in Monte Carlo $q\bar{q}\gamma$ events was greater than 95% over most of the sample. However a 15% π^0 background was present in events where the quark jet had less than 20 GeV energy. This may lead to a 15% gluon jet background in the quark jet sub-sample between 10-20 GeV. A correction was not made to the data to remove this background, so this may cause a bias in the data at low energy.

5.6.3 Possible biases due to energy mis-match of the jet sub-samples.

The jets in each sub-sample were weighted, such that the mean energy of the jets was in the centre of each 5 GeV energy range. Where the jet background in the sub-sample is large, the gluon jets and quark jets in each energy range may have different mean energies. The jet multiplicities are particularly dependent on the energy of the jet. If the gluon jets have slightly lower energy than the quark jets, then the gluon/quark jet multiplicity ratio might be lower than the true value. The jet sub-samples are reasonably pure over the whole energy range, so this bias is likely to be minimal, except perhaps at high-energy in the gluon jet sub-sample ($JET^{(gluon)}_{b\bar{b}g}$).

5.6.4 Possible biases due to the estimation of the jet purity.

The fractions of quark jets, gluon jets and "ambiguous" jets were extensively studied in Monte Carlo events. The fractions of each jet type in the sub-samples show sensible variation with energy. Similar purity values were obtained with HERWIG Monte Carlo events and with JETSET for the energy-ordered three-jet

sample. However it was necessary to rely on Monte Carlo events to estimate the jet purity, so it is possible that some bias remains due to the background subtraction.

5.6.5 Possible biases due to "ambiguous events".

A number of "ambiguous events" have been seen in Monte Carlo events, which appear to originate from "two-jet-like" or "four-jet-like" events at parton level. Following the event selection cuts, the background from these events would appear to be ~5%, but considerably less over most of the jet sub-sample energy range. These "ambiguous events" were ignored in the jet correction procedure, but it is unlikely that they could cause the effects described in Section 5.6 since they are a small fraction of events in each three-jet sample.

5.6.6 Possible biases due to b-jet background.

The effect of b-jets on the properties of the jet sub-samples was completely ignored. In Section 5.3 the highest-energy b-jet sub-sample ($JET^{(1)}_{b\bar{b}g}$) was shown to have higher multiplicity and lower mean particle p_t than the light quark jets. At high jet energy there may be a bias in the gluon jet properties due to the large (~10-20%) b-jet background in the gluon jet sub-sample. A correction was made for this using the quark samples, which consist mostly of *udsc*-jets.

5.6.7 The main systematic effect of biases.

The two gluon jet sub-samples were selected ($JET^{(gluon)}_{b\bar{b}g}$ and $JET^{(3)}_{q\bar{q}g}$) from three-jet event samples A and B. The estimated purity and types of background in each gluon jet sub-sample was different, yet over the common jet energy range (10-25 GeV) the sub-samples yielded similar results for all jet distributions. Two quark jet sub-samples were used ($JET^{(quark)}_{q\bar{q}\gamma}$ and $JET^{(2)}_{q\bar{q}g}$) and these gave similar results for most distributions over the common energy range (25-40 GeV). There was a slight mis-match in the multiplicities of the quark jet measurements, which can be attributed to the different b-jet fraction in each sub-sample. However the good agreement in the gluon jet measurements at low energies and the quark jet measurements at high energies, suggests that there is no significant systematic effects due to the selection of the jet sub-samples, or due to the purity correction process.

In the 10-25 GeV energy range only one quark jet sub-sample was selected ($JET^{(quark)}_{q\bar{q}\gamma}$), and there may be up to 15% gluon jet background in this sub-sample in the 10-20 GeV energy range. This gluon jet background in the quark jet sub-sample is likely to be the dominant systematic effect at low jet energy and

this was not corrected for in the measurement. The impact of this background would be to accentuate quark and gluon jet differences in the 10-20 GeV energy range. Consider, for example, the multiplicity ratio of gluon jets compared to quark jets. The gluon jets have higher multiplicity than the quark jets, so any gluon jet background in the quark sub-sample will increase the denominator, and thus lower the ratio. A correction for the gluon jet background in the quark sub-sample would thus raise the ratio, and thus lead to larger quark/gluon jet differences in the 10-20 GeV energy range.

There was only one gluon sub-sample in the 25-40 GeV range. Here the large quark jet background in this sub-sample was estimated to contain about 50% b-jets, yet the purity correction was made using quark sub-samples containing $\sim$11% and $\sim$22% b-jets. Consider, for example, the effect of correcting the gluon jet multiplicity for the b-jet background by using $udsc$-jets. Since the b-jets have higher multiplicity, but their effect is removed from the sub-sample using lower multiplicity jets, an overcorrection would occur, leading to a higher jet multiplicity than the true gluon jet multiplicity.

The two main systematic effects discussed above would lead to an enhancement of the results described in Section 5.6. This gives increased confidence that these quark/gluon measurements are real phenomena.

5.7 Summary.

A number of quark and gluon jet properties have been measured using tagged jet sub-samples from data, with background subtracted using purity values estimated from Monte Carlo. From the rapidity distributions of particles in the jets, it appears that particles lie closer to the jet axis in quark jets compared to gluon jets. The mean fragmentation function measurements indicate that there is a larger proportion of soft particles in gluon jets compared with quark jets.

Some jet distributions showed an interesting energy dependence. The measured gluon/quark jet multiplicity ratio is constant at $\sim$1.25 with jet energy, which is considerably below the perturbative prediction of $\sim$2. The gluon/quark jet charged multiplicity ratio decreases from $\sim$1.6 to $\sim$1.3 with increasing jet energy. Higher multiplicity ratios are seen in the jet cores. At low jet energy and narrow jet core, the charged multiplicity ratio was measured to be $\sim$1.8, which approaches the perturbative prediction. Systematic biases in the measurement are more likely to enhance these effects. Measurements of the mean p_t of tracks in the jets, and of the charged to neutral multiplicity ratios, also indicate that quark and gluon jets are more alike at high jet energy than at low jet energy. Current phenomenology suggests that perturbative QCD predicts jet properties at higher jet energies, with non-perturbative or long-range effects becoming

insignificant. The experimental results here suggest the opposite situation, with larger quark/gluon jet differences at low jet energies. At higher jet energy the quark and gluon jets appear to become more alike, with the jet properties moving away from the perturbative prediction.

Chapter 6

Particle flow in $q\bar{q}g$ and $q\bar{q}\gamma$ events.

6.1 Introduction.

A lower particle flow has been observed in the angular region between the quark jets in $q\bar{q}g$ events compared to $q\bar{q}\gamma$ events [42, 43, 44]. This is known as the "string effect", after its non-perturbative explanation using string fragmentation (Section 2.6). The effect can also be explained using a perturbative calculation of the radiation of soft gluons from the hard partons (Section 2.6.1). The three previous measurements of the "string effect" using $q\bar{q}g$ and $q\bar{q}\gamma$ events have been made at 29 GeV and 35 GeV. In this chapter a similar measurement is described at the Z^0 resonance using the three-jet events outlined in Chapter 3. A comparison is then made with the previous measurements to show the energy dependence of the "string effect". The data is also compared to the theoretical predictions.

6.2 Summary of the three-jet event samples.

The tagged three-jet event samples used in the "string effect" analysis were essentially the same event samples A, B and C ($q\bar{q}g$, $b\bar{b}g$ and $q\bar{q}\gamma$) that were used for the quark/gluon jet comparison, but with an additional event cut to remove events where the beam axis lay in or close to the plane of the event. The topology of the three-jet events did not change after this event cut. The angles between the jet projections are shown in Figure 6.1 for each event sample, and the calculated energies of each jet are shown in Figure 6.2. The mean jet projections of the event samples are given in Table 6.1. The mean angles between the quark jets in the energy-ordered sample are slightly different, since one of the quark jets in the other two samples had less than 25 GeV energy in some events. An

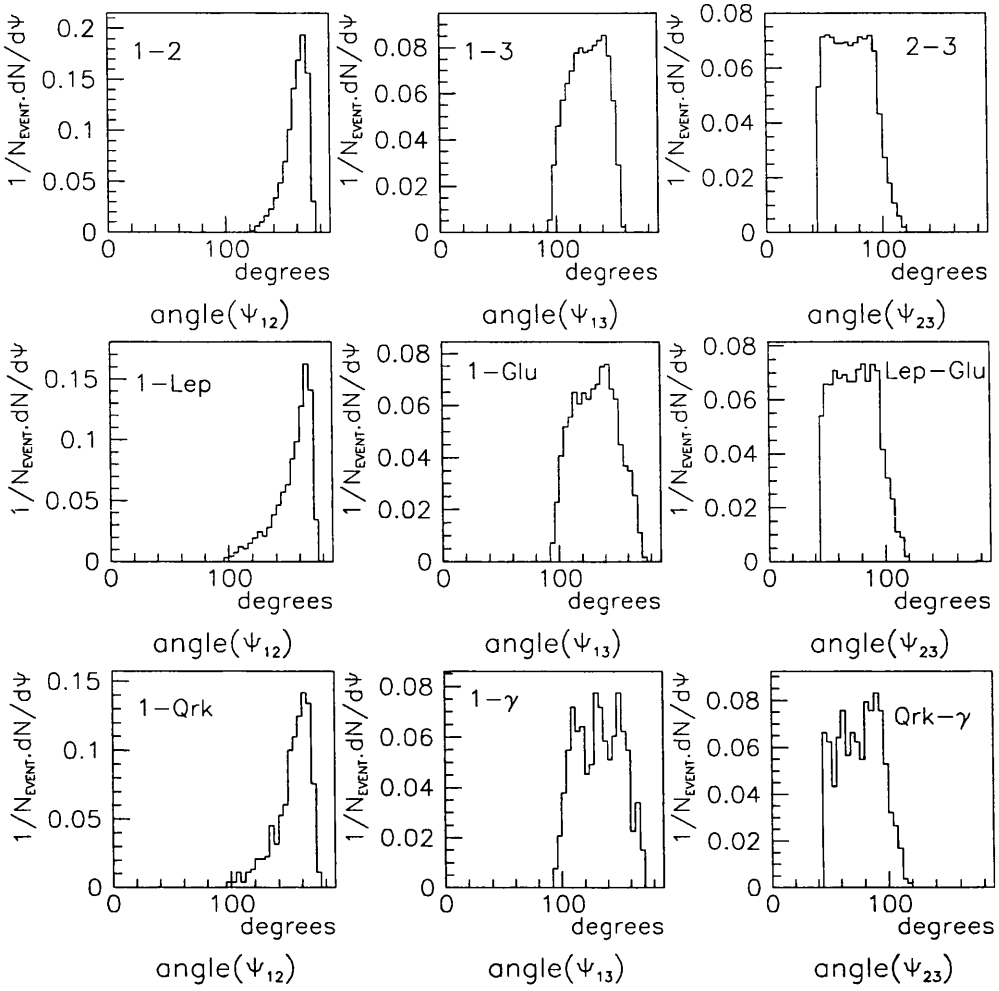

Figure 6.1: *Angle between each pair of jets in the event samples. The angles are determined from the projections of the jet axes on to the three-jet event plane.*

estimate of the mean purities of the jets in each sample was made using JETSET Monte Carlo events. The gluon and photon jet purities are given in Table 6.1.

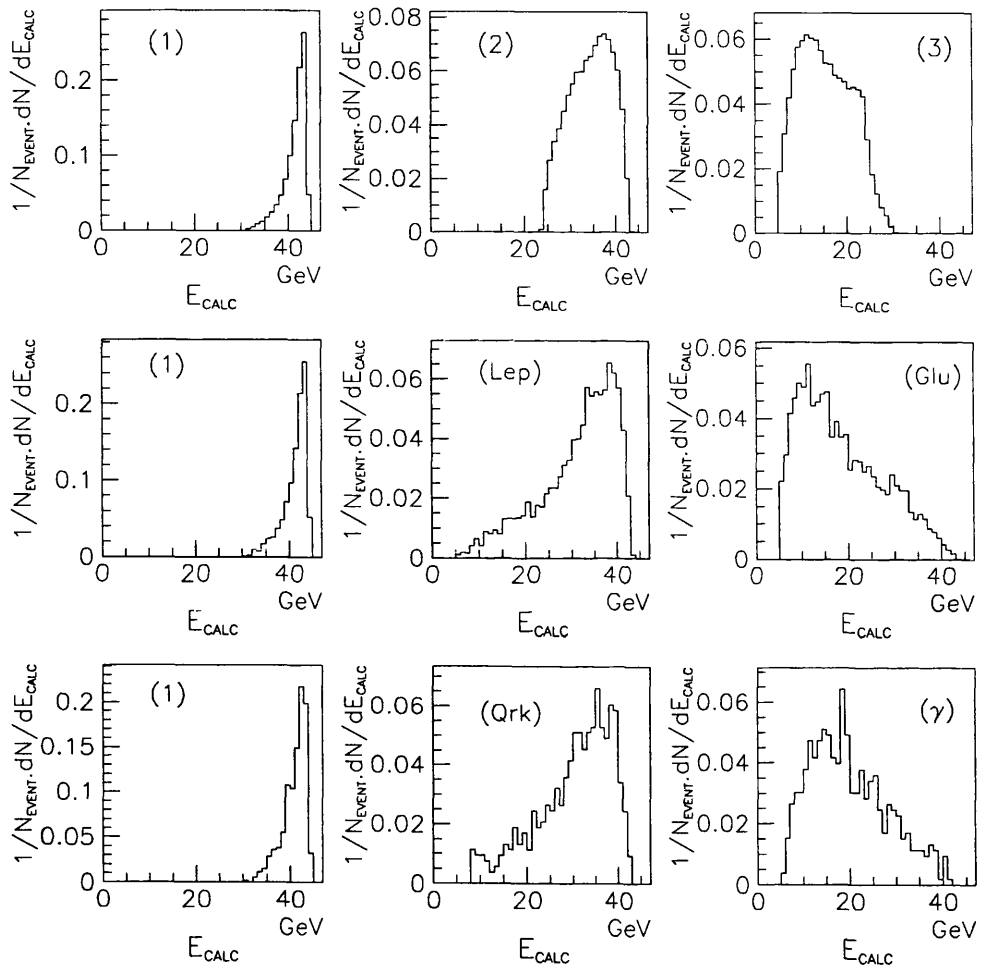

Figure 6.2: *Energy of the jets in each sample. The jet energies were determined from the opening angles of the jets.*

Event sample	*Angle* $q-\overline{q}$	*Angle* $q-g$ *or* $q-\gamma$	*Gluon jet purity*	*Photon jet purity*
TPC-2γ	153°	129°	60 %	?
MARK-II	$\sim$ 150°	$\sim$ 130°	65 %	85 %
JADE	155°	130°	64 %	88 %
ALEPH, $q\overline{q}\gamma$	152°	132°	-	96 %
ALEPH, $b\overline{b}g$	154°	132°	86 %	-
ALEPH, $q\overline{q}g$	159°	127°	74 %	-

Table 6.1: *Summary of the mean opening angles of the jets and the estimated gluon jet and photon jet purities in each event sample. The jet angles were determined with respect to the leading quark jet in the event.*

6.3 Particle flow in the event plane.

The tracks in each event were projected on to the three-jet event plane described in Section 4.4. The azimuthal angle of each track projection was measured with respect to the projection of the highest-energy quark jet, and in the direction of the other quark jet in the event. The overall particle flow in the event plane is shown in Figure 6.3 for each event sample. The particle flow prediction from JETSET Monte Carlo events is shown as the solid line. JETSET gives a good description of the particle flow in the event samples, although slightly worse in the $q\overline{q}\gamma$ events. The predicted particle flow was determined using the soft gluon calculation described in Sections 2.6.3- 2.6.4 with similar parton angles to the mean jet angles of the event samples (Figure 6.4). The prediction is only valid well away from the jet cores and singularities occur in the calculation at the parton directions. Both the data and the predictions show that the particle flow between the q and $\overline{q}$ in the $q\overline{q}g$ events is significantly lower than elsewhere in the event.

A normalised angle was determined for the tracks between the quark jets from

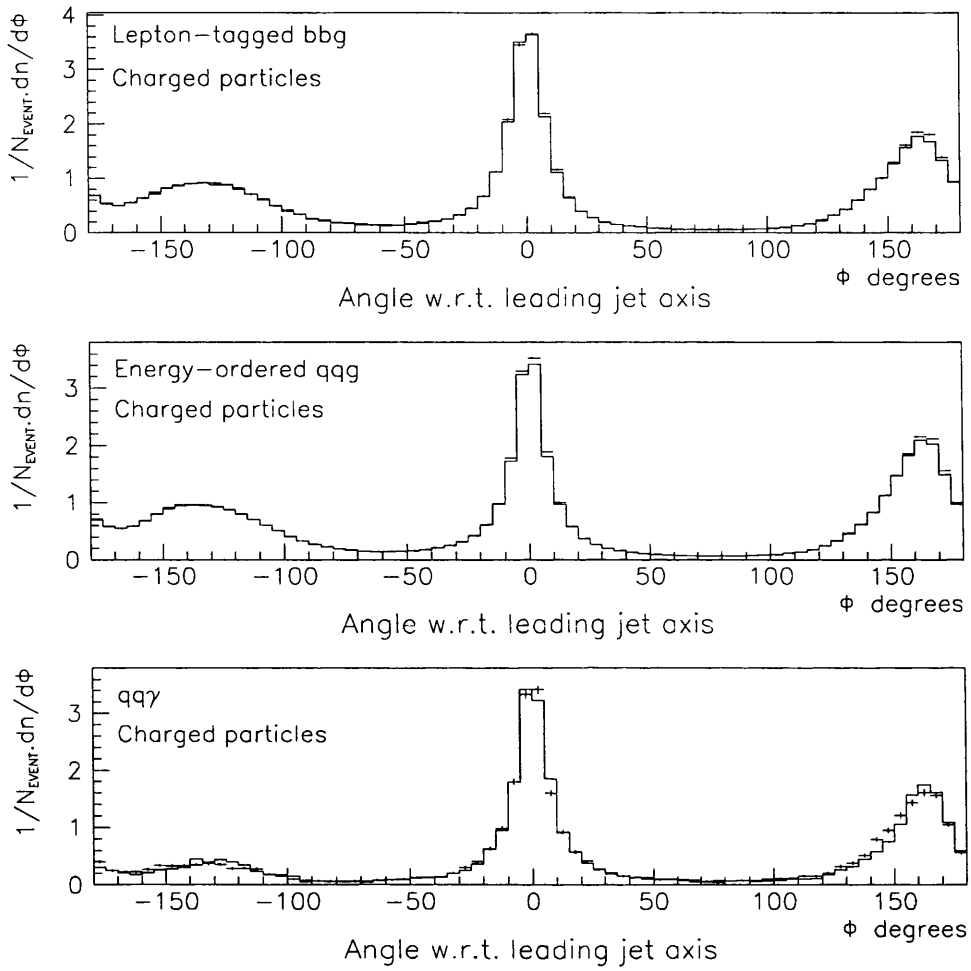

Figure 6.3: *Measured particle flow in the three-jet event plane as a function of the angle to the axis of the leading quark jet. All angles were determined from the projections of the particle momenta in the three-jet event plane. The non-leading quark jet is defined with positive angle ϕ and the gluon or photon jet with negative angle ϕ.*

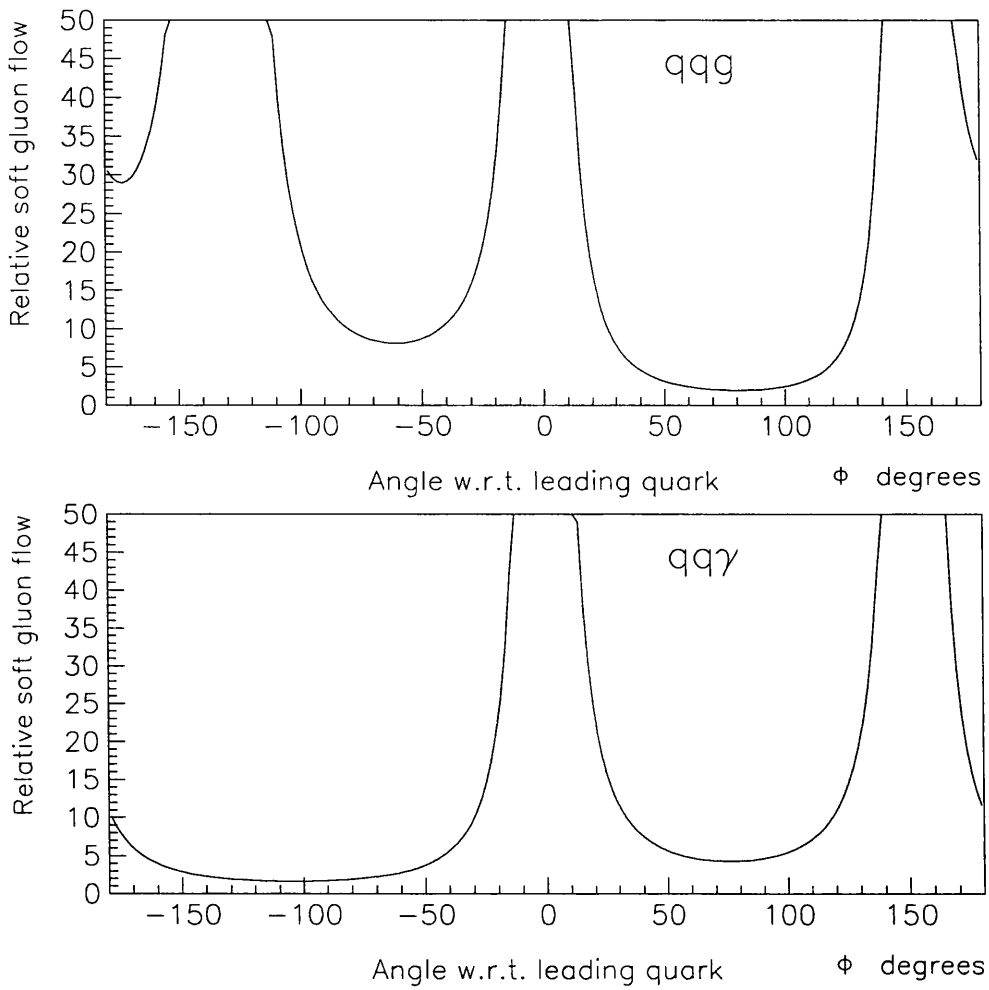

Figure 6.4: *Predicted soft gluon flow in the three-jet event plane as a function of the angle to the leading quark. The non-leading quark is defined with positive angle ϕ and the gluon or photon with negative angle ϕ. In this calculation the angles $q-\overline{q}$ and $q-g$ (or $q-\gamma$) were set to* 153° *and* 130° *respectively. Singularities occur in the direction of the partons, so the prediction is only valid between the partons.*

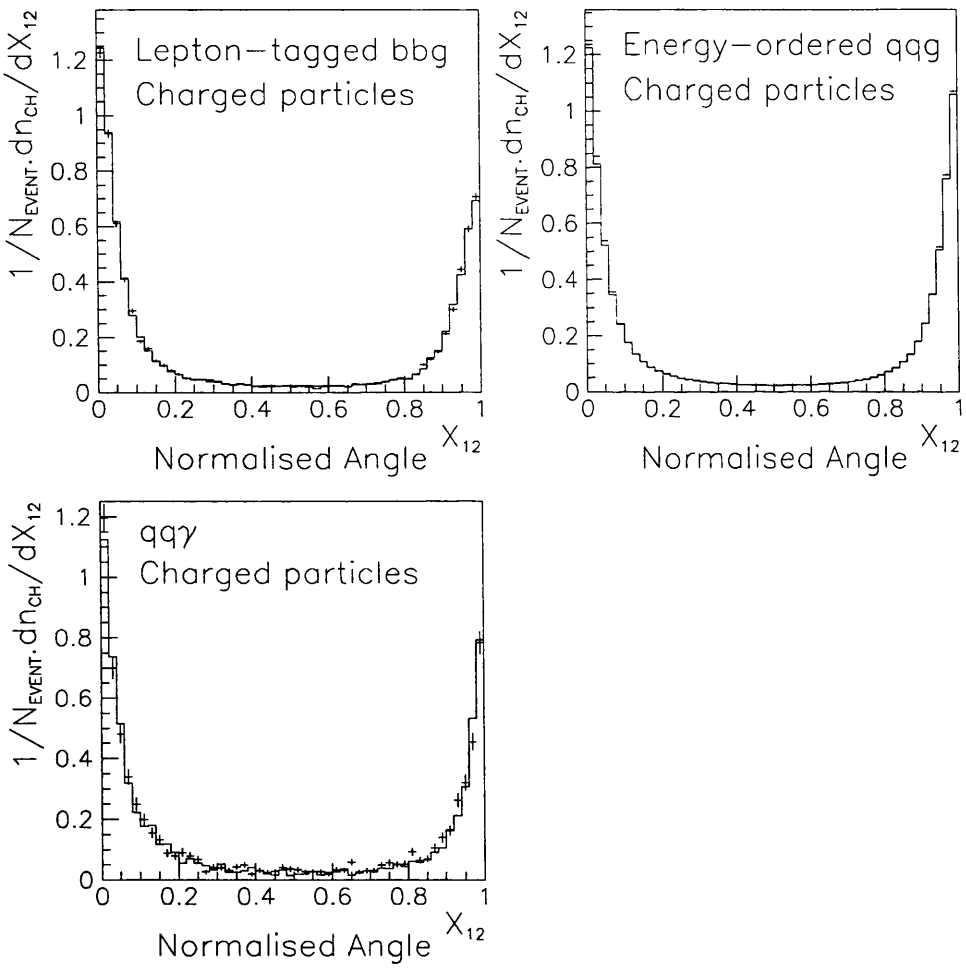

Figure 6.5: *Measured charged particle flow between the leading quark jet and the non-leading quark jet, as a function of the normalised angle between the jets. The solid line represents the particle flow from JETSET Monte Carlo events.*

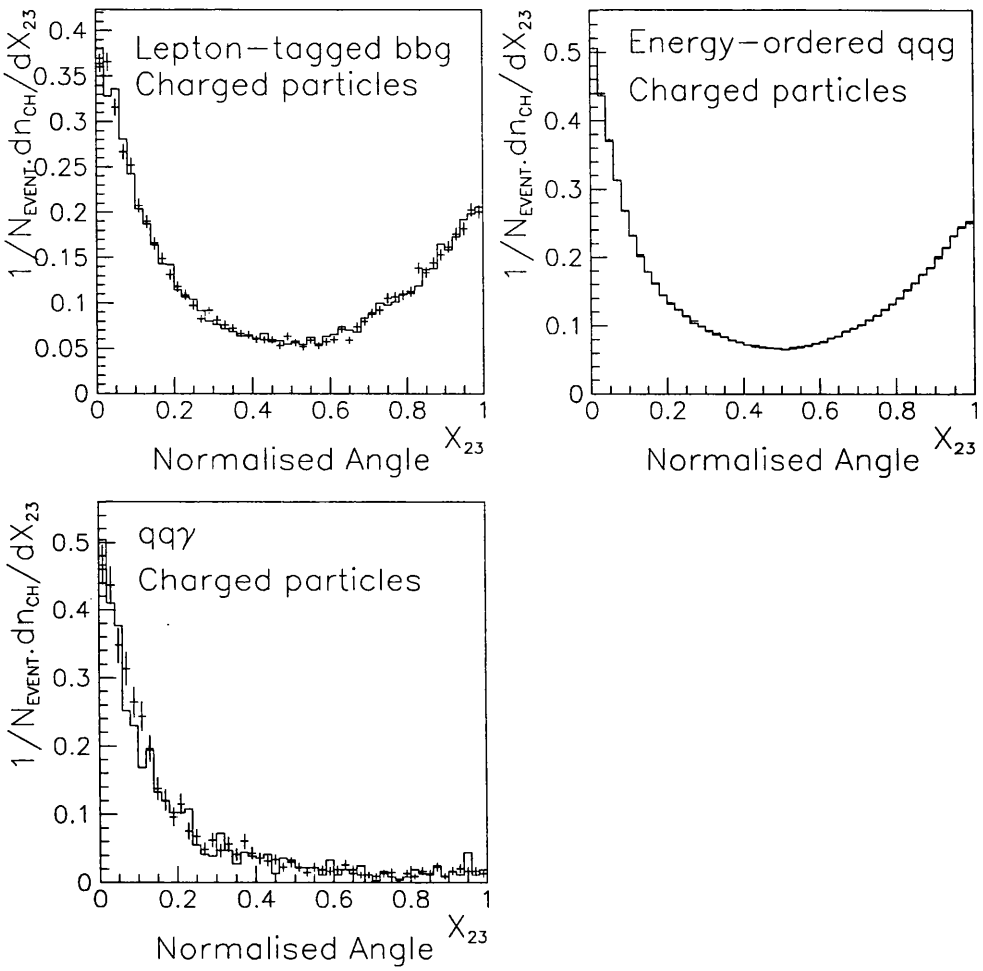

Figure 6.6: *Measured charged particle flow between the non-leading quark jet and the gluon or photon jet, as a function of the normalised angle between the jets. The solid line represents the particle flow from JETSET Monte Carlo events.*

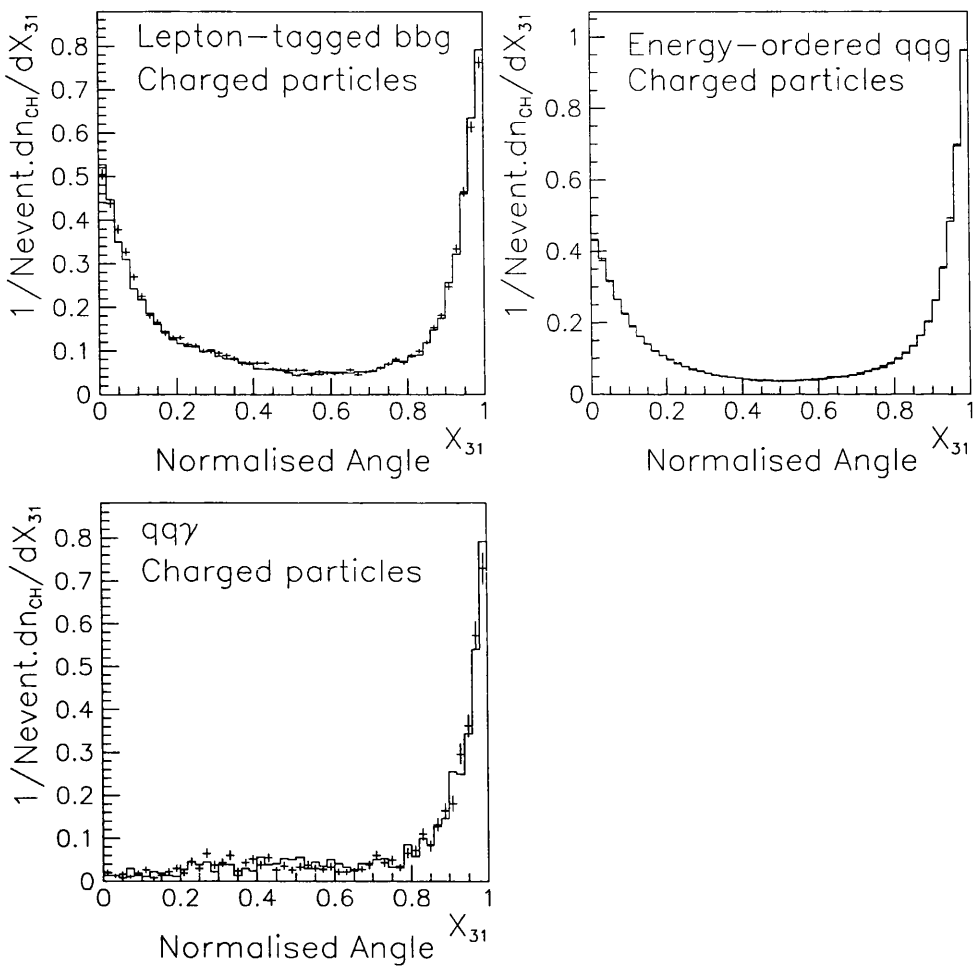

Figure 6.7: *Measured charged particle flow between the gluon or photon jet and the leading quark jet, as a function of the normalised angle between the jets. The solid line represents the particle flow from JETSET Monte Carlo events.*

the angle between the quark jets as follows:

$$X_{ij} = \frac{\phi_{[JET(i)-particle]}}{\phi_{[JET(i)-JET(j)]}}$$

This enabled the particle flow to be compared in events with different jet opening angles. The particle flow between each pair of jets in the samples is shown in Figures 6.5- 6.7 with respect to the normalised angle between the jets. The JETSET Monte Carlo prediction shown as a solid line matches the data well. The particle flow from the QCD prediction for these normalised angles is plotted in Figure 6.8.

The ratio between $q\bar{q}g$ and $q\bar{q}\gamma$ events was determined for the particle flow between the quark jets, as a function of the normalised angle $X_{q\bar{q}}$. This is shown in Figure 6.9 for the particle flow ratio $b\bar{b}g/q\bar{q}\gamma$ and for the ratio $q\bar{q}g/q\bar{q}\gamma$. There is a significant drop in the ratio below 1 between the q and $\bar{q}$. Close to either jet axis the ratio of the particle flows is greater than 1. This can be attributed to the higher b-jet fraction and the gluon jet background in the quark jets from the $b\bar{b}g$ and $q\bar{q}g$ samples, compared to the $q\bar{q}\gamma$ sample. The non-leading quark jets in the energy-ordered $q\bar{q}g$ sample also have higher mean energy than the other two samples. These features of the jet cores are not thought to bias the particle flow measurements well away from the jet cores in the inter-jet region. The predicted ratio of the soft gluon flow between the q and $\bar{q}$ is shown in Figure 6.10. In this calculation the angles $q - \bar{q}$ and $q - g$ (or $q - \gamma$) were set to 153° and 130°. The prediction is only valid for the inter-jet region, away from the jet cores.

6.4 Comparison with previous measurements.

Three measurements of the "string effect" have been made by TPC-2γ [42], MARK-II [43] and JADE [44]. The main features of these measurements are compared in Table 6.1. Each analysis used different event selection criteria, but had the following aspects in common:

- Three-jet events were selected from hadronic events using some form of clustering algorithm.
- A number of event selection cuts were made to improve the topology of the three-jet event samples. The mean angles between the jets in each analysis were similar.
- The $q\bar{q}g$ and $q\bar{q}\gamma$ events in each analysis were obtained using the same set of event selection cuts. The gluon jets in the $q\bar{q}g$ events were assumed to be the lowest-energy jets. The photon jet in the $q\bar{q}\gamma$ events also was required

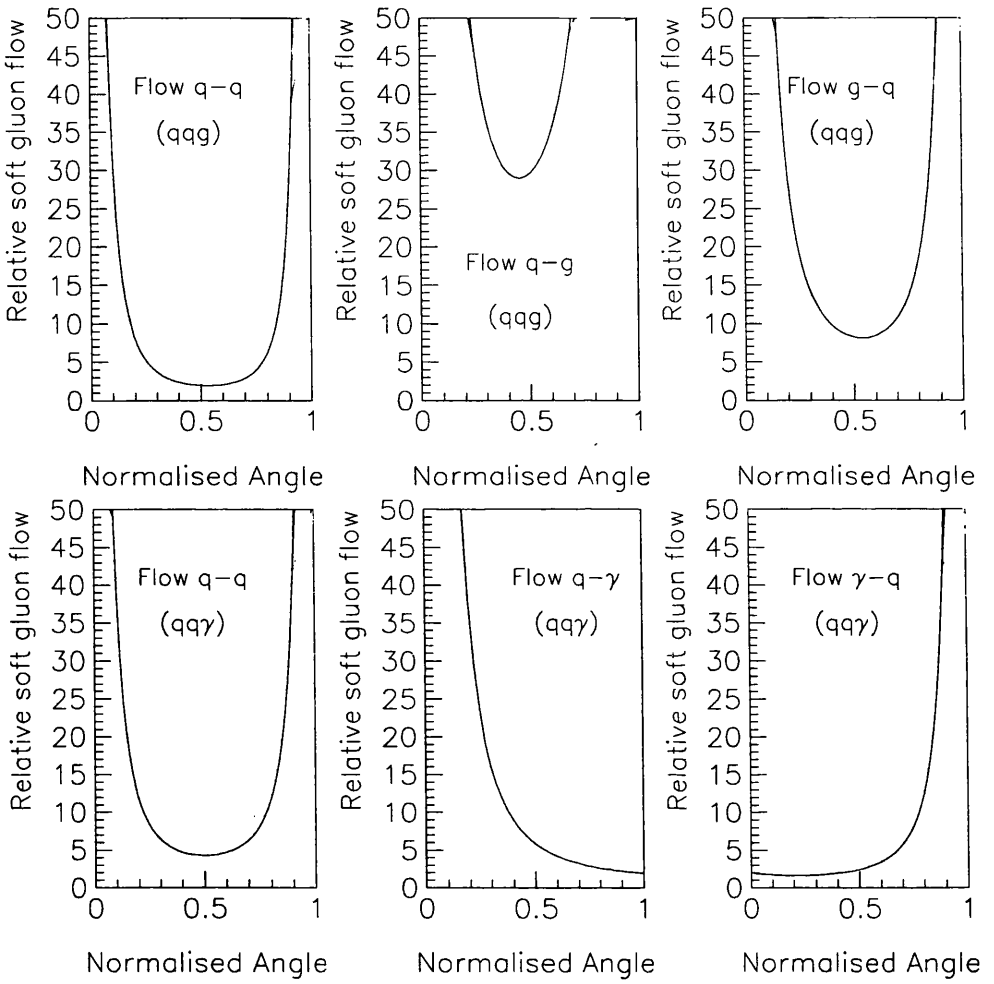

Figure 6.8: *Predicted soft gluon flow between the partons as a function of the normalised angle between the partons. In this calculation the angles* $q - \overline{q}$ *and* $q - g$ *(or* $q - \gamma$*) were set to* 153° *and* 130°. *Singularities occur in the direction of the partons, so the prediction is only valid between the partons.*

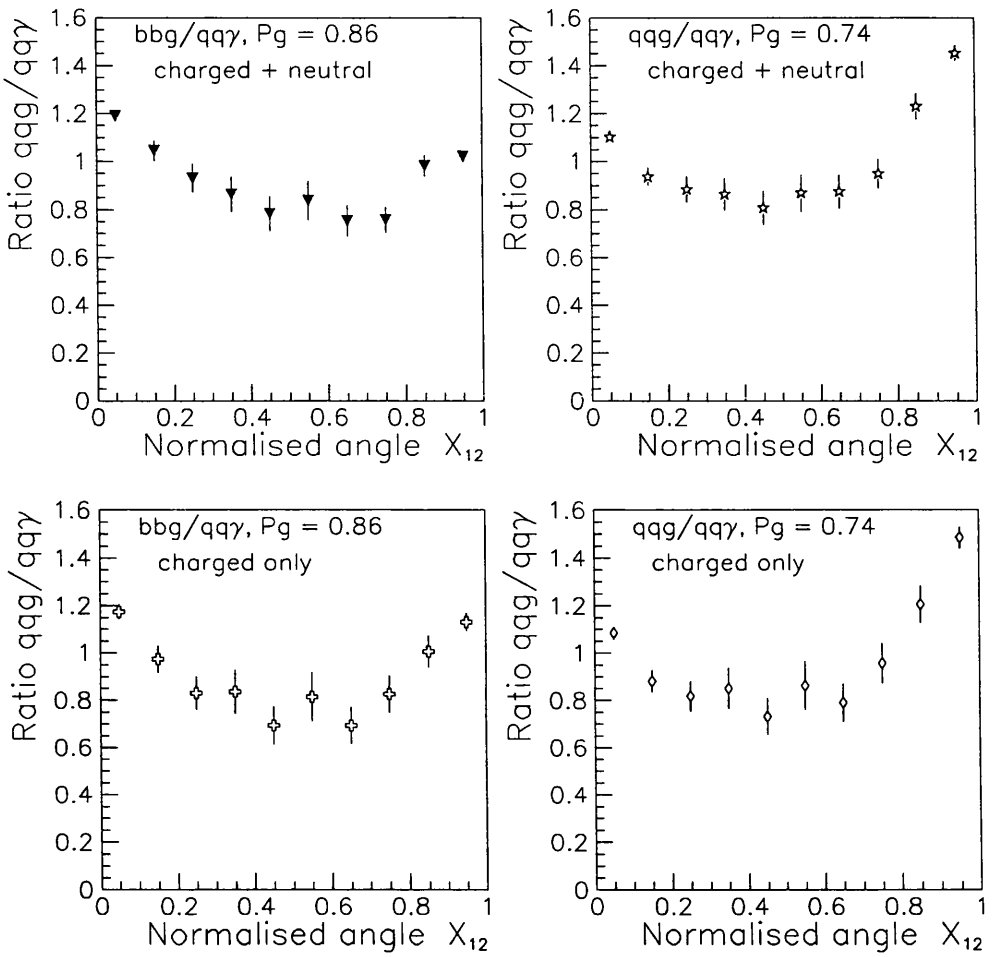

Figure 6.9: *Measured $q\bar{q}g/q\bar{q}\gamma$ ratio of the particle flow between the q and $\bar{q}$ using the $q\bar{q}g$, $b\bar{b}g$ and $q\bar{q}\gamma$ samples from the ALEPH data. The ratio is given as a function of the normalised angle between the q and $\bar{q}$ for all particles, and for charged particles only.*

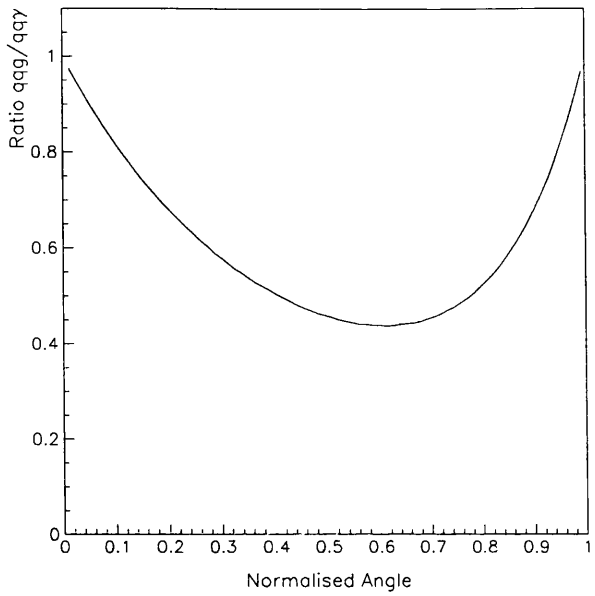

Figure 6.10: *Predicted $q\overline{q}g/q\overline{q}\gamma$ ratio of the soft gluon flow between the q and $\overline{q}$. The ratio is given as a function of the normalised angle between the q and $\overline{q}$. In this calculation the angles $q-\overline{q}$ and $q-g$ (or $q-\gamma$) were set to* 153° *and* 130°.

to be the lowest energy jet, so that the two event types had a similar range of kinematic properties.

- The purity of the tagged quark and gluon jets and the photon jet were estimated from Monte Carlo events.

- The $q\overline{q}g/q\overline{q}\gamma$ ratio of the particle flow between the quark jets was determined as a function of the normalised angle $X_{q\overline{q}}$. TPC-2γ and MARK-II measured the charged particle flow whereas JADE measured the flow of all particles.

A comparison of these measurements is given in [53]. The $q\overline{q}g/q\overline{q}\gamma$ ratio of the particle flows is shown in Figure 6.11. Halfway between the quark jets, the ratio from the three experiments is ~0.1-0.2 below the results from the ALEPH data. The mean value of the two data points closest to the bisecting angle of the q and $\overline{q}$ was determined for each measurement. This mean ratio is plotted in Figure 6.12 as a function of the centre of mass energy. The results using the ALEPH data lie 1-2 standard deviations above the measurements at lower $\sqrt{s}$,

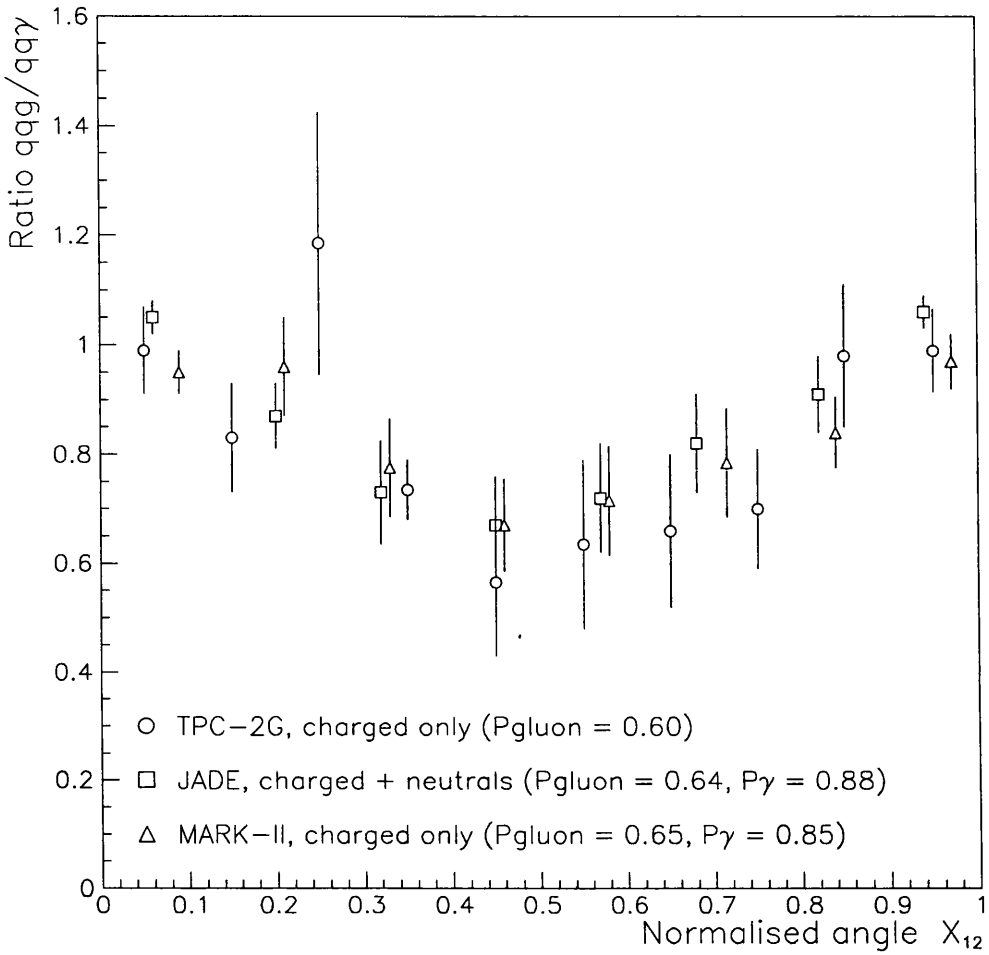

Figure 6.11: *Measured $q\bar{q}g/q\bar{q}\gamma$ ratio of the particle flow between the q and $\bar{q}$ for the different measurements at lower $\sqrt{s}$. The ratio is given as a function of the normalised angle between the q and $\bar{q}$.*

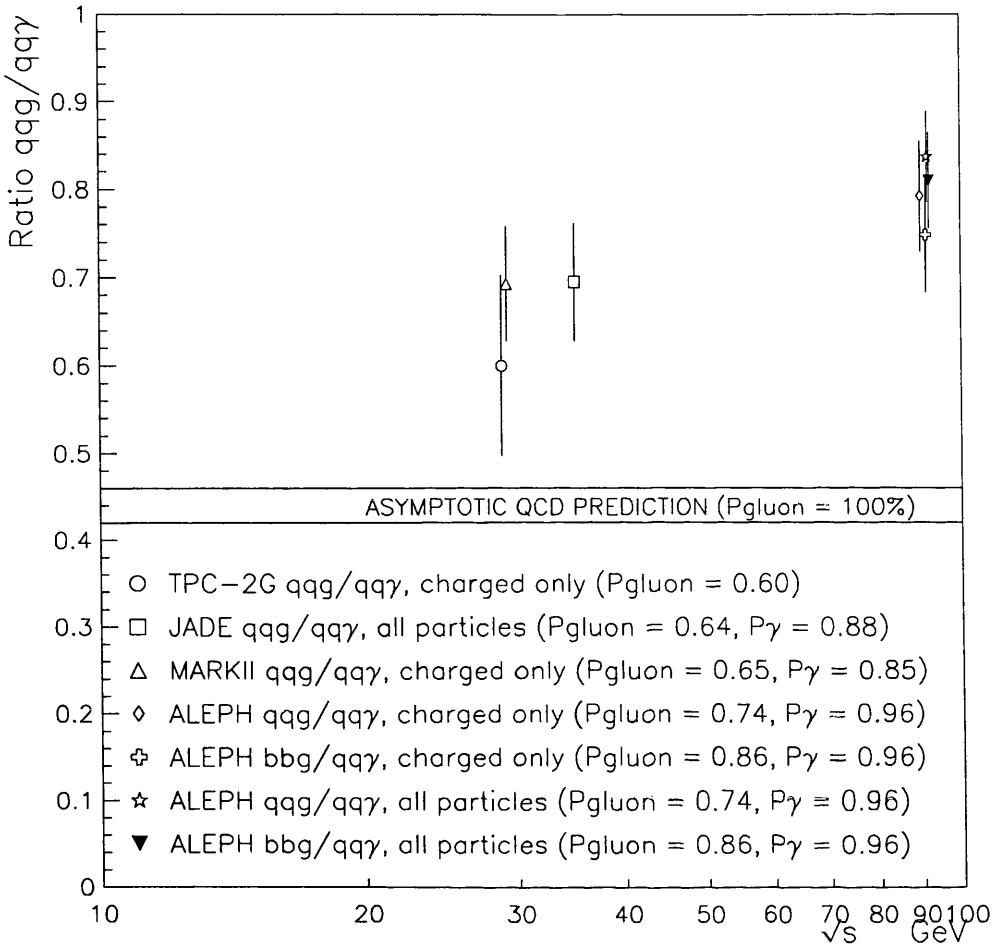

Figure 6.12: *Mean value of the $q\bar{q}g/q\bar{q}\gamma$ ratio of the particle flow between the q and $\bar{q}$ for different measurements. The QCD prediction depends on the exact opening angles of the jets, so a range of values is given.*

and the earlier measurements are 1.5-3.5 standard deviations above the predicted ratio from the soft gluon calculation.

In all the analyses there is a certain amount of quark and gluon jet misidentification, but more so in the lower $\sqrt{s}$ event samples. A greater particle flow is expected, and measured [24], in the region between each quark jet and

the gluon jet compared to the region between the quark jets. Any quark and gluon mis-identification in the $q\bar{q}g$ events will shift the measured ratio above the true ratio by an amount dependent on the level of wrongly-tagged jets. At lower $\sqrt{s}$ the gluon-tagged jets in the $q\bar{q}g$ events were estimated to have 60-65% gluon purity, so the true ratio may lie significantly below the measured values. The gluon-tagged jets in the $q\bar{q}g$ and $b\bar{b}g$ from the ALEPH data have higher estimated purity of 74% and 86% respectively. In these events the true ratios will be lower than the measured ratios, but much closer to the measured values than the previous analyses. The true ratio at lower $\sqrt{s}$ will be closer to the theoretical value, compared to the true ratio at $\sqrt{s} = 91$ GeV.

The π^0 background in the photon jets will also cause systematic shifts in the measured ratios, but the effect is uncertain. If these π^0 come from a quark at parton level, then some of the particle flow in the denominator will come from between quark and gluon jets in a $q\bar{q}g$ event. This may give a lower measured value, i.e. acting against the previous systematic effect. If the π^0 background comes from a gluon at parton level, then a higher measured value than the true ratio would result.

In an attempt to quantify the systematic effects of jet mis-identification, the soft gluon prediction was used to calculate the particle flow ratio for $q\bar{q}g$ and $q\bar{q}\gamma$ event samples with a similar proportion of mis-identified jets as are estimated in the data. In one instance, the π^0 background in the $q\bar{q}\gamma$ events was ignored. The calculation was repeated with the assumptions that the π^0 background was from a quark or from a gluon in a $q\bar{q}g$ event. These calculations are compared with the measured values in Table 6.2. The measured ratios from the ALEPH data lie significantly above the theoretical calculation. The ratios for charged particles are 2.5-3 standard deviations from the QCD prediction and the charged and neutral ratios are over 4 standard deviations from the theoretical prediction. The measured values from lower $\sqrt{s}$ data lie 0.5-3 standard deviations below the theoretical predictions. The purity correction to the QCD prediction is larger here, so the uncertainty in the corrected predictions is greater. The measured ratios at lower $\sqrt{s}$ are either compatible with or below the QCD predictions. The ratios predicted by JETSET for the ALEPH data lie 2 standard deviations above the ratios measured in the data.

6.5 Summary and conclusions.

The particle flow between the quark jets has been measured in energy-ordered $q\bar{q}g$ events, lepton-tagged $b\bar{b}g$ events and $q\bar{q}\gamma$ events. The $q\bar{q}g/q\bar{q}\gamma$ and $b\bar{b}g/q\bar{q}\gamma$ ratios of the particle flow between the q and $\bar{q}$ were determined and compared

Event samples	*Measured ratio*	*JETSET ratio*	*Ratio(A)*	*Ratio(B)*	*Ratio(C)*	*Ratio(D)*
TPC-2γ *(charged)*	0.60 $\pm$ 0.10	-	0.46	0.80	0.77	0.87
MARK-II *(charged)*	0.69 $\pm$ 0.07	-	0.46	0.76	0.73	0.83
JADE *(ch + neu)*	0.70 $\pm$ 0.07	-	0.44	0.74	0.71	0.79
ALEPH $b\bar{b}g/q\bar{q}\gamma$ *(charged)*	0.79 $\pm$ 0.06	0.97 $\pm$ 0.11	0.41	0.60	0.60	0.61
ALEPH $b\bar{b}g/q\bar{q}\gamma$ *(ch + neu)*	0.84 $\pm$ 0.05	0.93 $\pm$ 0.09	0.41	0.60	0.60	0.61
ALEPH $q\bar{q}g/q\bar{q}\gamma$ *(charged)*	0.75 $\pm$ 0.07	1.03 $\pm$ 0.11	0.45	0.57	0.56	0.58
ALEPH $q\bar{q}g/q\bar{q}\gamma$ *(ch + neu)*	0.81 $\pm$ 0.06	1.02 $\pm$ 0.11	0.45	0.57	0.56	0.58

Table 6.2: *Comparison of the measured particle flow ratios with the JETSET prediction and the asymptotic prediction for the soft gluon flow with the same parton opening angles as the mean jet opening angles. Four QCD predictions are shown; ratio(A) has no correction for the purity; ratio(B) has the same estimated level of background as the measured $q\bar{q}g$ or $b\bar{b}g$ events; ratio(C) also has the assumption that the π^0 background in the $q\bar{q}\gamma$ events comes from a gluon in a $q\bar{q}g$ event; ratio(D) has the assumption that the π^0 background in the $q\bar{q}\gamma$ events comes from a quark in a $q\bar{q}g$ event.*

with previous measurements at lower $\sqrt{s}$ and to the asymptotic QCD predictions. The measured ratios at $\sqrt{s} = 91.2$ GeV lie closer to 1 compared to the lower $\sqrt{s}$ results and significantly above the asymptotic QCD prediction.

None of the experimental measurements have been corrected for any systematic detector effects. The charged tracks in the ALEPH data have a minimum momentum of 200 MeV/c, whereas the asymptotic prediction has no cut-off energy for the gluons. Nevertheless, the ratio of the particle flow is insensitive to detector effects, particularly in the case of charged particles.

The prediction does not describe the data at $\sqrt{s} = 91.2$ as well as the data at $\sqrt{s} = 29$-35 GeV. The prediction assumes the soft gluons have a sufficiently large wavelength that they are not affected by the hard processes in the event. The final calculation does not involve the energies of the partons, only their opening angles. From the data it would appear that the relative particle flow does depend on the energy of the partons.

The JETSET predictions for the particle flow ratios in the samples lie 2 standard deviations above the measured values. The rate of $q\bar{q}\gamma$ events predicted by JETSET is lower than in the data. This may have an effect on the predicted particle flow in the simulated $q\bar{q}\gamma$ events. The JETSET prediction of the particle flow in $q\bar{q}g$ and $b\bar{b}g$ events closely matched the particle flow in the data. However the particle flow in $q\bar{q}\gamma$ events was modelled reasonably well by JETSET. The difference between the JETSET prediction and the data may be due to the low $q\bar{q}\gamma$ statistics. More data is required to check whether there is any significant difference between the data and the JETSET prediction.

Chapter 7

Conclusions.

7.1 Introduction

A study of quark and gluon jets in three-jet events was made which is described in Chapter 5. An analysis also has been made of the particle flow in $q\bar{q}g$ and $q\bar{q}\gamma$ events and is described in Chapter 6. The main results of these two studies are summarised in the following section. Conclusions are made in Section 7.3 about the success or otherwise of perturbative QCD in describing the properties of quark and gluon jets and the features of three-jet events. Finally recommendations for further experimental and theoretical study are given in Section 7.4.

7.2 Summary of results

The main results of this thesis are listed here. Detailed discussion of the results can be found in the particular sections, figures and tables that are cross-referenced. The variation in the jet properties with energy is described for the range 12.5-37.5 GeV.

7.2.1 Quark and gluon jet properties

- Mean jet multiplicities

  An approximately logarithmic increase in the quark and gluon jet multiplicities with jet energy was measured for all particles, for charged particles only and for neutral particles only (Section 5.5.1, Figures 5.17a, 5.18a, 5.19a and Table 5.1). The multiplicity of the event was seen to depend on the topology of the event (Section 5.6.1 and Table 5.4).

- Gluon/quark jet multiplicity ratio

A jet multiplicity ratio for all particles of 1.22-1.3 was measured, which was approximately constant with jet energy (Section 5.5.1, Figure 5.17b). The charged multiplicity ratio appears to decrease with jet energy from ~1.6 at 12.5 GeV to 1.3 at 37.5 GeV (Figure 5.18b), but a constant variation in the ratio cannot be ruled out statistically (Table 5.3). The neutral multiplicity ratio is constant or increases with jet energy and lies in the range 1.15-1.25 (Figure 5.19b). The ratios appear to depend on whether the quark jet comes from a $q\bar{q}g$ or a $q\bar{q}\gamma$ event.

- Charged/neutral multiplicity ratio

  The measured charged/neutral multiplicity ratio for gluon jets decreases with energy from 1.2-1.05 (Figure 5.20). The ratio for quark jets increases with jet energy from ~0.9-1.0.

- Mean p_t of particles in jet

  The mean p_t of particles increases slightly with the jet energy (Section 5.5.2, Figure 5.21). The gluon/quark jet p_t ratio appears to decrease slightly with jet energy from 1.1-1.0 for all particles (Figure 5.22). However the ratio is approximately constant with energy for all particles.

- Mean rapidity of particles to jet axis

  The measured mean rapidity of particles in a jet increases approximately logarithmically with the energy of the jet (Section 5.5.3, Figure 5.23). The gluon/quark jet ratio of particle rapidity is approximately constant with jet energy with a value of 0.85-0.9 (Figure 5.24). The mean rapidity of the energy flow in a jet increases with the energy of the jet (Figure 5.25). The gluon/quark jet rapidity ratio for the energy flow is approximately constant with energy at ~0.85 (Figure 5.26).

- Mean fragmentation function of jet

  A decrease in the mean fragmentation function with jet energy was seen (Section 5.5.4, Figure 5.27). The gluon/quark jet fragmentation function ratio is approximately constant with jet energy at ~0.8 for all particles and ~0.75 for charged particles (Figure 5.28).

- Jet core width

  The measured jet core width decreases with the energy of the jet (Section5.5.5, Figure 5.29). The gluon/quark jet core width ratio is approximately constant with jet energy, but increases with decreasing core size from ~1.25 for the 90% cores to ~1.7 for the 25% cores (Figure 5.30, Table 5.2).

- Gluon/quark core multiplicity ratio

  The multiplicity ratio for all particles in the jet cores is approximately constant with jet energy, but increases for decreasing core size from ~1.25 for the 90% cores to ~1.4 for the 50% cores (Section 5.5.6, Figure 5.31). The charged multiplicity ratios in the jet cores show a slight decrease with increasing jet energy, but the ratio is significantly higher in narrow jet cores (Figure 5.32, Table 5.3). For the jet cores containing 25% of the jet energy, the charged multiplicity ratio is ~1.8 for 12.5 GeV jets. This measured ratio is ~1 standard deviation from the perturbative prediction (Section 2.5.1).

None of the distributions were corrected for the effects of the detector on the measurements. The charged particle and energy flow measurements will be less affected by the detector than measurements involving the neutral particles. The detector corrections to the gluon/quark jet ratios of each measurement will be second-order effects.

7.2.2 Measurement of the "string effect".

- Ratio of the particle flow $q\bar{q}g/q\bar{q}\gamma$

  The $q\bar{q}g/q\bar{q}\gamma$ ratio of the particle flow between the quark jets in ALEPH data is significantly higher than the soft gluon prediction (Section 6.4, Table 6.2). The measured ratios at lower $\sqrt{s}$ are either compatible with or below the soft gluon prediction. The JETSET Monte Carlo gives a good representation of the particle flow in three-jet events in ALEPH data and the previous measurements at lower $\sqrt{s}$.

7.3 Conclusions

The results of the jet study show that jet multiplicities increase approximately logarithmically with jet energies, jets become more narrow at higher energies and have a softer fragmentation function. Comparing quark and gluon jets, gluon jets have higher multiplicity, wider jet cores and a softer fragmentation function. These statements agree with the previous results described in Section 2.5 and with theoretical understanding of quark and gluon fragmentation.

The results show that the gluon/quark jet ratio of the multiplicities is not constant, since the ratio depends on what partons were present after the Z^0 decay and the energies and angles of these partons. Nevertheless, the measured gluon/quark jet multiplicity ratios for the whole jets are considerably lower than the perturbative prediction (Section 2.5.1), and the charged multiplicity ratios

may actually decrease with increasing energy. This does not mean that the theoretical prediction is wrong. The calculation predicts the relative numbers of gluons emitted from partonic quarks and gluons and does not relate to the hadronisation stage of jet formation. The calculation also uses a fixed parton topology, so the interference effects from the other partons in the event are liable to be incorrect for the topologies measured. Furthermore, the calculation has no jet algorithm dependence, which may not be true for the soft particles at wide angles to the jets.

Perturbative QCD might be expected to describe better quark and gluon jet properties in the core of the jets, rather than for the whole jet, since hadronisation effects, interference from other partons and jet clustering systematics are likely to be less here. The results suggest this is the case, since the gluon/quark ratio of the multiplicities is higher in the core of the jets and closer to the perturbative prediction. Indeed for a narrow jet core inside 12.5 GeV jets, the measured charged multiplicity ratio is close to the perturbative prediction.

The measured charged multiplicity results suggest that the gluon/quark multiplicity ratio may decrease with energy, although an energy independent ratio cannot be ruled out statistically in the data. A decreasing ratio with jet energy might seem rather surprising, since higher energy quarks and gluons have more energy available for radiation of partons. The gluon/quark multiplicity ratio therefore is expected to increase towards the perturbative prediction at higher jet energies. A number of suggestions why this may not be the case are given below.

- It is possible that applying a jet algorithm to identify three-jet events and selecting high energy jets, favours those jets where comparatively less gluon radiation occurs in the core of gluon jets relative to quark jets. A significant fraction of the gluons radiated from a high energy gluon might be clustered into the q or $\overline{q}$ jets, causing the gluon/quark multiplicity ratio to be lower.

- The perturbative calculation of the multiplicity ratio is determined for a fixed parton topology. The interference effects from the other partons in the three-jet topologies measured might cause the multiplicity ratio to be energy dependendent.

- Two types of singularities commonly occur in QCD calculation from collinear gluon emission and infrared gluon emission. Is is possible that the treatment of one or both of these singularities in the perturbative prediction is not entirely satisfactory and leads to a failure in the calculation to fully describe the higher energy jets.

- There is also the possibility that a significant part of the jet multiplicity is a function of non-perturbative QCD, which is less well understood.

The study of particle flow in $q\bar{q}g$ and $q\bar{q}\gamma$ events indicates that the soft gluon prediction for the particle flow describes the particle flow ratio between the q and $\bar{q}$ significantly less well at $\sqrt{s} = 91$ GeV compared to $\sqrt{s} = 29 - 35$ GeV. For the soft gluon approximation, the calculation of the relative particle flow depends on the angles between the partons and has no dependence on the parton energies. This perhaps suggests that the soft gluon calculation is not completely correct, perhaps ignoring some factor dependent on the parton energies. Alternatively there is some non-perturbative mechanism which plays an important role in the inter-jet particle flow.

7.4 Further work

A number of suggestions for further work are listed below which might improve the measurement and understanding of quark and gluon jets and the "string effect". One motivation for this work is that hadronisation models are being used to predict the properties of higher $\sqrt{s}$ events at future colliders. The design of the detectors and the predicted physics are thus dependent on the ability of hadronisation models to predict fragmentation. A second motivating factor is that future searches for the Higgs boson will involve looking for its decay channel into b-jets from a background of hadronic jets. The ability to analyse these events will be greatly enhanced by the knowledge of jet fragmentation.

7.4.1 Quark/gluon jet studies

- The number of events in the lepton-tagged $b\bar{b}g$ and particularly the $q\bar{q}\gamma$ event samples used in the jet comparison was not large (see Table 4.3). If the ALEPH data from 1993 and 1994 is included in the study, this will increase the number of hadronic events by at least a factor of 2, giving greater statistical significance to the results.

- The differences between light quark jets and heavy quark jets was mostly ignored in this analysis. Instead of unfolding just quark and gluon jets, the b-jets could be unfolded separately from $udsc$-jets. B-jet samples could be obtained by lepton-tagging the leading jet in the three-jet events. The two lower energy jets in these tagged events will contain a mixture of gluon jets and mostly b-jets at various energies. Three samples containing mostly gluon jets, mostly b-jets and mostly $udsc$-jets could then be unfolded to obtain the gluon jet, b-jet and $udsc$-jet properties over the whole energy range.

- It would be desirable to attempt to compare the properties of low energy quark jets from $q\bar{q}\gamma$ events and $q\bar{q}g$ events separately, since low energy quark jets in the $q\bar{q}g$ are likely to be influenced by the hard gluon in the event. To unfold the properties of low energy quark jets in $q\bar{q}g$ events would require more detailed work on the unfolding process (see previous item).

- An additional source of gluon jets and b-jets can be obtained using vertex-tagging instead of lepton-tagging. It is desirable to obtain these extra samples as a cross-check of the unfolding procedure, the estimation of purities from Monte Carlo events and any biases introduce by the b-tagging method.

- An additional source of high-energy quark jets are available by using the two-jet events at $y_{cut} = 0.01$. By applying a b-tag to one of the jets in the event, samples of uds-jets, c-jets and b-jets could be obtained with high statistics.

- The effect of topology on the jet properties should be studied. Instead of defining jet sub-samples by energy, the sub-samples could be prepared by selecting events with specific opening angles. Different sub-samples containing various symmetric and asymmetric events could be analysed. If a small range of opening angles in each sub-sample is specified, then the jets in each sub-sample also will have a small energy range.

- The experimental results for the jet properties should be compared to the predictions from the various Monte Carlo models available. Mote Carlo events at hadron level with and without the detector simulation could be used to correct the data for detector effects. The corrected data could then be compared directly to Monte Carlo simulated jets which have been identified at parton level. It is important to check whether the models reproduce the data, since these simulate both perturbative and non-perturbative effects.

- The results in this analysis show that the gluon/quark jet multiplicity is closer to the perturbative prediction in the jet cores. It would be useful to check the ratio of the p_t and the fragmentation function in the jet cores to see whether there are more differences in the cores.

- The three-dimensional particle and energy flow in jets could be measured. The jets in two-jet events will have a circular particle flow profile, but the jets in three-jet events are thought to be asymmetric with an oval particle flow profile.

- The present and future data at LEP will give a clear picture of the properties of quark and gluon jets. More theoretical input would be useful, particularly further perturbative calculations of the jet properties as a function of energy (or scale).

7.4.2 "String effect" studies.

- The study of particle flow in three-jet events also would benefit from more statistics to increase the significance of the results. It would also be useful to separate different symmetric topologies in the same way as the OPAL study [24] and apply the soft gluon calculation to these specific topologies.

- The particle flow data should be corrected for detector effects, again using the Monte Carlo events. The data could then be compared to all the Monte Carlo models available to see which models provide the best description. .

- The particle flow between the q and $\overline{q}$ jets should be compared to the particle flow between between the q (or $\overline{q}$) and g. For "Mercedes" events the $q - g/q - \overline{q}$ ratio is predicted to be 22/7.

- The particle flow could be measured for separate hadron species and for particles with low and high transverse momentum to the event plane in the same manner as the JADE studies [23, 39]. Different ratios have been obtain previously for these measurements and these provide additional tests for the Monte Carlo models.

- In the near future the number of hadronic events available at LEP may be enough to study the inter-jet particle flow in four-jet events. In these events the string in the string fragmentation models can have several different configurations, so the perturbative and non-perturbative contributions to the particle flow may be more apparent.

Bibliography

[1] R. P. Feynman, *Space-Time Approach to Non-relativistic Quantum Mechanics, Rev. Mod. Phys.* **20** (1948) 367.
J. Schwinger, *Quantum Electrodynamics. I. A Covariant Formulation*, Phys. Rev. **74** (1948) 1439.
F.J. Dyson, *The Radiation Theories of Tomonaga, Schwinger and Feynman*, Phys. Rev. **75** (1949) 486.

[2] S. L. Glashow, *Partial-Symmetries of WeakInteractions, Nucl. Phys.* **22** (1961) 579.
A. Salam, *Elementary Particle Theory, Proc. 8th Nobel Symposium*, ed. N. Svartholm, Almquist and Wiksell, Stockholm, (1968).
S. Weinberg, *A Model of Leptons*, Phys. Rev. Lett. **19** (1967) 1264.

[3] D. Gross, F. Wilczek, *Phys. Rev. Lett.* **30** (1973) 1343.
S. Weinberg, *Phys. Rev. Lett.* **31** (1973) 494.
H. Fritzsch, M. Gell-Mann, H. Leutwyler, Phys. Lett. **B47** (1973) 365.
F. J. Indurain, *Quantum Chromodynamics: an Introduction to the Theory of Quarks and Gluons*, (Springer, New York, 1983).

[4] ALEPH Collab. D. Decamp et al., *Phys. Lett.* **B284** (1992) 151-162.
DELPHI Collab. P. Abreu et al., *Phys. Lett.* **B255** (1991) 466.
OPAL Collab. M.Z. Akrawy et al., *Z. Phys.* **C49** (1991) 49.

[5] LEP, *Large Electron Positron Storage Ring. Technical Notebook*, CERN Publications (1989).

[6] JADE Collab., W. Bartel et al., *Z. Phys.*, **C33** (1986) 23.
JADE Collab., S. Bethke et al., *Phys. Lett.* ,**B213** (1988) 235.

[7] ALEPH Collab., D. Buskulic et al., *Z. Phys.*, **C55** (1992) 209.

[8] G. Kramer, B. Lampe, *Z. Phys.*, **C39** (1988) 101.
G. Kramer, B. Lampe, *Z. Phys.*, **C37** (1989) 161.

[9] OPAL Collab., M. Z. Akrawy et al., *Phys. Lett.* **B235** (1990) 389.
DELPHI Collab., P. Abreu et al., *Phys. Lett.* **B247** (1990) 167.

[10] S. Catani, Yu.L. Dokshitzer, M. Olsson, G. Turnock, B.R. Webber, *Phys. Lett.* **B269** (1991) 432.
Durham Workshop, W.J. Stirling, *J. Phys.* G: *Nucl. Part. Phys.* **17** (1991) 1567.
N. Brown, W. J. Stirling, RAL preprint 91-049 (1991)
S. Bethke, Z. Kunszt, D.E. Soper, W.J. Stirling, CERN TH.6221/91 (1991)

[11] ALEPH Collab., D. Decamp et al., *Phys. Lett* **B284** (1992) 163.

[12] ALEPH Collab., D. Buskulic et al., *Phys. Lett***B307** (1993) 209.
ALEPH Collab., D. Buskulic et al., *Z. Phys.* **C60** (1993) 71.
ALEPH Collab., D. Decamp et al., *Phys. Lett* **B255** (1991) 623. ALEPH Collab., D. Decamp et al., *Phys. Lett* **B257** (1991) 479.

[13] R. Field, R.P Feynman, *Nucl. Phys.* **B136** (1978) 1.

[14] P. Hoyer, P. Osland, H.G.. Sander, T.F. Walsh, P.M. Zerwas, *Nucl. Phys.* **B161** (1979) 349.

[15] A. Ali, E. Pietarinen, G. Kramer, J. Willrodt, *Phys. Lett.* **B93** (1980) 155.

[16] G.C. Fox, S. Wolfram, *Nucl. Phys.* **B168** (1980) 285.

[17] R.D. Field, S. Wolfram, *Nucl. Phys.* **B213** (1983) 65.

[18] T.D. Gottschalk, *Nucl. Phys.* **B214** (1983) 201.

[19] R. Oderico, *Comp. Phys. Comm.* **32** (1984) 139; *Comp. Phys. Comm.* **59** (1990) 527.

[20] B.R. Webber, *Nucl. Phys.* **B238** (1984) 492.
G. Marchesini et al, *HERWIG Version 5.1, Comp. Phys. Comm.* **67** (1992) 465.

[21] T. Sjöstrand, *Pythia 5.6 and JETSET 7.3 Physics and Manual*, CERN-TH.6488/92.

[22] Ya. I. Azimov, Yu. L. Dokshitzer, V. A. Khoze, S. L. Troyan, *Phys. Lett.* **B165** (1985) 147.
Ya. I. Azimov, Yu. L. Dokshitzer, V. A. Khoze, S. L. Troyan, *Z. Phys.* **C44** (1985) 65.
B. Andersson, P. Dahlquist, G. Gustafson, *Z. Phys.* C44 (1989) 455, 461.

Yu. L. Dokshitzer, V. A. Khoze, A. H. Mueller, S. L. Troyan, *Basics of Perturbative* QCD, Editions Frontieres.

[23] JADE Collab., W. Bartel et al., *Phys. Lett.*, **B157** (1985) 340.

[24] OPAL Collab., M.Z. Akrawy et al., *Phys. Lett.* **B261** (1991) 334.

[25] E.L.Berger, X. Guo, J. Qiu, CERN-TH.6745/92.
G. Kramer, H. Spiesberger, *Workshop on photon radiation from quarks*, ed. S. Cartwright, CERN 92-04 (1992) 26.

[26] ALEPH Collab., D. Decamp et al., *Phys. Lett* **B264** (1991) 476.
ALEPH Collab., D. Buskulic et al., *Z. Phys.* **C57** (1993) 17.

[27] L3 Collab., G. Adriani et al., *Phys. Lett.* **B292** (1992) 472.

[28] OPAL Collab., M.Z. Akrawy et al., *Phys. Lett.* **B246** (1990) 285.
OPAL Collab., P.D. Acton et al., *Z. Phys.* **C54** (1992) 193.

[29] S.L. Wu, *Phys. Reports: e^+e^- physics at PETRA - the first five years.* **107** (1984) 127

[30] A.H. Mueller, *Nucl. Phys.* **B241** (1984) 141.

[31] JADE Collab., W. Bartel et al., *Z. Phys.* **C21** (1983) 37.

[32] HRS Collab., M. Derrick et al., *Phys. Lett* **B165** (1985) 449.

[33] MARK II Collab., A. Petersen et al., *Phys. Rev. Lett.* **55** (1985) 1954.

[34] TASSO Collab., W. Braunschweig et al., *Z. Phys.* **C45** (1989) 1.

[35] AMY Collab., Y.K. Kim et al., *Phys. Rev. Lett.* **63** (1989) 1772.

[36] H. Takaki et al., *Phys. Rev. Lett.* **71** (1993) 38.

[37] OPAL Collab., G. Alexander et al., *Phys. Lett* **B265** (1991) 462.

[38] OPAL Collab., P. D. Acton et al., *Z. Phys.* **C58** (1993) 387.

[39] JADE Collab., W. Bartel et al., *Phys. Lett* **B101** (1981) 129.
JADE Collab., W. Bartel et al., *Phys. Lett* **B134** (1984) 275.

[40] TPC Collab., H. Aihara et al., *Z. Phys.* **C28** (1985) 31.

[41] TASSO Collab., M. Althoff et al., *Z. Phys.* **C29** (1985) 29.

[42] TPC Collab., H. Aihara et al., *Phys. Rev. Lett.* **57** (1986) 945.

[43] MARK II Collab., P. Sheldon et al., *Phys. Rev. Lett.* **57** (1986) 1398.

[44] JADE Collab., W. Bartel et al., *Z. Phys.* **C39** (1988) 1.

[45] ALEPH Collaboration, The ALEPH handbook 1989, ALEPH 89-77.

[46] ALEPH Collaboration, D. Decamp et al, *Nucl. Instr. Meth.* **A294** (1990) 121.

[47] ALEPH Collaboration, D. Buskulic et al, CERN-PPE/94-023.

[48] T.Sjostrand, *QCD generators*, in : Z Physics at LEP 1, eds G. Altarelli, R. Kleiss and C. Verzegnassi, CERN Report 89-08 Vol 3.

[49] ALEPH Collab., D. Decamp et al., *Phys. Lett* **B244** (1990) 551.
ALEPH Collab., D. Decamp et al., *Phys. Lett* **B258** (1991) 236.
ALEPH Collab., D. Decamp et al., *Phys. Lett* **B278** (1992) 209.
ALEPH Collab., D. Decamp et al., *Phys. Lett* **B284** (1992) 177.
ALEPH Collab., D. Buskulic et al., *Phys. Lett* **B307** (1993) 194.
ALEPH Collab., D. Buskulic et al., *Phys. Lett* **B313** (1993) 498.

[50] V. Bertin, M.G. Smith, A.S. Thompson, J.C. Thompson, *A measurement of the quark to photon fragmentation function at LEP*, ALEPH 94-085, PHYSIC 94-073.

[51] Z. Kunszt and P. Nason, *QCD*, in : Z Physics at LEP 1, eds G. Altarelli, R. Kleiss and C. Verzegnassi, CERN Report 89-08 Vol 1.

[52] Ph. Ghez, W. Maitland, Ph. Odier, *Gluon Jet Identification in 3-jet Monte Carlo Events*, ALEPH 93-104, PHYSIC 93-085.

[53] T. Sjöstrand, *Int. J. Mod. Phys.* **3** (1988) 751-823.

Appendix A

Properties of the jet sub-samples.

Examples of the measured jet distributions from the gluon jet and lower-energy quark jet sub-samples are shown in this appendix. The figures are normalised by the total number of events in the sample multiplied by the bin width. A description of the measurements is given in Section 5.3.

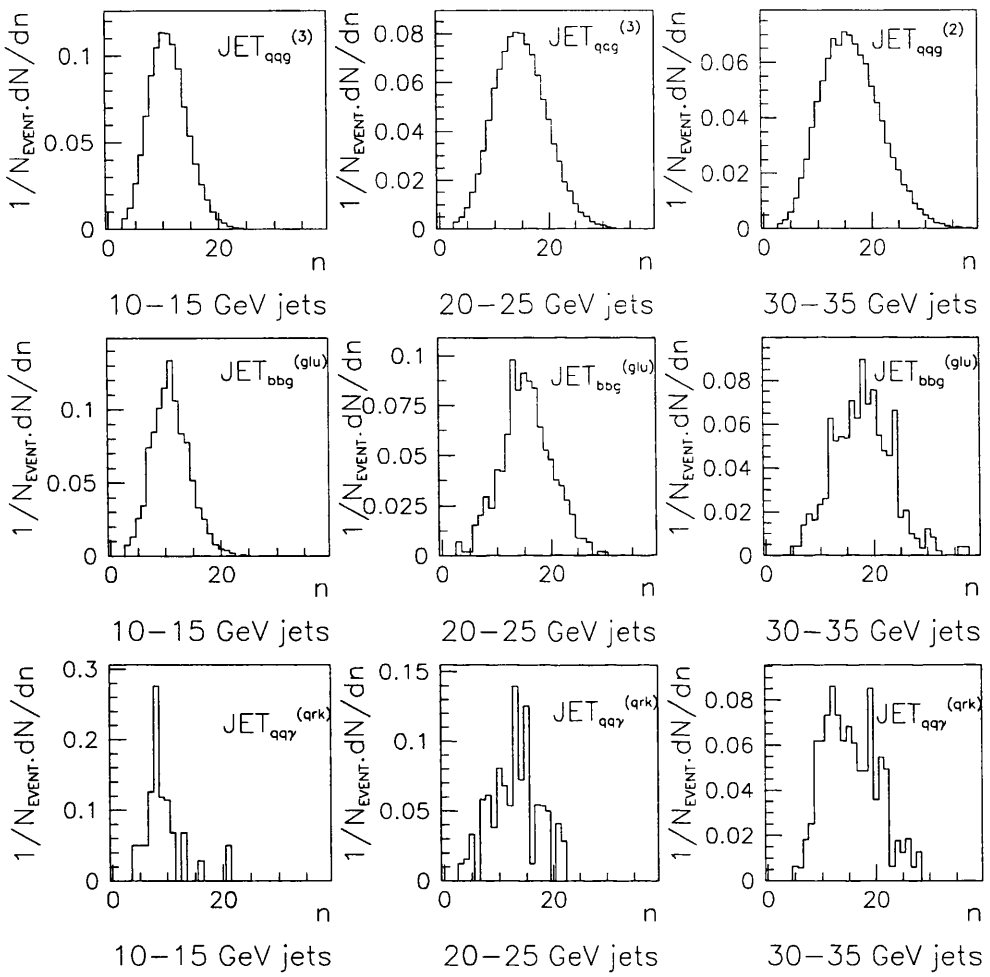

Figure A.1: *The multiplicity of charged and neutral particles in the gluon jet and lower-energy quark jet sub-samples. Three different jet energy ranges are given.*

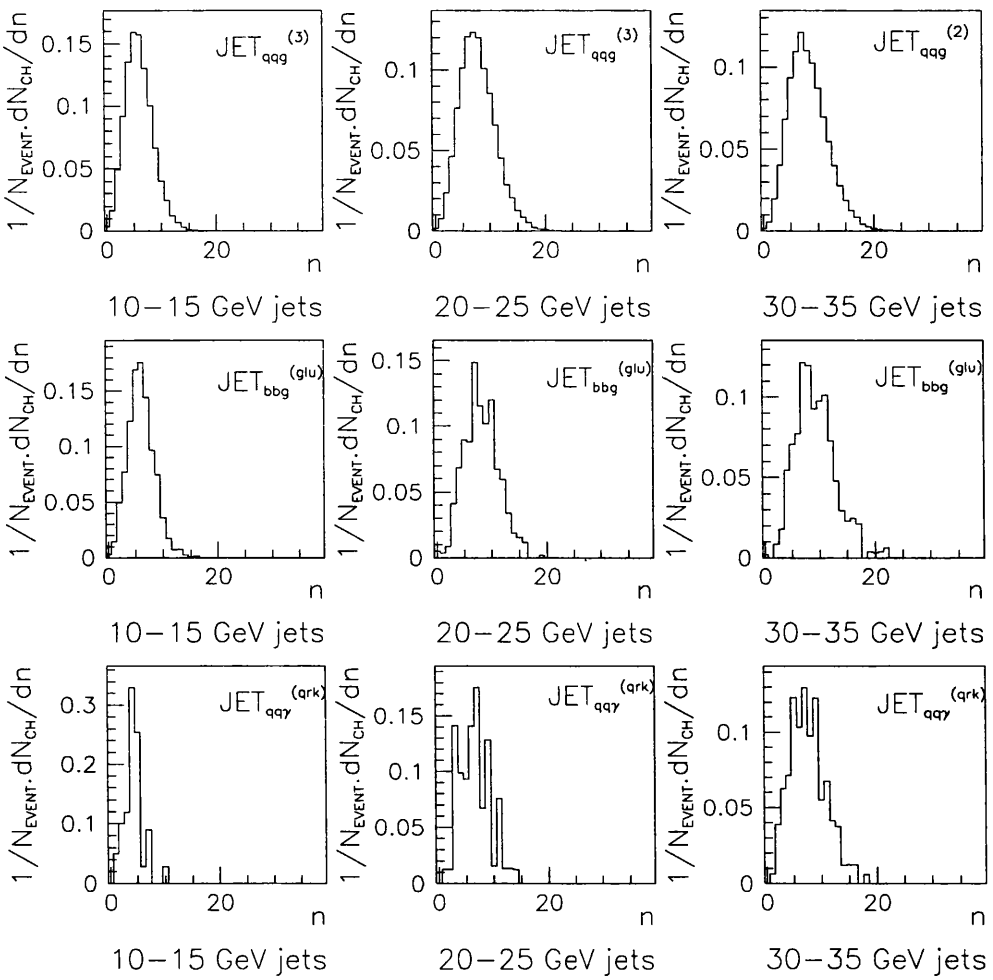

Figure A.2: *The multiplicity of charged particles in the gluon jet and lower-energy quark jet sub-samples. Three different jet energy ranges are given.*

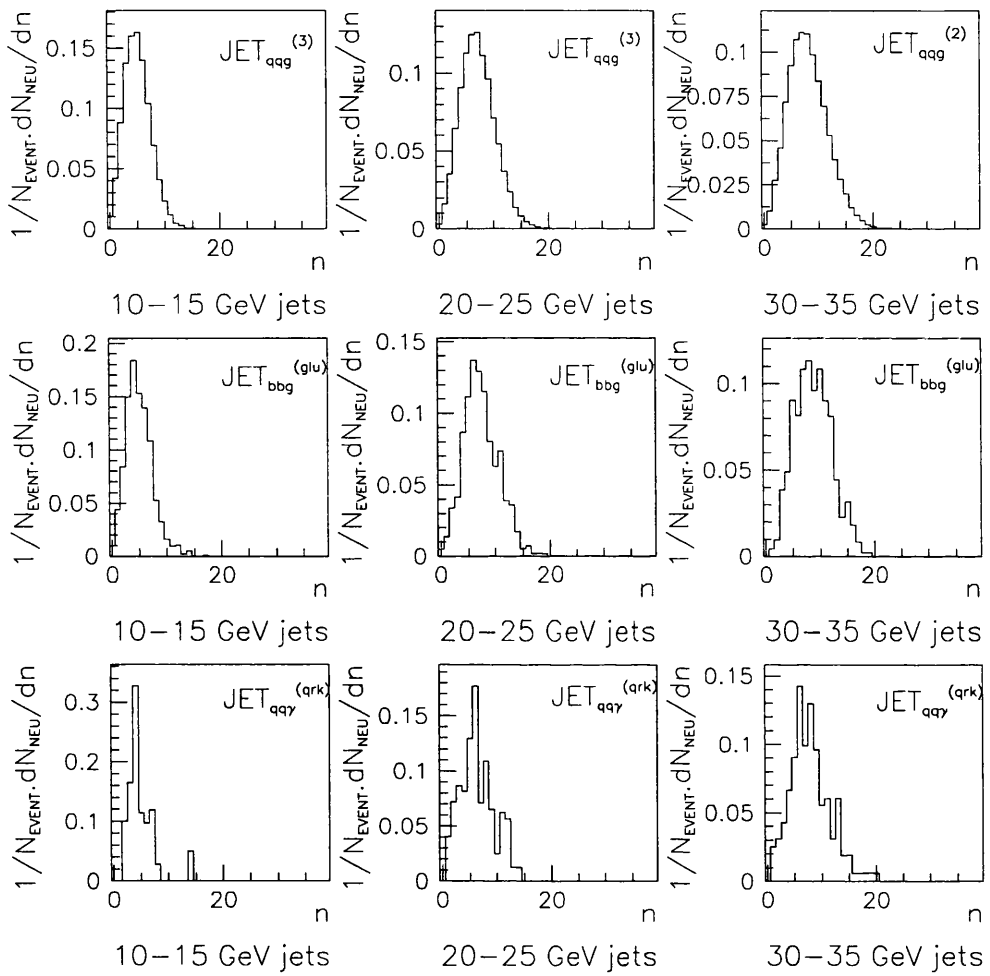

Figure A.3: *The multiplicity of neutral particles in the gluon jet and lower-energy quark jet sub-samples. Three different jet energy ranges are given.*

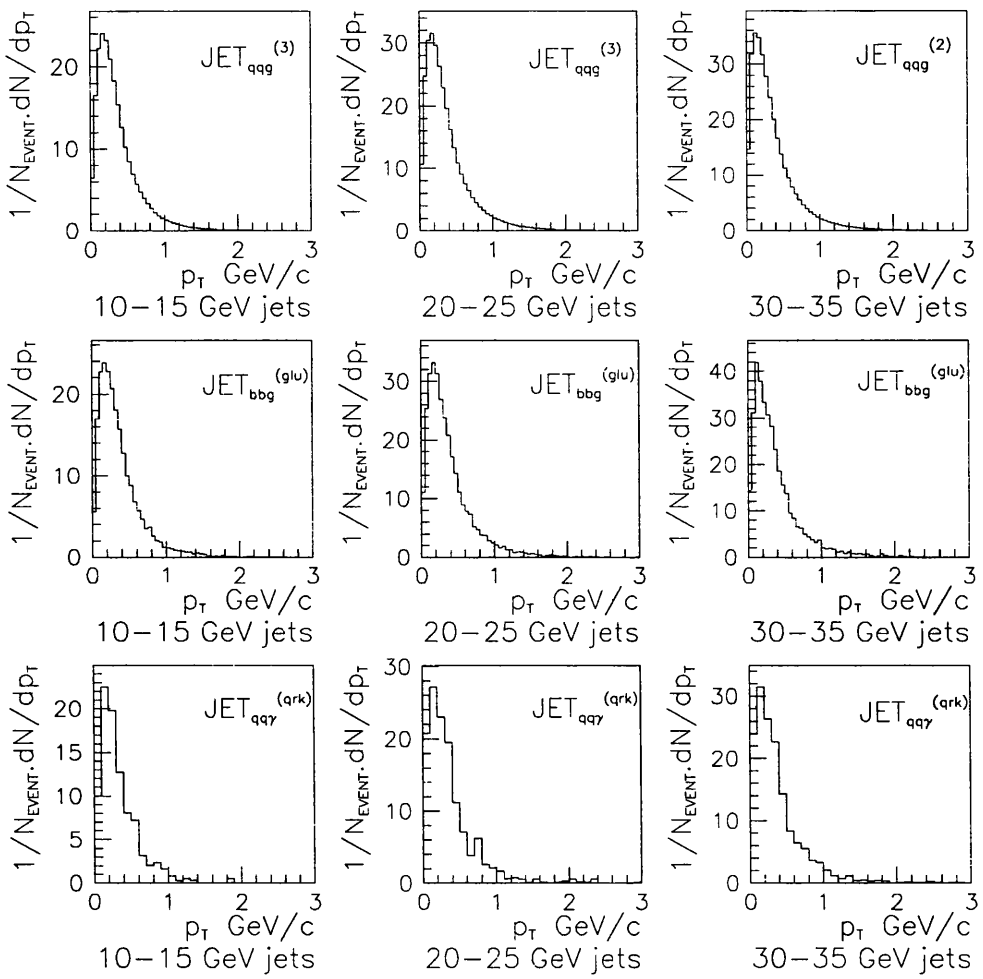

Figure A.4: *The transverse momentum of charged and neutral particles with respect to the jet axis in the gluon jet and lower-energy quark jet sub-samples. Three different jet energy ranges are given.*

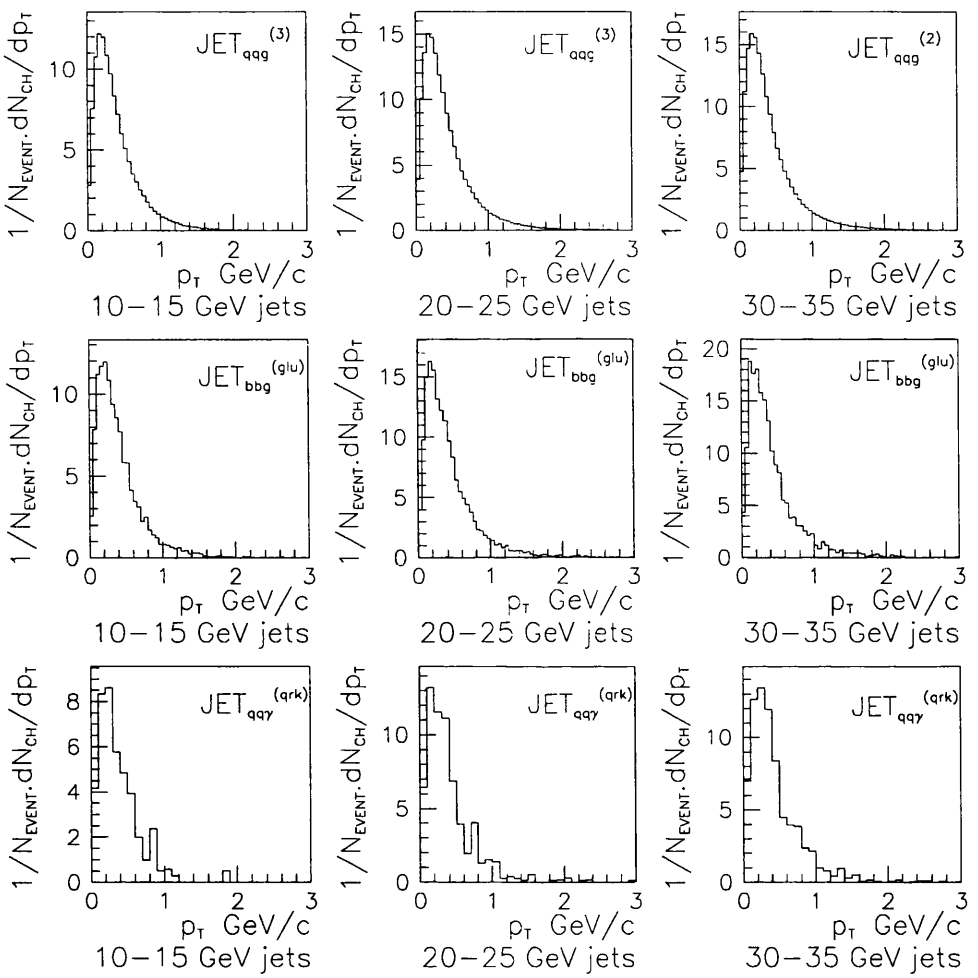

Figure A.5: *The transverse momentum of charged particles with respect to the jet axis in the gluon jet and lower-energy quark jet sub-samples. Three different jet energy ranges are given.*

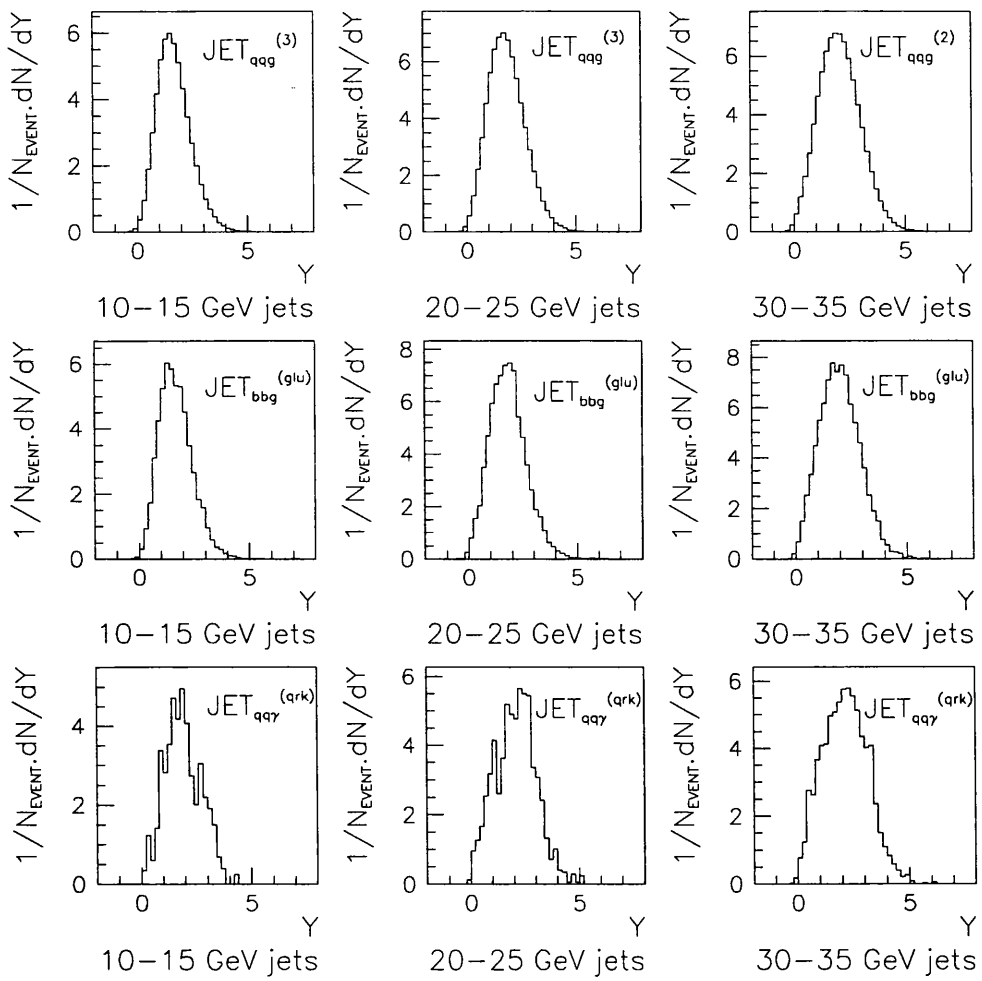

Figure A.6: *The rapidity of charged and neutral particles with respect to the jet axis in the gluon jet and lower-energy quark jet sub-samples. Three different jet energy ranges are given.*

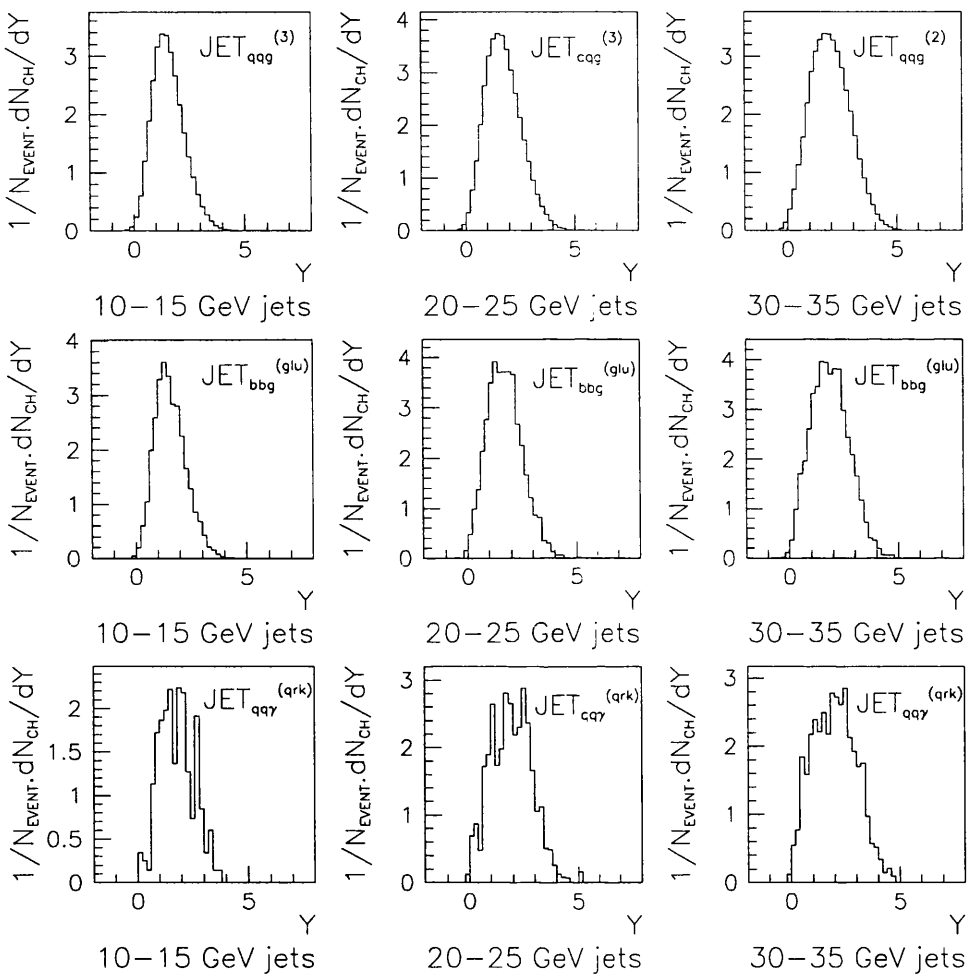

Figure A.7: *The rapidity of charged particles with respect to the jet axis in the gluon jet and lower-energy quark jet sub-samples. Three different jet energy ranges are given.*

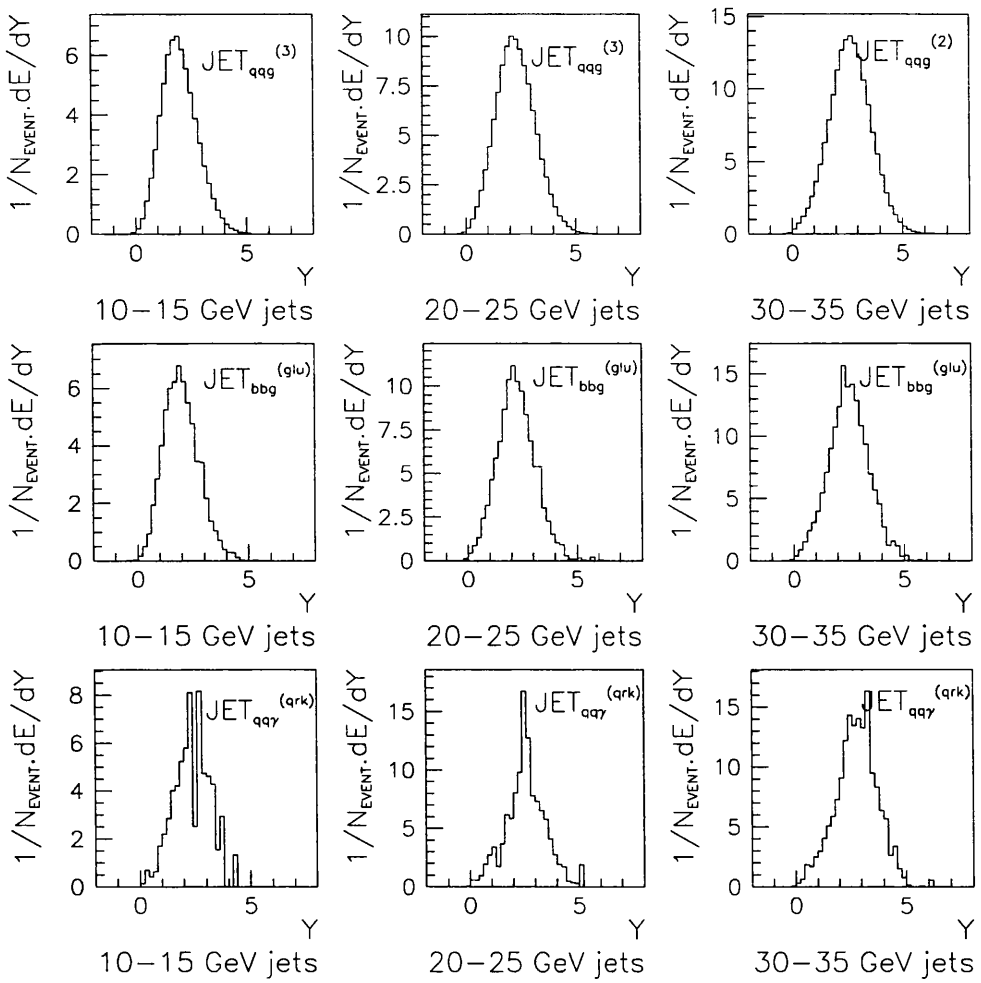

Figure A.8: *The rapidity of charged and neutral energy flow with respect to the jet axis in the gluon jet and lower-energy quark jet sub-samples. Three different jet energy ranges are given.*

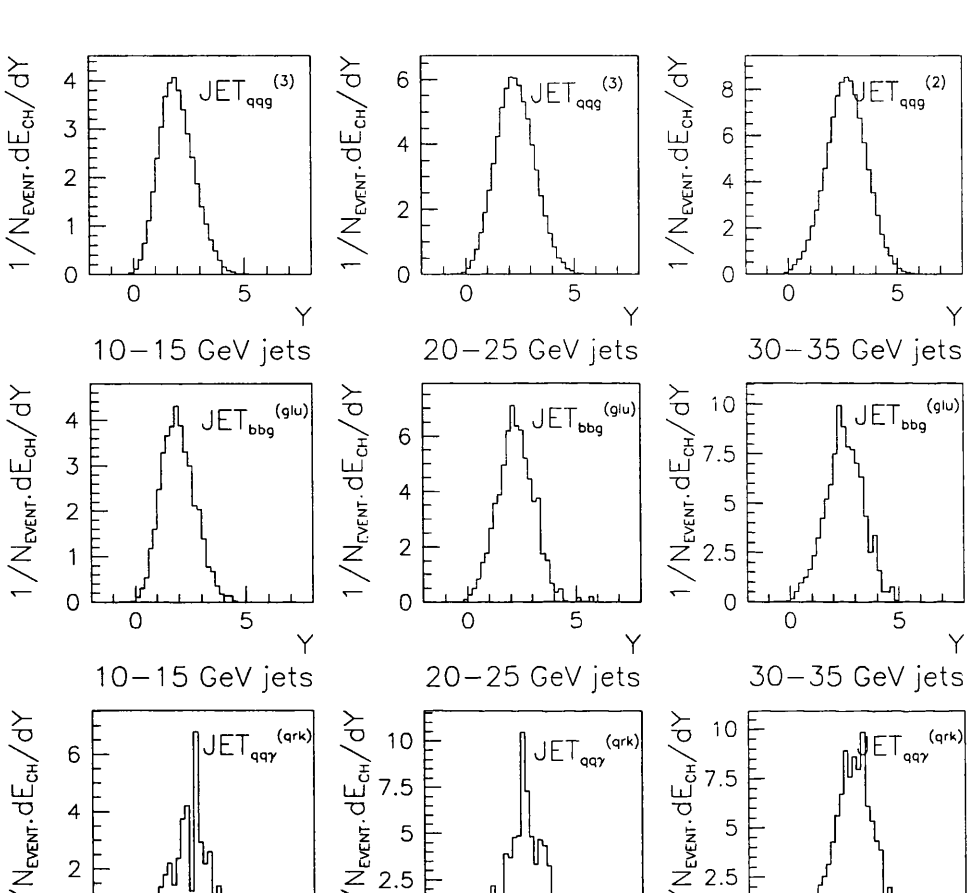

Figure A.9: *The rapidity of charged energy flow with respect to the jet axis in the gluon jet and lower-energy quark jet sub-samples. Three different jet energy ranges are given.*

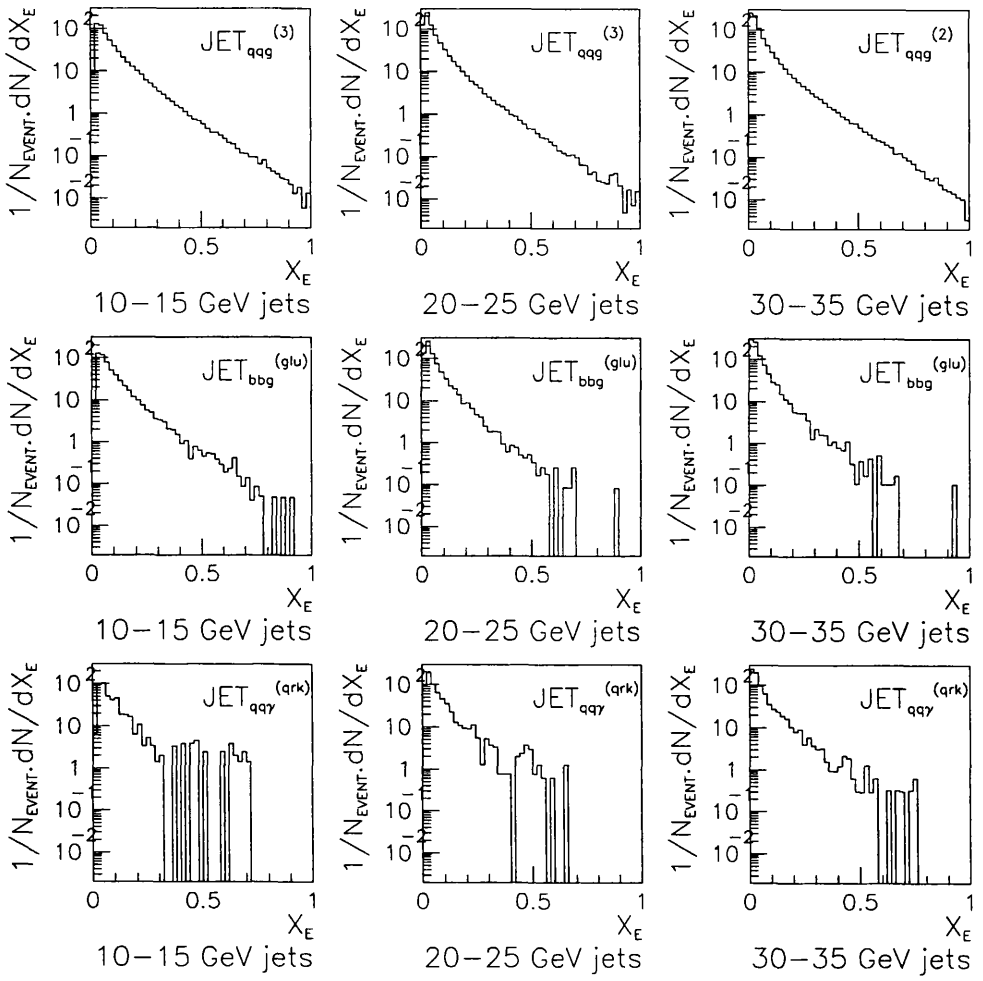

Figure A.10: *The fragmentation function of particles in the gluon jet and lower-energy quark jet sub-samples. Three different jet energy ranges are given.*

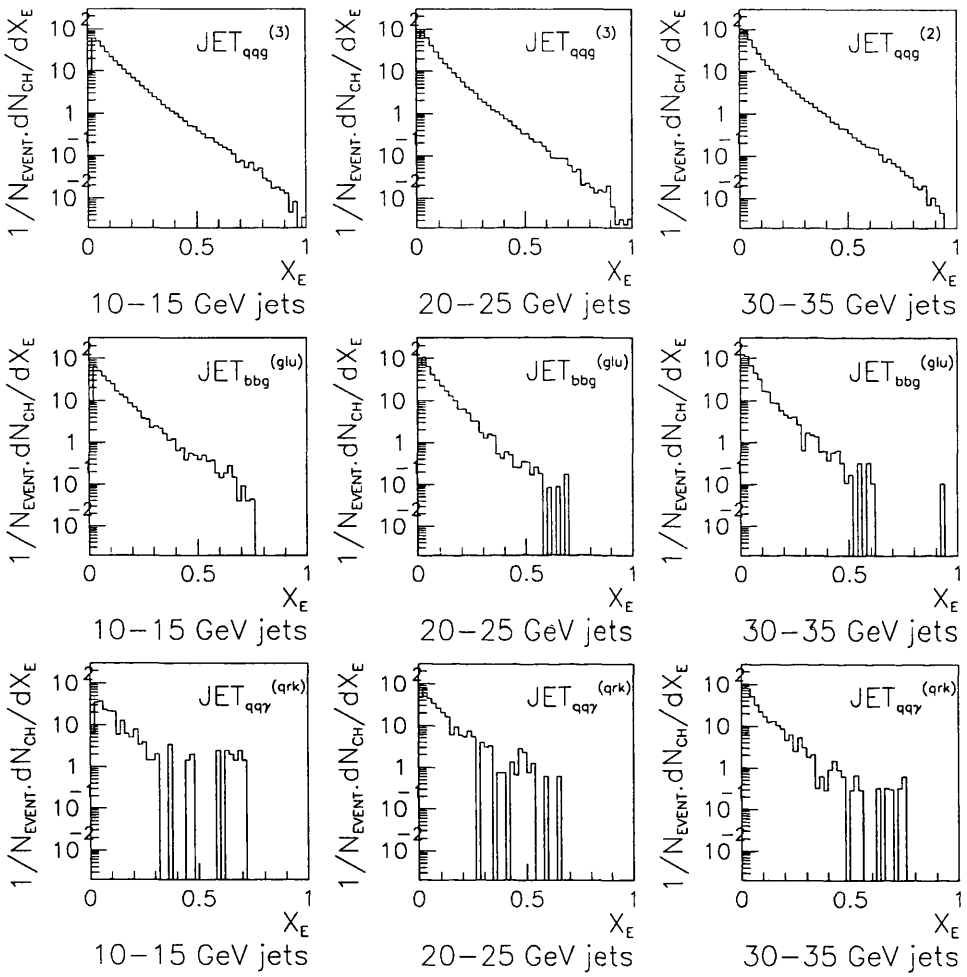

Figure A.11: *The fragmentation function of charged particles in the gluon jet and lower-energy quark jet sub-samples. Three different jet energy ranges are given.*

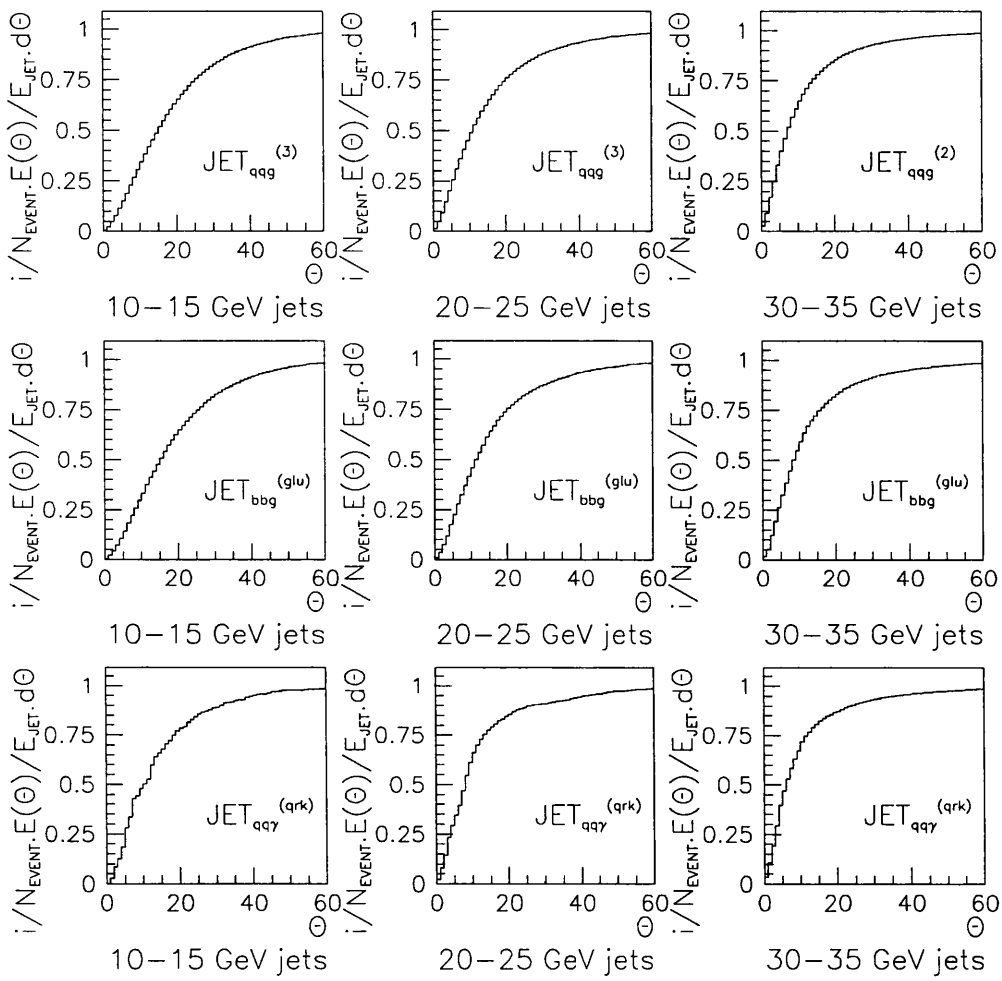

Figure A.12: *The fraction of the jet energy contained within cone angle θ around the jet axis in the gluon jet and lower-energy quark jet sub-samples. Three different jet energy ranges are given.*

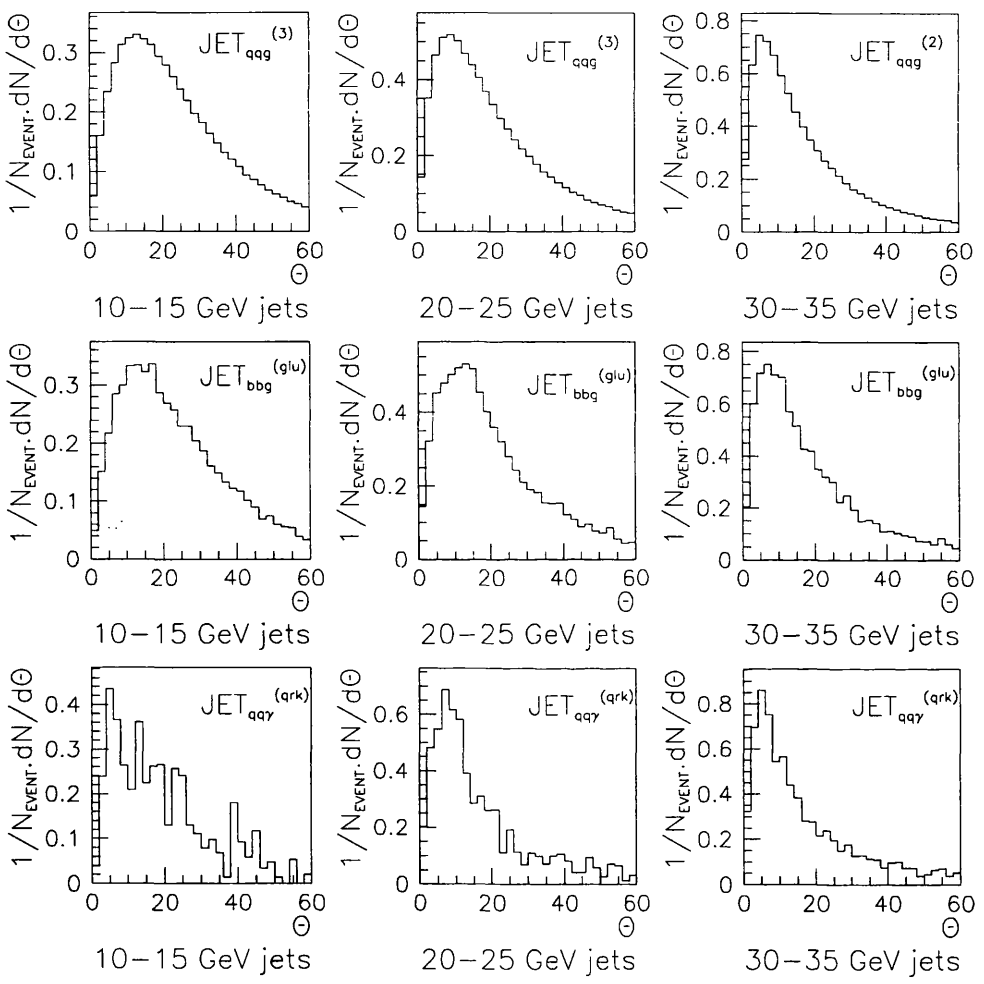

Figure A.13: *The multiplicity as a function of the angle to the jet axis in the gluon jet and lower-energy quark jet sub-samples. Three different jet energy ranges are given.*

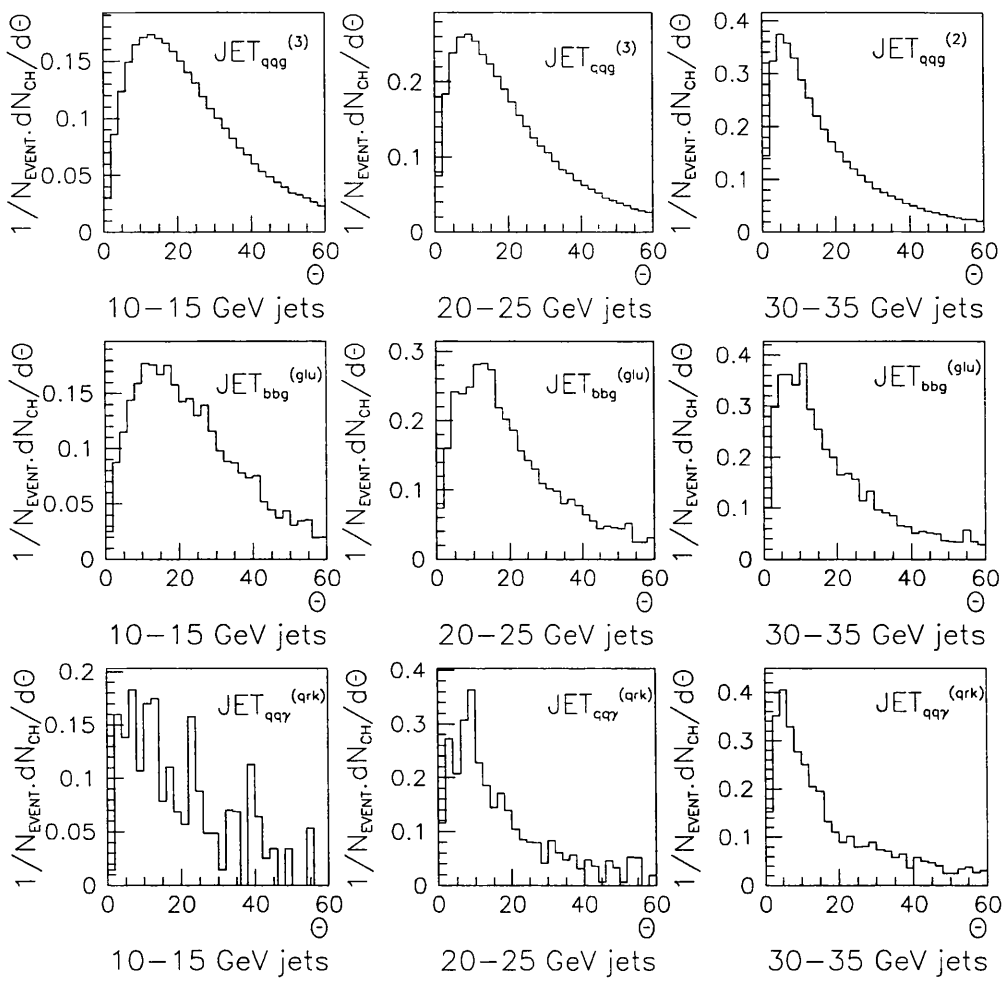

Figure A.14: *The charged multiplicity as a function of the angle to the jet axisin the gluon jet and lower-energy quark jet sub-samples. Three differentjet energy ranges are given.*

Appendix B

Unfolded quark and gluon jet properties.

The unfolded jet distributions for QUARK(C) and GLUON(B-C) are shown here. The explanation of the distributions can be found in Section 5.5. The distributions are normalised by the total number of events in the samples multiplied by the bin width. In each figure the QUARK(C) distribution is the dotted line and the GLUON(B-C) distribution is the solid line.

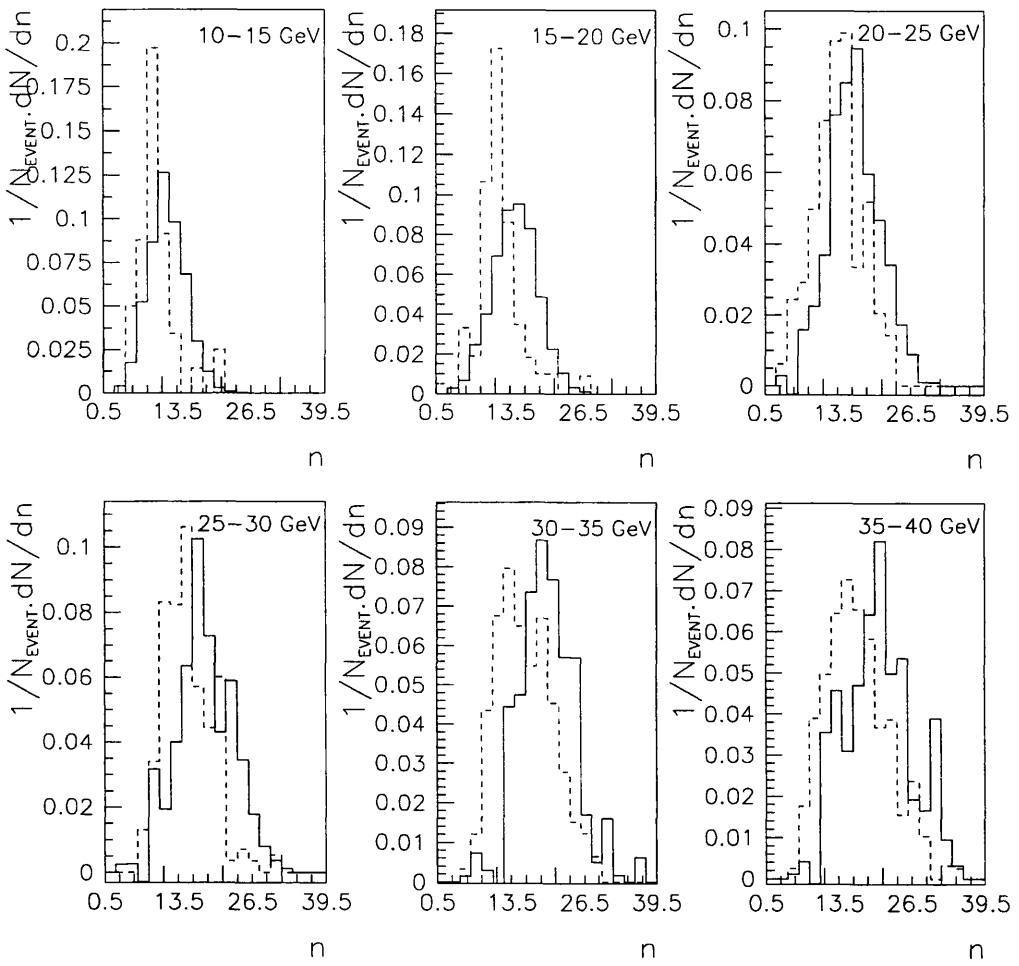

Figure B.1: *The multiplicity of charged and neutral particles for the QUARK(C) (dotted line) and unfolded GLUON(B-C) (solid line) measurements.*

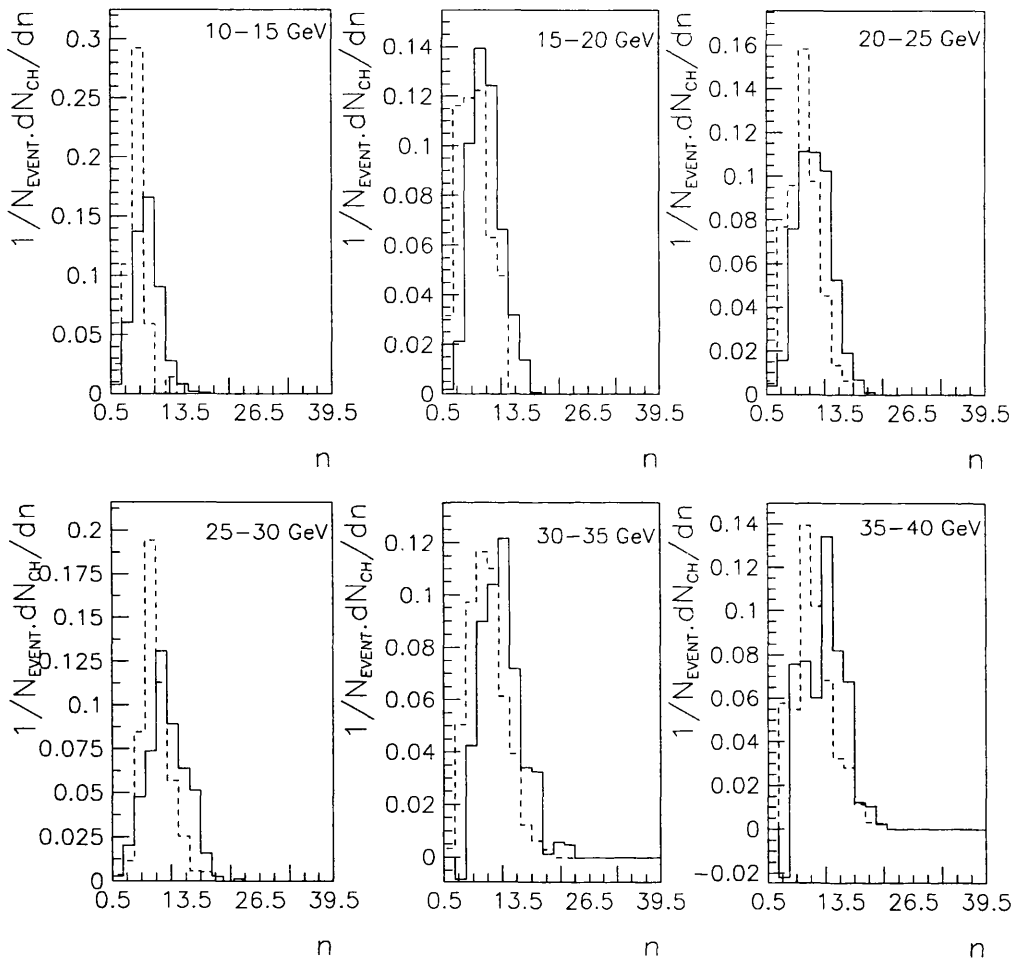

Figure B.2: *The multiplicity of charged particles for the QUARK(C) (dotted line) and unfolded GLUON(B-C) (solid line) measurements.*

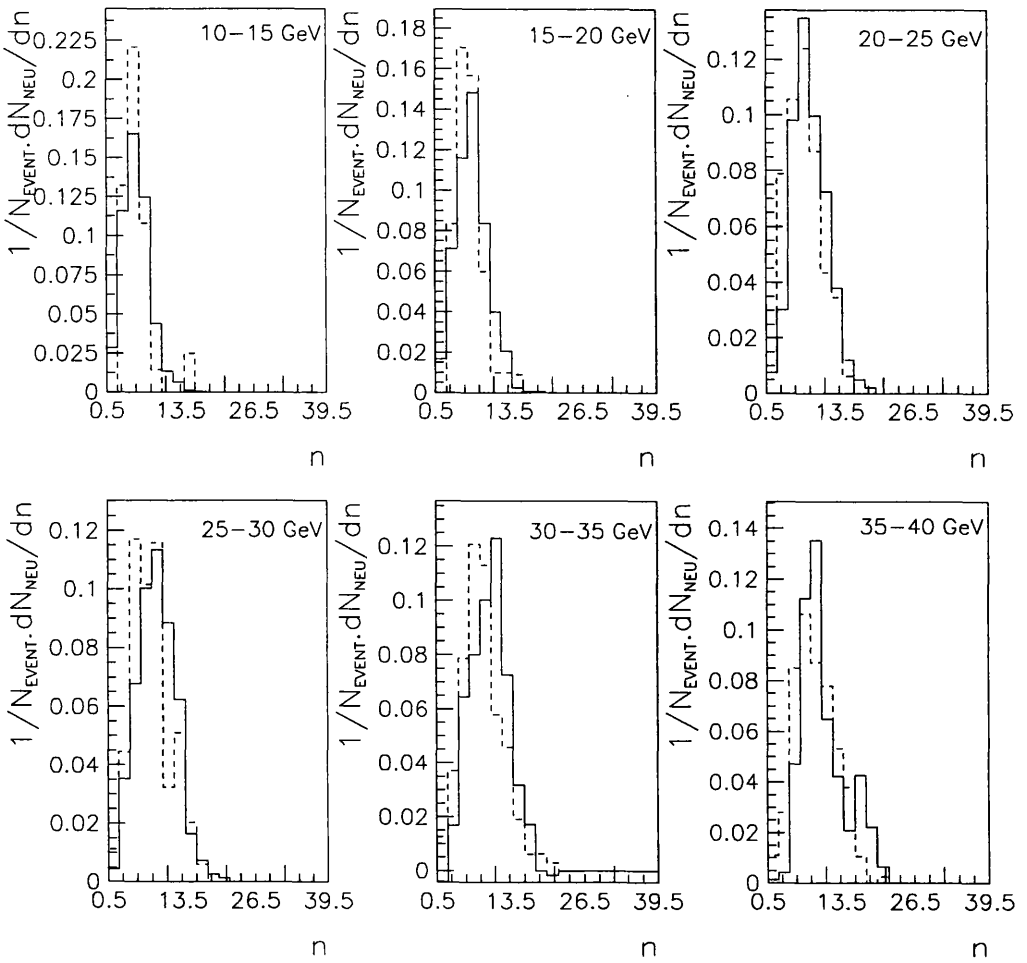

Figure B.3: *The multiplicity of neutral particles for the QUARK(C) (dotted line) and unfolded GLUON(B-C) (solid line) measurements.*

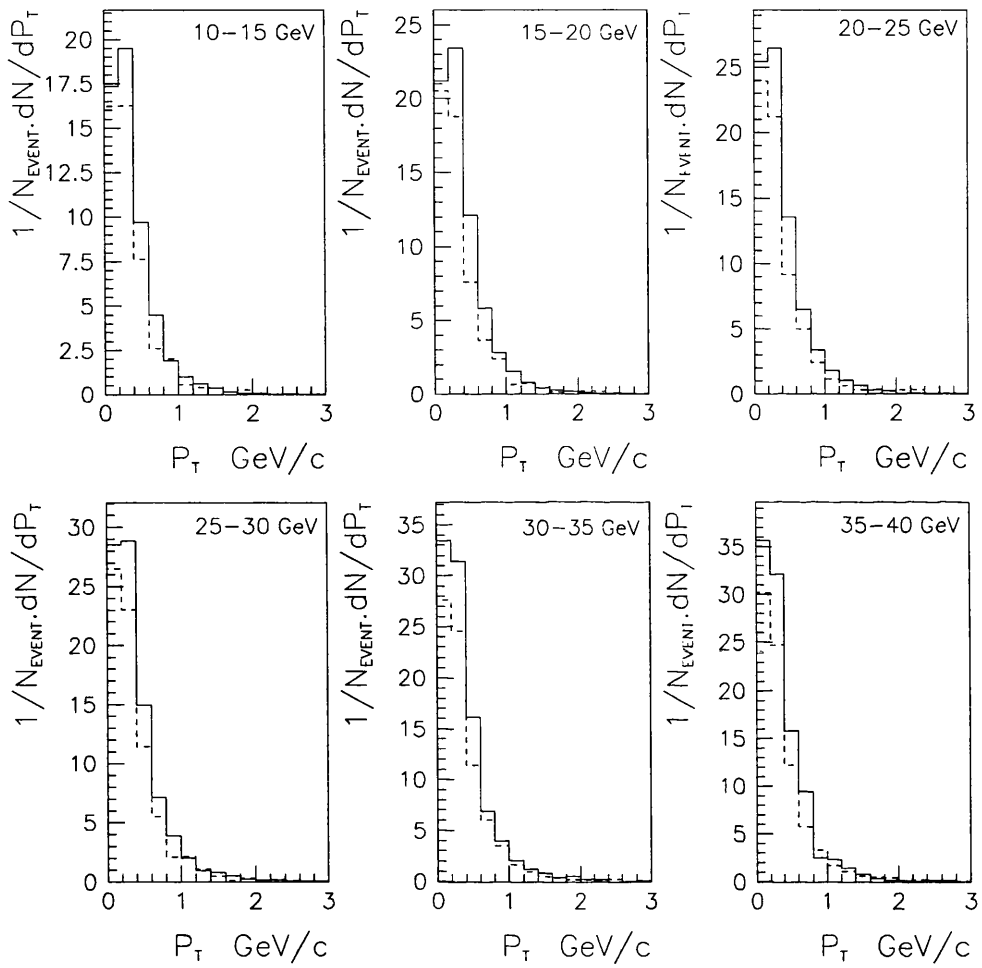

Figure B.4: *The transverse momentum of charged and neutral particles with respect to the jet axis for the QUARK(C) (dotted line) and unfolded GLUON(B-C) (solid line) measurements.*

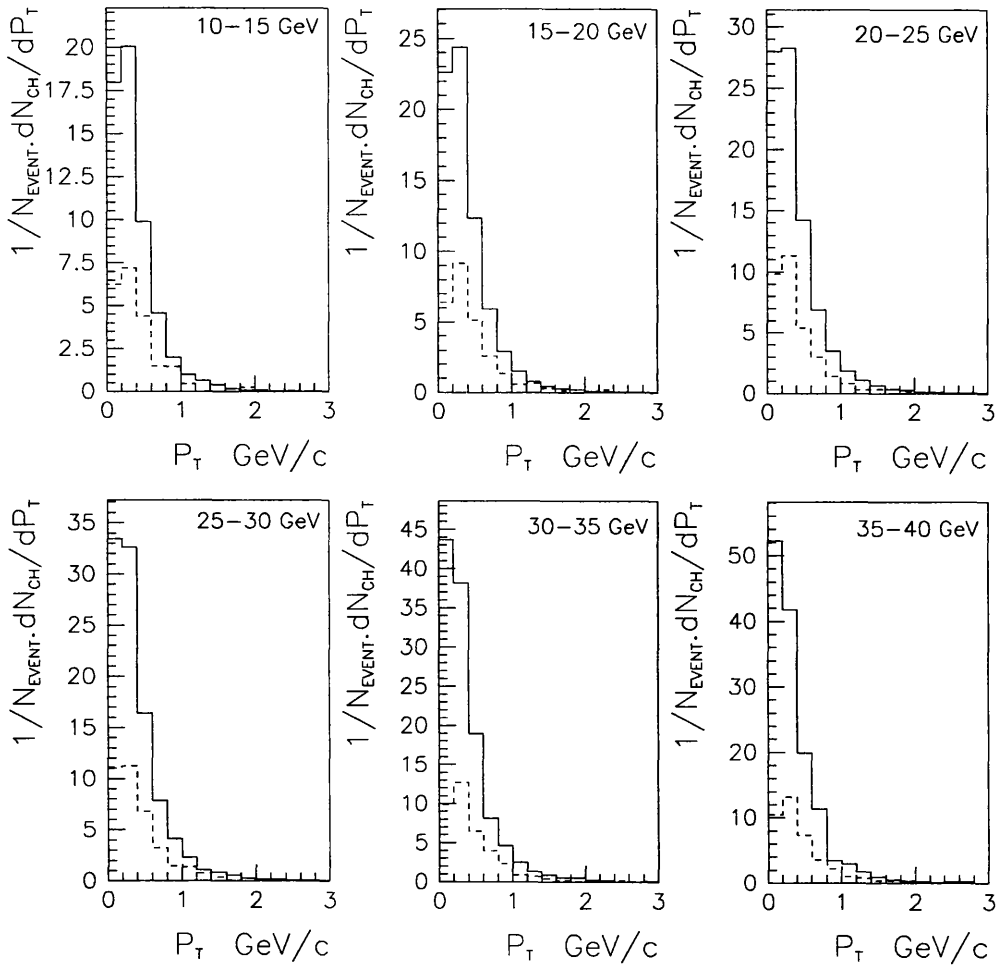

Figure B.5: *The transverse momentum of charged particles with respect to the jet axis for the QUARK(C) (dotted line) and unfolded GLUON(B-C) (solid line) measurements.*

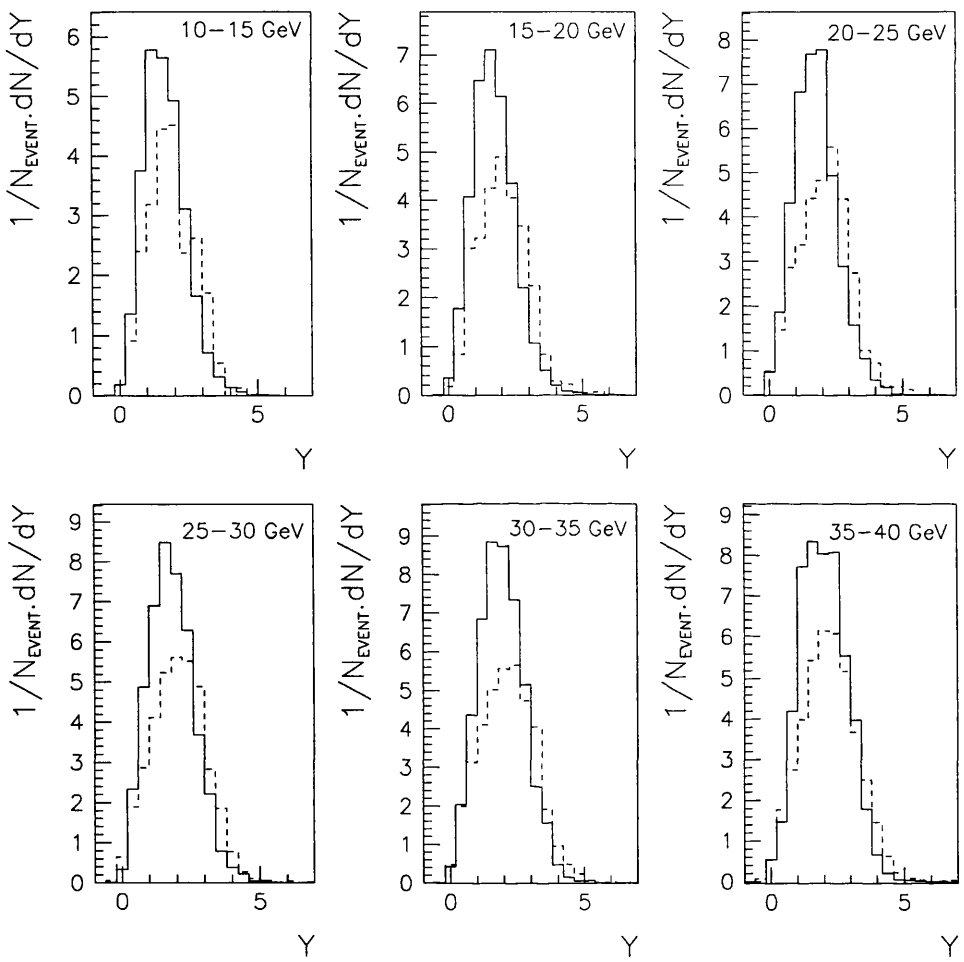

Figure B.6: *The rapidity of charged and neutral particles with respect to the jet axis for the QUARK(C) (dotted line) and unfolded GLUON(B-C) (solid line) measurements.*

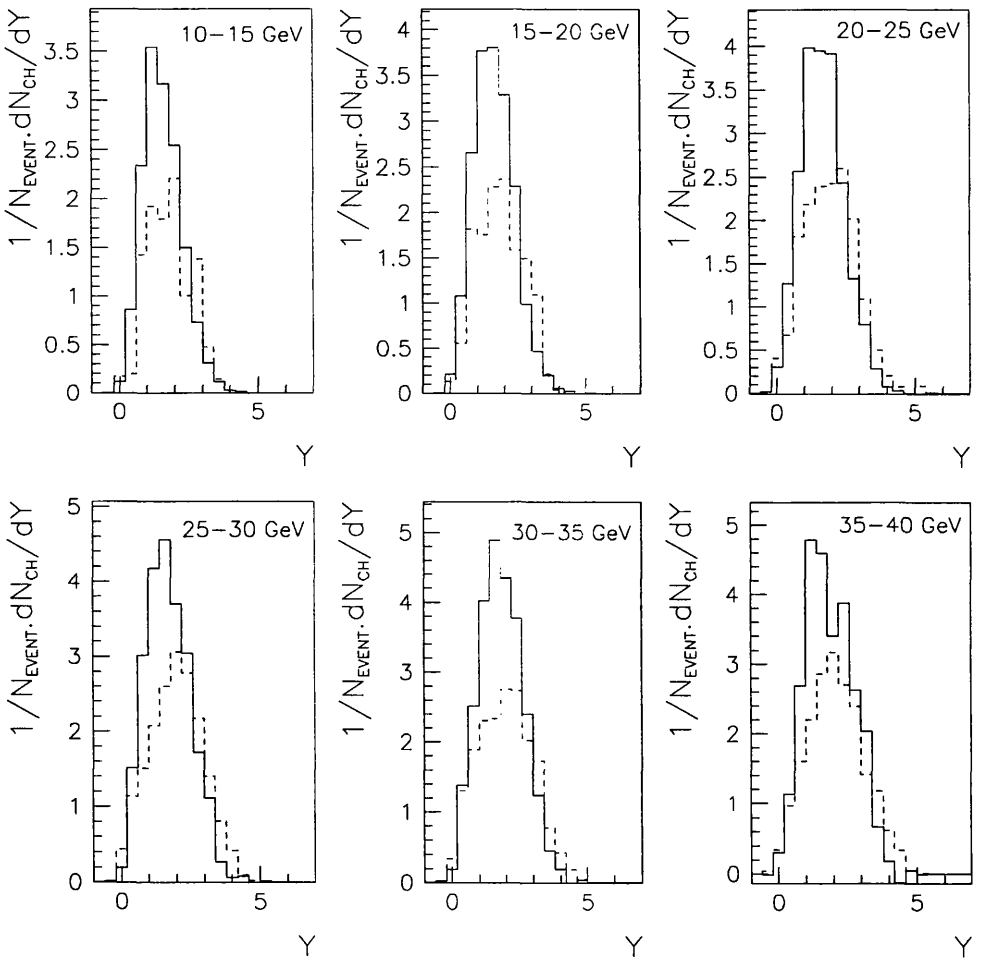

Figure B.7: *The rapidity of charged particles with respect to the jet axis for the QUARK(C) (dotted line) and unfolded GLUON(B-C) (solid line) measurements.*

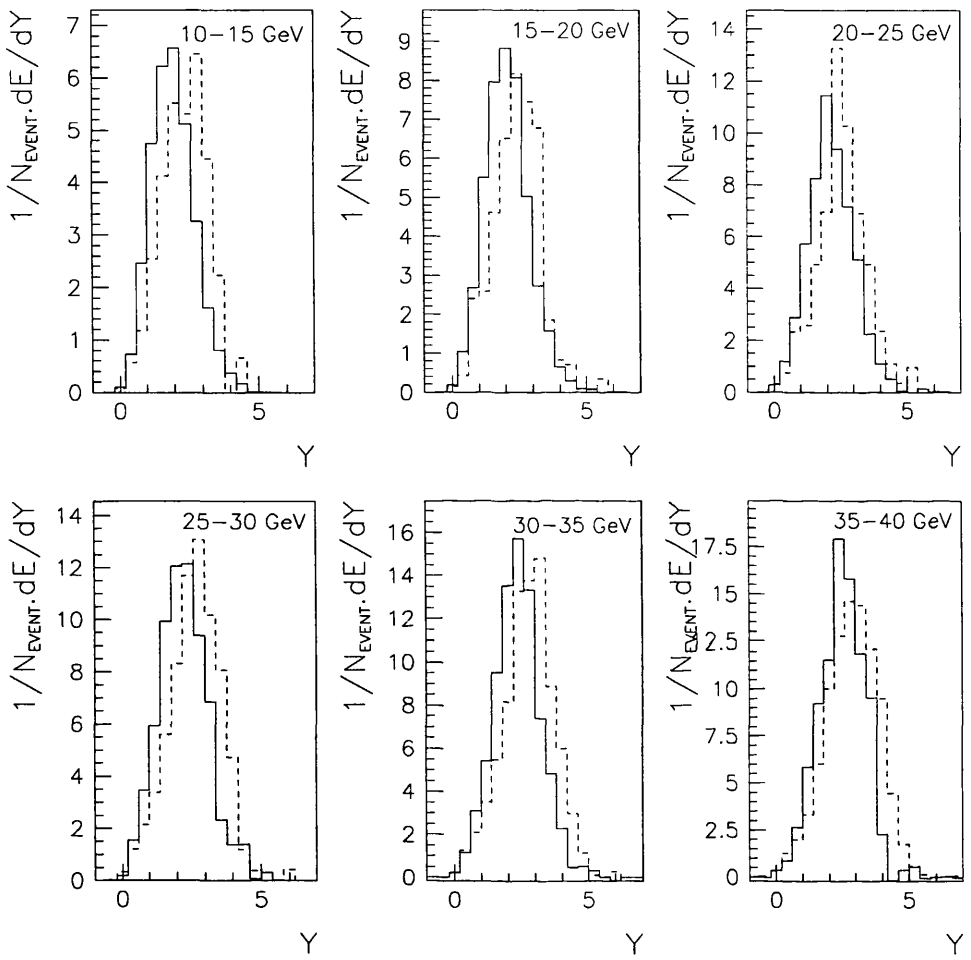

Figure B.8: *The rapidity of charged and neutral energy flow with respect to the jet axis for the QUARK(C) (dotted line) and unfolded GLUON(B-C) (solid line) measurements.*

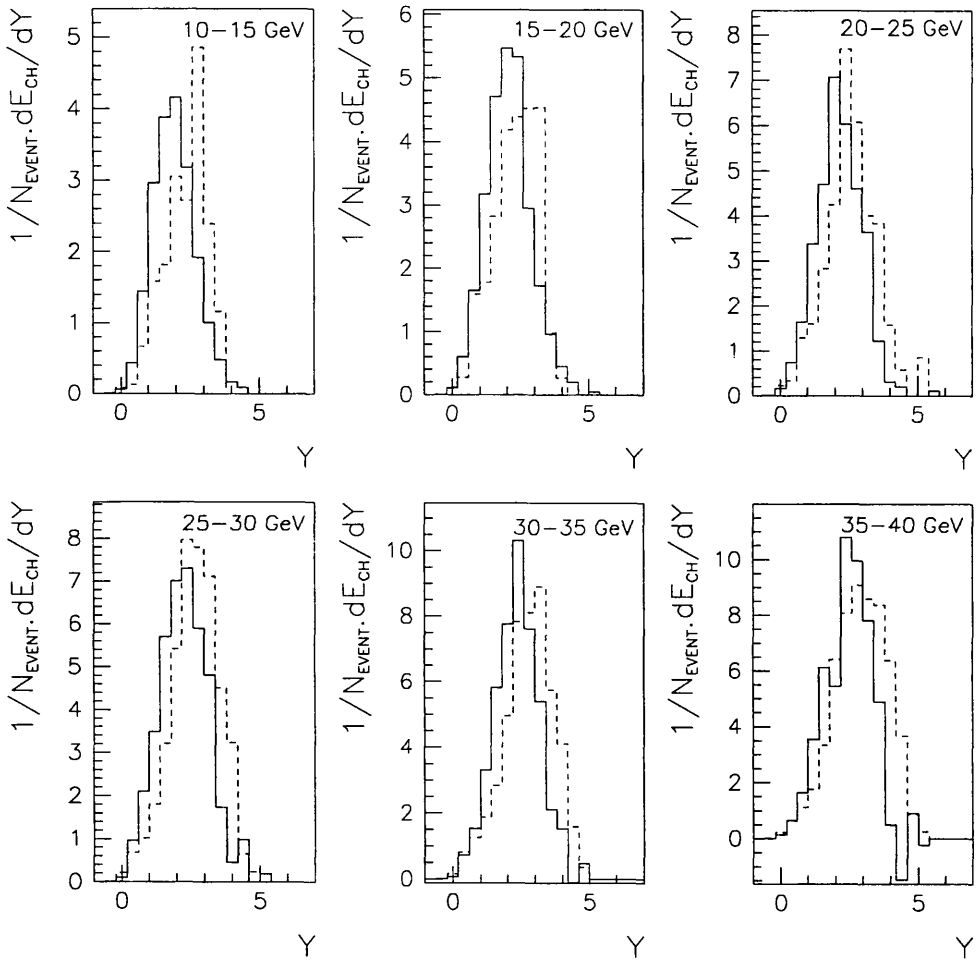

Figure B.9: *The rapidity of charged energy flow with respect to the jet axis for the QUARK(C) (dotted line) and unfolded GLUON(B-C) (solid line) measurements.*

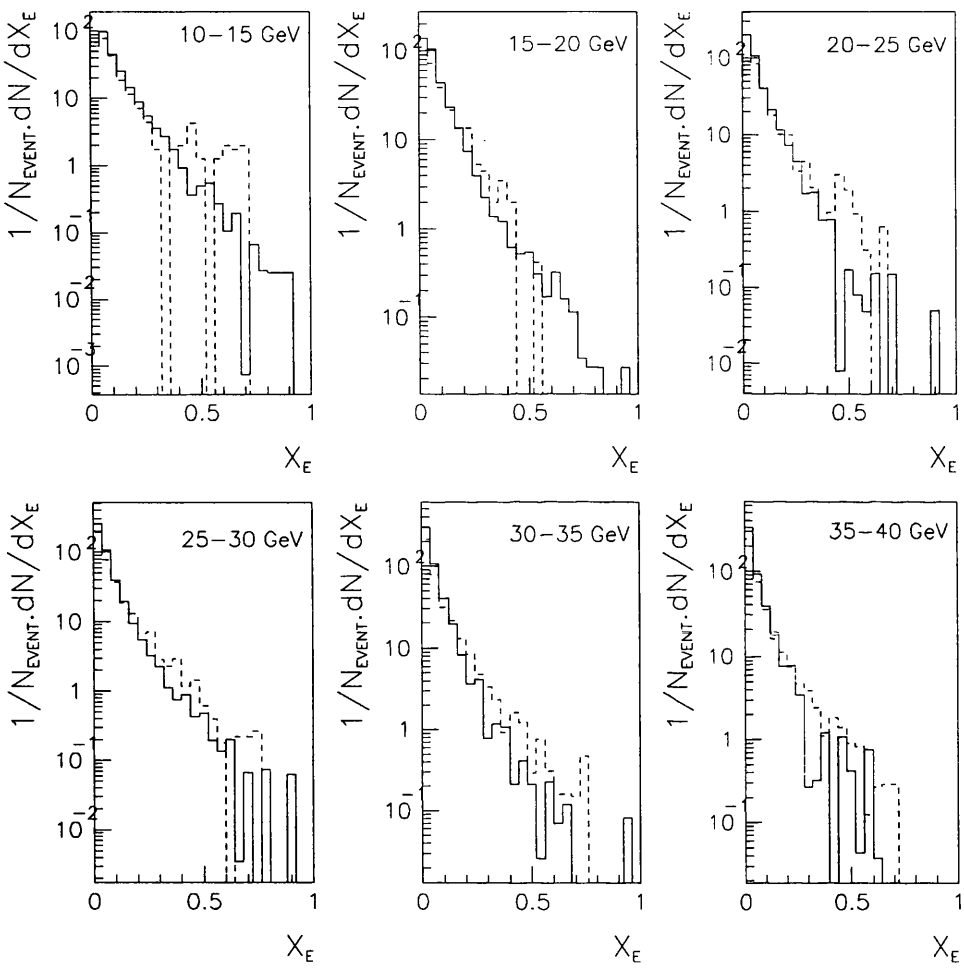

Figure B.10: *The fragmentation function of particles for the QUARK(C) (dotted line) and unfolded GLUON(B-C) (solid line) measurements.*

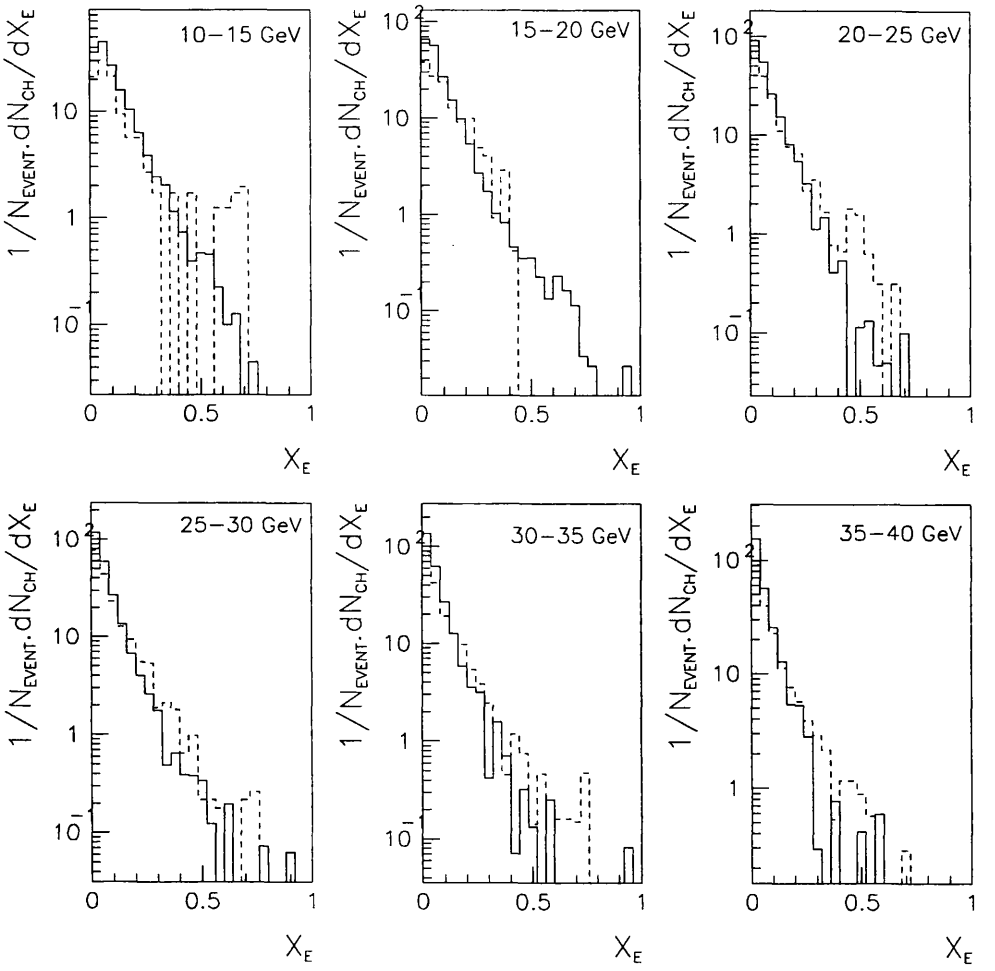

Figure B.11: *The fragmentation function of particles for the QUARK(C) (dotted line) and unfolded GLUON(B-C) (solid line) measurements.*

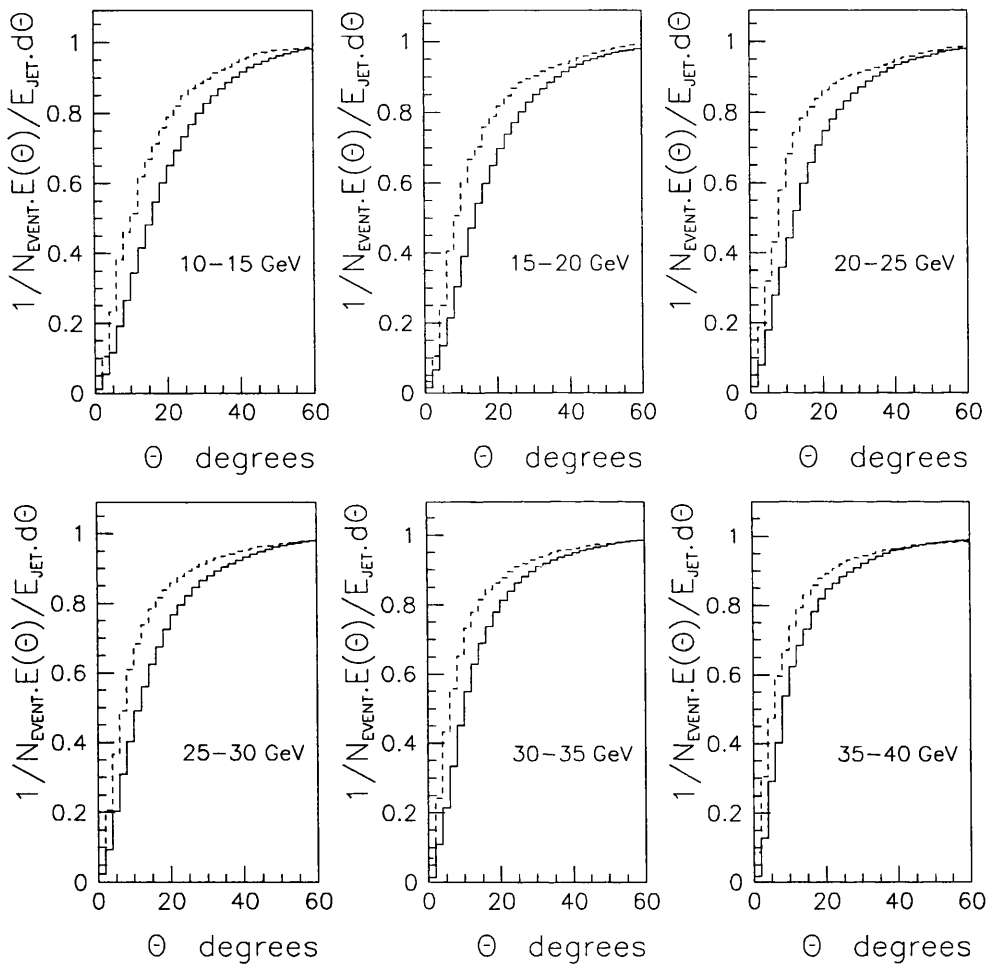

Figure B.12: *The fraction of the jet energy contained within cone angle θ around the jet axis for the QUARK(C) (dotted line) and unfolded GLUON(B-C) (solid line) measurements.*

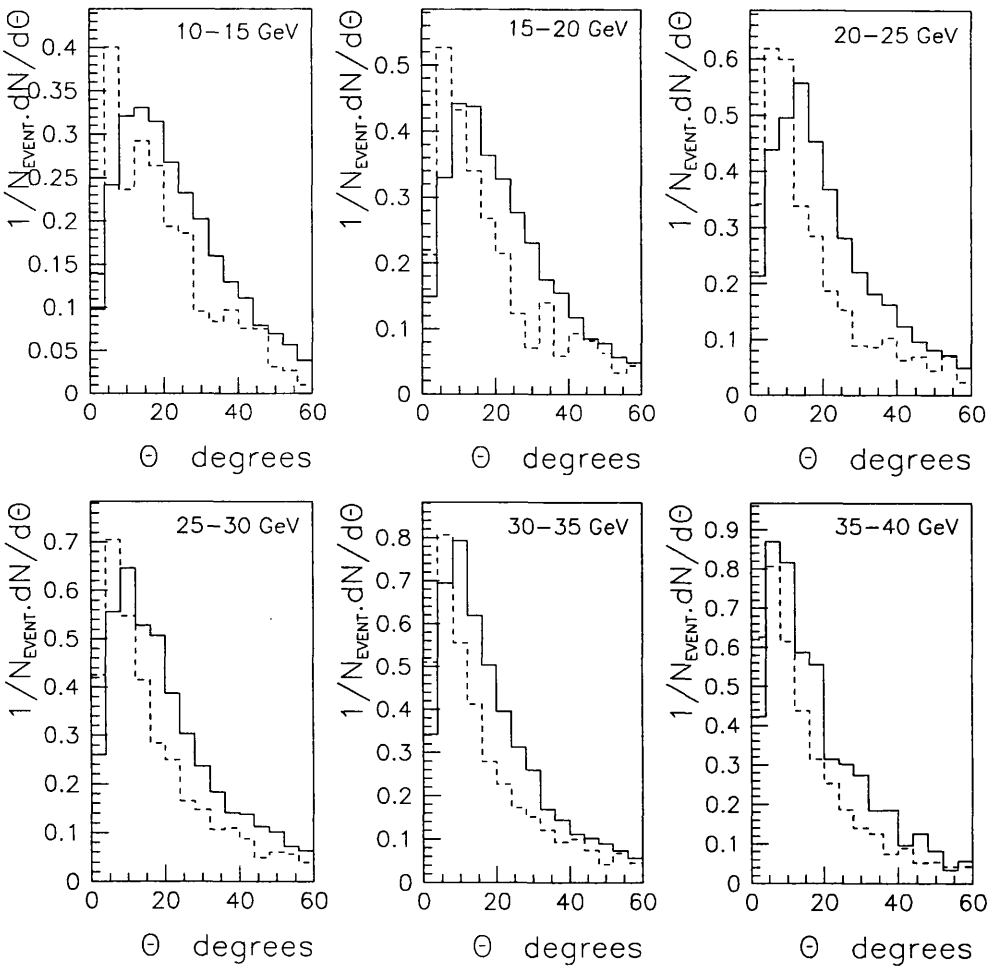

Figure B.13: *The multiplicity as a function of the angle to the jet axis for the QUARK(C) (dotted line) and unfolded GLUON(B-C) (solid line) measurements.*

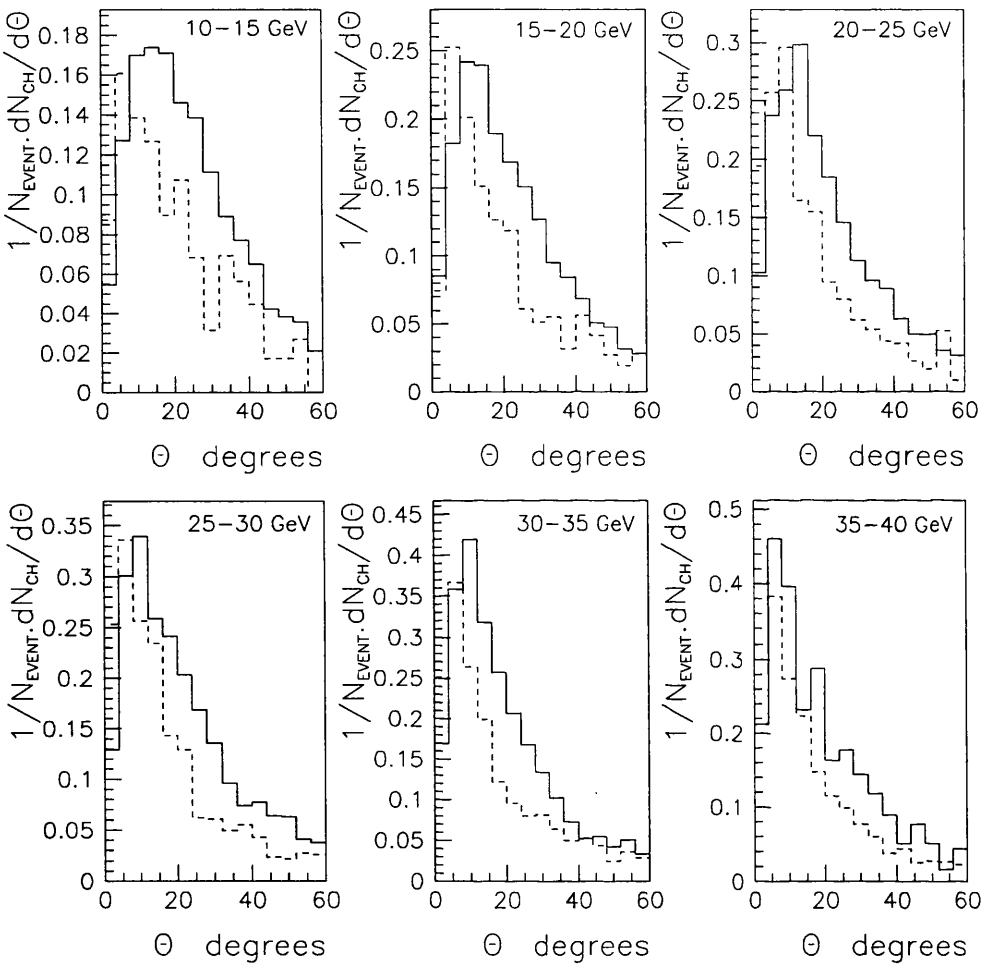

Figure B.14: *The multiplicity as a function of the angle to the jet axis for the QUARK(C) (dotted line) and unfolded GLUON(B-C) (solid line) measurements.*